EFFECTS OF HIGH STRENGTH STEEL BARS AND STEEL CASING ON THE RESPONSE OF DRILLED SHAFTS

Final Report

PROJECT SPR 765

Oregon Department of Transportation

EFFECTS OF HIGH STRENGTH STEEL BARS AND STEEL CASING ON THE RESPONSE OF DRILLED SHAFTS

Final Report

PROJECT SPR 765

by

Armin W. Stuedlein

Qiang Li

for

Oregon Department of Transportation
Research Section
555 13th Street NE, Suite 1
Salem OR 97301

and

Federal Highway Administration
1200 New Jersey Avenue SE
Washington, DC 20590

January 2018

Technical Report Documentation Page

1. Report No. FHWA-OR-RD-18-09	2. Government Accession No.	3. Recipient's Catalog No.

4. Title and Subtitle Effects of High Strength Steel Bars and Steel Casing on the Response of Drilled Shafts	5. Report Date January 2018 6. Performing Organization Code
7. Author(s) Armin W. Stuedlein, Qiang Li	8. Performing Organization Report No. SPR 765
9. Performing Organization Name and Address School of Civil and Construction Engineering Oregon State University 101 Kearney Hall, Corvallis, OR 97331	10. Work Unit No. (TRAIS) 11. Contract or Grant No.
12. Sponsoring Agency Name and Address Oregon Dept. of Transportation Research Section and Federal Highway Admin. 555 13th Street NE, Suite 1 1200 New Jersey Avenue SE Salem, OR 97301 Washington, DC 20590	13. Type of Report and Period Covered Final Report 14. Sponsoring Agency Code

15. Supplementary Notes: Technical Advisory Committee: Susan Ortiz (ODOT), Albert Nako (ODOT), Tanarat Potisuk (ODOT), Tim Rogers (FHWA), Kira Glover-Cutter (Research Coordinator, ODOT)

16. Abstract: The amount of steel reinforcement in drilled shaft foundations has increased over the past several decades to account for anticipated seismic hazards. Increased reinforcement may lead to a higher frequency of anomalies within shafts due to the increased difficulty for concrete to flow through reduced clearance between the reinforcement. High-strength steel reinforcement and permanent steel casing may be used to mitigate this concern. However, use of a lower steel area my serve to reduce flexural stiffness, and depending on the method of construction, steel casing may result in reduced axial load transfer to the surrounding soil. Thus, existing analytical approaches need to be evaluated for modern construction methods, and new approaches developed if necessary to ensure desired performance criteria are met. Four full-scale instrumented test shafts with various composite cross-sections were constructed to investigate load transfer under axial and lateral loads and the effect of high strength steel reinforcement and steel casing. Empirical, region-specific axial and lateral load transfer models were proposed for use with drilled shafts constructed in the Willamette Valley. The effects of permanent casing on axial load transfer were determined, and synthesized with existing observations to provide an up-to-date reference on the reductions expected based on construction sequencing and installation methods. The lateral responses of the test drilled shaft foundations indicated that the high-strength reinforcement could be used without detriment to the lateral performance; and that the shafts with permanent steel casing responded in a more resilient manner than uncased shafts at the same nominal diameter due to their significantly greater flexural rigidity.

17. Key Words Drilled shafts, lateral loading, axial loading, high-strength reinforcement, permanent steel casing	18. Distribution Statement Copies available from NTIS, and online at http://www.oregon.gov/ODOT/Programs/Pages/Research-Publications.aspx

19. Security Classification (of this report) Unclassified	20. Security Classification (of this page) Unclassified	21. No. of Pages 262	22. Price

Technical Report Form DOT F 1700.7 (8-72) Reproduction of completed page authorized ♻ Printed on recycled paper

SI* (MODERN METRIC) CONVERSION FACTORS

APPROXIMATE CONVERSIONS TO SI UNITS

Symbol	When You Know	Multiply By	To Find	Symbol
		LENGTH		
in	inches	25.4	millimeters	mm
ft	feet	0.305	meters	m
yd	yards	0.914	meters	m
mi	miles	1.61	kilometers	km
		AREA		
in^2	square inches	645.2	millimeters squared	mm^2
ft^2	square feet	0.093	meters squared	m^2
yd^2	square yards	0.836	meters squared	m^2
ac	acres	0.405	hectares	ha
mi^2	square miles	2.59	kilometers squared	km^2
		VOLUME		
fl oz	fluid ounces	29.57	milliliters	ml
gal	gallons	3.785	liters	L
ft^3	cubic feet	0.028	meters cubed	m^3
yd^3	cubic yards	0.765	meters cubed	m^3
NOTE: Volumes greater than 1000 L shall be shown in m^3.				
		MASS		
oz	ounces	28.35	grams	g
lb	pounds	0.454	kilograms	kg
T	short tons (2000 lb)	0.907	megagrams	Mg
		TEMPERATURE (exact)		
°F	Fahrenheit	(F-32)/1.8	Celsius	°C

APPROXIMATE CONVERSIONS FROM SI UNITS

Symbol	When You Know	Multiply By	To Find	Symbol
		LENGTH		
mm	millimeters	0.039	inches	in
m	meters	3.28	feet	ft
m	meters	1.09	yards	yd
km	kilometers	0.621	miles	mi
		AREA		
mm^2	millimeters squared	0.0016	square inches	in^2
m^2	meters squared	10.764	square feet	ft^2
m^2	meters squared	1.196	square yards	yd^2
ha	hectares	2.47	acres	ac
km^2	kilometers squared	0.386	square miles	mi^2
		VOLUME		
ml	milliliters	0.034	fluid ounces	fl oz
L	liters	0.264	gallons	gal
m^3	meters cubed	35.315	cubic feet	ft^3
m^3	meters cubed	1.308	cubic yards	yd^3
		MASS		
g	grams	0.035	ounces	oz
kg	kilograms	2.205	pounds	lb
Mg	megagrams	1.102	short tons (2000 lb)	T
		TEMPERATURE (exact)		
°C	Celsius	1.8C+32	Fahrenheit	°F

*SI is the symbol for the International System of Measurement

ACKNOWLEDGEMENTS

The authors wish to acknowledge the many agencies, firms, and individuals have contributed to this ongoing work. The authors are grateful for support from the Oregon Department of Transportation through Grant SPR 765 and the Pacific Northwest Transportation Consortium (PacTrans) through Grant DTRT12-UTC10. The West Coast Chapter (WCC) of the ADSC contributed funds to help offset material costs associated with construction of the test shafts, with critical coordination efforts and guidance provided by John Starcevich (Malcolm Drilling, Inc.), Becky Patterson (WCC ADSC), Rick Walsh (Hayward Baker, Inc.), and the co-leadership of the WCC ADSC portion of the work by Antonio Marinucci. Malcolm Drilling, Inc., constructed the test shafts, Pacific Foundation, Inc. installed the reaction piles, and Ralph's Concrete donated concrete pumping services. Grade 80 solid and hollow bar was contributed by ConTech Systems, whereas Grade 60 bar and all cage fabrication was donated by PJ's Rebar. Steel casing was donated by Skyline Steel, and Grade 150 reaction bar was contributed by Williams Form, Inc. Spacers and bar boots were provided by Foundation Technologies. Cross-hole sonic logging services was donated by Bernie Hertlein of GEI Consultants, and thermal integrity profilometer thermal wires and logging services were provided by Jim Zammataro and Daniel Belardo of Pile Dynamics, Inc. The significant contributions provided by these member firms and corresponding specific individuals were critical for accomplishing this work and are a testament to their interest in advancing the profession.

DISCLAIMER

TABLE OF CONTENTS

APPENDIX

LIST OF TABLES

LIST OF FIGURES

1.0 INTRODUCTION

1.1 STATEMENT OF PROBLEM

Drilled shafts provide significant geotechnical resistance for support of highway bridges and are widely used to meet their structural foundation requirements. Due to changes in construction methods and poor near-surface soils, the use of permanent steel casing for drilled shaft installation has increased. However, geotechnical design models for axial and lateral resistance of drilled shafts are largely based on soil-concrete interfaces, not soil-steel interfaces associated with large diameter steel casing. Owing to the improved understanding of our regional seismic hazards, the amount of steel reinforcement used in drilled shaft construction has increased over the past several decades, creating a construction concern for engineers: the greater steel area results in a reduced clearance between adjacent reinforcement bars in the steel cage, such that concrete has an increased difficulty in flowing through the cage and corresponding likelihood for voids and defects within the shaft, which can lead to poor structural and geotechnical performance. The use of high-strength reinforcement steel can lead to improved clearance within the steel cage, mitigating concreting issues. The use of steel casing, the amount of steel area, and the corresponding yield stress control the axial and lateral resistance of the shaft. However, depending on the method of construction, the steel casing may result in reduced axial load transfer to the surrounding soil. The use of high-strength reinforcement may lead to a softer flexural response owing to reduced steel area. Thus existing analytical approaches need to be evaluated for modern construction methods and new approaches developed if necessary to ensure desired performance criteria are met.

1.2 RESEARCH OBJECTIVES

The objective of this study is to improve the understanding of load transfer of drilled shaft foundations under axial and lateral loading at full-scale using various composite cross-sections. The objectives for this report are driven by gaps in knowledge regarding the use of high strength steel and steel casing in the performance of drilled shafts. The specific objectives of this report are to:

1. Evaluate the effects of high strength steel reinforcement bars on lateral resistance, steel casing on axial and lateral resistance, and steel casing without internal reinforcement on lateral resistance;

2. Develop recommendations to account for the effects of casing on axial and lateral resistance;

3. Evaluate the appropriateness of existing axial and lateral load transfer models to predict the performance of and for use with typical and proposed (i.e., steel-cased) drilled shafts;

4. Develop region-specific axial load transfer models if available models prove incapable of sufficiently capturing the observed performance;

5. Investigate the effects of deep foundation diameter on the lateral resistance of deep foundations and to establish an approach to account for “scale effects”;

6. Determine the suitability of hollow threaded bar for use of both structural and non-destructive integrity testing of drilled shaft foundations.

1.3 RESEARCH PROGRAM

The research program developed to accomplish the objectives of this study include the:

1. Review of the literature pertaining to the design, construction, and performance of drilled shaft foundations;

2. Development and analysis of a survey of state DOTs to characterize the standard-of-practice in drilled shaft construction, including the use of high strength reinforcement bar and permanent steel casing;

3. Characterization of the test site used to conduct the full scale tests, including geotechnical explorations and laboratory tests to establish the relevant soil properties;

4. Design and installation of four full-scale, instrumented test shafts, including two uncased shafts using mild and high strength steel reinforcement, and two shafts with steel casing with and without internal mild steel reinforcement;

5. Comparison of non-destructive tests used to evaluate potential for defects in shafts, with specific emphasis on the use of hollow bar for cross-hole sonic logging;

6. Evaluation of the full-scale performance of the test shafts in axial and lateral loading;

7. Evaluation and comparison of the performance between the cased and uncased test shafts under axial and lateral loads to study the effects of steel casing and the relevant load transfer;

8. Evaluation and comparison of the performance between the uncased test shafts under lateral loads to study the effects of high strength reinforcement on the mechanism and magnitude of lateral resistance;

9. Development of empirical load transfer curves, including t-z and q-z curves from axial loading tests and p-y curves from lateral loading tests (where t = unit axial shaft resistance, z = is relative soil-shaft interface displacement, q = bearing stress at toe, p = lateral soil reaction, and y = lateral displacement);

10. Formulation of region-specific axial load transfer models that are based on the cone penetration test and/or shear wave velocity measurements, in order to generalize the proposed models;

11. Establishing of a region-specific lateral load transfer model and empirically-justified approach to modify p-y curves to account for the apparent “scale effects” associated with larger diameter shafts and the effects of shaft interface roughness and installation method.

1.4 ORGANIZATION OF THIS DOCUMENT

Chapter 2 of this report presents a comprehensive literature review. Technical details regarding the engineering and construction of drilled shaft foundations are discussed, as well as the limited studies on the effect of high-strength reinforcement and permanent casing on performance. Efforts are made to describe shortcomings and data gaps in these studies. The literature review concludes with a brief discussion of some experimental and analytical design methods for drilled shafts with axial and lateral loads and a summary of those critical issues that require further study as addressed in this research.

Chapter 3 presents an overview of the DOT survey on the state-of-the-practice in drilled shaft design and construction and points the reader to the comprehensive survey results in an appendix.

Chapter 4 presents the characterization of the test site used to perform the full-scale loading.

Chapter 5 describes the experimental setup used to conduct the full-scale axial and lateral loading tests, including a discussion of the shaft construction and the instrumentation used to monitor the performance of the test shafts.

Chapter 6 presents the results of the axial loading tests, including the axial load-displacement curves, the axial load transfer distributions, and the back-calculated t-z and q-z curves. Then, selected axial load transfer models are evaluated and modified to produce region-specific axial load transfer models for uncased drilled shafts. Finally, the effect of permanent casing on the axial response is discussed, and recommendations for axial shaft reduction with casing are developed based on available test data, soil conditions, and construction sequencing.

Chapter 7 describes the results of the lateral loading tests, including the performance at the head of each shaft, lateral displacement profiles, and the back-calculated curvature, moment, and soil reaction-displacement (p-y) curves. Back-calculated p-y curves for each shaft are compared and used, along with widely-available p-y curve models, to simulate the lateral response of each shaft to form a basis for the evaluation of model suitability and differences in interface friction.

Chapter 8 presents the interface and diameter effects on the p-y curves. Recommendations are made to account for these effects, set within the framework of a newly-developed, region-specific lateral load transfer model that can be implemented in commonly-used software.

Finally, Chapter 8 summarizes the results and findings of this study, and identifies areas for future study. Body Text 1/2/3 follows headings 1, 2 and 3.

2.0 LITERATURE REVIEW

2.1 AN INTRODUCTION TO DRILLED SHAFT FOUNDATIONS

Drilled shaft foundations, also known as drilled piers, drilled caissons, caissons, cast-in-drilled-hole piles, bored piles, among other terms, are cast-in-place, reinforced concrete deep foundations constructed in a stabilized drilled borehole (Kulhawy 1991). Drilled shafts are capable of transferring loads from bridge or building superstructures to a competent bearing stratum; as such, they are designed to provide significant axial and lateral resistance, and for certain superstructures, torsional resistance. Drilled shafts have been used for a wide array of applications, including support for highway bridges, mast arm traffic sign and signal pole structures, landslide stabilization, and to support retaining walls and sound barriers.

Drilled shafts are distinguished from other types of deep foundations employed in transportation works, such as driven piles, micropiles, continuous flight auger piles and drilled displacement piles in that: (1) they are often significantly larger in size; (2) a single shaft is frequently used to support a single column without a pile cap; (3) they are frequently installed into a strong, stiff bearing layer to achieve adequate geotechnical resistance (Brown et al. 2010).

Drilled shafts can be used in urban settings where vibration tolerances are stringent or where shallow foundations could not provide sufficient bearing capacity (Gunaratne 2006). A convenient and cost-saving design feature of drilled shafts is the possibility of omitting the construction of pile caps for new foundations constructed near existing structures (Brown et al. 2010).

2.2 CLASSIFICATION OF SHAFTS

Ashour et al. (2004) classified shafts into three categories: short, intermediate, and long. The classification is based on shaft properties and soil conditions, including shaft length below ground surface (*L*) and relative stiffness (*T*) (Ashour et al. 2004). Relative stiffness, *T*, is defined as:

$$T = (EI / f)^{0.2} \tag{2.1}$$

where EI = the bending stiffness of a shaft and f = the subgrade reaction coefficient, which is a function of soil properties, as shown in Figure 2.1 (Norris 1986).

A shaft is classified as a long shaft when $L/T \geq 4$; it is classified as an intermediate shaft when $L/T < 2$; it is classified as a short shaft if the deflection shape of the shaft under lateral load is close to a straight line regardless of the shaft length (Ashour et al. 2004).

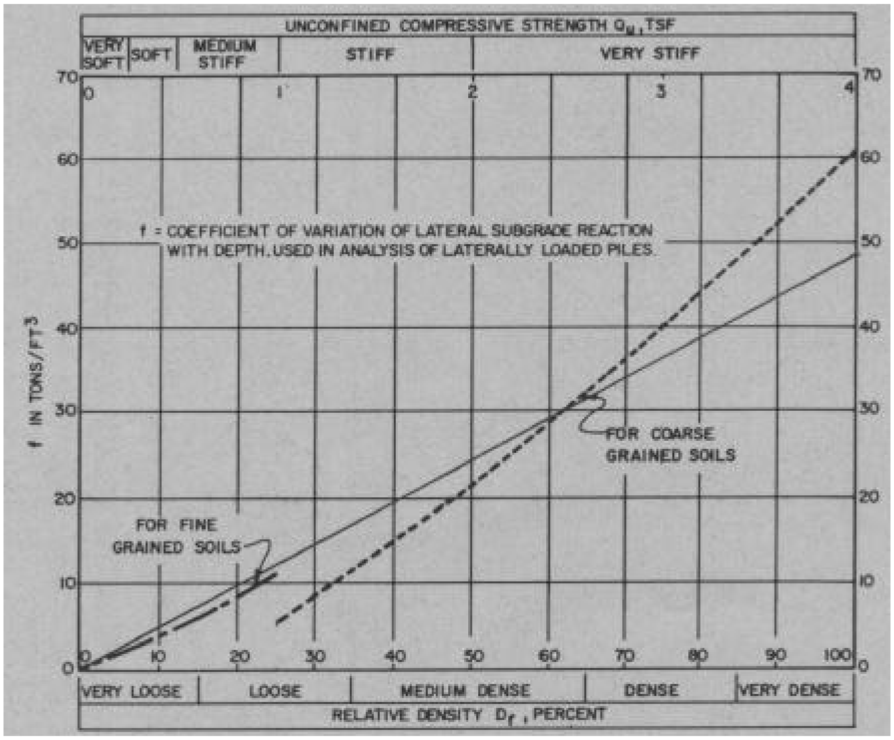

Figure 2.1: Relationship between coefficient of subgrade reaction (*f*) and soil properties for both fine grained soils and coarse grained soils (after Norris, 1986)

2.3 CONSTRUCTION OF DRILLED SHAFTS

Drilled shaft foundations are constructed by drilling a hole, investigating the site into which the shaft is formed, and constructing a cast-in-place reinforced concrete shaft in the hole (Brown et al. 2010). The three methods used to construct drilled shafts are: dry construction method, wet construction method, and casing construction method. The selection of the appropriate construction method depends on site conditions, and a combination of different methods may be used for construction of individual shaft.

2.3.1 Dry Construction Method

The dry method, as indicated by its name, is suitable for soil and rock above the water table and can be excavated to the designed depth under relatively dry conditions. It is required that soils do not cave or slump during excavation and installation of the drilled shaft. If water seepage exceeds tolerable levels, wet method should be employed. A surface casing can be used temporarily or permanently, since the drilling device may be bearing weight on the soil close to the hole and soils near the surface may cave (Brown et al. 2010).

The dry method procedure, as shown in Figure 2.2, is described briefly as follows (Owens and Reese 1982 and Brown et al. 2010):

1. Drill a hole using augers. Joffrion (2002) recommended that less than 30 cm (12 inches) of seepage are allowed at the bottom of the hole after four hours.

2. Remove loose debris and standing water at the bottom of the hole. Manual cleaning or a special clean-out bucket can be used.

3. Place a reinforcing cage into the hole after it is cleaned, inspected, and approved. Spacers or “feet” may be installed at the end of the longitudinal bars to place the cage into the hole. For a shaft with relatively low bending moments, the reinforcing cage may be placed only in the upper portion and supported by surface skids as the concrete hardens.

4. Place concrete into the hole. A drop chute or centering device can be employed for this purpose. The “free-fall” method can be employed by delivering the flow of concrete down the center of the shaft or the sides of hole and dislodging soil debris. Federal Highway Administration (Brown et al. 2010) recommended that before placing concrete, the water at the bottom of the excavation should be less than 8 mm (3 inches).

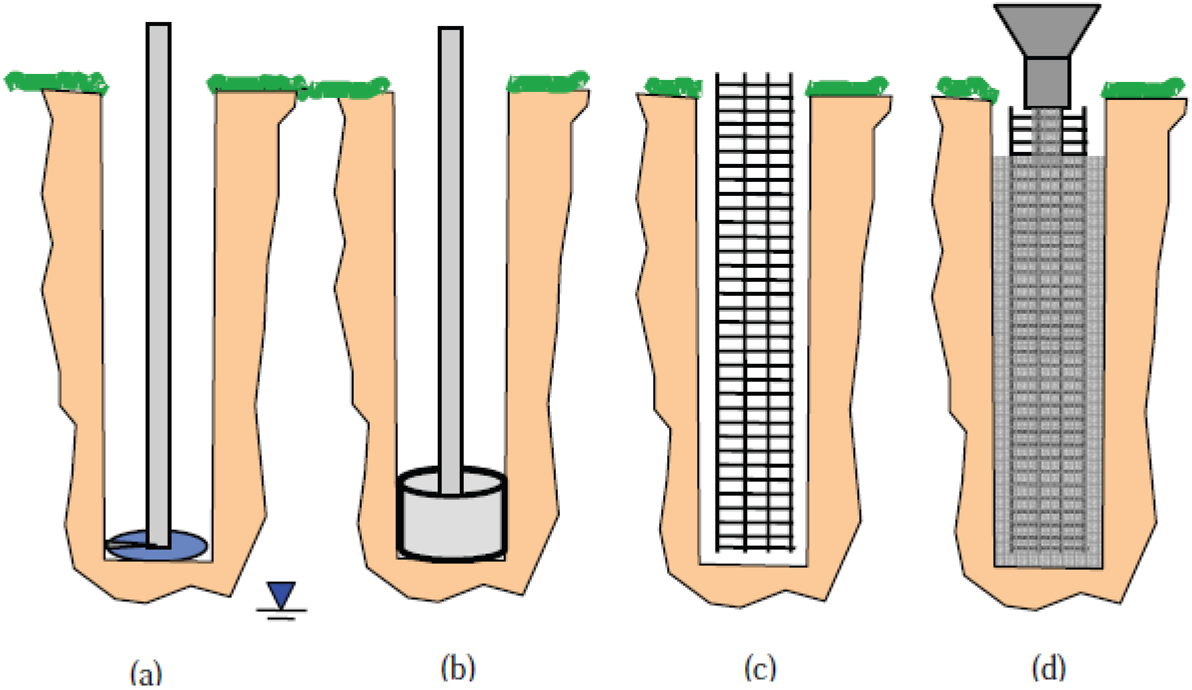

Figure 2.2 Dry method of dry construction: (a) drill a hole; (b) clean the bottom of the excavation; (c) place the reinforcement and (d) place the concrete into the hole (after Brown et al. 2010)

2.3.2 Wet Construction Method

If soils are unstable or the height of the groundwater table to prevent using the dry method, the wet method, called “slurry method”, can be utilized. In this method slurry or other drilling fluids are used to fill the hole during the process of excavation, the placement of a reinforcement cage, and adding concrete (Joffrion 2002 and Brown et al. 2010). The purpose of using drilling fluid is to maintain the stability of the excavation and prevent the inflow of groundwater. When the slurry in the hole is above the groundwater table, the fluid will be forced to flow out into the soil due to hydraulic gradient. The seepage pressure applied to the sidewall can help to stabilize the borehole wall (Brown et al. 2010).

The drilling fluid may be water, mineral or polymer slurry (Au and Lo 1993, Joffrion, 2002, and Brown et al. 2010). Water is effective when soils are permeable but not readily eroded by contact with water. For example, water can be used for sites with permeable sandstone and cemented sands. A mineral slurry is usually made from clay minerals, such as bentonite, attapulgite and sepiolite (Gray et al. 1980, Chilingarian and Vorabutr 1981, and Brown et al. 2010). Bentonite slurry is the most commonly used mineral slurry. Attapulgite and sepiolite are applicable for drilling in permeable soils in saline environments. The polymer slurry is the mixture of polymers and water. Acrylamide, acrylic acid, or a combination of polyacrylamides with other chemicals is commonly used polymers (Brown et al. 2010).

A brief description of the wet method procedure is provided in Figure 2.3 as follows (Brown et al. 2010):

1. Before excavation, place surface starter casing at the site, which extends deep enough to prevent surface cave-ins, but far enough above the ground surface to elevate the surface level of the drilling fluid.

2. Fill slurry into the hole to maintain the slurry head at 1.5 m (5 feet) or more above the water table throughout the operation.

3. Install a reinforcing cage after the excavation is completed and cleaned.

4. Perform concrete placement with concrete that maintains a sufficient workability to move easily through the reinforcing cage.

5. Pull the tremie while adding concrete keeping the outlet of the tremie 3 m (10 ft) or more below the concrete surface to prevent mixing with the slurry.

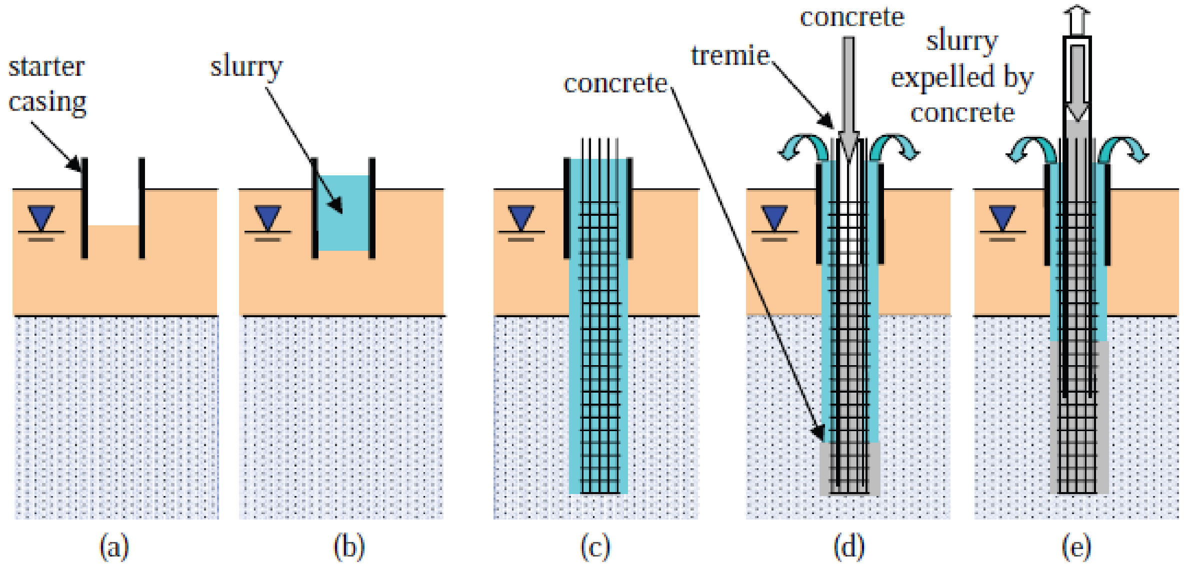

Figure 2.3 Slurry drilling process: (a) set surface casing; (b) fill the hole with slurry; (c) set reinforcing after cleaning excavation; (d) place concrete using tremie; (e) pull tremie while adding concrete (after Brown et al. 2010)

The drilling method and equipment used in the wet method are similar to those used in the dry excavation method. However, the equipment used in the wet method should offer a path for drilling fluids moving through or around the equipment. Figure 2.4 is an example of equipment with a slurry bypass included in the clean-out bucket. The withdrawal speed of a drilling tool should be controlled. Suction pressure may be built up under the tool with rapid withdrawal, which may lead to failure near the bottom of the excavation.

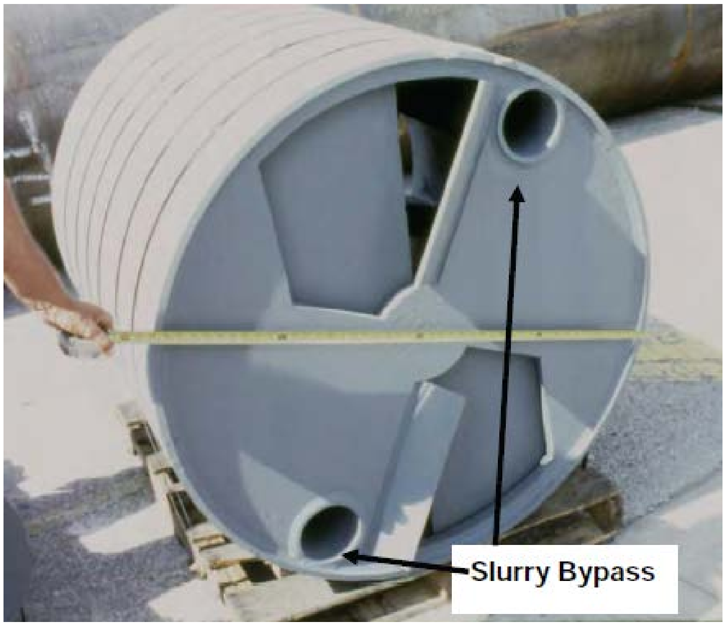

Figure 2.4 Bottom clean-out bucket with slurry bypass (after Brown et al. 2010)

2.3.3 Casing Construction Method

The casing method is often employed if soils are very unstable during excavation (Owens and Reese 1982). The excavation casing, which is usually made of steel, is pulled out either during or after concreting to form a rough pile surface (Lo and Li 2003). The excavation casing may be kept in place if difficult to remove or needed to be a structural element in the design of the drilled shaft (Brown et al. 2010).

There are three methods for installing of excavation casing as reported by Owens and Reese (1982) and Brown et al. (2010):

1. In this method, an oversized hole is drilled with slurry through the shallow permeable strata, and then the casing is introduced and pushed into the bearing stratum, as shown in Figure 2.5a. After sealing the casing, the slurry is bailed from the casing using a bailing bucket and (see Figure 2.5b). Reinforcing steel is placed and extends to the full depth of the excavation, as seen in Figure 2.5c. After placing reinforcing steel, the hole is filled with fresh concrete to head greater than external water pressure (see Figure 2.5d). Finally, the casing may be pulled while adding more concrete or left in place. Figure 2.5e shows the procedure of pulling out of casing. As mentioned before, the casing can also be kept in place

2. Unlike the previous method as shown in Figure 2.5, the casing can also be driven into the bearing formation using impact or vibratory hammers or casing oscillator or rotator (Figure 2.6a), and then the soil inside the casing is excavated in the dry (Figure 2.6b). Then the rest of construction procedures for placing reinforcing steel and pouring concrete into the hole are similar as those discussed in step 2.

3. If soils are dry or have slow seepage, the excavation of oversized hole can be done first using the dry method, and then the casing can be placed into the hole.

4.

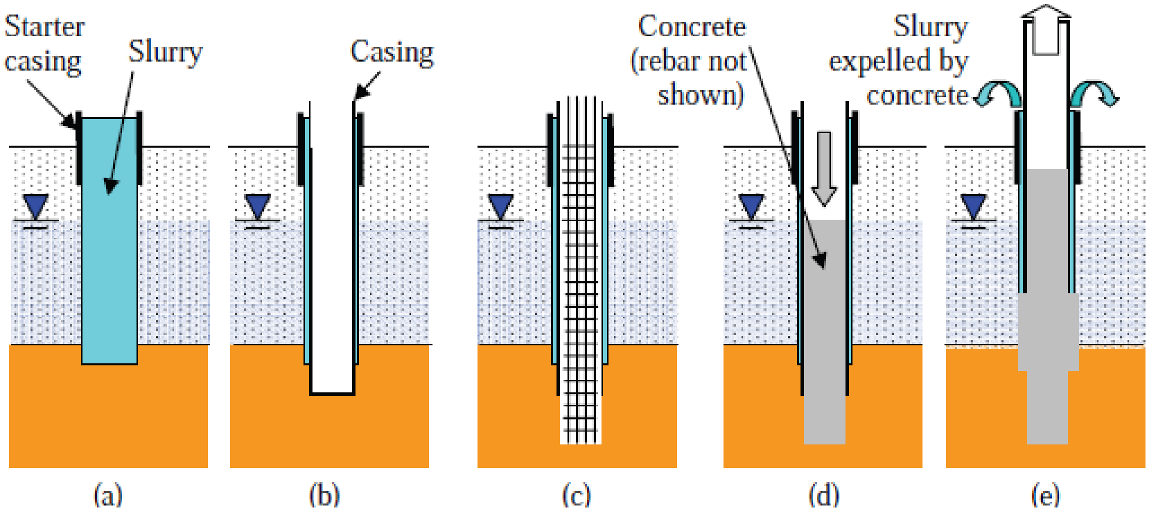

Figure 2.5 Construction using casing through slurry-filled starter hole: (a) set starter casing and drill with slurry; (b) place casing and remove slurry; (c) set reinforcing after cleaning excavation; (d) place concrete; (e) pull casing out of the hole (after Brown et al. 2010)

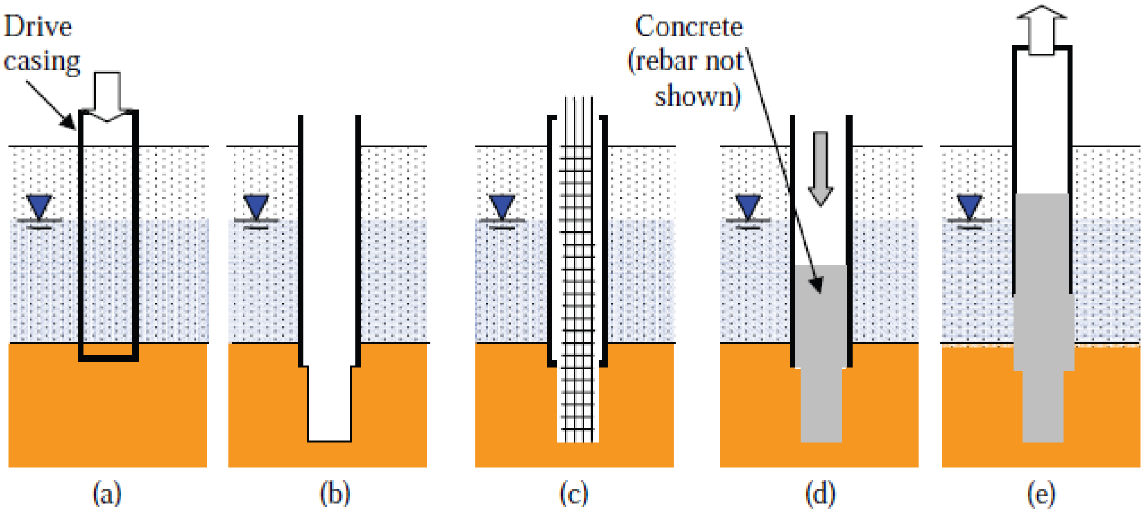

Figure 2.6 Construction using casing advanced ahead of excavation: (a) drive casing into the bearing formation of soil; (b) drill the hole through casing; (c) set reinforcing after cleaning excavation; (d) place concrete; (e) pull casing out of the hole (after Brown et al. 2010)

It is noted that during the construction, the casing must be sealed into a watertight formation to prevent the inflow of groundwater or sand around the bottom of the casing, which may cause cavity around the casing. It is important to keep sufficient space between bars of the reinforcing cage and good flow characteristics of the concrete to make sure the concrete can easily flow through the steel bars and fill the space between reinforcing and the sides of the hole.

Brown et al. (2010) recommended some equipment for driving casing ahead of the excavation. Figure 2.7 shows the vibratory hammer and oscillator that can be used to drive the casing into the bearing layer. Twister bar (Figure 2.7c) can be attached to the drill rig to apply torque and down force onto the casing. When the hard soil is encountered, the casing may be equipped with cutting teeth or carbide bits at the bottom to assist in penetration, as shown in Figure 2.8.

(a)

(b)

(c)

Figure 2.7 Use of (a) oscillator rig, (b) vibro-hammer, and (c) twister bar to advance casing (after Brown et al. 2010)

Figure 2.8 Cutting Teeth on the Casing (after Brown et al. 2010)

The hammer grabbing (HG) or reverse circulation drilling (RCD) are commonly used methods to excavate large-diameter bored piles (Lo and Li 2003). HG and RCD are capable of excavation of 3 m (10 feet) diameter to depths exceeding 70 m (230 feet). For the HG method (Figure 2.9a), an oscillator, rotator, or vibrating hammer are employed to sink a heavy-duty excavation casing, and a heavy grab is for excavating the soil inside the casing. In the RCD method, after a casing is sunk similar to the HG method, a drill rig is used for excavation and the excavated materials are flushed back to the ground by the reverse circulation technique.

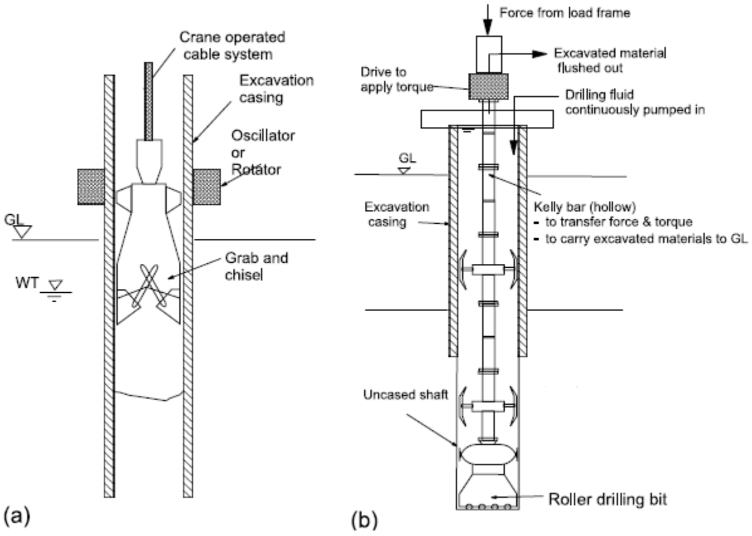

Figure 2.9 Construction of drilled shaft using: (a) hammer grabbing; (b) reverse

circulation drilling (after Lo and Li 2003)

2.4 DESIGN METHODS FOR AXIALLY LOADED SHAFTS

2.4.1 Indirect CPT Methods for Axial Shaft Capacity

Axial loads are supported by toe resistance and shaft resistance along the shaft length (Poulos and Davis 1980, Salgado 2008), as shown in Figure 2.10. Kulhawy (2004) summarized the formulation to compute the axial capacity (Q_c) of a drilled shaft in compression as:

$$Q_c = Q_{sc} + Q_{tc} - W \tag{2.2}$$

where Q_s = shaft resistance, Q_t = toe resistance, and W = shaft weight, which is the effective weight for drained loading or the total weight for undrained loading.

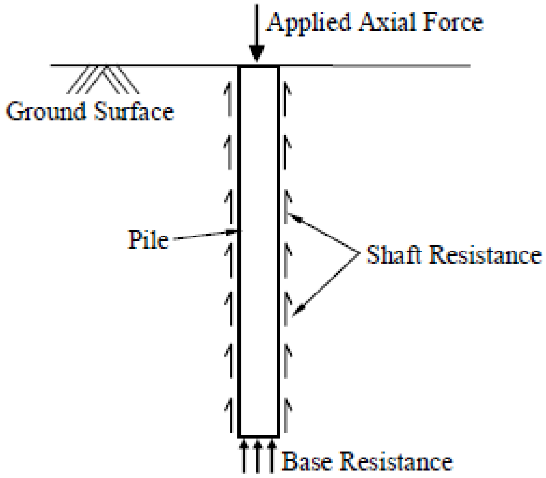

Figure 2.10 Load Transfer Mechanism of Axially Loaded Piles (after Salgado 2008)

Alpha and Beta Method for Skin Friction

Kulhawy (1991), East Japan Railway et al. (1996), and Chen and Kulhawy (2002) reported that skin friction is about the same in uplift and compression tests. The side resistances for both undrained loading and drained loading, using α and β methods, respectively, are given by (Kulhawy 2004):

$$Q_{sc} = Q_{su} = \pi B \alpha (K/K_o) \int_0^D s_u(z) dz \qquad \textit{for undrained loading} \qquad (2.3)$$

$$Q_{sc} = Q_{su} = \pi B \int_0^D \beta(z) \sigma_v' dz = \pi B \int_0^D f(z) dz \qquad \textit{for drained loading} \qquad (2.4)$$

where B = shaft diameter, D = shaft length, β = a coefficient related with the effective stress friction angle (δ) for the soil-shaft interface, f = unit side resistance along the shaft, α = an empirical adhesion factor obtained from an α-s_u correlation, K = coefficient of horizontal earth stress, K_o = coefficient of earth pressure at rest, K/K_o = a factor that represents the change in the horizontal total stress as a function of the construction method, which is equal to 1.0 for dry construction, 5/6 for casing construction, 2/3 for slurry construction, and 11/12 for combined dry/casing construction (Chen and Kulhawy 2002), s_u = undrained shear strength, and z = depth.

Jamiolkowski (2003) reported that f can be obtained through undrained shear strength (s_u), as expressed by:

$$f = \alpha s_u \qquad (2.5)$$

where α =a empirical factor. Based on the results of a large database on bored piles, α is given by Chen & Kulhawy (1994):

$\alpha = 0.21 + 0.26(P_a/s_u) < 1$ (2.6)

where P_a = atmospheric pressure.

O’Neill (2001) also developed a correlation, as shown in Figure 2.11, for drilled shafts based on an analysis of parts of two load test databases. O’Neill (2001) assumed that s_u is characterized using the results of UU triaxial compression tests. O’Neill and Reese (1999) and Brown et al. (2010 proposed the following equation for the value of *a*:

$$\alpha = 0.55 \qquad \text{for} \qquad \frac{s_u}{P_a} \le 1.5 \tag{2.7a}$$

$$\alpha = 0.55 - 0.1\left(\frac{s_u}{P_a} - 1.5\right) \qquad \text{for} \qquad 1.5 \le \frac{s_u}{P_a} \le 2.5 \tag{2.7b}$$

$$\alpha = 0.45 \qquad \text{for} \qquad \frac{s_u}{P_a} > 2.5 \tag{2.7c}$$

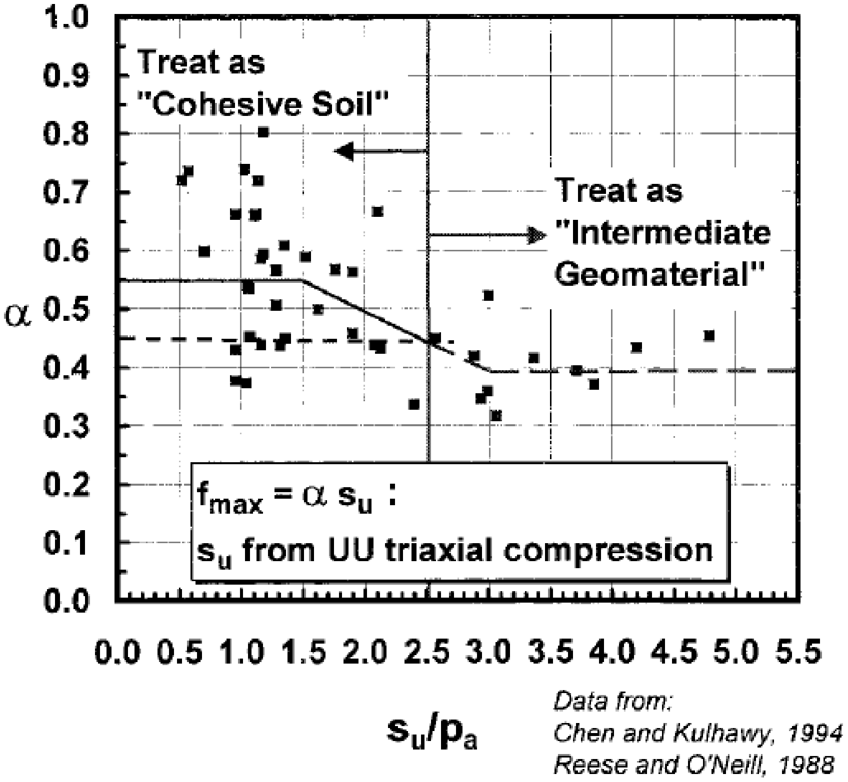

Data from:
Chen and Kulhawy, 1994
Reese and O'Neill, 1988

Figure 2.11 Suggested Design Relation to a to s_u/p_a in Drilled Shafts (after O’Neill 2001)

Reese and O'Neill (1988) proposed an empirical method based on a set of load tests for drilled shafts to calculate the unit side resistance, *f*, of a drilled shaft in sand, which is given as:

$$f = \beta \, \sigma'_z \leq 200 \text{ kPa} \tag{2.8}$$

where σ'_z = vertical effective stress in soil at depth z (m) and β = side resistance coefficient. There are two widely used approaches to estimate β. The first approach is called depth-dependent β method (O'Neill and Reese 1978). In this method β is only related with depth and can be obtained by:

$$\beta = 1.5 - 0.245\, z^{0.5} \qquad 1.2 \geq \beta \geq 0.25 \tag{2.9}$$

For loose sand layers with standard penetration test (SPT) blow counts less than or equal to 15, O'Neill (1994) suggested that β should be scaled down by the ratio of (N_{60}/15) and σ'_z can be calculated using measured water tables and unit weight of soils (γ) estimated by the SPT blow counts (N).

However, Brown et al. (2010) pointed out that this method fails to account explicitly for the in-situ state of stress and the soil shear strength and provides a conservative side resistance for most soil profiles.

Based on the work done by Kulhawy (1991), Mayne and Harris (1993), Chen and Kulhawy (2002), Kulhawy and Chen (2007), Brown et al. (2010) recommended the following equation to estimate β:

$$\beta = K_o \left(\frac{\mathrm{K}}{K_o}\right) \tan\phi' \tag{2.10}$$

where ϕ' = effective stress friction angle. The β-coefficient can also be determined using the method recommend by Brown et al. (2010):

$$\beta = (1 - \sin\phi') \cdot \mathrm{OCR}^{\sin\phi'} \tan\phi' \leq K_p \tan\phi' \tag{2.11}$$

where OCR = overconsolidation ratio, computed using an empirical estimate of the normalized vertical effective preconsolidation stress, σ'_p :

$$\frac{\sigma'_p}{P_a} = 0.47 \cdot \left(N_{60}\right)^m \tag{2.12}$$

where N_{60} = average standard penetration resistance in blows per 300 mm for a hammer delivering 60% of the theoretical applied energy.

Meyerhof Method for Skin Friction

The ultimate side resistance (*f*) of drilled shafts in cohesionless soils is proposed by several researchers, e.g., Meyerhof (1976), Reese and O'Neill (1988), and Kulhawy (1991). The Meyerhof method (1976) is based on the results of field load tests and the *f* of a drilled shaft as given by:

$$f\left(kPa\right) = N_{60} \tag{2.13}$$

Bearing Capacity Method for Tip Resistance

The tip resistance of the shaft in compression is calculated using the bearing capacity of the soil under shaft tip, as represented by:

$$Q_{tc} = q_{ult} A_{tip} \tag{2.14}$$

where q_{ult} = ultimate bearing capacity and A_{tip} = shaft tip area. The general solution for ultimate bearing capacity q_{ult} is the Terzaghi-Buisman equation (e.g.,Vesic 1975) given by:

$$q_{ult} = cN_c + 0.5B\gamma N_\gamma + qN_q \tag{2.15}$$

in which c = soil cohesion, γ = soil unit weight, q = vertical stress at the shaft tip (= γD), D = shaft depth, and N_c, N_γ, N_q = bearing capacity factors given by:

$$N_q = \tan^2(45^o + \phi / 2)\exp(\pi \tan\phi) \tag{2.16}$$

$$N_c = (N_q - 1)\cot\phi \tag{2.17}$$

$$N_\gamma = 2(N_q + 1)\tan\phi \tag{2.18}$$

Further research for calculating q_{ult} has been conducted by Hansen (1970), Vesic (1975), and Kulhawy et al. (1985) to extend the ultimate bearing capacity solution to actual field conditions with the consideration of foundation shape, depth, and rigidity using modifiers (ξ). The ultimate bearing capacity for drained compression loading and undrained compression loading is given by Kulhawy (1991):

$$q_{ult} = 0.5B\gamma N_\gamma \xi_{\gamma s}\xi_{\gamma d}\xi_{\gamma r} + qN_q \xi_{qs}\xi_{qd}\xi_{qr} \tag{2.19}$$

$$q_{ult} = 6.17 s_u \xi_{cd}\xi_{cr} + q \tag{2.20}$$

The tip resistance in uplift is developed from tension and suction, as represented by:

$$Q_{tu} = s_t A_{tip} = s_s A_{tip} \tag{2.21}$$

where s_t = tip tension, which is the minimum tensile strength of the soil or the concrete and s_s = tip suction, which is zero in drained loading. In undrained loading, s_s can be evaluated as follows (Stas & Kulhawy 1984):

$$s_s = (W / A_{tip}) - u_i = (W / A_{tip}) - \gamma_w (D - h) \tag{2.22}$$

where h = depth to water table.

2.4.2 Direct CPT Method for Axial Pile Capacity

There are many proposed direct CPT methods for estimating the unit side resistance (f_p) and end bearing resistance (q_b). The following review is limited to the methods relevant to drilled shafts.

Laboratoire Central des Ponts et Chaussées (LCPC) Method

Bustamante and Gianeselli (1982) proposed the LCPC method, which offers versatility in the variety and types of deep foundation systems and geomaterials that can be accommodated. In this method, f_p and q_b depend on the measured cone tip resistance (q_c), as given by:

$$f_p = q_c / \alpha \tag{2.23}$$

$$q_b = k_c \cdot q_c \tag{2.24}$$

where α = a coefficient depend on the pile and soil types and the q_c values, k_c = penetrometer bearing capacity factor.

Alsamman (1995) made a revision, as seen in Figure 2.12, on the LCPC method based on the interpretation of a large database of full scale load tests on bored piles in coarse grained soils.

Politecnico di Torino (PT) Method

Fioravante et al. (1995) developed the PT method to estimate the f_p of drilled shafts in clear quartzitic uncemented NC sands, as given by:

$$f_p(\text{MPa}) \approx [q_c\ (\text{MPa})/274]^{0.75} \tag{2.25}$$

Unicone Method

In the Unicone Method, which is suitable for a variety of soils, f_p and q_b are calculated by the following expressions (Eslami and Fellenius 1997, Eslami 2006):

$$f_p = C_{se} \cdot q_c \tag{2.26}$$

$$q_b = C_{te} \cdot q_E = C_{te} \cdot (q_c - u_2) \tag{2.27}$$

where q_E = effective cone resistance, u_2 = the measured pore water pressure, C_{se} and C_{te} = the side and the toe correlation coefficients. C_{se} varies with soil type, as shown in Figure 2.13. C_{te} is determined by (Fellenius 2017):

$$C_{te} = 1 \qquad \text{if } D < 0.4 \text{ m} \tag{2.28}$$

$$C_{te} = 1/3D \qquad \text{if } D \geq 0.4 \text{ m} \tag{2.29}$$

where D = the pile toe diameter in meters.

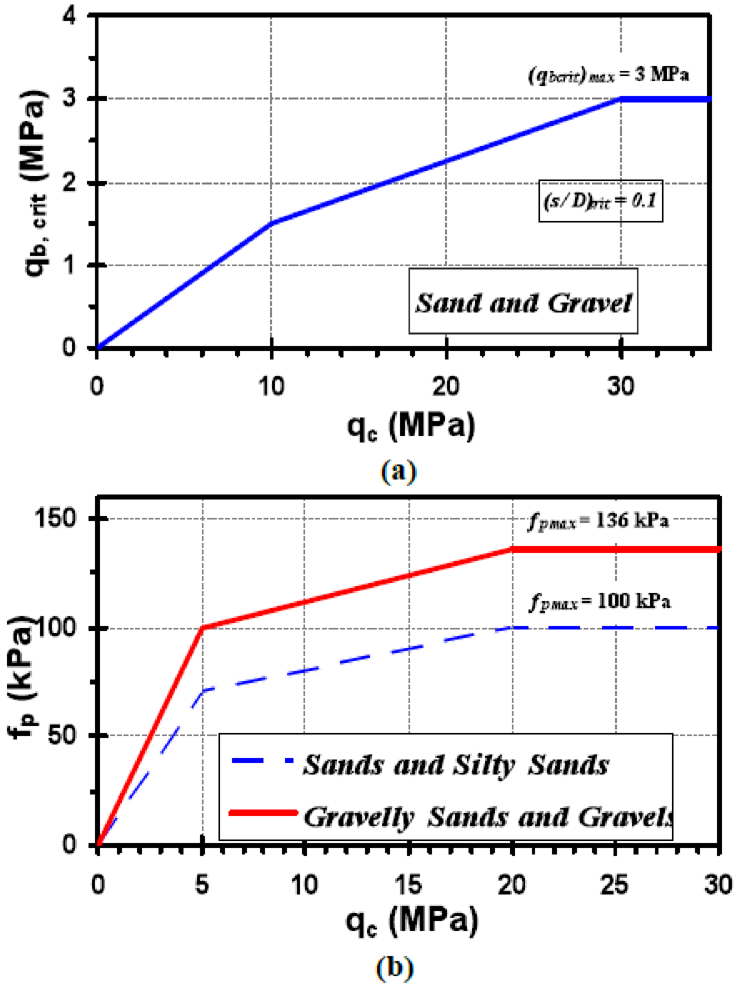

(a)

(b)

Figure 2.12 (a) Critical unit base resistance, and (b) side friction from CPT (after Alsamman 1995)

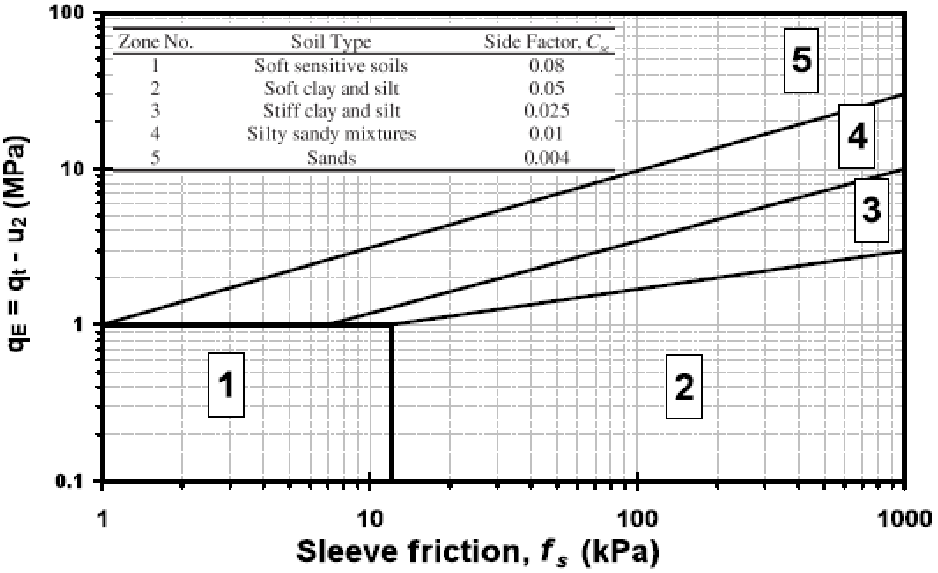

Figure 2.13 Unicone chart to determine soil type and C_{se} (after Eslami & Fellenius 1997)

Kajima Technical Research Institute (KTRI) Method

The KTRI method is applicable to drilled shafts in variety of ground conditions (Takesue et al. 1998). In this method, f_p can be evaluated using the measured f_s and excess porewater pressures (Δu_2), as presented in Figure 2.14.

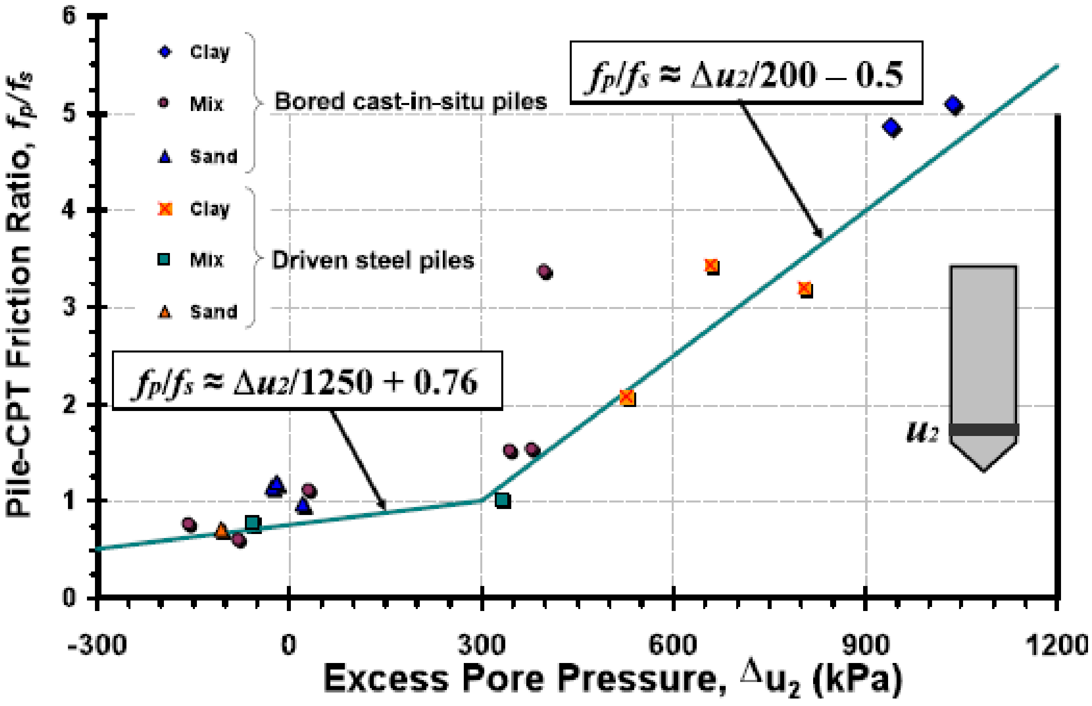

Figure 2.14 KTRI method for evaluating side friction of piles in different soils (after Takesue et al. 1998)

2.4.3 Load-Transfer Method (*t-z* and *p-z* Curves)

As Armaleh and Desai (1987) mentioned, the soil reaction around the shaft and under the tip can be represented by discrete nonlinear springs distributed along the shaft (*t-z* curves), and at the shaft tip (*q-z* curves), respectively. Figure 2.15 shows an idealized model of *t-z* and *p-z* method.

The approach to develop load-transfer curves includes an empirical procedure based on field and experimental data (Coyle and Reese 1966, Coyle and Sulaiman 1967, Holmquist and Matlock 1976, and Grosch and Reese 1980), numerical techniques (Poulos and Davis 1968, Butterfield and Banerjee 1971), theoretical method (Chin 1970, Randolph and Worth 1978, Kraft et al. 1981, Chow 1986, McVay, et al., 1989, Randolph 1994, and Poulos 2001), and finite element method.

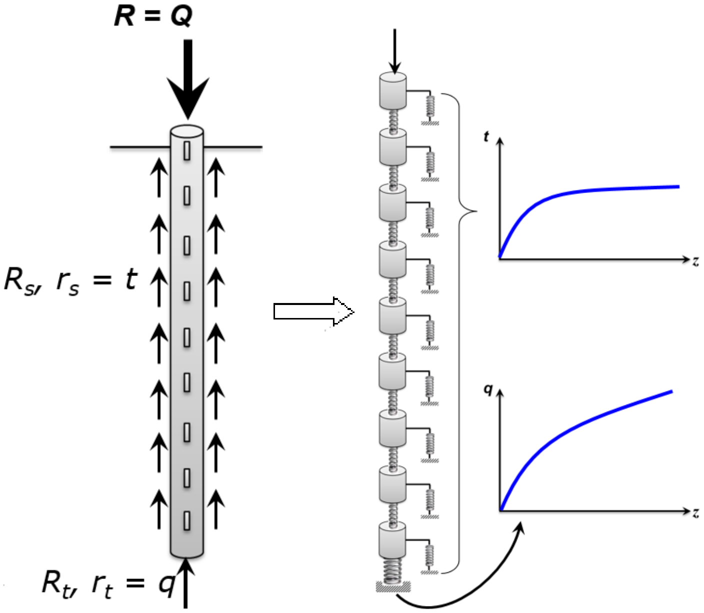

Figure 2.15 Schematic concept used in t-z and p-z method (modified from Pando et al. 2006).

2.4.4 Empirical t-z Curves

The *t-z* curve method is widely used for the axially loaded pile surrounded by stratified soil with nonlinear responses (Pando et al. 2006). Seed and Reese (1957) first proposed *t-z* curve method using the vane shear test to determine the relationship between the vertical displacement along the pile shaft and the induced shear stress, as shown in Figure 2.16. Coyle and Reese (1966) performed a series of pile load tests and proposed the t-z curve as shown in Figure 2.17.

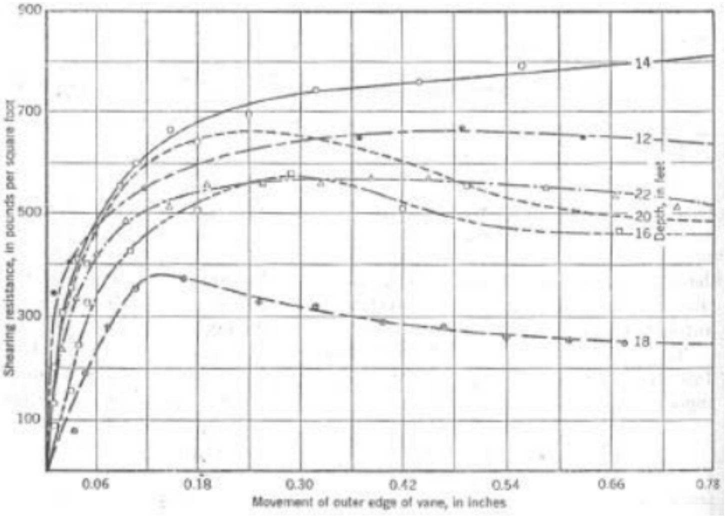

Figure 2.16 Relationship between movement and shear resistance obtained by vane shear test (after Seed and Reese 1957)

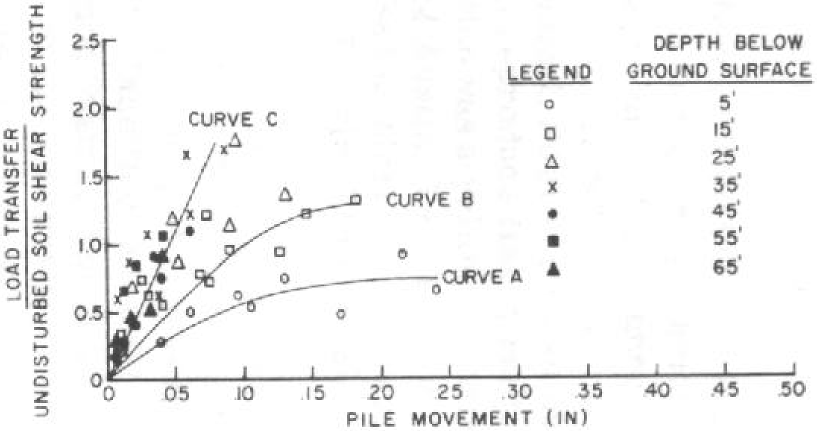

Figure 2.17 Relationship between the ratio of load transfer to undisturbed soil shear strength and the pile movement (after Coyle and Reese 1966)

2.4.5 Vijayvergiya (1977) Proposed t-z Curves

Vijayvergiya (1977) proposed the relationship between the mobilized unit side shear (τ_s) and the shaft movement (z):

$$\tau_s = \tau_{s,\max}\left(2\sqrt{\frac{z}{z_c}} - \frac{z}{z_c}\right) \qquad \text{for } z \le z_c \tag{2.30}$$

$$\tau_s = \tau_{s,\max} \qquad \text{for } z > z_c \tag{2.31}$$

where $\tau_{s,\max}$ = the maximum side friction, and z_c = critical pile displacement which is required to mobilize $\tau_{s,\max}$. The typical shape of the *t*-*z* curve is shown in Figure 2.18.

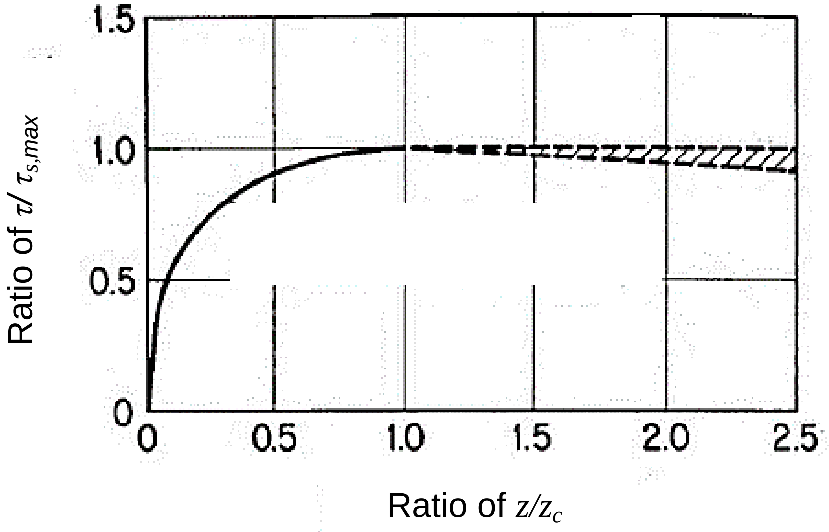

Figure 2.18 Normalized t-z curve for clay and sand (after Vijayverjia 1977).

The critical pile displacement (z_c) is dependent on the pile and soil conditions (Vijayvergiya 1977, Kulhawy 1985 and Srivastava et al. 2008). A literature review about z_c was conducted by Vijayvergiya (1977) for pile embedded in clay and sand, as listed in Table 2.1 and Table 2.2, respectively.

Table 2.1: Summary of critical pile displacement in clay (modified from Vijayvergiya 1977)

Pile Size (in)	Range of z_c (in)	References
-	-	Burland et al. (1966)
16	0.1 to 0.3	Coyle et al.(1973)
12 - 3/4	-	Darragh and Bell (1969)
24	0.3 to 0.4	McCammon and Golder (1970)
30 to 90	0.2 to 0.4	O’Neill and Reese (1972)
6	0.12	Seed and Reese (1957)
12 to 24	-	Skempton (1959)
30	0.4 to 0.8	Vijayvergiya (1969)

* D = pile diameter

Table 2.2: Summary of critical pile displacement in sand (modified from Vijayvergiya 1977)

Pile Size (in)	Range of z_c (in)	References
16	0.2 to 0.4	Coyle et al. (1973)
12 - 3/4	0.3 to 0.4	Coyle and Sulaiman (1967)
12 - 3/4	0.25	Darragh and Bell (1969)
24	0.4	McCammon and Golder (1970)
16	0.2 to 0.4	Mansur and Hunter (1970)
18	-	Vesic (1970)
18	0.5 to 1.0	Vijayvergiya (1971)

2.4.6 Vijayvergiya (1977) Proposed q-z Curves

Based on the experiment data, Vijayvergiya (1977) developed the *q-z* curve, as given by:

$$q = (\frac{z}{z_c^b})^{1/3} q_{\max} \qquad (2.32)$$

where q = pile tip resistance, $q_{\max}$ = maximum tip resistance, z_c^b = critical pile displacement which is required to mobilize $q_{\max}$, which is summarized in in Table 2.1 and Table 2.2 for clay and sand, respectively.

2.4.7 Empirical Load-Transfer Curves Recommended by API (1993)

API recommended the *t-z* Curves (Figure 2.19) for non-carbonate soils in the absence of more definitive criteria. In Figure 2.19, D = pile diameter, $t = \tau$ = mobilized unit skin friction, $t_{res} = \tau_{res}$ = residual unit skin friction, and $t_{max} = \tau_{\max}$ = maximum unit skin friction, as given by:

$$\tau_{\max} = K_h \sigma_v' \tan\delta \qquad \text{for granular soils} \qquad (2.33)$$

$$\tau_{\max} = \alpha c \qquad \text{for cohesive soils} \qquad (2.34)$$

where K_h = coefficient of lateral earth pressure, σ'_v =effective normal stress, δ = friction angle at interface, α = a dimensionless factor, and c = undrained shear strength of the soil. The factor α can be estimated by the following equations:

$$\alpha = 0.5\left(\frac{c}{\sigma_v'}\right)^{-0.5} \le 1.0 \qquad \text{for} \qquad \frac{c}{P_a} \le 1.0 \qquad (2.35)$$

$$\alpha = 0.5\left(\frac{c}{\sigma_v^{'}}\right)^{-0.25} \leq 1.0 \qquad \text{for} \qquad \frac{c}{P_a} > 1.0 \tag{2.36}$$

The value of the residual unit skin friction ratio $\tau_{res} / \tau_{\max}$ is in the range of 0.70 to 0.90 and can be estimated from laboratory tests, in situ or model pile tests (API 1993).

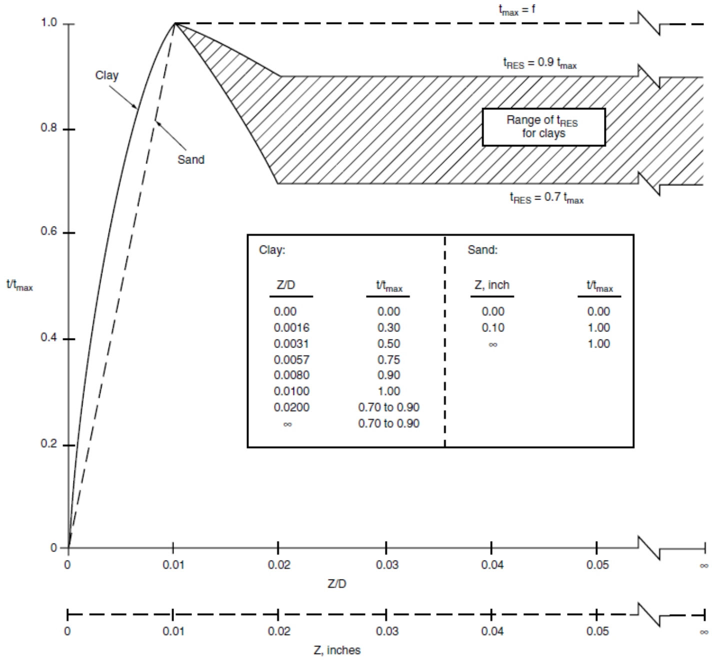

Clay:

Z/D	t/t_{max}
0.00	0.00
0.0016	0.30
0.0031	0.50
0.0057	0.75
0.0080	0.90
0.0100	1.00
0.0200	0.70 to 0.90
∞	0.70 to 0.90

Sand:

Z, inch	t/t_{max}
0.00	0.00
0.10	1.00
∞	1.00

Figure 2.19 API (1993) recommended *t-z* curves

In the absence of more definitive criteria, API recommended the pile tip load (Q)-displacement (z) curve, as illustrated in Figure 2.20. In the figure, D = pile diameter, $t_{max} = \tau_{\max}$ = maximum unit skin friction, and Q_p = total end bearing = qA_p, A_p = end area of pile and q = unit end bearing capacity, which can be estimated by:

$$q = 9c \qquad \text{for cohesive soils} \tag{2.37}$$

$$q = \sigma_v^{'} \cdot N_q \qquad \text{for cohesive soils} \tag{2.38}$$

where N_q = dimensionless bearing capacity factor and the recommended values are summarized in Table 2.3.

Table 2.3 Recommended values for N_q (API 1993)

Density	Soil Description	Soil-Pile Friction Angle, δ (deg)	N_q
Very Loose to Medium	Sand, Sand to Silt, Silt	15	8
Loose to Dense	Sand, Sand to Silt, Silt	20	12
Medium to Dense	Sand, Sand to Silt	25	20
Dense to Very Dense	Sand, Sand to Silt	30	40
Dense to Very Dense	Gravel, Sand	35	50

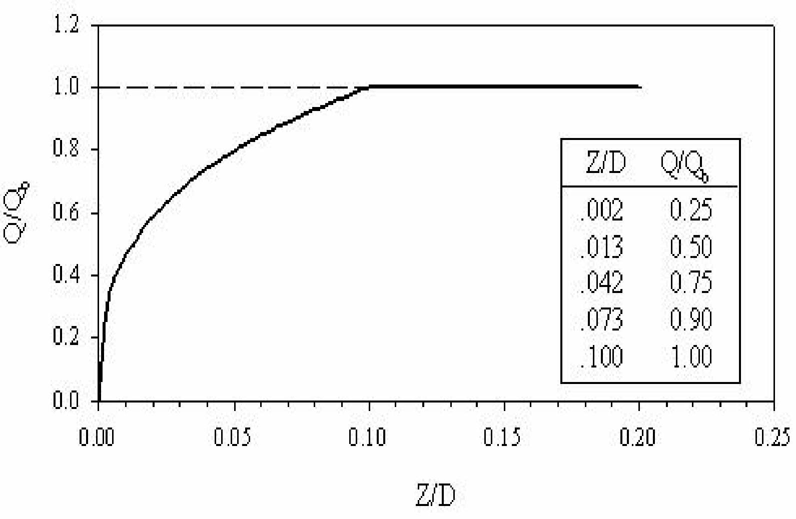

Figure 2.20 API (1993) recommended *q-z* curve

2.4.8 Theoretical Load-Transfer Curves for Linear Soils

With the concentric cylinder approach (Cooke 1974, Frank 1974, and Baguelin, et al. 1975), Randolph and Wroth (1978) proposed a *t-z* curve model for linear elastic soil with no radial variation of shear modulus ($G(r) = G$, in which r = radial distance). The concentric cylinder model is used to model the deformation of the soil around the pile, as illustrated in Figure 2.21.

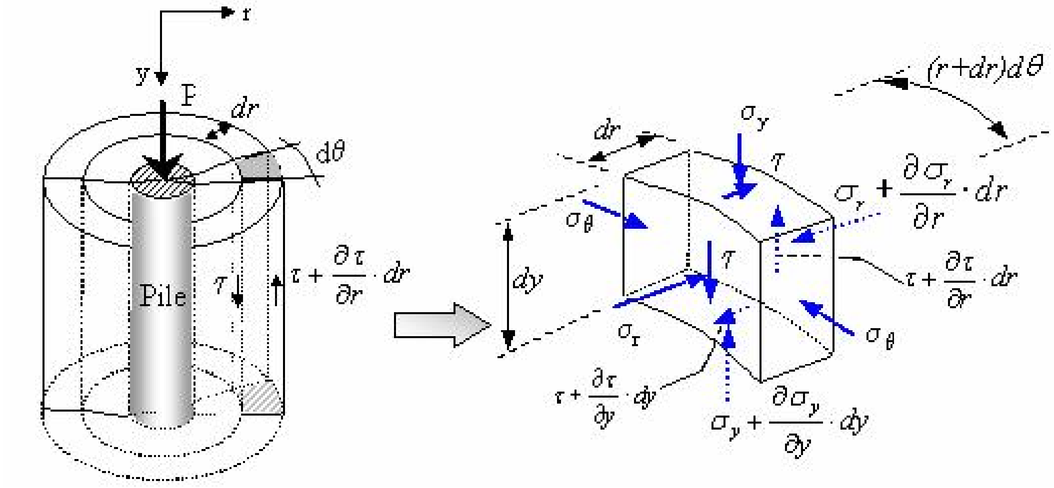

(a) Concentric cylinders around loaded pile (b) Stresses in soil element

Figure 2.21 Concentric cylinder model for settlement analysis of axially loaded piles (after Pando et al. 2006 originally from Randolph and Wroth 1978).

The *t-z* curve model was developed by considering the vertical equilibrium of the annular-shaped soil element and is given by (Randolph and Wroth 1978):

$$z = \frac{\tau r_0}{G_i} \ln\left(\frac{r_m}{r_0}\right) \tag{2.39}$$

where τ = shear resistance on the pile-soil interface ≤ the maximum shear resistance ($\tau_{\max}$), r_0 = the pile radius, r_m ,= the radial distance beyond which the shear stresses are negligible and the soil does not deform, which can be estimated by:

$$r_m = 2.5/\rho(L - \nu) \tag{2.40}$$

where L = pile length, ρ = the ratio of the soil shear moduli at depths $L/2$ and the pile tip, ν = Poisson’s ratio.

The Randolph and Wroth (1978) model can be illustrated by an example shown in Figure 2.22.

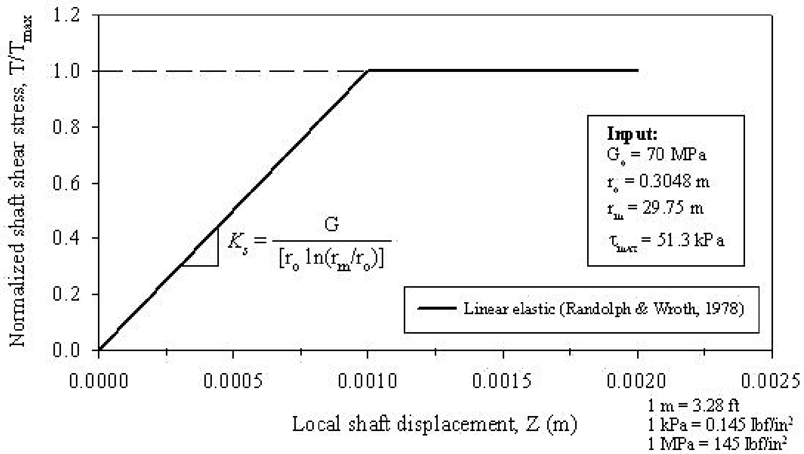

Figure 2.22 An example of the linear t-z curve (after Pando et al. 2006)

Poulos and Davis (1990) used Boussinesq's theory to approximate the *q-z* curve for a rigid footing resting on an elastic half-space, as expressed as:

$$z_b = \frac{qA_b(1-\nu)}{4Gr_0} \tag{2.41}$$

where z_b = pile tip displacement, q = pile tip pressure, A_b = pile tip area, ν = Poisson's ratio. A linear *q-z* curve is shown in Figure 2.23, in which the pile tip load, $Q_b = q \cdot A_b$.

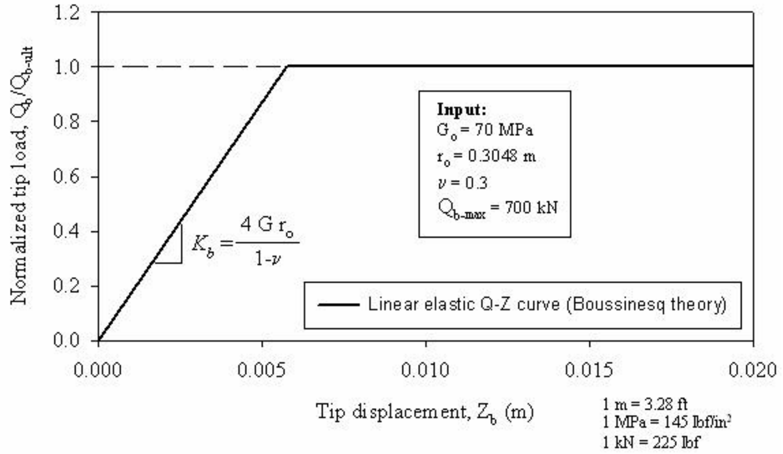

Figure 2.23 An example of the linear *q-z* curve (after Pando et al. 2006)

2.4.9 Theoretical Load-Transfer Curves for Nonlinear Soils

Based on the work done by Randolph and Wroth (1978), Kraft et al. (1981) proposed a *t-z* curve model for piles embedded in nonlinear soils. The hyperbolic stress-strain model of soil can be expressed by (Kraft, et al., 1981, Chow 1986, McVay, et al., 1989):

$$G = G_i\left(1-\frac{\tau_0 R_f}{\tau_{\max}}\right) \tag{2.42}$$

where G_i = initial shear modulus at small strains, R_f = failure ratio and can be obtained from triaxial tests, $\tau_{\max}$ = shear stress at failure = $K_h\sigma_v^{'}\tan\delta$.

The initial shear modulus can be computed using laboratory tests (Janbu 1963) and empirical correlations with in situ CPT tests (e.g., Baldi et al 1989, Rix and Stokoe 1991, Chow 1996, and Lunne et al. 1997).

The method proposed by Janbu (1963) is given by:

$$G_i = E_i / [2(1+\upsilon)] \tag{2.43}$$

$$E_i = Kp_a\left(\frac{\sigma_3}{p_a}\right)^n \tag{2.44}$$

where E_i = the initial Young's modulus, σ_3= confining pressure = $K\,\sigma'_v$, K and n are constants and can be obtained from triaxial tests. The constant K quantifies the initial modulus magnitude as a multiple of P_a and coefficient n shows how the modulus is dependent on earth pressure (Lapos and Moore 2002).

Chow (1996) developed the correlation between the CPT tip resistance, q_c, and the initial shear modulus based on the calibration chamber tests conducted by Baldi, et al. (1989) , as given by:

$$G_i = \frac{q_c}{A + B\eta - C\eta^2} \tag{2.45}$$

$$\eta = \frac{q_c}{\sqrt{P_a\sigma_v^{'}}} \tag{2.46}$$

where A, B, C are constants and A = 0.0203, B = 0.00125, $C = 1.216\times10^{-6}$ for uncemented quartzitic sands, and P_a = atmospheric pressure. Then, the *t-z* curves proposed by Kraft et al. (1981) are expressed by:

$$z = \frac{\tau r_0}{G_i}\ln\left(\frac{r_m / r_0 - \psi}{1-\psi}\right) \tag{2.47}$$

where τ = shear resistance on the pile-soil interface, r_0 = the pile radius, $\psi = \tau R_f / \tau_{\max}$.

Since the hyperbolic model is only appropriate when the initial shear modulus is from conventional laboratory tests, the modified hyperbolic model proposed by Fahey and Carter

(1993) can be used if the initial shear modulus is obtained from dynamic test measurements (Randolph 1994). The modified hyperbolic stress-strain model is given by (Fahey and Carter 1993):

$$G = G_i \left[1 - f \left(\frac{\tau_0}{\tau_{\max}} \right)^g \right] \tag{2.48}$$

where *f* and *g* are empirical curve fitting parameters. It can be seen that this modified hyperbolic model would become a standard hyperbolic model for $f = R_f$ and $g = 1$.With this stress-strain model the *t-z* curve can be derived as:

$$z = \frac{\tau r_0}{G_i g} \ln \left(\frac{(r_m / r_0)^g - f(\tau / \tau_{\max})^g}{1 - f(\tau / \tau_{\max})^g} \right) \tag{2.49}$$

A comparison of *t-z* curves between the modified hyperbolic model, standard hyperbolic model and linear elastic model was performed by Pando et al. (2006) with $R_f = 1.0$, as presented in Figure 2.24. The hyperbolic *t-z* curve has the same initial stiffness as the linear curve. When $R_f = 0$, the nonlinear *t-z* curve is identical to the linear curve.

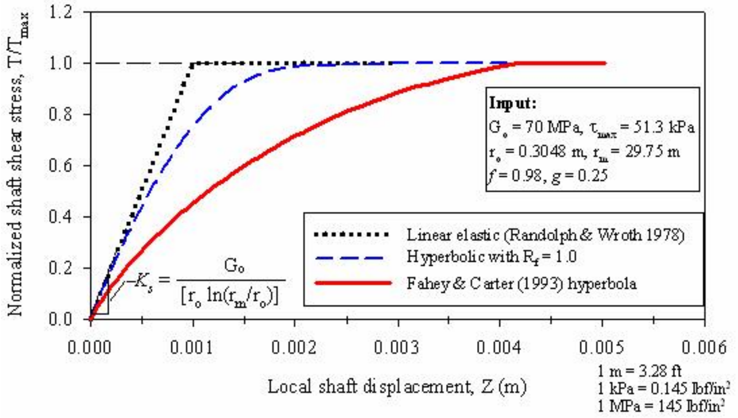

Figure 2.24 An example of the t-z curve as $R_f = 1.0$ (after Pando et al. 2006)

Fahey and Carter (1993) developed a *q-z* curve model with a hyperbolic load-deformation relationship proposed by Chow (1986), in which the tangent stiffness K_t^b is given by:

$$K_t^b = K_o^b \left(1 - f(q_b / q_{b-\max})^g \right) \tag{2.50}$$

where K_o^b = initial elastic soil stiffness = $4G_i \cdot r_0 / (1 - \nu)$ and $q_{b-\max}$ = ultimate pile tip pressure. Then, the *q-z* curve is obtained by:

$$z_b = \frac{q_b A_b}{K_o^b \left(1 - f\,(q_b / q_{b-\max})^g\right)} \tag{2.51}$$

For comparison purpose an example of the hyperbolic and the linear elastic *q-z* curves are shown in Figure 2.25.

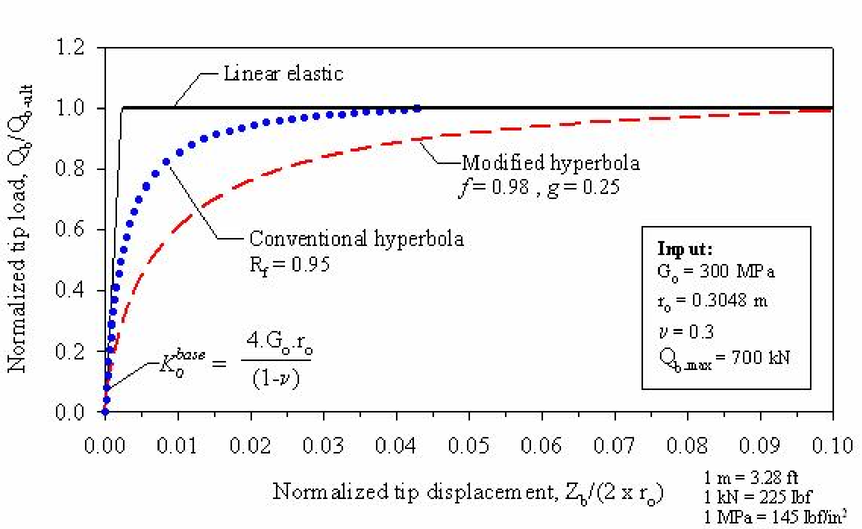

Figure 2.25 Comparison of the hyperbolic and the linear elastic *q-z* curves (after Pando et al. 2006)

For drilled shafts constructed with permanent steel casing, AASHTO (2007) and Brown el. (2010) states that a reduction in the axial capacity should be considered. AASHTO (2007) states that no specific data are available and that reduction factors of 0.6 to 0.75 are commonly used. However, as reported by Camp et al. (2002), the reduction factor can be as low as 0.20. Therefore, more axial loading tests on both cased and uncased drilled shafts embedded in similar soil conditions would be helpful to address this issue.

2.5 DESIGN METHODS FOR LATERALLY LOADED PILES

Pushover analysis is commonly used to develop the load-deflection relationship for drilled shaft. Several models have been developed to evaluate the lateral response of a soil-shaft system, including the elastic pile and soil model, the finite element or continuum soil model, rigid pile and plastic soil model, and the nonlinear pile and *p-y* soil model (Wallace et al. 2001).

2.5.1 Elastic Pile and Soil Approach

This method is based on the beam on elastic foundation concept proposed by Hetenyi (1946). It is assumed that loads applied on the pile are small and both the pile and soil are linear elastic. The relationship between lateral soil reaction per unit length (*p*) and the pile lateral deflection (*y*) is linear and presented by the modulus of subgrade reaction (*K*), which is provided by Terzaghi (1955). This method was employed by Polous and Davis (1980) to evaluate the interaction between single piles and soil under variety of cases of loading. The limitation of this method is that it is not suitable for assessing the large deformation response or collapse potential of a pile in nonlinear soil (Wallace et al. 2001).

2.5.2 Continuum Approach

Finite element (FE) analysis can be used to evaluate the interaction between pile and soil. Two-dimensional FE models were firstly used Yegian and Wright (1973) and Thompson (1977) to study pile behavior. Yegian and Wright (1973) investigated the lateral soil resistance-displacement relationships for pile embedded in soft clays, in which a nonlinear model was used for the soil. Thompson (1977) successfully developed a FE model for predicting soil response curves which agreed well with the results of full-scale testing near the ground surface. Kuhlemeyer (1979) and Randolph (1981) were among the first to develop a three-dimensional (3-D) FE model with linear soil elements. Trochanis et al. (1988) employed Drucker-Prager model for soil in their 3-D FE model to calculate the axial and lateral response of piles to monotonic and cyclic loading. Kooijman (1989) and Brown et al. (1989) developed nonlinear 3-D FE model for the soil-pile system using elasto-plastic formulations to investigate lateral soil-resistance and pile deflection relations.

2.5.3 Rigid Pile and Plastic Soil Approach

For rigid pile in plastic soil, the ultimate lateral resistance can be obtained using the equations developed by Broms (1964a). This method assumed that ultimate lateral resistance for a short rigid pile is governed by the passive earth pressure of the surrounding soil. The minimum dimensions of a pile that are required to resist the design lateral load can be evaluated using this method. Therefore, this approach can be employed to provide preliminary assessment for the soil-pile interaction.

2.5.4 Beam-on-Foundation Approach with Nonlinear Model for Pile and Soil

As shown in Figure 2.26, the nonlinear reaction of soil along the depth of a laterally loaded pile can be modeled with discrete springs (*p-y* curves) (Reese et al. 1975). Although the soil is not considered as continuum in this approach, the commonly used *p-y* curves are derived from full-scale tests with continuum effect implicitly incorporated (Wallace et al. 2001). For example, the American Petroleum Institute (API 1993) recommended *p-y* curves were back-calculated based on the data from full-scale lateral-load testing of slender piles with both monotonic and cyclic loading. Specifically, the *p-y* curves 1) for soft clays with free water are derived from the tests conducted by Matlock (1970) with 320 mm (12.75 inches) diameter steel-pipe piles; 2) for stiff clays with free water are derived from the experiments with 610 mm (24 in) diameter steel-pipe piles performed by Reese et al. (1975); 3) for stiff clays without free-water are established on tests with 760 mm (30 in) diameter reinforced concrete drilled piles achieved by Reese and Welch (1975); and 4) sands are obtained from tests with 610 mm (24 in) diameter steel-pipe piles by Cox et al. (1974).

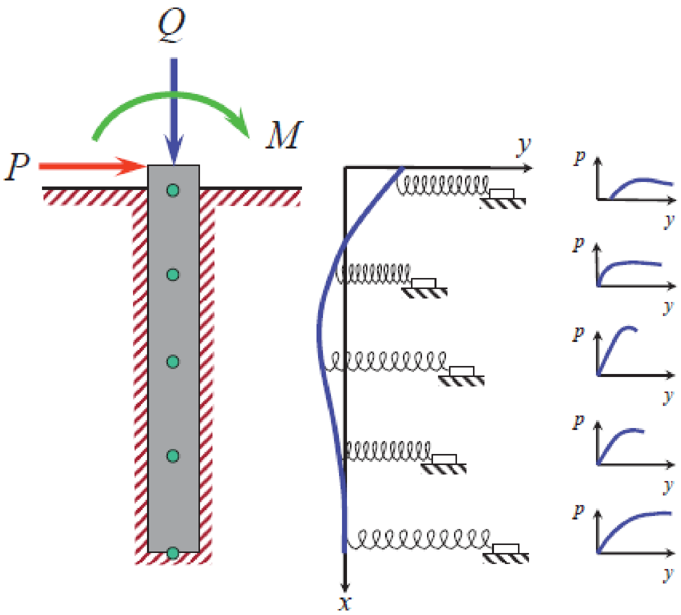

Figure 2.26 Nonlinear pile and *p*-*y* curves for laterally loaded piles (after Isenhower and Wang 2015)

As described by Wallace et al. (2001), this curve can be divided into three portions: linear portion (from origin to point ‘a’), nonlinear portion (from points ‘a’ to ‘b’), and constant (straight-line) portion (beyond point ‘b’). When the deflection of pile in soil is small, the shear strains in the soil are small and the relationship between p and y is linear. The modulus of the *p*-*y* curve is dependent on the soil elastic modulus, E_s. The nonlinear portion of the *p*-*y* curve is empirical and derived from full-scale lateral load tests. The constant portion indicates that the soil is behaving plastically. The ultimate resistance p_{ult} is related to the pile dimensions and soil properties.

2.5.5 *p-y* Curve For Soft Clay with Free Water

Matlock (1970) describe lateral load tests employing a steel-pipe piles that are 12.8 m (42 ft) long, with a diameter of 320 mm (12.75 inches). The pile was driven into soft clay deposit near Lake Austin, Texas, which can be classified as CH according to the Unified Soil Classification System. The undrained shear strength was found from field vane shear tests and averaged 29 Kpa (0.6 ksf) with the consideration for creep and anisotropy. The axial strain at 50% of the failure load (ε_{50}) was measured from triaxial tests and was found to be 0.012. Both static and cyclic lateral loads were applied on the pile just above ground surface. The water table was maintained above the ground surface during loading.

With the test results, Matlock proposed the *p*-*y* curves for soft clay. The characteristic shape of the proposed soft clay *p*-*y* curves is shown in Figure 2.27. For static loading, *p*-*y* curves can be constructed by:

$$\frac{p}{p_u} = 0.5\left(\frac{y}{y_{50}}\right)^{1/3} \tag{2.52}$$

$$p_u = N_p s_u D \tag{2.53}$$

$$y_{50} = 2.5\varepsilon_{50} D \tag{2.54}$$

where p_u = ultimate soil resistance, y_{50} = the soil displacement at one-half of ultimate soil resistance, s_u = soil undrained shear strength, D = pile diameter, ε_{50} = the strain at one-half of the maximum principal stress difference (0.020 for soft clay), N_p = coefficient related to soil unit weight (γ), depth (z) as proposed by Matlock (1970) and Reese and Welch (1975). Stevens and Audibert (1980), Randolph and Houlsby (1984), Murff and Hamilton (1993), Martin and Randolph (2006), and Georgiadis and Georgiadis (2010) developed other methods to obtain N_p taken into account pile roughness using pile-soil adhesion factor (α).

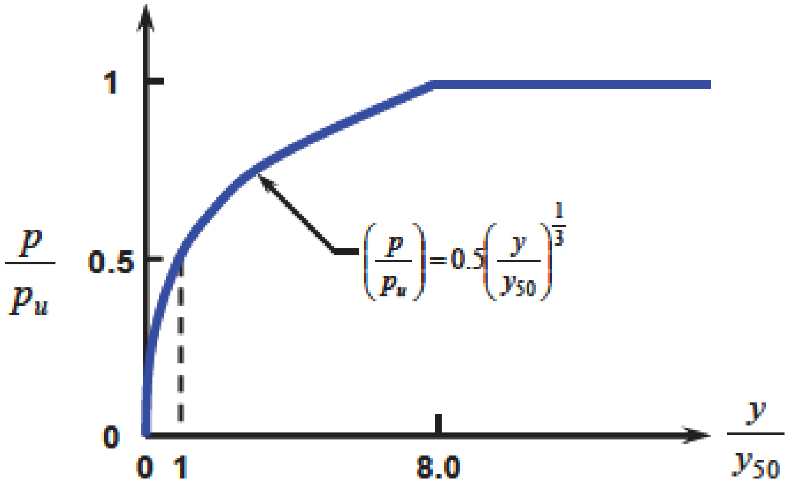

Figure 2.27 Characteristic shapes of p-y curves for soft clay in the presence of free water under static loading (after Isenhower and Wang 2015 originally from Matlock, 1970)

2.5.6 *p-y* Curve for Stiff Clay with Free Water

Reese et al. (1975) conducted full-scale lateral-loading tests on two 610 mm (24 inches) diameter, 15.2 m (50 feet) long steel pipe piles, which were driven into a stiff clay site near Manor, Texas. Unconsolidated-undrained triaxial tests were employed to measure the undrained shear strength of soil, which varied from around 70 kPa (1.5 ksf) near the surface to 1100 kPa (22 ksf) at the toe of the piles. The axial strain at 50% of the failure load (ε_{50}) was measured from triaxial tests and was found in the range from 0.004 to 0.007. Water table was maintained above the ground surface of the site for several weeks before obtaining the soil properties through experiments. One pile was applied static loading and the second one was under cyclic loading. The loading point was 0.3 m (1 ft) above ground surface for both piles. The typical shape of *p-y* curves in stiff clay for static loading is illustrated in Figure 2.28. It is noted that a large loss of soil resistance is shown in this model, compared to the Matlock (1970) soft clay *p-y* curves. It is probably due to the soil at this site was expansive and continued to absorb water as the testing progressed (Juirnarongrit 2002).

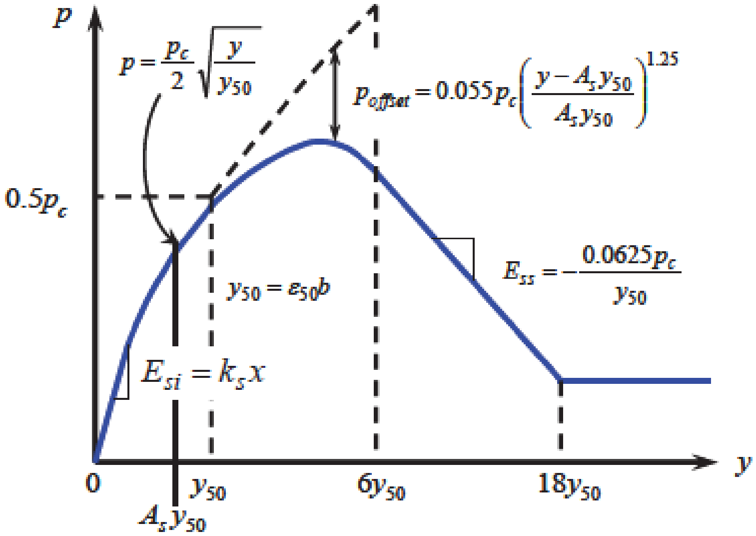

Figure 2.28 Characteristic shape of *p-y* curves for stiff clay in the presence of free water under static loading (after Isenhower and Wang 2015 originally from Reese et al. 1975)

The *p-y* curves in stiff clay for static loading can be derived as follows (Reese et al. 1975):

Compute ultimate Soil Resistance (p_u) from the lessor of two expressions reflecting shallow wedge failure and deep flow failure, as given by:

$$p_{ut} = 2c_a D + \gamma' Dz + 2.83 c_a z \quad \textit{Wedge Failure} \tag{2.55}$$

$$p_{ud} = 11 s_u D \quad \textit{Flow Failure} \tag{2.56}$$

where c_a = average undrained shear strength over depth z, D = pile diameter, γ' = effective soil unit weight, and s_u = soil undrained shear strength.

Construct the initial linear portion of the *p-y* curves by:

$$p = (k_{py} z) y \tag{2.57}$$

where k_{py} = coefficient of change subgrade reaction constant (units: F/L^3), which increases linearly with depth (Reese et al. 1975).

Estimate the first parabolic portion of the *p-y* curves by:

$$p = 0.5 p_u (\frac{y}{y_{50}})^{0.5}, y_{50} = \varepsilon_{50} D \tag{2.58}$$

where y_{50} = the soil displacement at one-half of ultimate soil resistance, ε_{50} = the strain at one-half of the maximum principal stress difference (0.004-0.007)

Establish the second parabolic portion of the *p-y* curves, from $A_s y_{50}$ to $6A_s y_{50}$, by:

$$p = 0.5 p_u (\frac{y}{y_{50}})^{0.5} - 0.055 p_u (\frac{y - A_s y_{50}}{A_s y_{50}})^{1.25} \tag{2.59}$$

where A_s = constants, which can be determined from Figure 2.29.

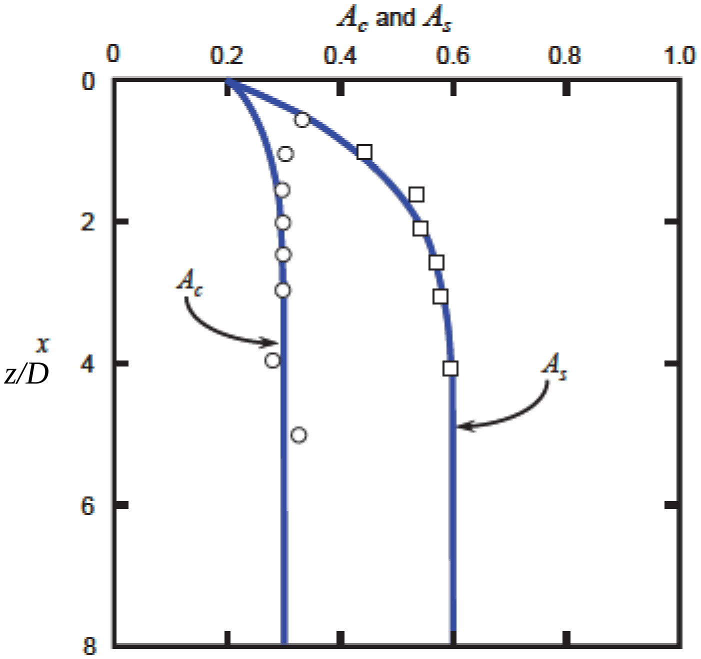

Figure 2.29 Chart for determination of constant A_s for stiff clay below water table (after Isenhower and Wang 2015 originally from Reese et al. 1975)

1. Establish straight-line portion, from $6A_s y_{50}$ to $18A_s y_{50}$, by:

$$p = 0.5 p_u (6A_s)^{0.5} - 0.411 p_u - \frac{0.0625}{y_{50}} p_u (y - 6A_s y_{50}) \tag{2.60}$$

2. Determine the final straight-line portion by:

$$p = 0.5 p_u (6A_s)^{0.5} - 0.411 p_u - 0.75 p_u A_s \tag{2.61}$$

2.5.7 *p-y* Curve for Stiff Clay without Free Water

Reese and Welch (1975) conducted full-scale lateral-load tests with a 760 mm (30 inches) diameter, 12.8 m (42 ft) long reinforced concrete drilled piles at a site in Houston, Texas. The site consisted of overconsolidated, fissured clay with a water table of 5.5 m (18 ft). Unconsolidated-undrained triaxial compression tests were utilized to measure the undrained shear strength of soil, which averaged between 75 kPa (1.5 ksf) and 163 kPa (3.4 ksf). The axial strain at 50% of the failure load (ε_{50}) was measured from triaxial tests and averaged 0.005. The typical shape of *p-y* curves in stiff clay without free water for static loading is illustrated in Figure 2.30. It is seen that the shape and formulation of this *p-y* curves are similar to those for soft clay with free water proposed by Matlock (1970). The forth degree of parabola relationship was used to represent the curve.

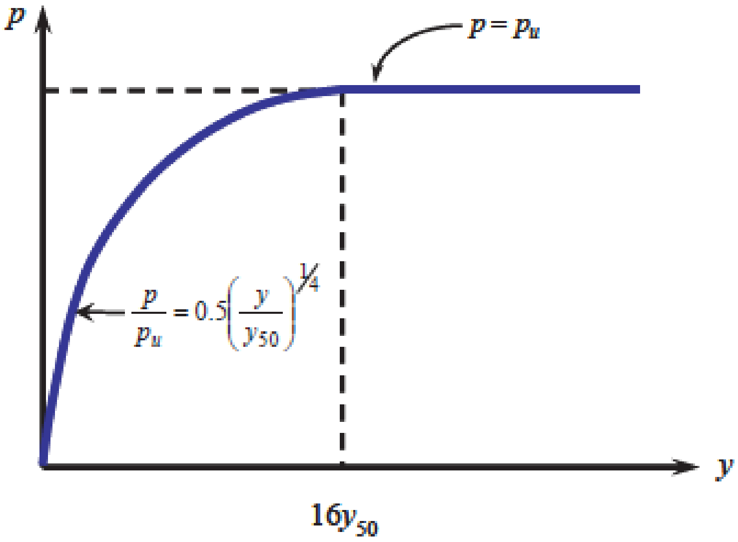

Figure 2.30 Characteristic shape of *p-y* curves for static loading in stiff clay without free water (after Isenhower and Wang 2015, originally from Reese and Welch 1975)

The *p-y* curves in stiff clay without free water for static loading can be obtained as follows (Reese and Welch 1975):

1. Compute Ultimate Soil Resistance, p_u, from the lessor of two expressions, as given by:

$$p_u = \left(3 + \frac{\gamma'}{s_u} z + \frac{J}{D} z\right) s_u D \tag{2.62}$$

$$p_u = 9 s_u D \tag{2.63}$$

where s_u = undrained shear strength, z = depth, D = pile diameter, γ' = effective soil unit weight, and J = constant = 0.5.

2. Determine the pile deflection at one-half the ultimate soil resistance, y_{50}

$$y_{50} = 2.5\varepsilon_{50}D$$

3. Develop *p-y* curves by:

$$\frac{p}{p_u} = 0.5\left(\frac{y}{y_{50}}\right)^{0.25} \qquad for\ \ y \le 16y_{50} \tag{2.64}$$

$$p = p_u \qquad for\ \ y \le 16y_{50} \tag{2.65}$$

2.5.8 *p-y* Curve for Sand Proposed by Reese et al. (1974)

Cox et al. (1974) reported the results of a test of two steel-pipe piles with a diameter of 610 mm (24 in) and penetration length of 21 m (70 ft) at the site on Mustang Island, Texas. Both of the piles were driven into a deposit of submerged, dense, fine sand with a friction angle of 39 degrees. The water table was maintained above the mudline through the experiments. One pile was applied static loading and the second one was under cyclic loading. The characteristic shape of *p-y* curves for sand is illustrated in Figure 2.31, in which *b* is pile diameter and *x* is depth.

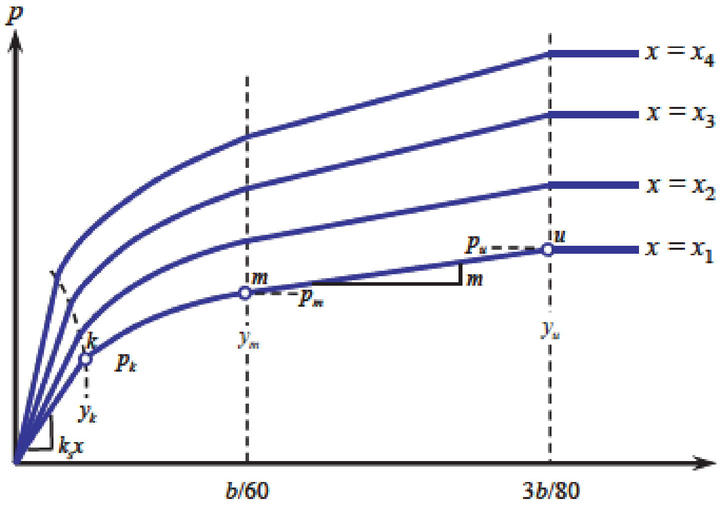

Figure 2.31 Characteristic Shapes of *p-y* Curves for Sand (after Isenhower and Wang 2015 originally from Cox et al., 1974)

The procedure of constructing the *p-y* curves for sand is shown as follows (Reese et al. 1974):

1. Compute parameters that needed for constructing the *p-y* curves:

$$\alpha = \frac{\phi}{2}, \beta = 45 + \frac{\phi}{2}, K_0 = 0.4, K_a = \tan^2(45 - \frac{\phi}{2}) \tag{2.66}$$

   where ϕ = friction angle.

2. Compute govern ultimate soil resistance (p_s) from the lessor of two expressions reflecting shallow wedge failure and deep flow failure, as given by following equations:

$$p_{st} = \gamma' z \left[\begin{array}{l} \dfrac{K_0 z \tan\phi \sin\beta}{\tan(\beta-\phi)\cos\alpha} + \dfrac{\tan\beta}{\tan(\beta-\phi)}(D + z\tan\beta\tan\alpha) \\ + K_0 z \tan\beta(\tan\phi\sin\beta - \tan\alpha) - K_a D \end{array} \right] \tag{2.67}$$

$$p_{sd} = K_a D\gamma' z(\tan^8\beta - 1) + K_0 D\gamma' z\tan\phi\tan^4\beta \tag{2.68}$$

where z = depth, γ' = effective soil unit weight. This method for computing ultimate soil resistance was proposed by Reese et al. (1974), as shown in Figure 2.32. Many other methods have also been proposed by Brinch (1961), Broms (1964), Poulos and Davis (1980), Fleming et al. (1992), Zhang et al. (2005).

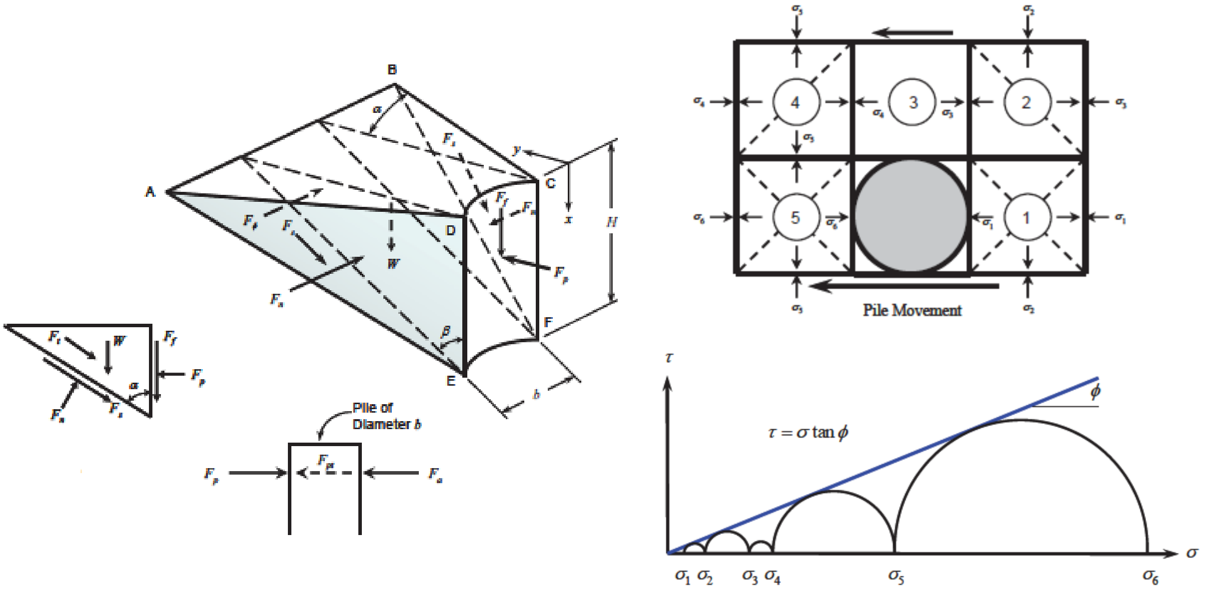

(a) Passive Wedge Failure (b) Lateral Flow Failure

Figure 2.32 Sand failure modes for laterally loaded pile for (a) shallow passive wedge failure and (b) deep flow failure (after Isenhower and Wang 2015 originally from Reese et al. 1974)

3. Calculate ultimate soil resistance (p_u) :

$$p_u = \overline{A}_s p_s \tag{2.69}$$

where $\overline{A}_s$= adjustment coefficient for static *p-y* curves, which can be obtained from Figure 2.33a.

4. Compute soil pressure (p_m) :

$$p_m = B_s p_s \tag{2.70}$$

where B_s = nondimensional coefficient for static *p-y* curves, which can be found from Figure 2.33b.

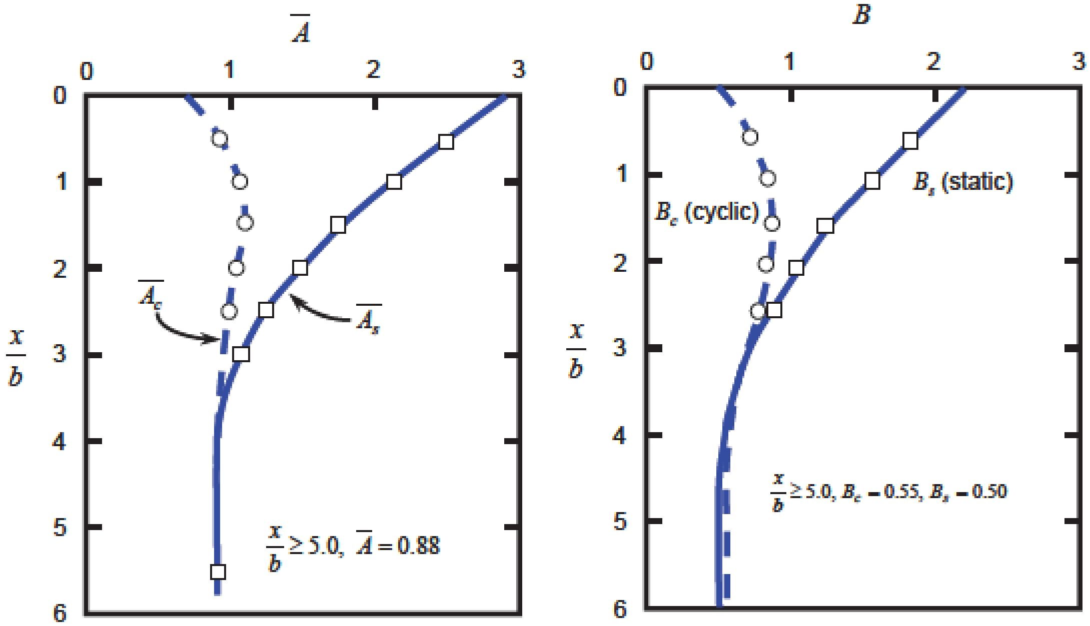

(a) (b)

Figure 2.33 Charts used for determining a) Coefficient A and b) Coefficient B for developing *p-y* curves for sand (after Isenhower and Wang 2015 originally from Reese et al. 1974)

5. Construct initial straight-line portion

$$p = (k_{py} z) y \tag{2.71}$$

where k_{py} = coefficient of change subgrade reaction constant (F/L^3), which can be obtained from Table 2.4.

Table 2.4 Values of Coefficients of Change Subgrade Reaction Constant (after Reese et al. 1974)

Soil Type	Submerged	Above Water
Loose Sand	20	25
Medium Dense Sand	60	90
Dense Sand	125	225

6. Establish parabolic section using the following expressions:

$$p = \overline{C} y^{1/n}, m = \frac{p_u - p_m}{y_u - y_m}, n = \frac{p_m}{m y_m}, \overline{C} = \frac{p_m}{y_m^{1/n}}, y_k = \left(\frac{\overline{C}}{k_{py} z} \right)^{n/n-1} \tag{2.72}$$

2.5.9 *p-y* Curve for Sand Proposed by API (1987)

API (1987) presented an alternative method for constructing *p-y* curves for sand. This method is easier to follow compared to the method proposed by Reese et al. (1974). In this method, the *p-y* curves for sand were given with a hyperbolic tangent function.

The API procedure for *p-y* curves in sand is shown as following:

1. Compute govern ultimate soil resistance (p_s) from the lessor of two expressions reflecting shallow wedge failure, as given by:

$$p_{st} = (C_1 z + C_2 D)\gamma' z \tag{2.73}$$

$$p_{sd} = C_3 D \gamma' z \tag{2.74}$$

where C_1, C_2, C_3 = coefficients from Figure 2.34a.

2. Determine adjustment coefficient $\overline{A_S}$, as given by

$$\overline{A}_s = \left(3.0 - 0.8 \frac{z}{D} \right) \geq 0.9 \tag{2.75}$$

3. Develop characteristic shape of *p-y* curves for sand

$$p = \overline{A}_s p_s \tanh\left(\frac{kz}{\overline{A} p_u} y \right) \tag{2.76}$$

where k = coefficient of change of modulus of subgrade reaction F/L^3, from Figure 2.34b.

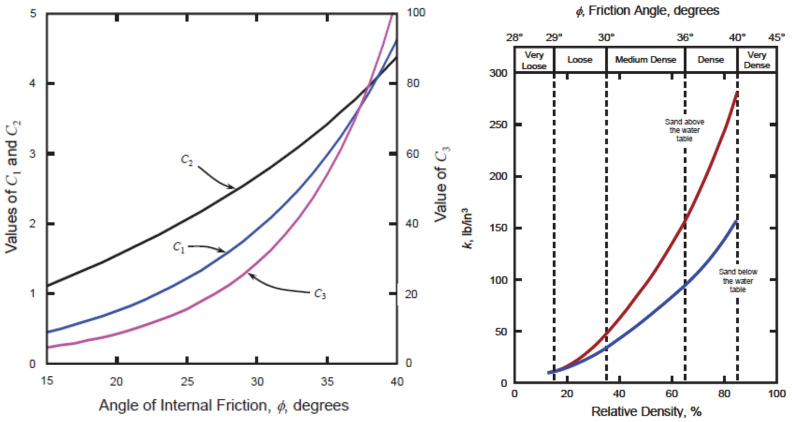

(a) (b)

Figure 2.34 Charts used for developing p-y curves for sand (after Isenhower and Wang 2015 originally from API 1987)

2.5.10 *p-y* Curve for *c-ϕ* Soils

Ismael (1990) conducted full-scale lateral loading tests of 305-mm (12-in) diameter reinforced concrete bored piles with lengths of 3 m (10 ft) and 5 m (16.4 ft). The site was selected in South Surra, Kuwait and consisted of cemented sands with cohesion of 20 kPa (420 psf) and friction angle of 35 degrees, based on drained triaxial test results. Ismael (1990) found that Resse et al. (1974) sand *p-y* curves underestimated the measured pile response with no consideration of cohesion. Ground water was below the bottom of the drilled shafts. The characteristic shape of *p-y* curves in cemented sand is illustrated in Figure 2.35.

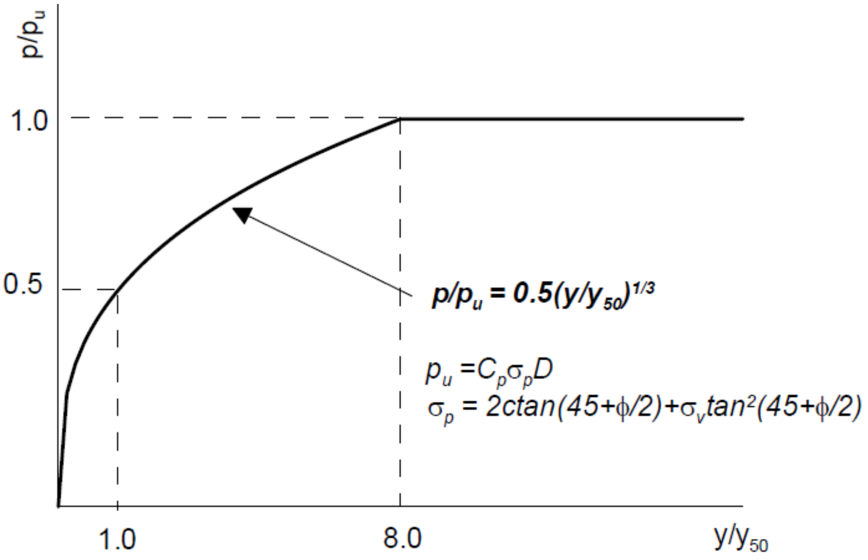

Figure 2.35 Characteristic shape of *p-y* curve for cemented sand (after Ismael 1990)

The procedure in establishing the *p-y* curves for cemented sand is shown as follows (Ismael 1990):

1. Compute the ultimate soil resistance, p_u, as given by:

$$p_u = C_p \sigma_p D \tag{2.77}$$

Where C_p = correction factor, which is related to soil friction angle (ϕ), σ_p = passive earth pressure, which is a function of soil cohesion (c) and friction angle (ϕ). C_p and σ_p can be obtained from the following expressions:

$$C_p = 1.5 \text{ for } \phi \le 15^o \tag{2.78}$$

$$C_p = \frac{\phi}{10} \text{ for } \phi > 15^o \tag{2.79}$$

$$\sigma_p = 2c\tan(45 + \frac{\phi}{2}) + \sigma_v \tan^2(45 + \frac{\phi}{2}) \tag{2.80}$$

2. Establish the *p*-*y* curves for cemented sands

$$\frac{p}{p_u} = 0.5\left(\frac{y}{y_{50}}\right)^{1/3} \tag{2.81}$$

where y_{50} = the soil displacement at one-half of ultimate soil resistance, which is a function of strain (ε_c) at ($\sigma_1 - \sigma_3$) and pile diameter (D), as given by:

$$y_{50} = 2.5\varepsilon_c D \tag{2.82}$$

The *p*-*y* curves proposed by Ismael (1990) employed a polynomial function similar to soft clay *p*-*y* curves (Matlock 1970), which implies that the *c*-*φ* soil behaves more like cohesive soil than cohesionless soil. Reese and Van Impe (2001), however, suggested that the behavior of the cemented soils is more like that of cohesionless soil and that strain softening should occur after reaching peak strength, as shown Figure 2.36.

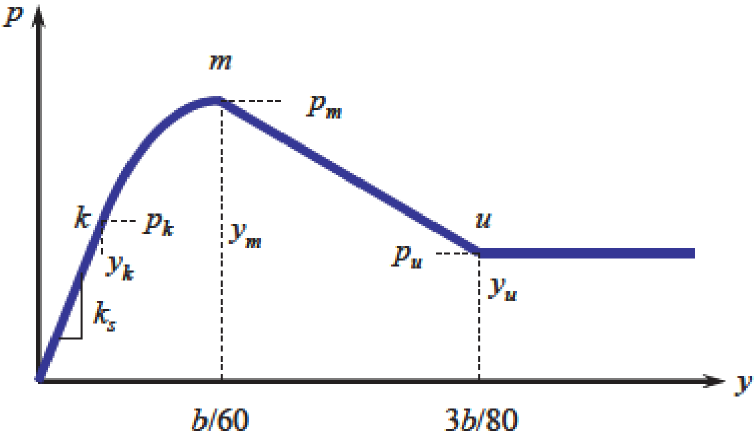

Figure 2.36 Characteristic shape of *p-y* curve for c-φ soil (after Isenhower and Wang 2015 originally from Reese and Van Impe 2001)

The procedure in establishing *p-y* curves in cemented sand proposed by Reese and Van Impe (2001) is shown as following:

1. Compute parameters that needed for constructing the *p-y* curves in cemented sand:

$$\alpha = \frac{\phi}{2}, \beta = 45 + \frac{\phi}{2}, K_0 = 0.4, K_a = \tan^2(45 - \frac{\phi}{2}) \qquad (2.83)$$

2. Compute ultimate soil resistance (p_u) considering both friction component ($p_{u\phi}$) and cohesion component (p_{uc}), as given by:

$$p_u = \overline{A}_s p_{u\phi} + p_{uc} \qquad (2.84)$$

where $\overline{A_s}$ = adjustment coefficient.

3. Compute the friction component ($p_{u\phi}$) from the lessor of two expressions:

$$p_{st} = \gamma' z \left[\frac{K_0 z \tan\phi \sin\beta}{\tan(\beta - \phi)\cos\alpha} + \frac{\tan\beta}{\tan(\beta - \phi)}(D + z\tan\beta\tan\alpha) \right] \qquad (2.85)$$
$$+\gamma z\left[K_0 z \tan\beta(\tan\phi\sin\beta - \tan\alpha) - K_a D\right]$$

$$p_{u\phi} = K_a D\gamma' z(\tan^8\beta - 1) + K_0 D\gamma' z\tan\phi\tan^4\beta \qquad (2.86)$$

4. Compute the cohesion component (p_{uc}) from the lessor of two expressions :

$$p_{uc} = \left(3 + \frac{\gamma'}{c}z + \frac{J}{D}z\right)cD \qquad (2.87)$$

$$p_{uc} = 9cD \tag{2.88}$$

where c = soil cohesion, and J = constant.

5. Estimate soil pressure at $D/60$, as given by:

$$p_m = B_s p_{u\phi} + p_{uc} \tag{2.89}$$

where B_s = nondimensional coefficient for static *p*-*y* curves from Figure 2.33b.

6. Establish initial straight-line portion by:

$$p = (k_{py} z) y, k_{py} = k_c + k_\phi \tag{2.90}$$

where k_c and k_ϕ = Initial subgrade reaction constant from cohesion and friction components, respectively (from Figure 2.37).

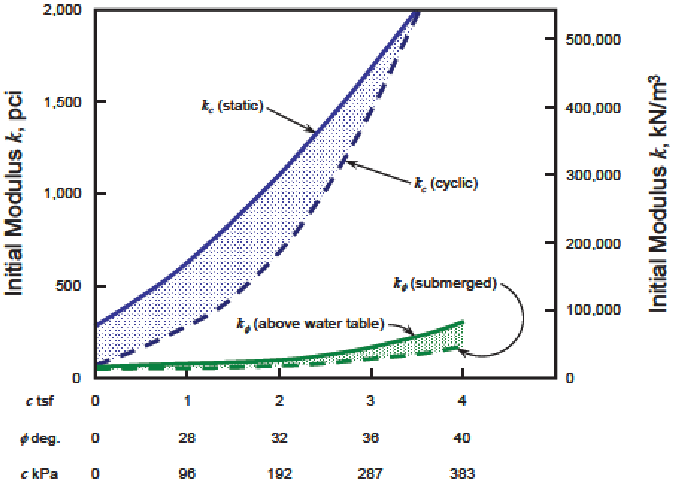

Figure 2.37 Initial subgrade reaction constant with values of k_c and k_ϕ (after Isenhower and Wang 2015 originally from Reese and Van Impe 2001)

7. Determine parabolic section of the *p*-*y* curves, as given by:

$$p = \overline{C} y^{1/n}, m = \frac{p_u - p_m}{y_u - y_m}, n = \frac{p_m}{m y_m}, \overline{C} = \frac{p_m}{y_m^{1/n}}, y_k = \left(\frac{\overline{C}}{k_{py} z} \right)^{n/n-1} \tag{2.91}$$

Juirnarongrit (2002) reported that the pile response predicted using the *p*-*y* curves proposed by Ismael (1990) agreed well with the observation from the field tests for cast-in-drilled-hole (CIDH) piles in weakly cemented sand and gave better prediction than silt *p*-*y* curves proposed by Reese and Van Impe (2001).

2.5.11 Hyperbolic Soil Model

Kondner (1963) proposed the hyperbolic *p-y* curves, as shown in Figure 2.38, based on the stress–strain relationship of soil in triaxial compression tests. The *p-y* curves are expressed by:

$$p = \frac{y}{\frac{1}{K} + \frac{y}{p_u}} \tag{2.92}$$

where K = initial slope, p_u = ultimate soil resistance. This method has been adopted by some researchers (e.g., Carter 1984, Georgiadis et al. 1991, Rajashree and Sitharam 2001, Kim et al. 2004, Liang et al. 2009, Georgiadis and Georgiadis 2010, and Nimityongskul 2010).

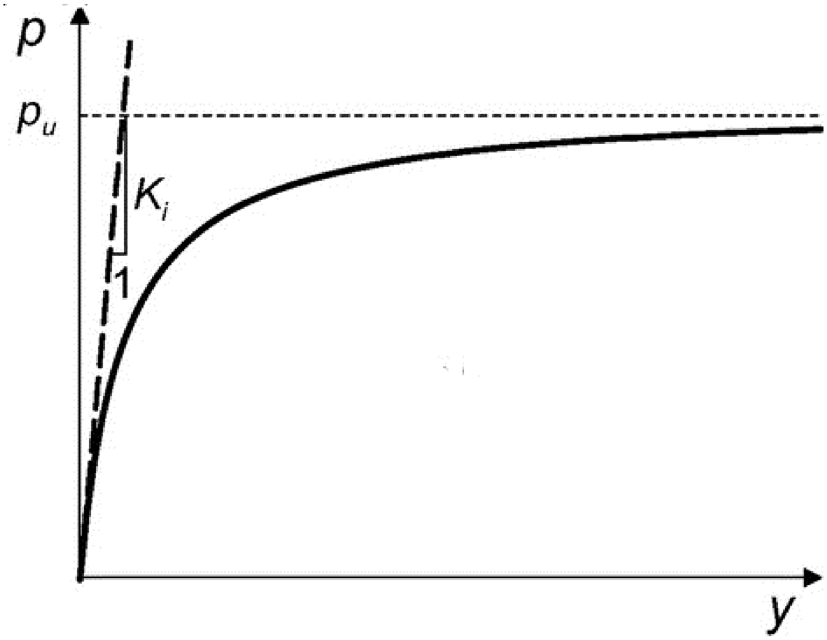

Figure 2.38 Shape of hyperbolic *p-y* curves (after Georgiadis and Georgiadis 2010)

The procedure in creating *p-y* curves in clay for static undrained lateral loading is shown as following (Georgiadis and Georgiadis 2010):

1. Estimate ultimate soil resistance (p_u)

   $$p_u = N_p S_u D \tag{2.93}$$

   where S_u = undrained shear strength, D = pile diameter, and N_p = lateral bearing capacity factor, which is given by:

   $$N_p = N_{pu} - (N_{pu} - N_{po})e^{-\lambda(z/D)} \tag{2.94}$$

$$N_{po} = 2 + 1.5a \tag{2.95}$$

$$N_{pu} = \pi + 2\Delta + 2cos\Delta + 4(cos\frac{\Delta}{2} + sin\frac{\Delta}{2}) \tag{2.96}$$

$$\Delta = sin^{-1}a \tag{2.97}$$

$$\lambda = 0.55 - 0.15a \tag{2.98}$$

where N_{pu} = ultimate lateral bearing capacity factor, N_{po} = lateral bearing capacity factor at the ground surface, λ = non-dimensional factor, z = depth, a = pile-soil adhesion factor, which can be obtained from Figure 2.39.

2. Compute the initial stiffness of *p*-*y* curves:

$$K_i = \frac{1.3E_i}{1-\nu^2}\left(\frac{E_i D^4}{E_p I_p}\right)^{1/12} \tag{2.99}$$

where ν = Poisson's ratio, $E_p I_p$ = pile stiffness, and E_i = initial modulus of elasticity and is related with the elasticity modulus (E_{50}) at 50 percent of the failure stress from triaxial compression test, as given by:

$$E_i = 1.67E_{50} \tag{2.100}$$

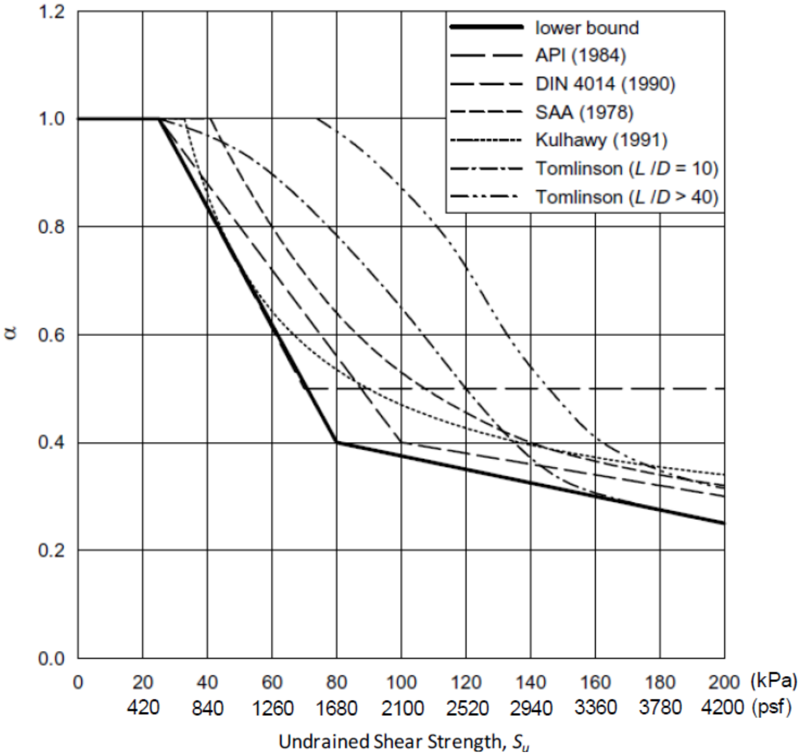

Figure 2.39 Summary of adhesion factor (a) versus undrained shear strength (s_u) relationships for piles and drilled shafts (after Georgiadis and Georgiadis 2010)

3. Develop *p-y* curves, as shown in the following hyperbolic expression

$$p = \frac{y}{\frac{1}{K} + \frac{y}{p_u}} \tag{2.101}$$

2.5.12 Other *p-y* Curves Models

Li and Yang (2017) proposed a *p-y* curve model for frozen silt, which is not discussed in detail herein. Murchison and O'Neill (1984) proposed a *p-y* curve model from back analyses of full-scale instrumented pile load test on sand. The model is expressed as follows:

$$p = \eta A p_u \tanh\left(\frac{k_h}{\eta A p_u} y\right) \tag{2.102}$$

where η = is the pile shape factor, A = empirical adjustment factor, and p_u = ultimate soil resistance. A bilinear *p-y* curve model was developed by Scott (1980) using the results of centrifuge tests. The function is given by:

$$p_k = \frac{\sigma_0^{'} D}{\frac{1}{\pi}\left(\frac{1}{\sin^2\phi} + \frac{1}{3-4D}\right)^{0.5}} \tag{2.103}$$

$$\sigma_0^{'} = (\sigma_1^{'} + \sigma_2^{'} + \sigma_3^{'})/3 \tag{2.104}$$

With the results of full-scale and model tests, Det Norske Veritas (1980) proposed a combined hyperbolic and linear model, as given by:

$$p = \frac{y}{\frac{1}{k_h} + \frac{y}{ap_d}} \tag{2.105}$$

$$a = 1/(1 - p_d / k_h y_d) \tag{2.106}$$

Wesselink et al. (1988) developed a *p-y* curve model from the full-scale in calcareous sand of the Bass Strait, as expressed by the following function:

$$p = R \cdot D \left(\frac{z}{z_0}\right)^n \left(\frac{y}{D}\right)^m \tag{2.107}$$

where R, n, m = curve fitting parameters.

2.5.13*p-y* Curves for Layered Soils

Davission and Gill (1963), Khadilkar et al. (1973), Naik and Peyrot (1976), Dordi (1977), and Lee and Karunaratne (1987) have evaluated the lateral behavior of piles embedded in layered soil based on the assumption that the soil is elastic. To consider the nonlinearity of soil, Georgiadis (1983) developed a method, which has been used in the LPILE program (Isenhower and Wang 2015), to construct *p-y* curves in a layered soil system. In this approach, the *p-y* curves of the top layer can be defined as those for homogeneous soils. The *p-y* curves of the lower layers are affected by the upper layers and the effects are taken into account by the equivalent depth for each of the underlying layers based on strength parameters.

The determination of equivalent depths is shown in Figure 2.40. The equivalent depth h_2 of first layer needs to be determined prior to computing the *p-y* curves of second layer. At first, the total force (F_1) acting on pile above point 1, which is at the interface of first layer and second layer, at the time of soil failure, can be computed by:

$$F_1 = \int_0^{H_1} p_{u1} dH \tag{2.108}$$

where p_{u1} = ultimate resistance of the *p-y* curves of the first layer and H_1 = the thickness of the first layer. Then, assume that the first layer of soil have the properties of the second layer. Therefore, the equivalent depth (h_2) of first layer can be calculated by the following equation:

$$F_1 = \int_0^{H_1} p_{u2} dH \tag{2.109}$$

where p_{u2} = the ultimate soil resistance of the *p-y* curves which is dependent on the equivalent depth, the actual overburden pressure and the strength properties of the second layer. Finally, the *p-y* curves of the second layer can be determined using the conventional *p-y* method with the assumption that the total depth of second layer is the sum of h_2 and H_2. The *p-y* curves for other soil layers can be computed with the similar concept.

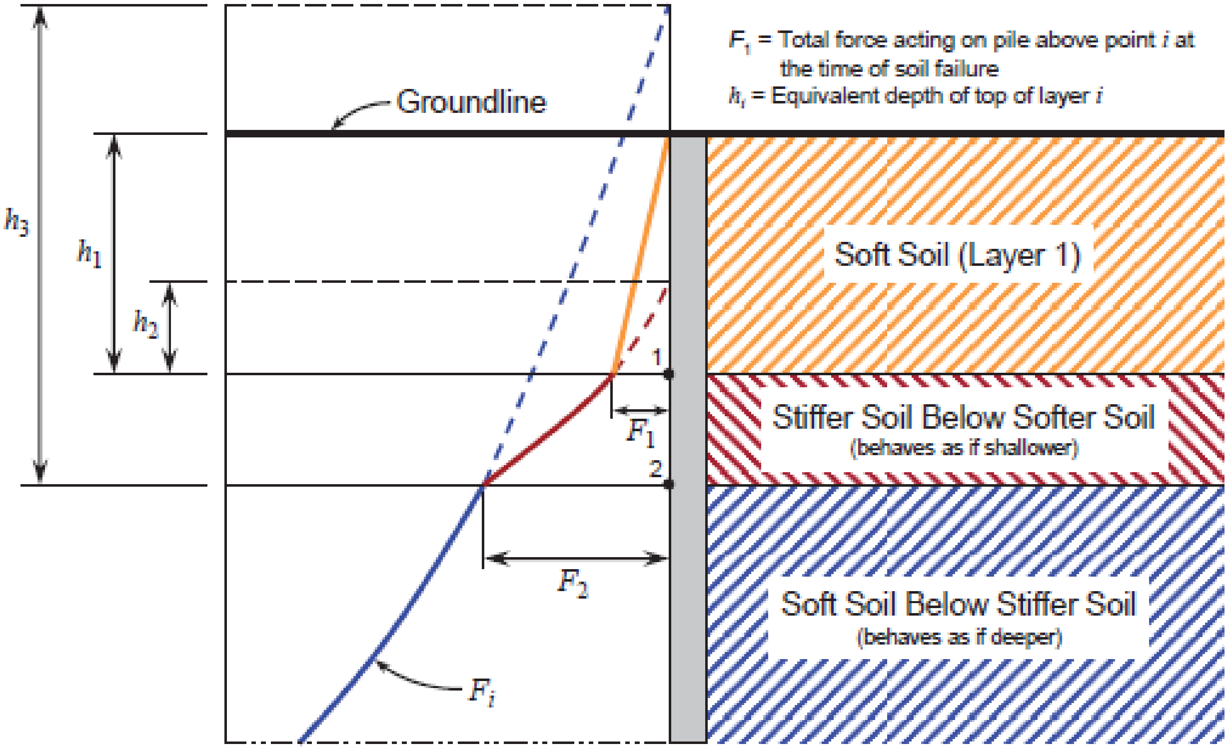

Figure 2.40 A typical method to determine the equivalent depths in a layered soil profile (after Isenhower and Wang 2015 originally from Georgiadis, 1983)

2.6 ESTIMATION OF *P-Y* CURVES USING IN-SITU TESTS

2.6.1 Pressuremeter (PMT) Expansion Test

Pressuremeter (PMT) expansion test, which was developed by Menard and Rousseau (1962) and modified by Baguelin et al. (1978) and Briaud and Shields (1979), can be used to predict movements of laterally loaded piles (Briaud et al. 1984) by measuring the pressure versus strain relationship. The pressuremeter, as shown in Figure 2.41, includes two parts: a read-out unit resting on the ground surface and a long cylindrical probe inserting into the borehole. The probe has three independent cells (two guard cells and one measuring cell) inflated as a pressurized fluid injecting into the pressuremeter. The borehole walls deform with the increasing of measuring cell pressure. The deformation of walls can be estimated using the increase of volume of measuring cell.

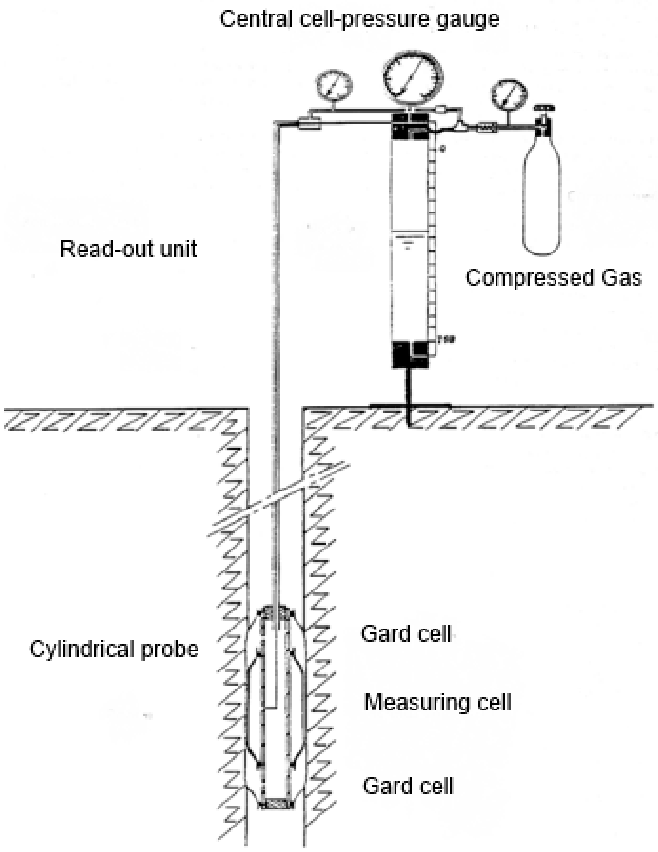

Figure 2.41 Schematic of a pressuremeter test in a borehole (after Gambin and Rousseau, 1988)

In this method, the PMT expansion curve can be derived. Briaud et al. (1982, 1983) proposed a method to correlate the PMT expansion curve to the pile *p*-*y* curve based on field testing, as shown in Figure 2.42. In this method, lateral soil reaction per unit length (*p*) and the pile lateral deflection (*y*) is given by:

$$p = p_{PMT} \times D \times S \qquad (2.110)$$

$$y = y_{PMT} \times \frac{R_{pile}}{R_{PMT}} \qquad (2.111)$$

where p_{PMT} = the net pressuremeter pressure, D = pile width or diameter S = a shape factor, which is 1.0 for square piles and 0.75 for round piles, y_{PMT} = increase in radius of the soil cavity in the pressuremeter test, R_{pile}= pile radius, and R_{PMT} = initial radius of the soil cavity in the pressuremeter test.

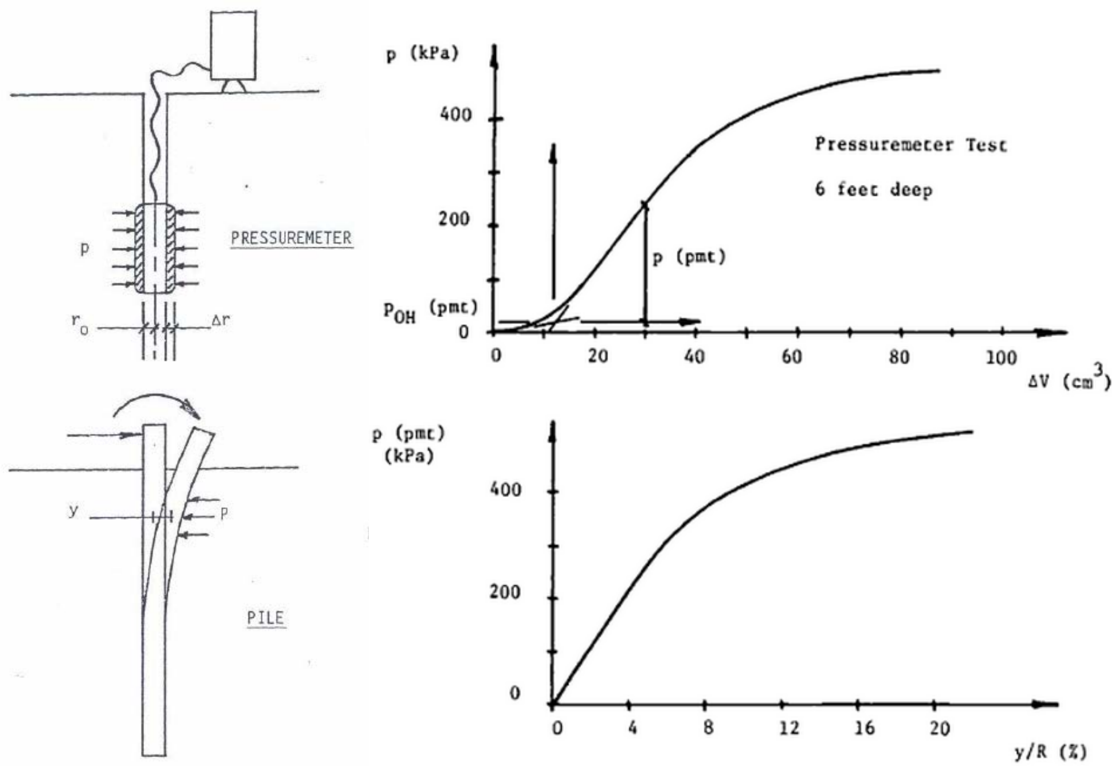

Figure 2.42 Pressuremeter pile analogy (after Briaud et al. 1983 and Briaud et al. 1984)

2.6.2 Dilatometer (DMT) Test

Dilatometer (DMT) test, which was originally developed by Marchetti et al. (1977), is another commonly used approach to estimate *p-y* curves (Gabr and Borden, 1988; Robertson et al., 1989). The DMT, as shown in Figure 2.43, consists in a stainless steel blade and a thin flat circular expandable membrane in one of its sides with electrical sensors to detect its position. The DMT blade is jacked into the ground and the membrane is inflated by means of pressurized gas at desired depths. One reading is recorded for the pressure required to just begin to move the membrane, and another reading is taken for the pressure required to move the membrane center 1.00 mm into the soil.

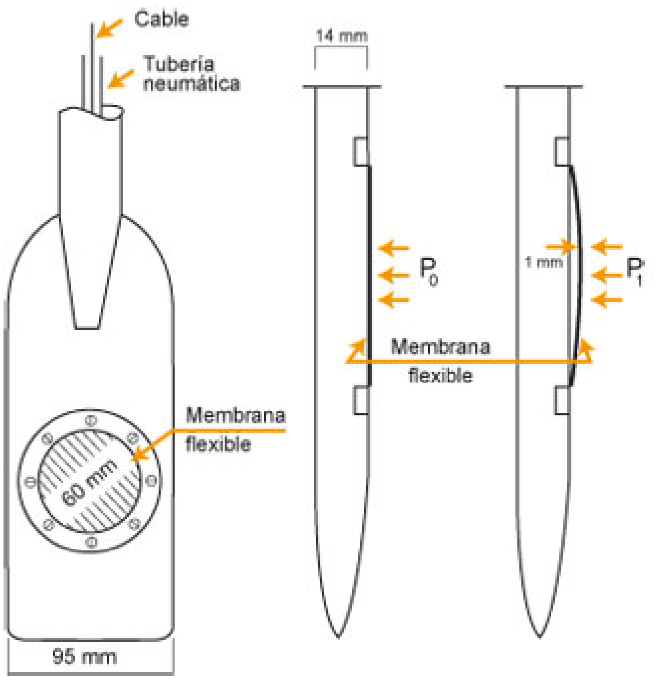

Figure 2.43 Flat plate dilatometer (after Robertson et al., 1989)

Gabr and Borden (1988) and Robertson et al. (1989) developed two methods to derive *p-y* curves from DMT data for static monotonic short-term one-way loading. Robertson et al. method adapted the methods proposed by Matlock (1970) for estimating *p-y* curves utilizing soil properties obtained from laboratory testing, as presented in section 2.5.5. Robertson et al. (1989) proposed the following equations to evaluate the ultimate soil resistance (p_u) and the soil displacement at one-half of ultimate soil resistance (y_{50}).

$$p_u = N_p \cdot C_u \cdot D \qquad (2.112)$$

$$y_{50} = \frac{23.67 \cdot C_u \cdot D^{0.5}}{F_C \cdot E_D} \qquad (2.113)$$

where C_u = undrained shear strength (from DMT) , σ'_{vo} = effective vertical stress at depth z, J = empirical coefficient (0.50 for soft clay), D = pile diameter, F_C = empirical factor (suggested to be 10), E_D = dilatometer modulus, and N_p = non-dimensional ultimate clay resistance coefficient (≤ 9), which is given by:

$$N_p = 3 + \frac{\sigma'_{vo}}{C_u} + J \cdot \frac{z}{D} \qquad (2.114)$$

Gabr and Borden method suggested that the *p-y* curves can be estimated by a hyperbolic tangent function as given by:

$$\frac{p}{p_u} = \tanh\left(\frac{E_{si} \cdot y}{p_u}\right) \tag{2.115}$$

with

$$E_{si} = 6.5 \cdot \left(\frac{p_0 - \sigma_{h0}}{b}\right) \cdot D \tag{2.116}$$

where E_{si} = initial tangent soil modulus, p_0 = first DMT reading, σ_{ho} = in situ total horizontal at-rest pressure, and b = half blade thickness = 7 mm.

2.7 EQUIVALENT CANTILEVER APPROACH

Greimann and Wolde-Tinsea (1988) and Abendroth et al. (1989) proposed the equivalent cantilever method for designing piles of integral bridges. This method can also be used to investigate the responses of laterally loaded piles. The equivalent cantilever method, as shown in Figure 2.44, assumes that the soil-pile system can be replaced by an equivalent cantilever that is fully restrained against lateral translation and rotation at the base (Caltrans 1986, Dowrick, 1987, Chai and Hutchinson 1999, Chai 2002). For elastic response of pile, the equivalent depth-to-fixity (L_f) is used to account for the flexibility of the embedded pile. The L_f depends on the relative stiffness between the pile and surrounding soil and may be calculated by equating the lateral stiffness of the soil-pile system to the lateral stiffness of an equivalent cantilever (Chai 2002). A design chart, as shown in Figure 2.45, has been developed to determine the depth of fixity for various soil types.

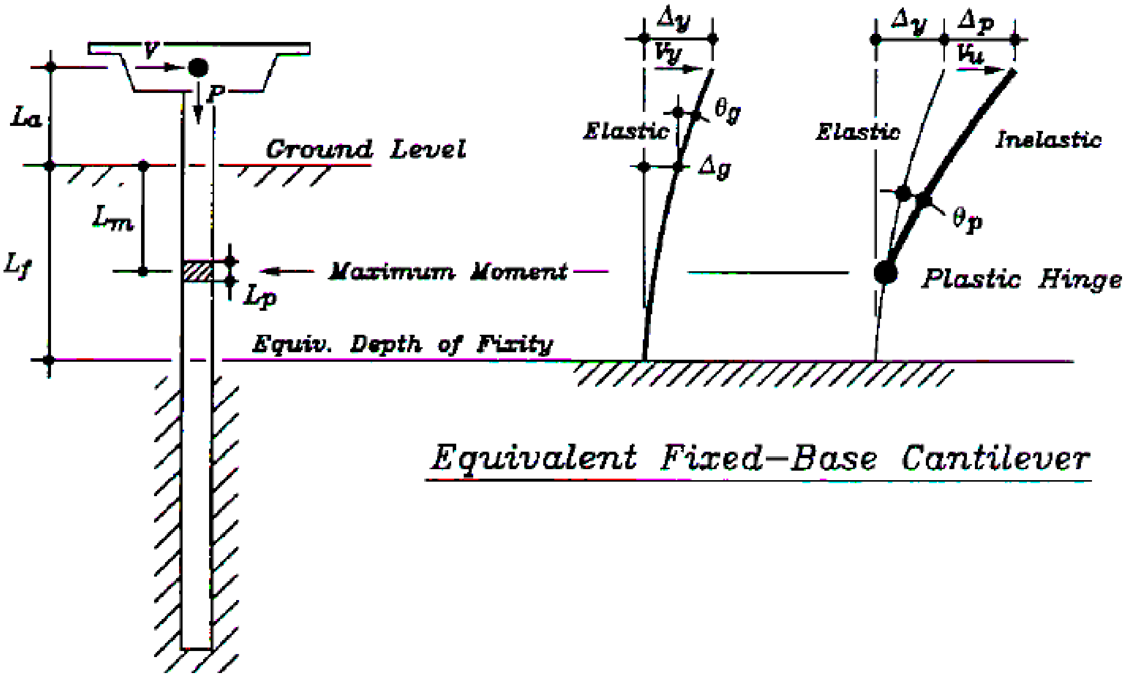

Figure 2.44 Concept of Equivalent Cantilever Beam Method (after Chai and Hutchinson 1999)

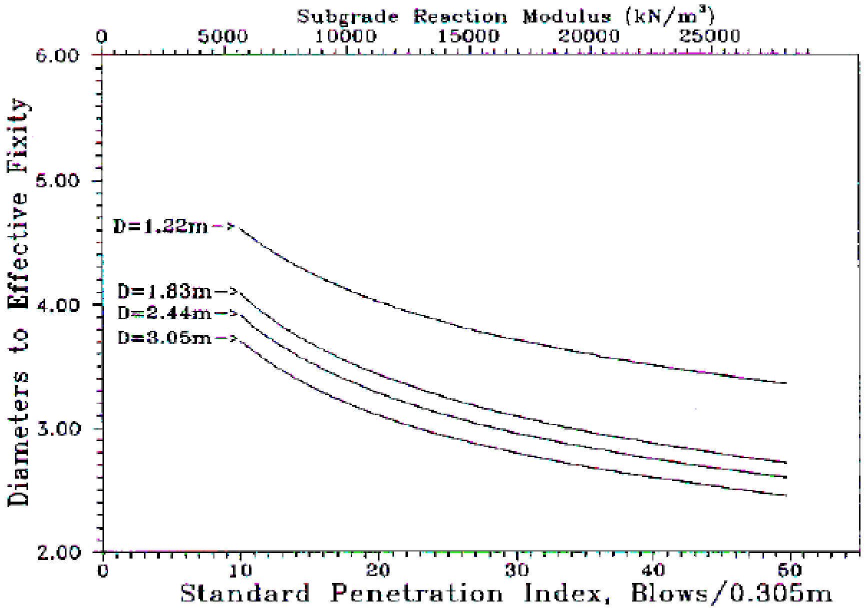

Figure 2.45 Design Chart for Determining Depth of Fixity (after Budek 1997)

2.7.1 Equivalent Depth-to-Fixity for Cohesive soils

In this method, the elastic Winkler foundation with a linearly increasing modulus of horizontal subgrade reaction is employed to model the lateral stiffness of the cohesive soil. The equivalent depth-to-fixity for cohesive soil can be estimated as presented below (Chai 2002). The characteristic length, R_c, is given by:

$$R_c = \sqrt[4]{\frac{EI_e}{k_h}} \tag{2.117}$$

where EI_e = effective flexural rigidity of the pile, k_h = constant modulus of horizontal subgrade reaction in unit of force/length^2. Davisson (1970) proposed an expression, which was adopted by Prakash and Sharma (1990), for calculating the modulus of horizontal subgrade reaction:

$$k_h = 67 s_u \tag{2.118}$$

where s_u= undrained shear strength of the cohesive soil.

For a pile with an embedded length greater than 3.5 times the characteristic length, the lateral displacement Δ_g and rotation θ_g of the pile at the ground level can be determined by (Poulos and Davis 1980):

$$\Delta_g = \frac{V(L_a + \sqrt{2}R_c)}{k_h R_c^2} \tag{2.119}$$

$$\theta_g = \frac{V(\sqrt{2}L_a + R_c)}{k_h R_c^3} \tag{2.120}$$

where L_a = above ground height, V = lateral force applied at the top of the cantilever The displacement of the pile head Δ is given by:

$$\Delta = \Delta_g + \theta_g L_a + \Delta_{L_a} \tag{2.121}$$

where L_a = above ground height, Δ_{L_a}= flexural deflection of the pile above the ground, which is given by:

$$\Delta_{L_a} = \frac{VL_a^3}{3EI_e} \tag{2.122}$$

The lateral stiffness of the soil-pile system can be written as

$$K_{sp} = \frac{V}{\Delta} = \frac{3k_h R_c}{3\sqrt{2} + 6\zeta_a + 3\sqrt{2}\zeta_a^2 + \zeta_a^3} \tag{2.123}$$

where $\xi_a = R_c/L_a$. The elastic lateral stiffness of a prismatic pile is given by:

$$K_c = \frac{V}{\Delta} = \frac{3EI_e}{(L_f + L_a)^3} \tag{2.124}$$

The coefficient for equivalent depth-to-fixity ξ_f (= R_c/L_f) can be obtained by equating the lateral stiffness of the soil-pile system and that of the equivalent cantilever, as expressed by

$$\zeta_f = \sqrt[3]{4.24 + 6\zeta_a + 4.24\zeta_a^2 + \zeta_a^3} - \zeta_a \tag{2.125}$$

In this case, the characteristic length is given by:

$$R_n = \sqrt[5]{\frac{EI_e}{n_h}} \tag{2.126}$$

where n_h = rate of increase of modulus of horizontal subgrade reaction in unit of force/length^3, which is the ratio of k_h and depth z and can be estimated from Figure 2.46. Poulos and Davis (1980) proposed the expressions for the estimation of the lateral displacement Δ_g and rotation θ_g of the pile at the ground level:

$$\Delta_g = \frac{V}{EI_e}\left[2.40R_n^3 + 1.60L_a R_n^2\right] \tag{2.127}$$

$$\theta_g = \frac{V}{EI_e}\left[1.60R_n^2 + 1.74L_aR_n\right] \tag{2.128}$$

Similar to the method used for cohesive soils, assume the coefficient for above ground height ξ_a and coefficient for equivalent depth-to-fixity ξf, can be written as

$$\zeta_a = \frac{R_n}{L_a} \tag{2.129}$$

$$\xi_f = \frac{R_n}{L_f} \tag{2.130}$$

The lateral stiffness of the soil-pile system can be given as

$$K_{sp} = \frac{V}{\Delta} = \frac{EI_e}{R_n^3}\frac{1}{2.4 + 3.2\xi_a + 1.74\xi_a^2 + \xi_a^3/3} \tag{2.131}$$

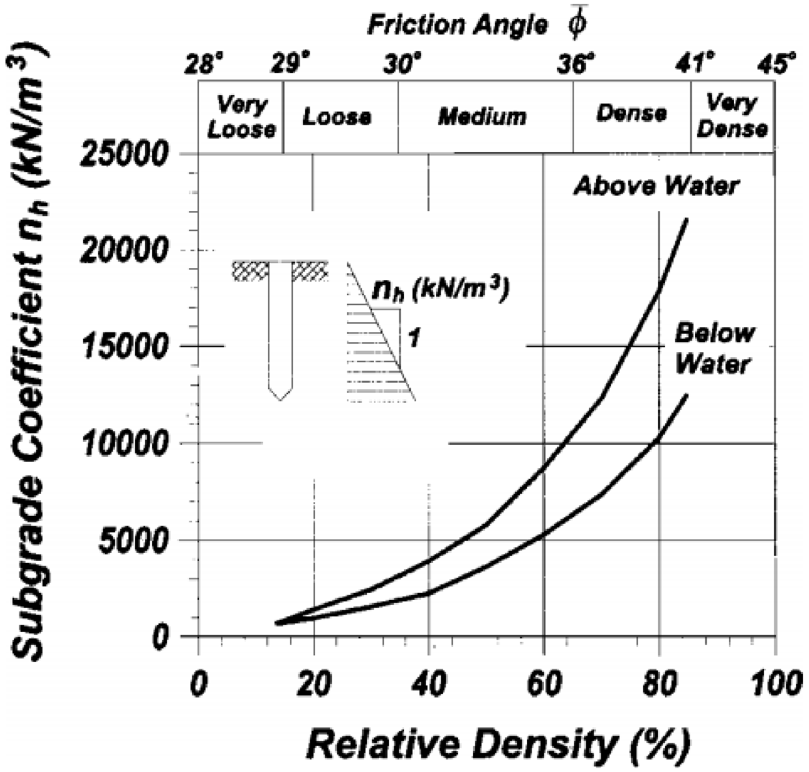

Figure 2.46 Subgrade coefficient and effective friction angle of cohesionless soils (after Chai 2002)

Then, the coefficient for equivalent depth-to-fixity can be estimated by equating the lateral stiffness of the soil-pile system to the lateral stiffness of the equivalent cantilever, as expressed by:

$$\xi_f = \sqrt[3]{7.2 + 9.6\xi_a + 5.22\xi_a^2 + \xi_a^3} - \xi_a \tag{2.132}$$

2.8 STRAIN WEDGE APPROACH

2.8.1 Introduction of Strain Wedge Model

The strain wedge (SW) approach was developed by Norris (1986) and Ashour et al. (1996, 1998) using a Mohr-Coulomb representation of soil strength. This approach is applicable to predict the behavior of flexible piles under lateral loading and offers a theoretical method to develop *p-y* curves with the consideration of soil properties and pile properties, such as pile shape, bending stiffness of pile, and pile head fixity conditions (fixed, free, or other) (Ashour et al. 2004).

The SW model is developed based on a passive wedge of soil in front of the pile, as shown in Figure 2.47. Ashour et al. (2004) summarized the correlation between the complex three-dimensional SW model and the simpler one-dimensional beam on elastic foundation (BEF) characterization in three aspects: 1) the pile deflection (*y*) in BEF model to the horizontal strain (ε) of soil in front of the pile; 2) the soil-pile reaction (*p*) associated with BEF characterization to the horizontal soil stress change ($\Delta\sigma_h$) in the developing passive wedge; and 3) the modulus of soil subgrade reaction ($K = p/y$) related with BEF model to the Young's modulus ($E = \Delta\sigma_h / \varepsilon$) of the soil. Then, the following fourth order differential equation can be solved with the appropriate selection of BEF parameters to evaluate the behavior of the pile under lateral loading.

$$E_p I_p \frac{d^4 y}{dz^4} + Ky = 0 \tag{2.133}$$

where E_pI_p = flexural rigidity of the pile, K = the modulus of subgrade reaction, and z = depth.

2.8.2 Soil Passive Wedge Configuration

As shown in Figure 2.47, a passive wedge develops in front of the pile when the pile is loaded laterally. The parameters used to characterize the mobilized passive wedge in front the pile are given in the following equations:

$$\theta_m = 45 - \frac{\varphi_m}{2} \tag{2.134}$$

$$\beta_m = 45 + \frac{\varphi_m}{2} \tag{2.135}$$

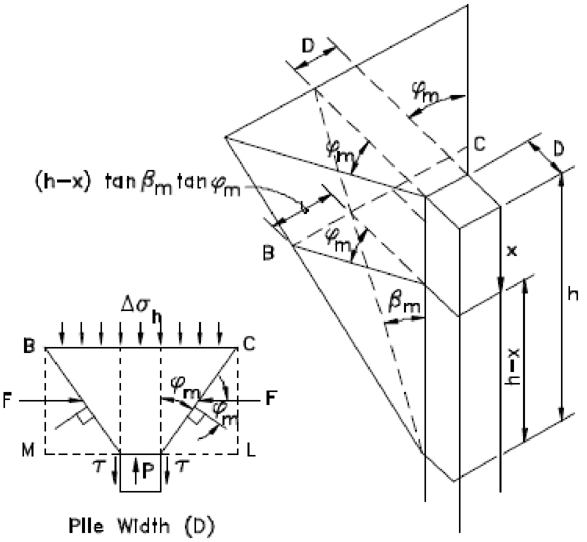

a. Basic Strain Wedge in Uniform Soil

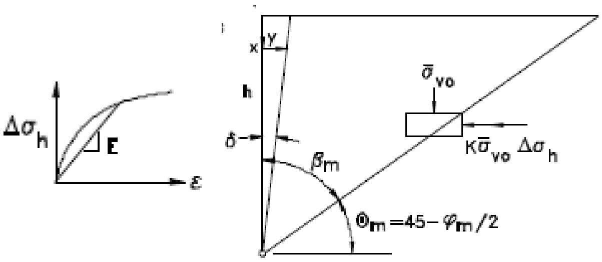

b. Deflection Pattern of a Laterally Loaded Pile and Associated Strain Wedge

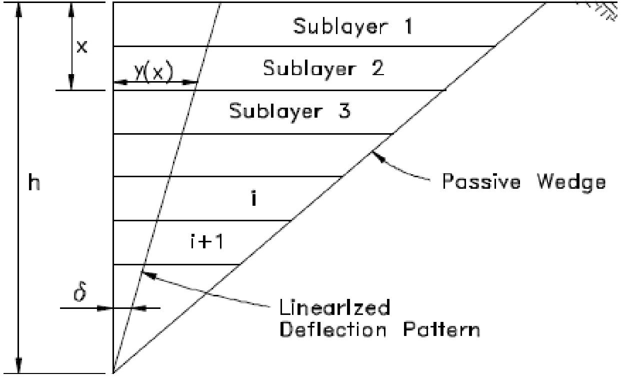

c. Strain Wedge Model Sublayers

Figure 2.47 Basic Configuration of SW Model (after Ashour and Norris 2000)

$$\overline{BC} = D + (h-x)2\tan\beta_m \tan\varphi_m \tag{2.136}$$

where θ_m and β_m = base angles, φ_m = the spread of the wedge fan angle, which is the mobilized friction angle, h = current passive wedge depth, D = width of the pile cross-section, $\overline{BC}$ = the width of the wedge face, and x = depth below the passive wedge surface. The total depth of the passive wedge (h) is related to the soils properties and the stress levels, (SL) the flexural rigidity of pile (EI), and pile head fixity conditions. It is noted that for layered soil conditions the wedge fan angle may be different for each soil sublayer. The lateral soil resistance of the passive wedge, as shown in Figure 2.47a, includes of the stress change at the front of the passive wedge ($\Delta\sigma_h$) and the shear on the side of the passive wedge (τ). The SW model assumes a linear deflection pattern of pile in the depth of passive wedge. This leads to a linearized deflection angle (δ) as seen in Figure 2.47b.

The problem with multiple different types of soil layers (Figure 2.47c and Figure 2.48) can be handled by dividing the soil profile and the pile into sublayers and segments of constant thickness (H), respectively. The soil properties of each sublayer are identical. The nonlinear elastic pressure applied on each segment of pile is assumed to be uniform. In addition, the deflection of the pile is assumed to be continuous.

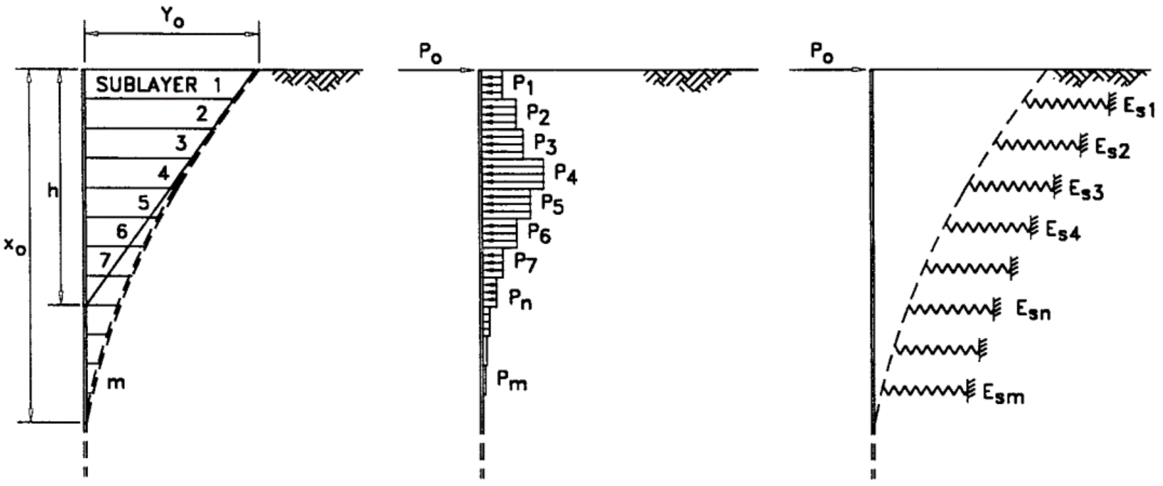

(a) PILE DEFLECTION PATTERN (b) SOIL REACTION DISTRIBUTION ALONG THE PILE (c) SOIL–PILE MODELING

Figure 2.48 Distribution of soil-pile reaction along deflected pile (after Ashour and Norris 2000)

2.8.3 Prediction of *p-y* Curve Using SW Model

The soil-pile reaction *p* from BEF analysis is given by

$$p_i = A_i \cdot D(\Delta\sigma_h)_i = A_i \cdot D \cdot E_i \cdot \varepsilon \qquad (2.137)$$

where *i* = the number of soil sublayer in the mobilized passive wedge counting from tip (i.e. lowest sublayer, *i* = 1); *E* = Young’s modulus of the soil; *A* = coefficient related to the dimensions of developing passive wedge and pile, soil properties, and applied load; ε = strain. It is defined by:

$$A_i = S_i\left(I + \frac{(h - x_i)2(\tan\beta_m \tan\varphi_m)_i}{D} \right) + \frac{2S_2\left(\overline{\sigma}_{vo}\right)_i\left(\tan\phi_s\right)_i}{(\Delta\sigma_h)_i} \quad \text{in sand} \qquad (2138)$$

$$A_i = S_i\left(I + \frac{(h - x_i)2(\tan\beta_m \tan\overline{\varphi}_m)_i}{D} \right) + \frac{S_2(SL_i)_i}{SL_i} \quad \text{in clay} \qquad (2.139)$$

where S_1 and S_2 = shape factors that are 0.75 and 0.5, respectively, for circular piles, and 1.0 for square piles (Briaud et al. 1984), *SL* = the stress level in the soil and can be estimated by:

$$\frac{\Delta\sigma_h}{\Delta\sigma_{hf}} = \frac{\tan^2(45+\varphi_m)-1}{\tan^2(45+\varphi)-1} \quad \text{in sand} \qquad (2140)$$

$$SL = \frac{\Delta\sigma_h}{\Delta\sigma_{hf}} = \frac{\Delta\sigma_h}{2S_u} \quad \text{in clay} \tag{2.141}$$

in which $\Delta\sigma_{hf}$ =horizontal stress change failure and S_u = undrained shear stress.

After soil- soil-pile reaction *p* is obtained, the lateral deflection *y* of the pile can be evaluated by

$$y = \sum y_i, i = 1, ..., n \tag{2.142}$$

$$y_i = p_i / (E_s)_i \tag{2.143}$$

where *n* = the current number of sublayers counted from the tip (*i* = 1) up to the point in question (*i* = *n*).

2.8.4 Prediction of Vertical Side Shear Resistance

Ashour et al. (2004) assumed that the vertical side shear stress distribution around the shaft follows a cosine function (Figure 2.49) and no contact exists on the backside of the shaft due to the lateral deformation. The total vertical side friction (V_v) along a unit length of the shaft is given by

$$V_v = 2\int_0^{\pi/2} qr\cos\theta d\theta = 2q(r\sin\theta)_0^{\pi/2} = Dq \tag{2.144}$$

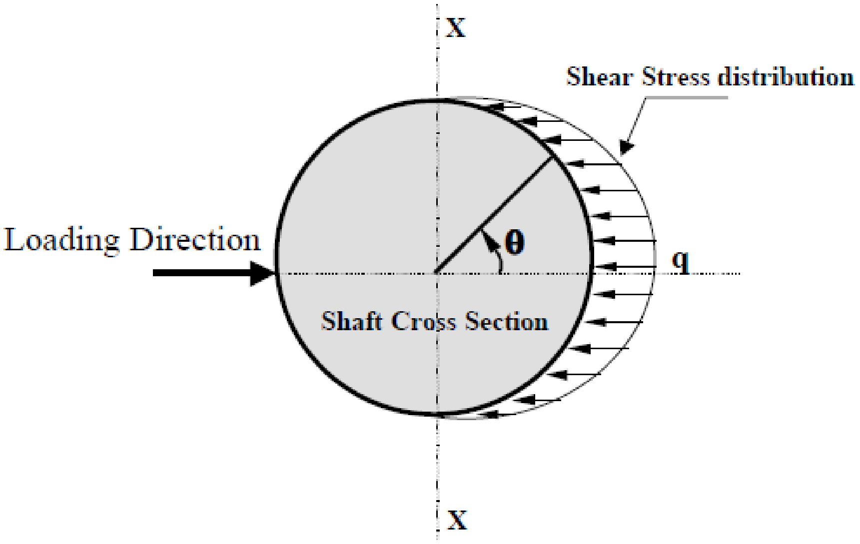

Figure 2.49 Vertical Side Shear Stress Distribution around the Shaft (after Ashour et al. 2004)

2.8.5 Prediction of Vertical Base Resistance

In the SW model, the shear resistance carried by the shaft base (V_b) is associated with the soil shear stress (τ_b) at shaft base, which can be determined by:

$$V_b = \tau_b A_b \tag{2.145}$$

$$\tau_b = SL\, s_u \quad \text{in clay} \tag{2.147}$$

$$\tau_b = 0.5\, SL\, \Delta\sigma_h \quad \text{in sand}$$

where A_b = the cross sectional area of the shaft base, s_u = the undrained shear strength.

2.9 BACK-CALCULATION OF *P-Y* CURVES FROM TESTING

With the observed experimental data, *p-y* curves can be back-calculated using simple beam theory. The lateral soil reaction (p) can be estimated by double differentiating the discrete bending moment (M) data with respect to depth (z) with the assumption that the flexural rigidity of the pile (EI) is constant, as given by:

$$p(z) = \frac{d^2}{dz^2} M(z) \tag{2.148}$$

where z = depth. Bending moment can be evaluated from curvature (ϕ) measurements according to the moment-curvature relationship.

The curvature (ϕ) can be computed with the measured axial strain ($\varepsilon(z)$) or slop ($s(z)$) at depth z using the following equations:

$$\phi(z) = \frac{\varepsilon_T(z) - \varepsilon_C(z)}{h} \tag{2.149}$$

$$\phi(z) = \frac{d}{dz} s(z) \tag{2.150}$$

where $\varepsilon_T(z)$ and $\varepsilon_C(z)$ = measured tensile and compressive strain at depth z, h = horizontal distance between the strain gauges. The moment-curvature relationship can be obtained using either computer program or filed data.

Before conducting the differentiation of the bending moment, interpolation techniques, including cubic splines, polynomial functions, and weight residual approach, can be employed to fit the discrete bending moment data (Wilson 1998 and Wallace et al. 2001).

2.9.1 Polynomial Interpolation Method

Polynomial interpolation method has been widely used by researchers (e.g., Matlock and Ripperger 1956, Reese and Welch 1975, Ting 1987, Dunnavant 1986, Brown et al. 1988, Dunnavant and O'Neill 1989, Wilson 1998) to fit bending moment data for deriving soil resistance. Matlock and Ripperger (1956) recommended low order piecewise polynomial using least-square technology. Dunnavant (1986) chose every five successive moment data points to construct a third-order polynomial function, as shown in Figure 2.50. The first and last polynomial functions, which are derived from the first five moment data and the last five moment data, respectively, are used to calculate the soil reaction for the upper three points and bottom three points, respectively. Other polynomials are used to compute the soil reaction at the center of two data points.

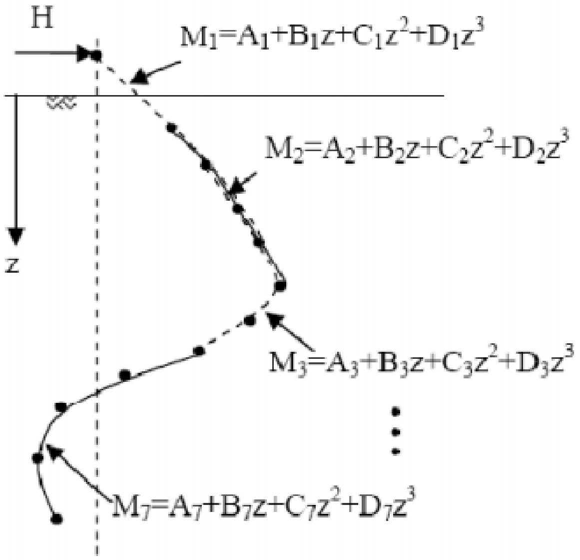

Figure 2.50 Procedure for curve fitting of moment data using piecewise polynomial (after Dunnavant 1986)

Reese and Welch (1975), Ting (1987) and Wilson (1998) used single high order polynomials to fit bending moment data. In order to fulfil the constraints of zero lateral resistance at the surface of the soil, Wilson (1998) considered two special polynomial functions. One is a six-order polynomial without quadratic term, as expressed as:

$$M(z)=a+bz+dz^3+ez^4+fz^5+gz^6 \tag{2.151}$$

The other is a five-order polynomial contains non-integer fitting terms, as expressed by:

$$M(z)=a+bz+cz^{2.5}+dz^3+ez^4+fz^5 \tag{2.152}$$

Wilson (1998) reported that the non-integer function provided more reasonable approximation. With the polynomial, the soil reaction can be estimated by directly double differentiating of the polynomial function. This single polynomial is easy to implement, although it is only applicable if the trend of the moment profile, especially near the ground surface, can be captured (Yang and Liang 2006).

2.9.2 Cubic Spline Method

Cubic spline interpolation functions are piecewise cubic polynomials for every interval of data points. Assuming there is a set of *n* pairs of data points, i.e., (z_1, M_1), (z_2, M_2), (z_n, M_n), the i^{th} piece of the spline, $S_i(z)$, is given by:

$$S_i(z) = a_i(z - z_i)^3 + b_i(z - z_i)^2 + c_i(z - z_i) + d_i\,. \qquad i = 1, 2, \ldots, n\text{-}1 \tag{2.153}$$

where z_i = the i^{th} depth , M_i = the i^{th} bending moment at depth z_i , a_i , b_i , c_i , d_i = unknown parameters. The cubic splines pass through each data point and have a continuous first and second derivative at the data points. These conditions can be expressed by:

$$S_i(z_i) = M_i \qquad i = 1, 2, \ldots, n\text{-}1 \tag{2.154}$$

$$S_i(z_{i+1}) = M_{i+1} \qquad i = 1, 2, \ldots, n\text{-}1 \tag{2.155}$$

$$S_i^{'}(z_{i+1}) = S_{i+1}^{'}(z_{i+1}) \qquad i = 1, 2, \ldots, n\text{-}2 \tag{2.156}$$

$$S_i^{''}(z_{i+1}) = S_{i+1}^{''}(z_{i+1}) \qquad i = 1, 2, \ldots, n\text{-}2 \tag{2.157}$$

Natural cubic spline boundary condition is given by:

$$S_0^{''}(z_0) = 0\,,\; S_{n-1}^{''}(z_n) = 0\,. \qquad i = 1, 2, \ldots, n\text{-}1 \tag{2.158}$$

The cubic spline method is smooth, easy to compute, and has good fit to both nonlinear and linear data set. (Halang et al. 1978). However, it is prone to high frequency noise due to the property that it passes through every data point (Wilson 1998).

2.9.3 Weighted Residual Method

Wilson (1998) utilized the concept of minimizing weighted residual in the finite element method to estimate shear force profiles by differentiating the moment profiles, and then derive soil reaction profiles by differentiating the obtained shear force profiles. In this method, a shaft is discretized into *n* elements by considering the locations of measured bending moment as nodes. The node number can be presented by *i*, which ranges from 0 to *n*.

If the continuous bending moment along the shaft is presented by $M(z)$, the shear force, $V(z)$, can be derived by:

$$V(z) = M^{'}(z) = \frac{dM(z)}{dz} \tag{2.159}$$

where z = depth $\in (0, L)$, L = length of shaft. However, when only discrete bending moment data, $M(z_i)$, which can be expressed by M_i for short, at depth z_i are known, a weak (or variational) relationship of $V_i = M_i^{'}$ can by established by minimizing the difference of $V(z)$ and $M^{'}(z)$, as written by:

$$\int_0^L [V(z) - M^{'}(z)] \cdot \psi(z) dz = 0 \tag{2.160}$$

in which $\psi(z)$ = an arbitrary weighting function.

As used in the finite element method (e.g., Cook et al. 1989), $V(z)$ and $M(z)$ can be expressed as linear combinations of finite-element-like basis functions, as expressed by:

$$V(z) = \sum_{i=0}^{n} V_i \cdot \psi_i(z) \tag{2.161}$$

$$M(z) = \sum_{i=0}^{n} M_i \cdot \psi_i(z) \tag{2.162}$$

where $\psi_i(z)$ = the i^{th} piecewise basis function. Linear Lagrange functions (Figure 2.51) were used by Wilson (1998) as basis functions. Then, it can be given that:

$$\int_{z_0}^{z_1} \left\{ \sum_0^n V_i \psi_i(z) - \frac{d\left[\sum_0^n M_i \psi_i(z)\right]}{dz} \right\} \psi(z) dz = 0 \tag{2.163}$$

Considering a typical element between nodes i and i+1, as shown in Figure 2.52, the basis functions for this element can be expressed as:

$$\psi_i(z) = \frac{z_{i+1} - z}{z_{i+1} - z_i} \tag{2.164}$$

$$\psi_{i+1}(z) = \frac{z - z_i}{z_{i+1} - z_i} \tag{2.165}$$

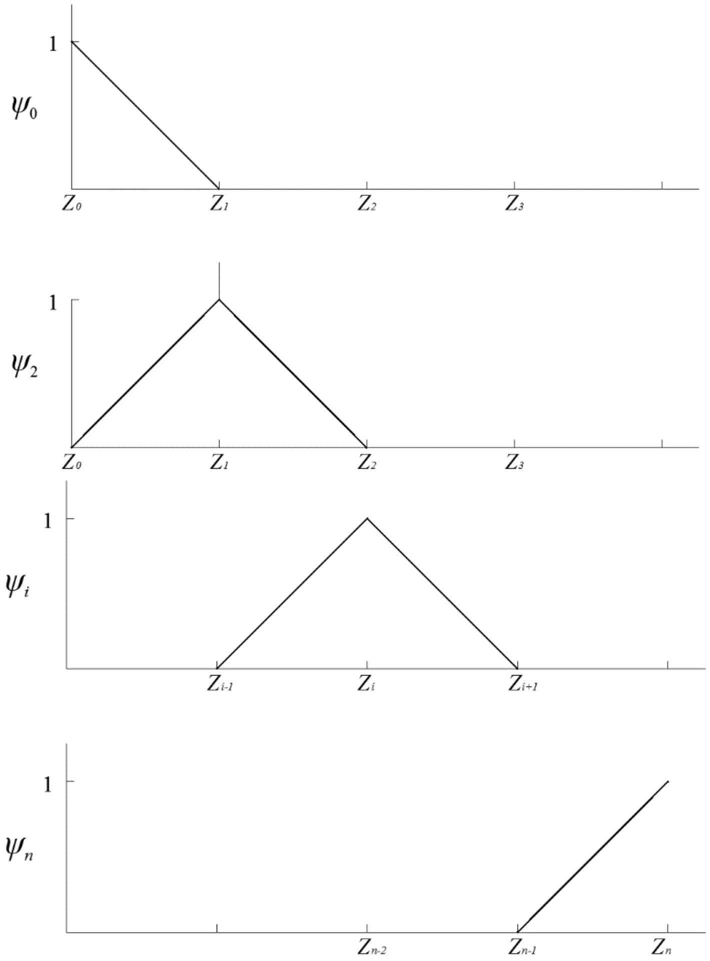

Figure 2.51 Linear Lagrange basis functions

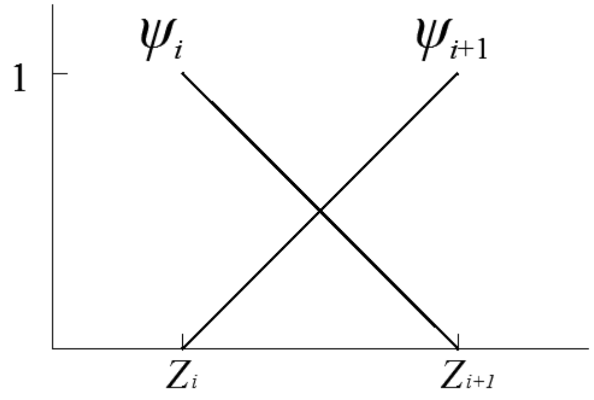

Figure 2.52 Basis functions for a typical element

The bending moment and shear force in this element can be written as:

$$M(z) = M_i \frac{z_{i+1} - z}{z_{i+1} - z_i} + M_{i+1} \frac{z - z_i}{z_{i+1} - z_i} \tag{2.166}$$

$$V(z) = V_i \frac{z_{i+1} - z}{z_{i+1} - z_i} + V_{i+1} \frac{z - z_i}{z_{i+1} - z_i} \tag{2.167}$$

The equation for the first element can be obtained and expressed as:

$$\int_{z_0}^{z_1} \frac{\{(M_1 - M_0) - [(z_1 - z)V_0 + (z - z_0)V_1]\}(z_1 - z)}{(z_1 - z_0)^2} dz = 0 \tag{2.168}$$

Similarly, the equation for the general element is given by:

$$\begin{aligned} &\int_{z_{i-1}}^{z_i} \frac{\{(M_i - M_{i-1}) - [(z_i - z)V_{i-1} + (z - z_{i-1})V_i]\}(z - z_{i-1})}{(z_i - z_{i-1})^2} dz + \\ &\int_{z_i}^{z_{i+1}} \frac{\{(M_{i+1} - M_i) - [(z_{i+1} - z)V_i + (z - z_i)V_{i+1}]\}(z_{i+1} - z)}{(z_{i+1} - z_i)^2} dz = 0 \end{aligned} \tag{2.169}$$

For the last element, the equation can be expressed by:

$$\int_{z_0}^{z_1} \frac{\{(M_n - M_{n-1}) - [(z_n - z)V_{n-1} + (z - z_{n-1})V_n]\}(z - z_{n-1})}{(z_n - z_{n-1})^2} dz = 0 \tag{2.170}$$

After integrating and simplifying the Equations:

$$V_0 \frac{z_1 - z_0}{3} + V_1 \frac{z_1 - z_0}{6} = \frac{M_1 - M_0}{2} . \tag{2.171}$$

$$V_{i-1} \frac{z_i - z_{i-1}}{6} + V_i \frac{z_{i+1} - z_{i-1}}{3} + V_{i+1} \frac{z_{i+1} - z_i}{6} = \frac{M_{i+1} - M_{i-1}}{2} . \tag{2.172}$$

$$V_{n-1} \frac{z_n - z_{n-1}}{6} + V_n \frac{z_n - z_{n-1}}{3} = \frac{M_n - M_{n-1}}{2} . \tag{2.173}$$

The equation group contains 3*n* equations, which can be expressed by matrices as follows:

$$\left\{\begin{matrix} M_1-M_0 \\ M_2-M_1 \\ M_3-M_2 \\ \vdots \\ M_{n-1}-M_{n-2} \\ M_n-M_{n-1} \end{matrix}\right\} = \frac{1}{3}\begin{bmatrix} 2(z_1-z_0) & (z_1-z_0) & 0 & 0 & \cdots \\ (z_1-z_0) & 2(z_2-z_0) & (z_2-z_1) & 0 & \cdots \\ 0 & (z_2-z_1) & 2(z_3-z_1) & (z_3-z_2) & \cdots \\ \vdots & \vdots & \vdots & \vdots & \ddots \\ \cdots & 0 & (z_{n-1}-z_{n-2}) & 2(z_n-z_{n-2}) & (z_n-z_{n-1}) \\ \cdots & 0 & 0 & (z_n-z_{n-1}) & 2(z_n-z_{n-1}) \end{bmatrix}\left\{\begin{matrix} V_0 \\ V_1 \\ V_2 \\ \vdots \\ V_{n-1} \\ V_n \end{matrix}\right\} \tag{2.174}$$

If the above matrix is expressed by $\boldsymbol{M} = \boldsymbol{ZV}$, the shear force at each node can be obtained by:

$$\boldsymbol{V} = \boldsymbol{Z}^{-1}\boldsymbol{M} \tag{2.175}$$

Then, similar procedure can be repeated to shear force V_i to estimate the derivative of shear force in term of depth, i.e., the soil reaction, as expressed by:

$$p(z) = V^{'}(z) = \frac{dV(z)}{dz} \tag{2.176}$$

Finally, the soil reaction at each node can be obtained from bending moment by:

$$\boldsymbol{p} = (\boldsymbol{Z}^{-1})^2\boldsymbol{M} \tag{2.177}$$

2.10 STUDIES OF DRILLED SHAFTS WITH STEEL CASING

Permanent steel casing can be left in place in caving ground conditions and also be utilized to provide additional stiffness (or rigidity) to the reinforced concrete drilled shaft. Steel casing provides significant flexural resistance and confinement to the concrete in-filled concrete, which leads to an increase of inelastic deformation capacity and better seismic performance (Roeder and Lehman 2012). This type of deep foundation is called as Cast-In-Steel-Shell (CISS) pile foundation or concrete filled steel tubes (CFT) and has been commonly used by the Departments of Transportation in Washington, California, and Alaska (Gebman et al. 2006; Roeder and Lehman 2012; Yang et al. 2012; and Yang et al. 2017).

2.10.1 Impact of Permanent Steel Casing on Axial Capacity of Drilled Shafts

Limited axial loading tests have been conducted to study the impact of casing on axial capacity of drilled shafts and subsequently reported in the literature. The two studies available are summarized here. Owens and Reese (1982) conducted full-scale tests to investigate the effect of permanent steel casing on the axial capacity of drilled shafts. Six drilled shafts were tested. Four of them, designated G-1, G-2, G-3, and G-4, were constructed at a site in Galveston, Texas. Two shafts, designated E-1 and E-2, were constructed at an undisclosed site in eastern Texas. The soil profiles at the Galveston site and the eastern Texas site are shown in Figure 2.53 and Figure 2.54, respectively. In this section, only the comparisons for the uncased shafts G-1 and E-2, the partially cased shaft G-3, and the fully cased shaft E-1 are presented. Shaft G-1, which was 1.21

m (48 inches) and 18.3 m (60 ft) in diameter and length, respectively, was an uncased shaft. A 1.22-m (48-inch) casing was driven into a depth of 15.8 m (52 ft); then, an auger of 1.17-m (46-inch) diameter was used to excavate the soil inside the casing and to advance the hole to the depth of 18.3 m (60 ft). The steel casing was pulled out during placement of concrete. Shaft G-3, which was 0.91 m (36 inches) and 18.3 m (60 ft) in diameter and length, respectively, was constructed with diameter permanent casing installed to a depth of 12.2 m (40 ft). Inside a 1.07-m (42-inch) surface casing extended to a depth of 3 m (10 ft), a 0.91-m (36-inch) hole was augured to a depth of 10.7 m (35 ft); then the casing was screed into a depth of 12.2 m (40 ft). The excavation was continued with 0.83-m (34-inch) auger to the depth of 18.3 m (60 ft). Axial loads were applied in equal increments of 150 kN (15 ton). Figure 2.55 compares the maximum load transfer in shaft resistance versus depth for shaft G-1 and G-3. The maximum load transfer in the region 0 to 12 m (40 ft) for G-3 is much smaller than that for G-1.

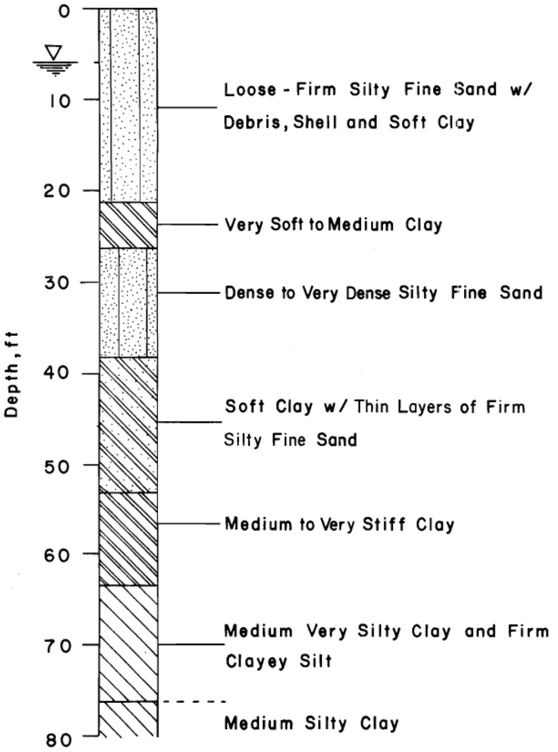

Figure 2.53 Soil profile at the Galveston site (after Owens and Reese 1982)

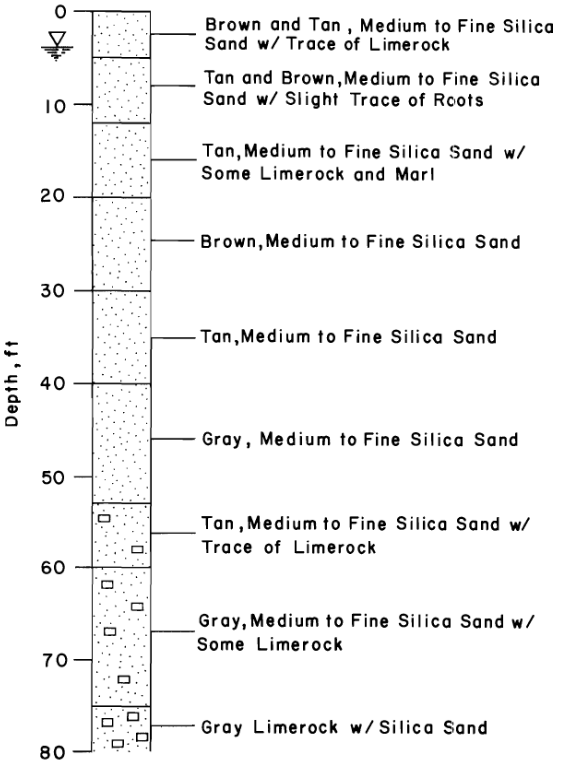

Figure 2.54 Soil profile at the Eastern site (after Owens and Reese 1982)

Comparison of the axial performance of shafts E-1 and shaft E-2 was also conducted; both of these shafts were constructed with a 0.91 m (36 inches) and 18.3 m (60 ft) diameter and length, respectively. Shaft E-1 was constructed with full-length casing. The casing was driven into ground and excavation was performed inside the casing. Shaft E-2 was installed without casing. In these tests, shaft E-1 carried a total load of 2,450 kN (246 tones) in shaft resistance; and 4,435 kN (445 tones) was carried by shaft E-2 in shaft resistance. A comparison of the ultimate load transfer in shaft resistance versus depth is shown in Figure 2.56. It reveals that the overall load transfer of the shaft E-2 is higher than that of the shaft E-1. Owens and Reese (1982) concluded that the capacity of the test shaft was significantly lower if the casing was left in place irrespective of whether the casing was driven or installed in an over-sized borehole. To mitigate the effects of the casing on the reduced shaft resistance, Owens and Reese (1982) recommended grouting of annular spaces that may develop in an over-drilled borehole. As shown in Figure 2.55, after grouting of the top 12 m of shaft G-3, the load transfer increased significantly in the grouted region. If the casing was installed using impact of vibratory driving, then grouting is not feasible. Drilled shafts with driven casing may require larger diameters, longer lengths, or installation in groups in the event the axial capacity is not sufficient for a given substructure element.

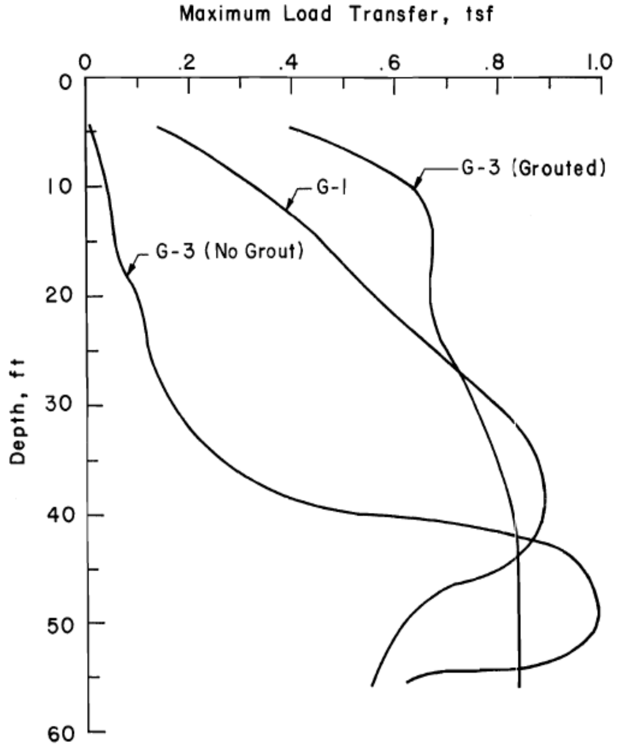

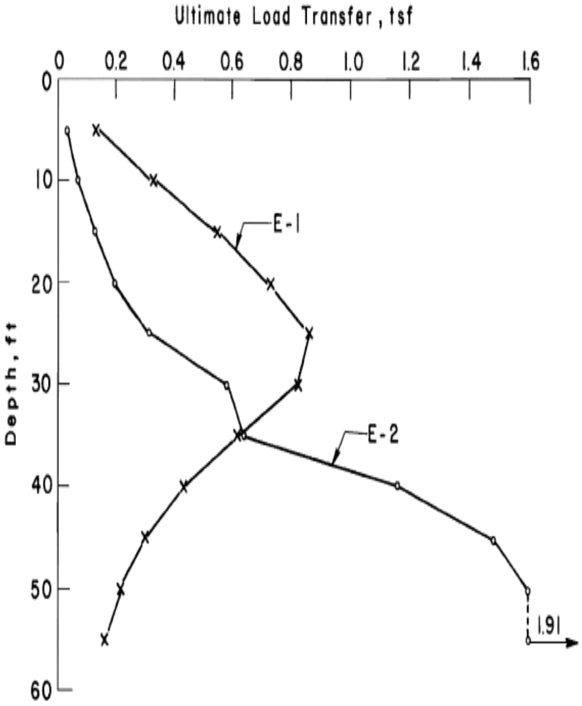

Figure 2.55 Load transfer versus depth (after Owens and Reese 1982)

Figure 2.56 Load transfer versus depth (after Owens and Reese 1982)

Camp et al. (2002) conducted axial loading tests on a total of 12 instrumented drilled shafts at three different test sites in Charleston, South Carolina. The test shafts were either 1.8 or 2.4 m (corresponding to 5.9 or 7.9 ft) in diameter with embedded length of either 30 or 46 m (corresponding to 98 or 151 ft). Eight of the drilled shafts were constructed with permanent casing, which was driven though loose sands and/or soft clays into Cooper Marl. The length of casing varied from 17.7 to 23.3 m (corresponding to 58 or 76 ft). Unit shaft resistances for both cased and uncased portion of the test shafts into the Cooper Marl were reported for three of the test shafts (designated MP1, MP3, and MP4) and summarized in Table 2.5. It was found that for the Cooper Marl, a stiff calcareous clay or silt (CH/MH), the unit shaft resistance developed for the cased portion was substantially lower than that for the uncased portion.

Table 2.5 Comparison of the unit shaft resistance at cased portion and uncased portion for the axial loading test conducted by Camp et al. (2002).

Shaft	Unit Shaft Resistance, kPa (psf)		Ratio of Unit Shaft Resistance at Cased Portion over uncased Portion
	Cased Portion	Uncased Portion	
MP1	32 (668)	163 (3,404)	20%
MP3	100 (2,089)	172 (3,592)	58%
MP4	47 (982)	192 (4,010)	24%

2.10.2 Impact of Permanent Steel Casing on Lateral Capacity of Drilled Shafts

A number of lateral loading tests and lateral load transfer studies have been performed on drilled shafts with and without permanent casing (e.g., Welch and Reese 1972; Bierschwale et al. 1981; Davidson et al. 1982; Mayne et al. 1992; Duncan et al. 1994;.Wallace et al. 2001; Hulsey et al. 2011). Brown and Camp (2002) describe some lateral loading test results of drilled shafts with and without casing, and showed that the uncased shaft exhibited greater flexural strains and at shallower depths than the cased shaft; however, no detailed load transfer analyses were presented. The lateral performance of drilled shafts with and without permanent casing in similar soil conditions needs to be further studied.

2.10.3 Design Methods for Concrete Filled Steel Tubes (CFTs)

Few guidelines on the design of concrete filled tubes (CFTs) are available, particularly regarding the calculations of the strength and stiffness of these members (Roeder and Lehman 2012). The American Institute of Steel Construction (AISC) LRFD (AISC 2005), the American Concrete Institute (ACI) 318 Specifications (ACI 2008), and the American Association of State Highway and Transportation Officials (AASHTO) LRFD Specifications and the Seismic Design Guidelines (AASHTO 2009, 2007) provide three approaches to estimate the strength and stiffness of CFT members. Roeder and Lehman (2012) compared these three codes in term of estimation of flexural resistance, stability limits, and effective stiffness; a review of their findings follows.

The AISC Specification (2005) allows using the plastic stress distribution (Figure 2.57a) or the strain compatibility methods (Figure 2.57b) to predict the flexural and axial resistance of circular CFT elements. The plastic distribution method assumes that: (1) each component of the section (i.e., the concrete and longitudinal steel), has reached the maximum plastic stress, and (2) no slip occurs between the steel and the concrete. As shown in Figure 2.57a, the uniform compressive stress of concrete is $0.95f'_c$ which is higher than the typical value of $0.85\ f'_c$ due to the confinement provided by steel casing to the concrete, and the tensile and compressive stresses of the steel are F_y. Then, the axial loading and flexural capacity can be estimated by equaling the stresses over the cross-section.

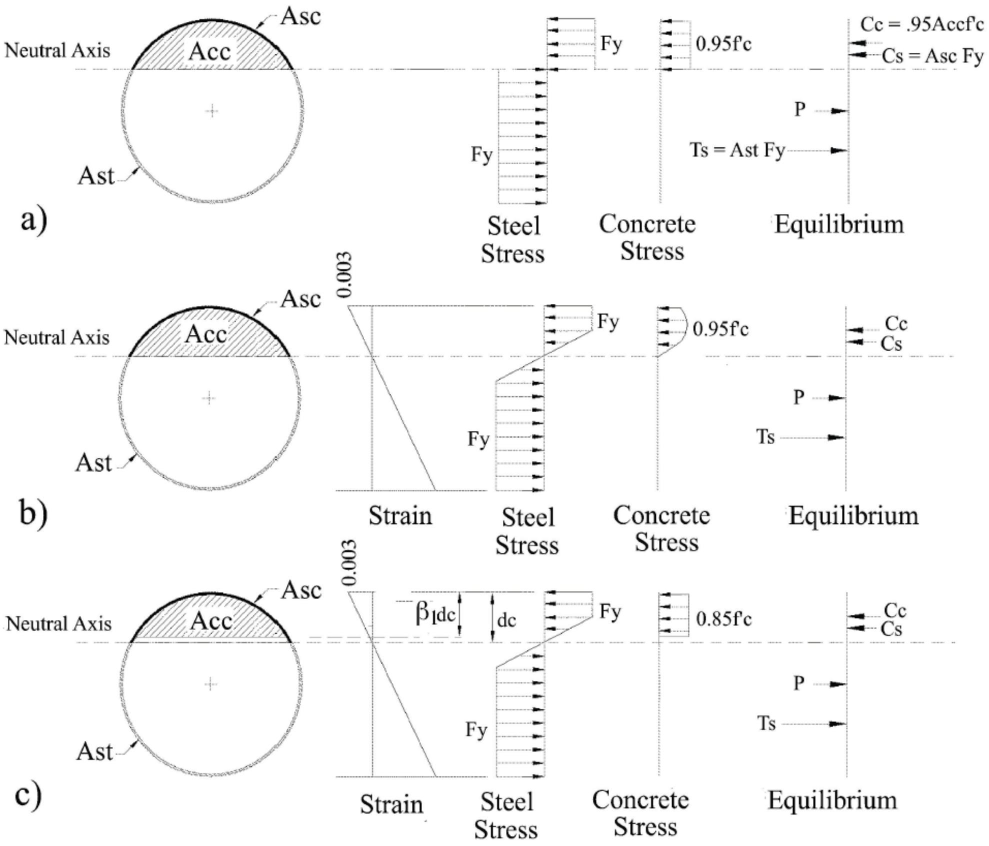

Figure 2.57 Approaches for estimating of resistance of CFT; a) AISC plastic stress distribution method, b) AISC strain compatibility method, and c) ACI method (after Roeder and Lehman 2012).

The strain compatibility method assumes that (1) no slip occurs between the concrete components and the steel components, and (2) the strain distribution is linear, as show in Figure 2.57b. The commonly used material model for the steel is elastic-perfectly plastic model and a parabolic curve for the concrete. The axial stress and flexural strength is for a maximum compressive strain in the concrete of 0.003.

The ACI (2008) method (Figure 2.57c) is similar to the AISC strain compatibility method. In this method, the compressive stress of concrete is assumed to be $0.95f'_c$ and acting along a depth $\beta_1 dc$, where dc is the depth from the neutral axis to the maximum compressive strain and β_1 is a function of concrete strength.

The AASHTO LRFD Specification (2009) assumes that the axial load capacity is determined by the concrete compressive stress of $0.85f'_c$ and the yield stress of steel. The AISC axial load-bending moment interaction curves, as shown in Figure 2.58, can be used for CFT. The AASHTO Guide Specification for LRFD Seismic Bridge Design provides a similar design method as the AISC plastic stress distribution method.

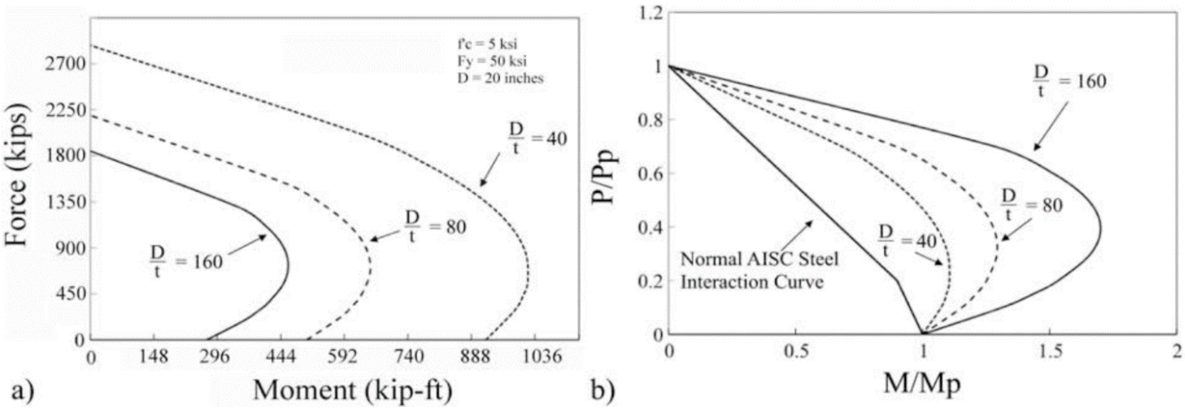

Figure 2.58 Axial load-bending moment interaction curves for CFT: (a) plastic stress distribution, (b) normalized (after Roeder and Lehman 2012).

The AISC, ACI, and AASHTO LRFD Specifications provide expressions to limit local buckling of the tube through use of Eqs. (2.178), (2.179), and (2.180), respectively.

$$\frac{D}{t} \le 0.15\frac{E}{F_y} \tag{2.178}$$

$$\frac{D}{t} \le \sqrt{8\frac{E}{F_y}} \tag{2.179}$$

$$\frac{D}{t} \le 2\sqrt{\frac{E}{F_y}} \tag{2.180}$$

where D = diameter of the tube, t = thickness of the tube, E = composite elastic modulus of the CFT, and F_y equals the yield strength of the steel. Additionally, the AISC and AASHTO provisions suggest that calculation of column buckling may be performed using:

$$P_{cr} = 0.658^{P_o/P_e} P_o \text{ for stocky columns, } P_e < 44P_o \tag{2.181}$$

$$P_{cr} = 0.877P_e \text{ for slender columns, } P_e > 44P_o \tag{2.182}$$

where P_e = the Euler buckling load, and P_o= ultimate axial crushing load, given by:

$$P_o = 0.95 f_c^{'} \cdot A_c + F_y \cdot A_s \tag{2.183}$$

where A_c and A_s = areas of concrete and steel, respectively. For circular CFT columns, the resistance factor is 0.75; and the axial load ratio P/P_o in interaction curves (i.e., Figure 2.58) is limited to 0.75 in provisions (Roeder and Lehman 2012).

2.10.3.1 Effective Stiffness

The AISC, ACI, and AASHTO LRFD Specifications describe different methods to estimate the effective member flexural rigidity (EI_{eff}) of CFT, given by Eqs.(2.184), (2.185), and (2.186), respectively:

$$EI_{eff} = E_s I_s + E_c I_c \left(0.6 + \frac{A_s}{A_s + A_c} \right) \tag{2.184}$$

$$EI_{eff} = E_s I_s + \frac{0.2 E_c I_g}{1 + \beta_d} \tag{2.185}$$

$$EI_{eff} = E_s I_s + 0.4 \frac{E_c A_c}{A_s} I_s \tag{2.186}$$

where E_s and E_c = the elastic modulus of the steel and concrete, respectively, I_s and I_c = the moment of inertia of the section for the steel and concrete, respectively, I_g = moment of inertia of the gross concrete section, and β_d = a parameter that is usually approximately 1.0.

2.11 RELATED STUDIES ON HIGH-STRENGTH REINFORCEMENT

Commonly used types of reinforcing steels for drilled shaft foundations are summarized in Table 2.6. The yield strength of the steel used in the reinforcement cages ranges from 280 MPa (40 ksi) to 420 MPa (60 ksi). In order to fulfil structure requirements, the number and section area of the steel reinforcement can be great, which leads to reduced rebar spacing and difficulty for concrete to flow through the reinforcement. This may cause voids in the shaft and can result in poor structural and geotechnical performance, depending on a given loading case (serviceability vs. strength limit) or location. In cases where a significant number of bars are required, high strength steel may be used to substitute the lower strength steel which can in turn reduce the number or size of the steel reinforcement bar and increase the rebar spacing.

Table 2.6 Reinforcing Steel Recommended for Drilled Shaft (Brown et al. 2010).

Designation	Description	Yield Strength, f_y, MPa (ksi)
AASHTO: M31 ASTM: A615	Deformed and plain billet-steel bars	280/420 (40/60)
AASHTO: M42 ASTM: A616	Deformed and plain rail-steel bars	350/420 (50/60)
ASTM: A706	Deformed low-alloy steel bars	420 (60)

For the design of reinforced concrete structures, the yield strength values of steel are limited to 550 MPa (80 ksi) and 515 MPa (75 ksi) by the ACI edition of ACI 318 (2008) and the AASHTO LRFD Bridge Design Specification (2007), respectively. The use of 690 MPa (100 ksi) steel yield strength is permitted only for the spiral transverse reinforcement in compression members (ACI 318 2008). These limits were developed in consideration of the limiting strain in the concrete and considerations for crack development and limitation of crack width under service loads; the limitation of the maximum stress in steel members to a strain of 0.3% is thought to facilitates the limitation of strain in the concrete (Shahrooz et al. 2011). Of note, both ACI 318 (2008) and AASHTO LRFD Bridge design Specification (2007) limit only the value of the yield strength that may be used in design; these codes do not exclude the used of higher strength grades of steel (Zeno 2009).

For a beam or column, using of high-strength rebar may increase the structural performance. Hassan et al. (2008) conducted tests with six large-size reinforced concrete beams with either conventional steel of Grade 60 (f_y = 420 MPa) or high-strength steel microcomposite multistructural formable (MMFX) steel (f_y = 827 MPa) and found that the beams with high-strength steel had higher shear strength (which increased as much as 80%) and less stress area (40% less). Trejo et al. (2014) and Barbosa et al. (2015) studied the seismic performance of 0.6-m (24-inch) diameter circular reinforced concrete bridge columns using ASTM A706 Grade 60 and Grade 80 reinforcement and found that comparing with Grade 60 columns, Grade 80 columns had equal or greater maximum drift ratio, and that both grades exhibited similar column drift (i.e., lateral displacement) and ductility. However, no axial or lateral loading test data have been found in the literature for drilled shafts constructed with high-strength internal reinforcement.

2.12 SUMMARY

This chapter reviewed the relevant studies on the use of steel casing and high-strength reinforcement in drilled shafts, including available axial loading tests and selected structural tests on concrete beams or columns using high-strength reinforcement and casings (i.e., steel tubes). The chapter concluded with a discussion of design methods for axially- and laterally-loaded drilled shafts.

Owing to the increased understanding of the regional seismic hazards in the Pacific Northwest, the amount of steel reinforcement used in drilled shaft construction has increased over the past several decades. This may lead to a reduced rebar spacing and increased difficulty for concrete to flow through the reinforcement, such that it may cause voids and defects within the shaft and result in poor structural and geotechnical performance. To mitigate this problem, high strength steel can be employed in design to reduce the amount of steel and increase the rebar spacing, or the contribution of steel casing to flexure can be considered avoiding the use of congested reinforcement cages. Concrete filled tubes (CFTs) have been widely used in some states due to the large inelastic deformation capacity and better seismic performance. However, little information is available on the effect of soil-structure interaction associated with CFTs and the effect of high-strength steel on the performance of drilled shafts. For example, no full-scale experiments have been conducted to study the difference in the lateral response between cased and uncased shafts in the same soil conditions, and no studies have been found in the literature that evaluate the effect of high-strength reinforcement on the geotechnical performance of drilled shafts. Therefore, full-scale loading tests on the drilled shafts with permanent casing and high-strength reinforcement would help to address the gap.

For both axially- and laterally- loaded shafts, the load transfer approach for estimating the deflection associated with a given load are well established. However, few lateral load transfer models have been developed specifically for drilled shaft foundations with concrete interfaces. Additionally, the commonly used load transfer models for laterally-loaded deep foundations were developed from loading tests of small diameter piles Therefore, accurate load transfer models for cased and uncased drilled foundations should be developed from axial and lateral loading tests with relatively larger diameter, drilled, cast-in-place deep foundations.

3.0 SURVEY OF DEPARTMENTS OF TRANSPORTATION

One of the objectives of this study was to assess the state-of-the-practice for certain drilled shaft design and construction procedures among state department of transportation (DOT) and provincial Ministry of Transportations (MTOs) agencies. To accomplish this objective, a questionnaire was prepared for and submitted to state DOTs and provincial MTOs to help determine the benchmarks and practices for the use of permanent steel casing and high-strength steel reinforcement. Twenty-three surveys, including 22 from US and one from Alberta, CA, were returned and analyzed. Table 3.1 summarizes the survey participant groups. The questions in the survey and the corresponding responses are shown in Appendix A.

Table 3.1 Summary of Survey Participant Groups

STATE	GROUP	NAME	TITLE
Alaska	Statewide Materials	David Hemstreet	State Foundation Engineer
Alberta, CA	Alberta Transportation	Roger Skirrow	Director, Geotechnical Section
Arizona	Bridge Group	Amin Aman	Bridge Tech- Section Leader
California	Substructure Committee	Amir Malek	Senior Bridge Engineer
Connecticut	Soils and Foundations	Michael McDonnell	Trans Supervising Engineer
Idaho	-	Tri Buu	Geotechnical Engineer
Illinois	Bridge office Foundations unit	Bill Kramer	Foundations unit chief
Iowa	-	Ahmad Abu-Hawash	Chief Structural Engineer
Kentucky	Geotechnical Branch	Darrin Beckett	Transportation Engineer Specialist
Louisiana	Pavement & Geotechnical Services	Chris Nickel	Geotechnical Engineer Manager
Michigan	--	Richard Endres	Supervising Engineer Geotechnical Services
Missouri	Bridge Division	David Hagemeyer	Senior Structural Designer
Montana	Geotechnical Section	Jeff Jackson	Geotechnical Engineer
Nebraska	Department of Roads	Nikolas Glennie	Bridge Foundation Engineer
Nevada	Geotechnical	Mike Griswold	Chief Geotechnical Engineer
New Hampshire	Geotechnical Section NHDOT	Thomas Cleany	Geotechnical Engineer
North Carolina	Geotechnical Engineering Unit	Scott Hidden Greg Bodenheimer	Support Services Supervisor
North Dakota	Materials and Research	Jeff Jirava	Geotechnical Engineer
Oklahoma	-	Steve Jacobi	Engineering Manager
Vermont	Geotechnical Engineering Group	Chris Benda	Geotechnical Engineering Manager
Washington		Bijan Khaleghi	Bridge Design Engineer
Wisconsin	Department of Transportation	Bob Arndorfer	Geotechnical Engineering Supervisor
Wyoming	WYDOT	Keith Fulton	State Bridge Engineer

4.0 SUBSURFACE CONDITIONS AT THE GEFRS TEST SITE

4.1 OVERVIEW

The Geotechnical Engineering Field Research Site (GEFRS) at Oregon State University (OSU), the site where the experimental shafts were constructed and tested in this study, is located near the western edge of the main portion of the OSU campus, adjacent to the Hinsdale Wave Research Lab (Figure 4.1). This test site has been used for over twenty years to conduct geotechnical experiments at full-scale. The geotechnical explorations, stratigraphy, and corresponding subsurface conditions for the site, and specifically the location of the test shafts, are presented in this chapter.

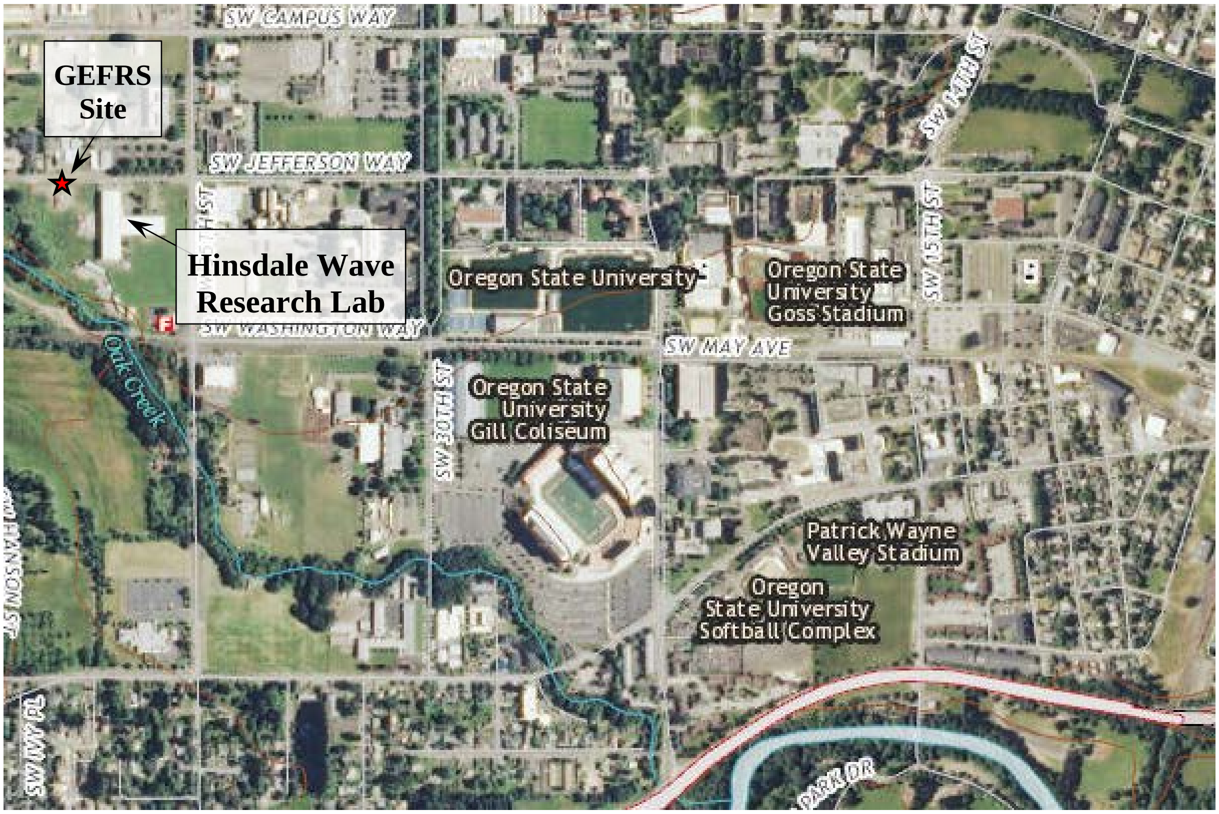

Figure 4.1: Project site (adapted from USGS National Map Viewer, 2015)

4.2 SITE SPECIFIC GEOTECHNICAL EXPLORATION

Several geotechnical explorations have been conducted at the GEFRS with soil information summarized in Dickenson and Haines (2006), Nimityongskul (2010), Li et al. (2017), and Martin (2018). Based on samples retrieved from borings distributed across the GEFRS, Dickenson and Haines (2006) summarized the general the range in water contents and Atterberg limits with depth as shown in Figure 4.2. Figure 4.3 shows the corrected standard penetration test (SPT) blow counts versus depth. Dickenson and Haines (2006) generally describe the stratigraphic sequence of GEFRS to consists of, beginning from the ground surface, the upper Willamette Silt, underlain by an intermittent lens of silty gravelly sand, followed by the lower Willamette Silt, underlain by a thicker lens of silty gravelly fine sand, and then a thick deposit of blue-gray clay (which actually consists of clayey silt). Based on the SPT results, the upper and lower Willamette Silt layer ranges from medium stiff to very stiff; in the experience of the authors, the consistency of the upper Willamette Silt layer depends upon the season and depth to groundwater. Figure 4.4 presents the Atterberg limits in the form of the plasticity chart for soil samples retrieved at the GEFRS, including those from Dickenson and Haines (2006) and from this project (as discussed subsequently). A wide range of liquid limits and plasticity indices was observed for Willamette Silt (both upper and lower Willamette Silt) from low plasticity silt (ML) to highly plastic clay (CH) across the entire GEFRS. The blue-grey clay can be classified as high plasticity clayey silt (MH).

Based on consolidation tests on soil samples retrieved from GEFRS, Dickenson and Haines (2006) constructed estimated profiles of the current (σ'_{v0}) and maximum past effective or preconsolidation stress (σ'_p), as shown in Figure 4.5, which indicates that the Willamette Silt and blue-gray clay are moderately to highly overconsolidated with typical overconsolidation ratios (OCRs) from four to seven and with some values as high as fourteen.

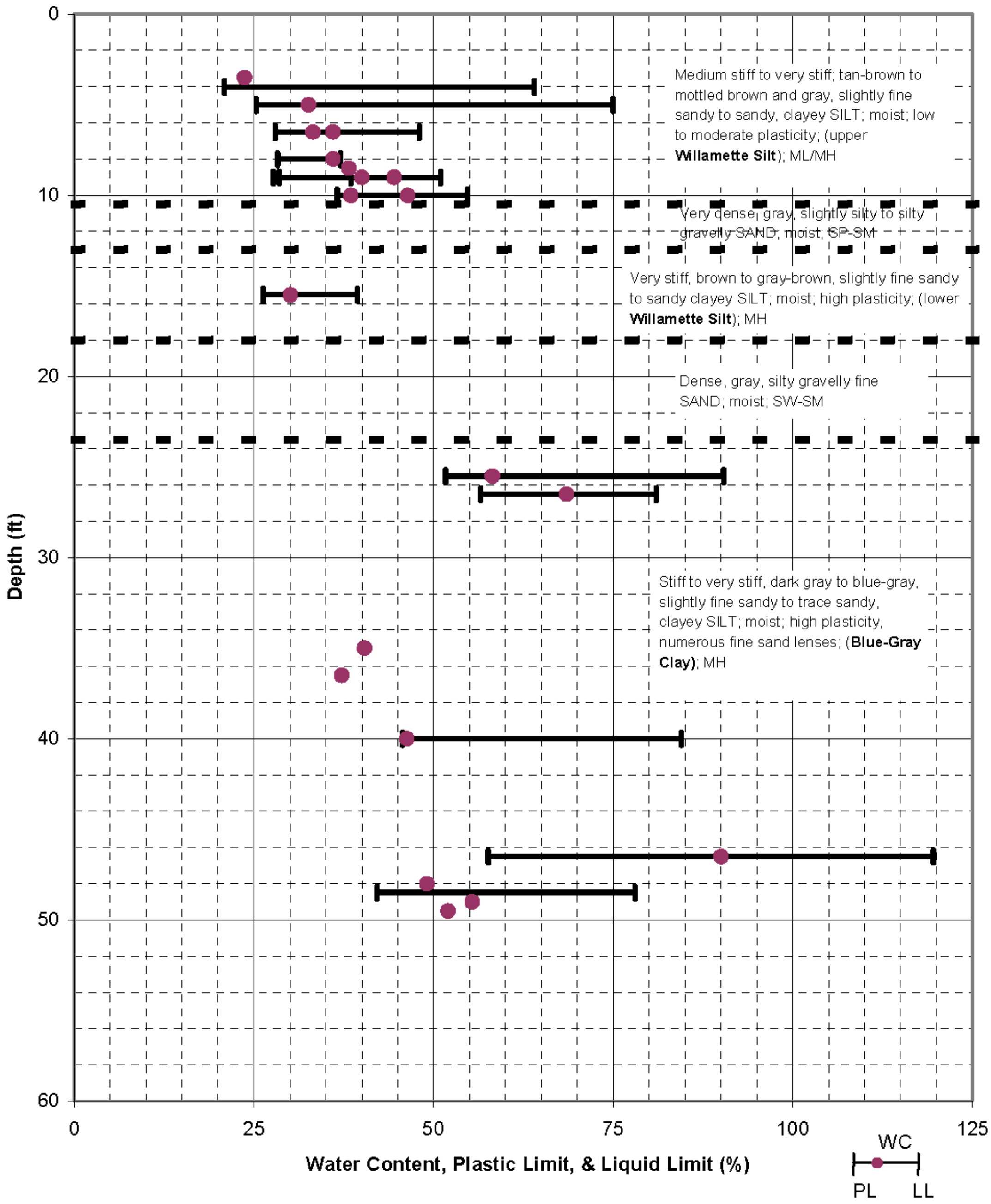

Figure 4.2: Water content and Atterberg limits at GEFRS (Dickenson and Haines 2006)

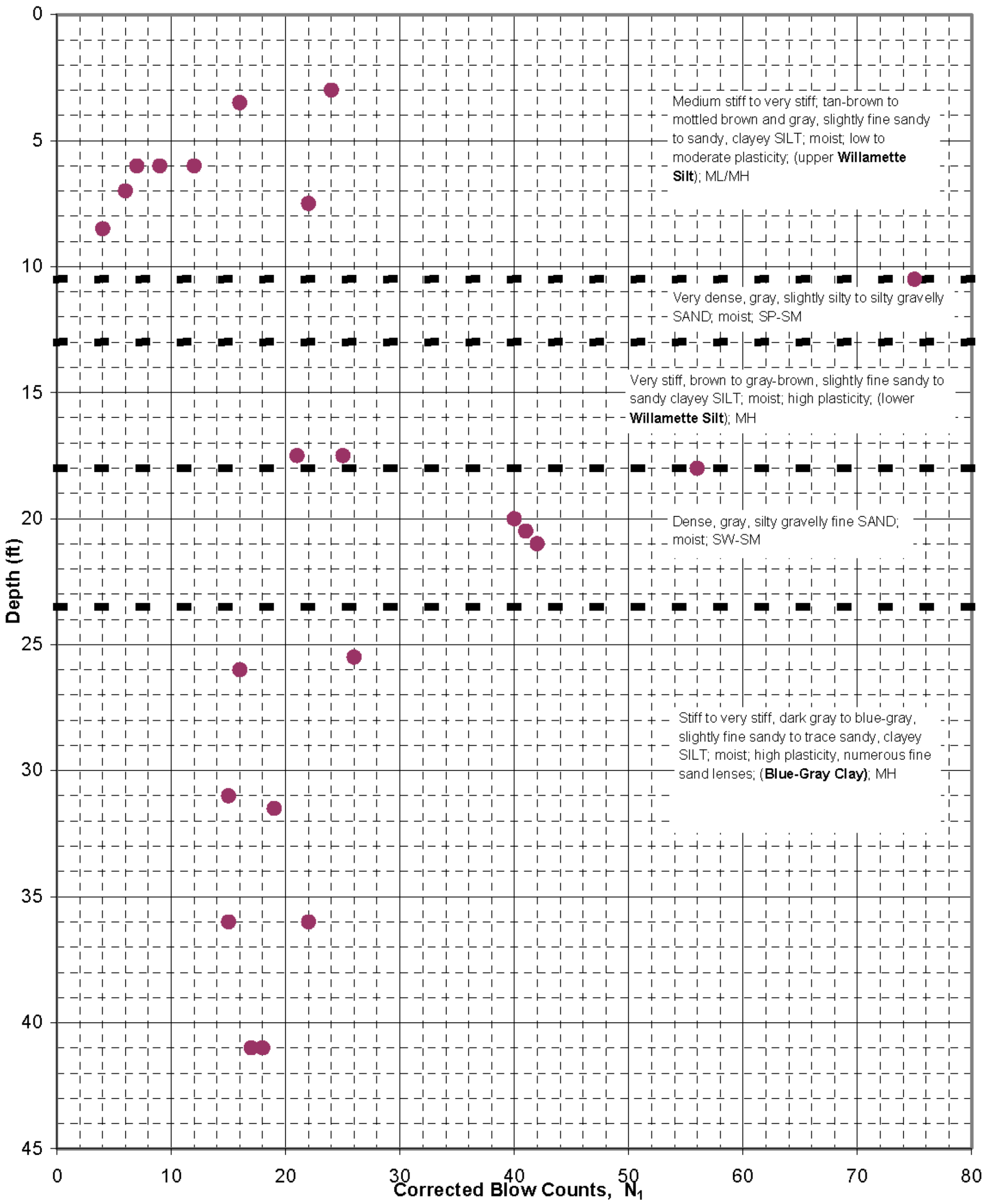

Figure 4.3: Corrected SPT blow count versus Depth at GEFRS (Dickenson and Haines 2006)

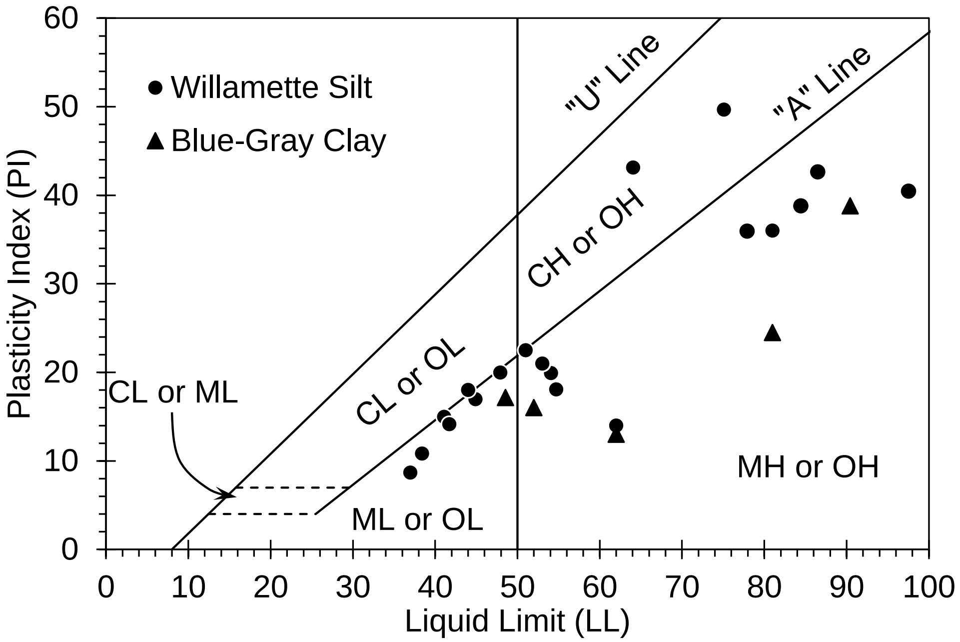

Figure 4.4: Soils classification using plasticity chart at GEFRS based on Dickenson and Haines (2006), Nimityongskul (2010), and soil samples obtained from this project.

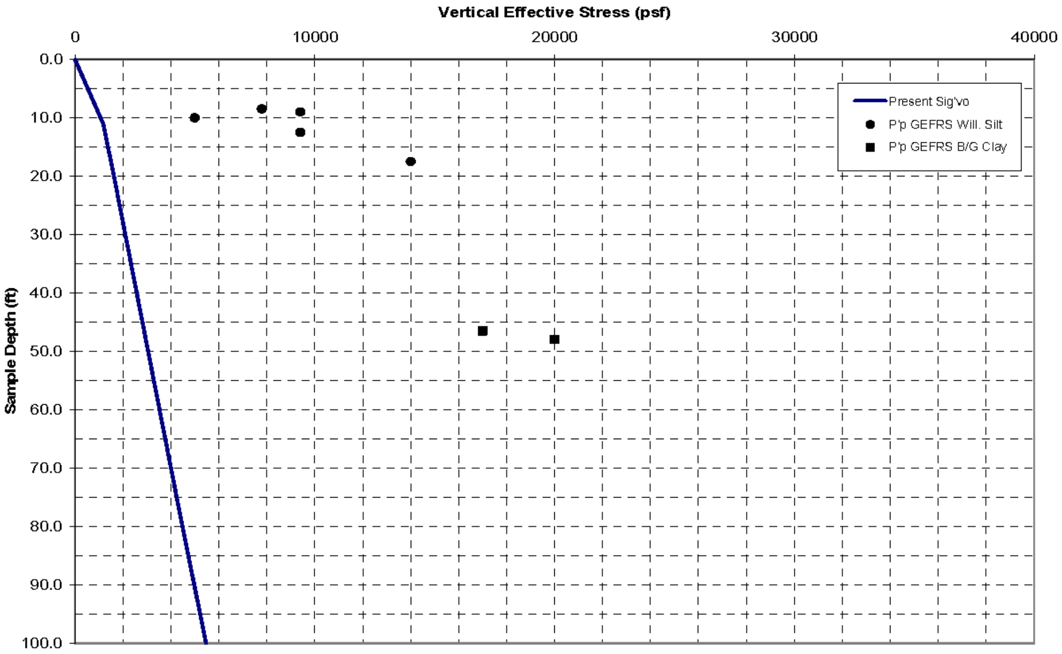

Figure 4.5: Current and maximum effective stress versus depth at GEFRS (Dickenson and Haines 2006). Note: *Sig'vo* = σ'_{v0} = current effective overburden stress, *P'$_p$* = σ'_p maximum past effective stress

To obtain more geotechnical information of the specific testing area considered in this study, site-specific explorations, including the cone penetration test (CPT) and six seismic CPTs (SCPTs), were made, as shown in Figure 4.6. Nearby borings conducted to support tests of drilled shafts in torsion were also considered. The specific testing footprint is approximately 20 m (66 ft) south of the area where the full-scale torsional response of drilled shafts was evaluated, as reported by Li et al. (2017). Appendix A presents all of the CPT and SCPT results. The shear wave velocity profile for SCPT-1, -2 and -3 was estimated using the corrected vertical travel time versus depth analysis method (Redpath 2007), as shown in Figure 4.7. The shear wave velocity was used to estimate the maximum shear modulus, G_{max} for the cased and uncased shafts.

The testing area-specific soil profile, shown in Figure 4.8, was developed using the results of the CPTs, recent and historical nearby borings, and Atterberg limit tests on split-spoon and grab samples collected during drilling. The native soil profile consists of stiff to very stiff, plastic Willamette Silt to a depth of approximately 5.2 m (17 ft), with an intermittent, thin sand lens at a depth of approximately 3 m (10 ft). A layer of dense silty sand with gravel and intermittent seams of sandy silt follows, with an approximate thickness of 6.5 m (21.3 ft) separates the Willamette Silt deposits from a thick and deep deposit of plastic, stiff to very stiff sandy clayey silt with intermittent seams of silty sand that grades finer to silty clay to clayey silt (referred to as blue-grey clay by Dickenson and Haines 2006). The piezometric surface varies between a depth of 0.6 and 2.5 m (2 to 8 ft) below the ground surface throughout the year, and was located at a depth between 1.6 and 1.8 m (5 and 6 ft) during the axial loading tests of the test shafts. Some groundwater flows through the thin sand lens at depth of about 3 m, but is generally concentrated in the silty sand and sandy silt layer at about 5 m depth below ground surface.

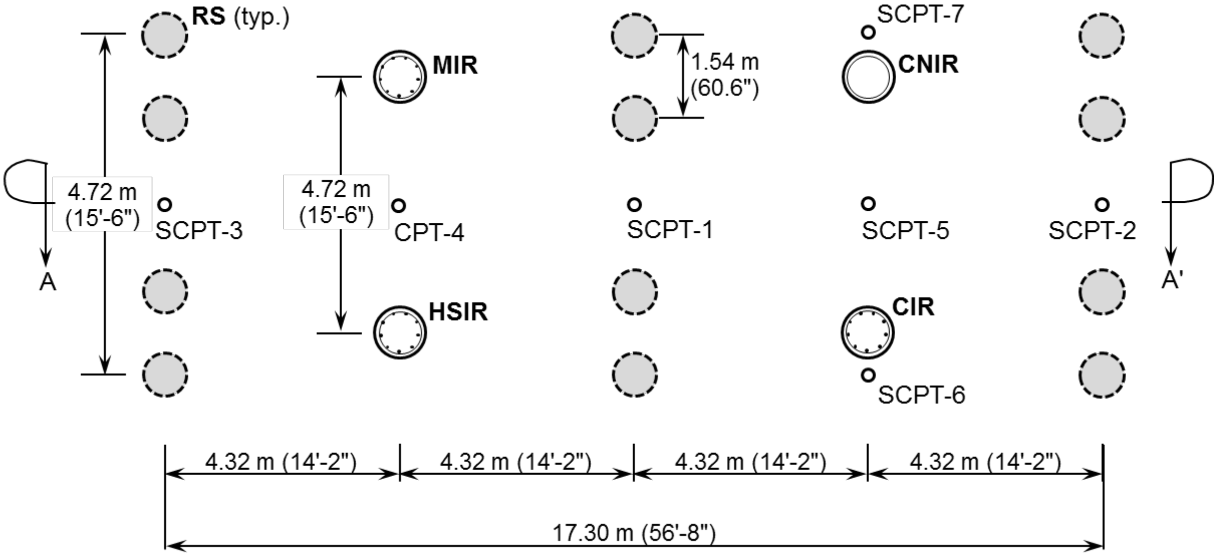

Figure 4.6: Test site layout, including (a) site and exploration plan.

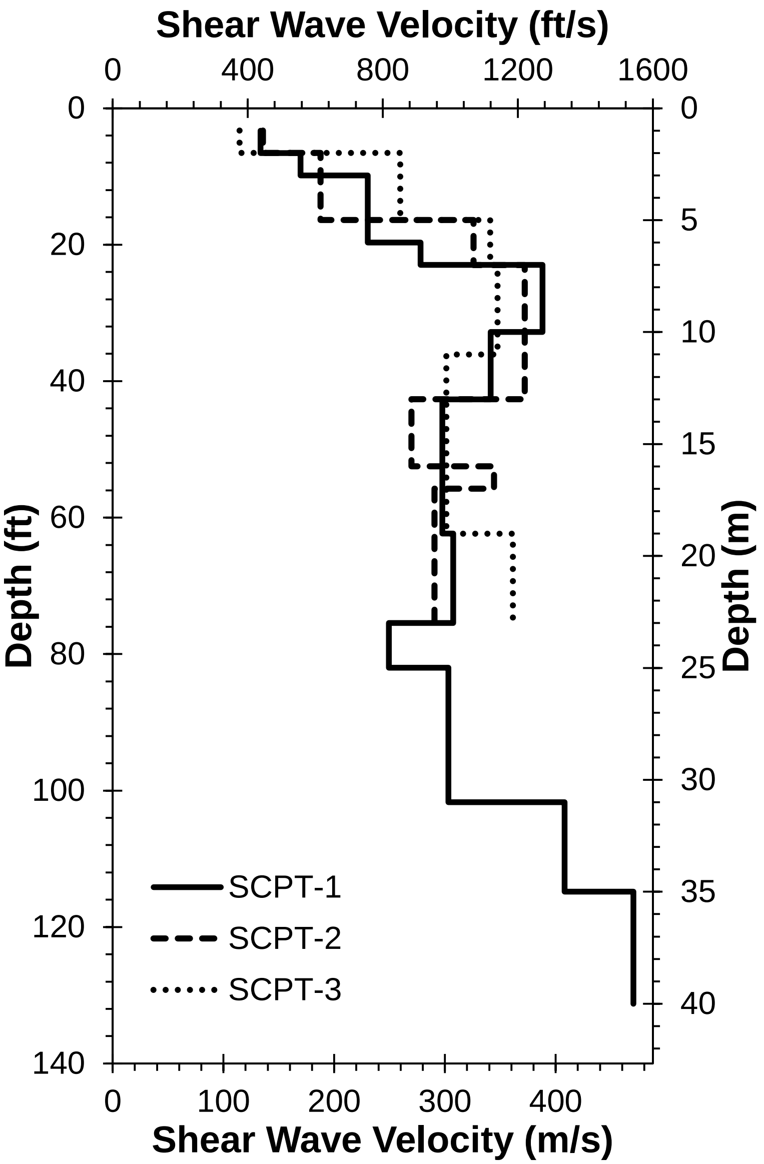

Figure 4.7: Profiles of shear wave velocity, V_s, for SCPT-1, -2 and -3 of axial and lateral loading tests

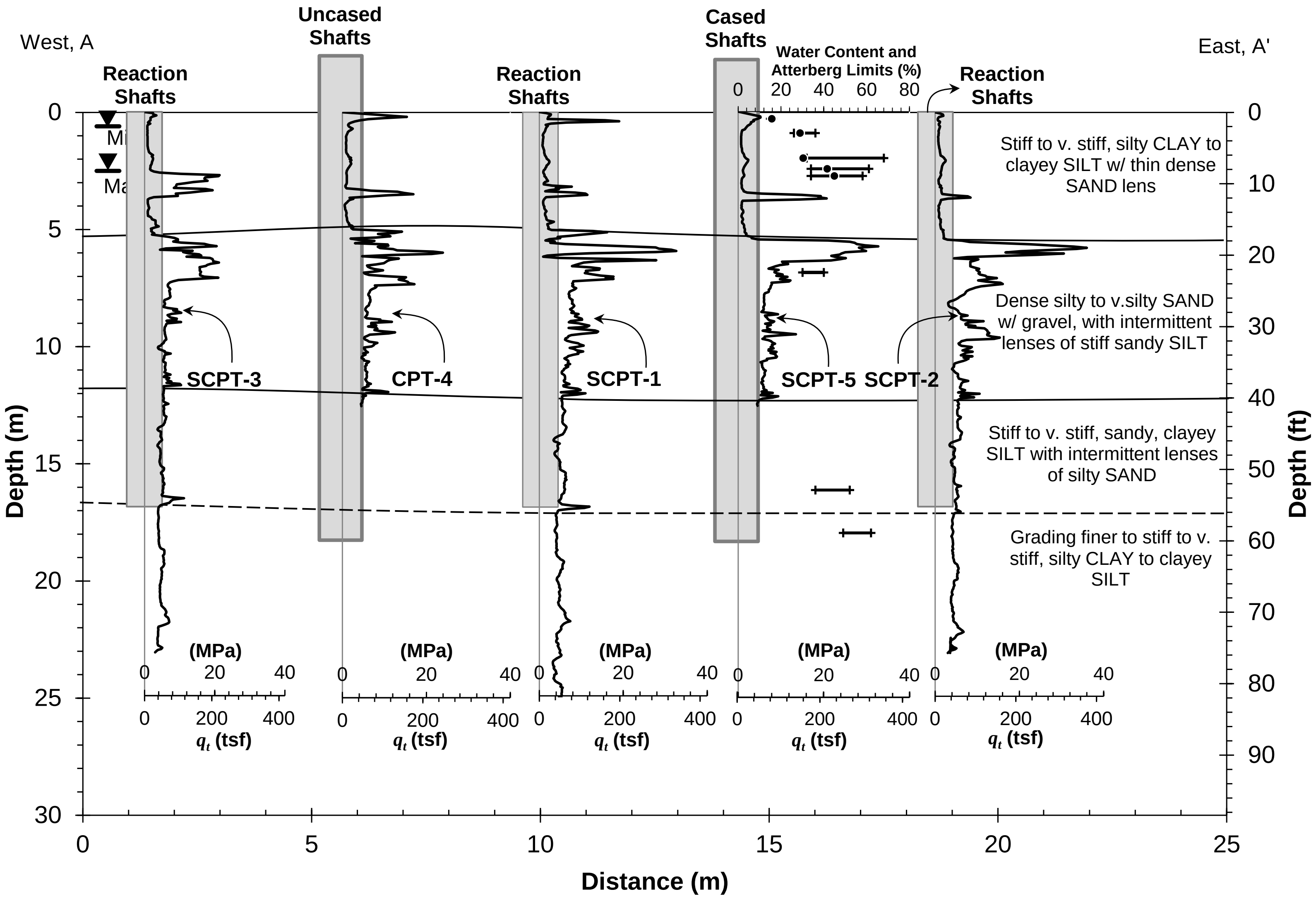

Figure 4.8: Subsurface profile at test site indicating the location of the test shafts, cone tip resistance, and Atterberg limits.

5.0 EXPERIMENTAL PROGRAM

The thrust of this research study centers on the performance of four instrumented, drilled shaft test specimens in axial loading and in lateral loading. This chapter introduces the design and construction of the test specimens and describes the various kinds of instrumentation used to observe their performance. The results of two types of non-destructive tests (NDTs) are described and compared with regard to reliability and interpretation of integrity. The chapter concludes with a discussion of the experimental setup used to load the shafts in axial and lateral loading. Chapters 6, 7, and 8 follow, and present the detailed results of the loading test program and their interpretation and use in forward design analyses.

5.1 TEST SHAFTS CONFIGURATION

The four test shafts were designed with an embedded length of 18.3 m (60 ft), and a nominal diameter of 915 mm (36 in); the actual diameter varied, sometimes significantly, as a function of construction sequence and installation method, as described below. All of the test shafts extended 1.5 m (5 ft) above ground surface to facilitate the loading test setup, described subsequently. The uncased shaft with mild (Grade 60) internal reinforcement (designated MIR) represents a typical production shaft for the Oregon Department of Transportation and was designed in collaboration with members of the Technical Advisory Committee for this study. Shaft MIR therefore serves as the baseline for comparison to the three other shafts. The steel reinforcement of MIR consisted of nine No. 14 longitudinal steel bars with 2% longitudinal steel ratio and two No. 5 spirals at a center-to-center spacing of 150 mm (6 in). Table 5.1 summarizes the salient features of MIR, whereas Figure 5.1a presents the typical cross-section, including the information of the internal reinforcement and the locations of the PVC crosshole sonic logging (CSL) access tubes, thermal wires used for thermal integrity profiling (TIP), inclinometer casing, and strain gages, as described subsequently. To reduce the congestion of the reinforcement cage as compared to MIR and reduce possibility of anomalies associated with poor concrete flowing through the cage, high-strength (Grade 80) reinforcement was used along with hollow threaded bars in shaft HSIR (high strength internal reinforcement). The internal reinforcement for HSIR could be designed with longitudinal steel ratio of 1.5% to achieve the same nominal structural axial resistance as MIR according to Section 5.7.4.4 of the AASHTO provisions (AASHTO 2014). Nine No. 11 bars and two No. 5 spirals at a center-to-center spacing of 200 mm (8 in) were nominally selected to provide the required longitudinal reinforcement. However, as shown in Figure 5.1b, three No. 11 bars were substituted with 73/56 hollow threaded bars which provided the necessary structural requirements in addition to access for cross-hole sonic logging tests (Josef 2011).

The two experimental cased shafts included one with internal reinforcement (designated CIR) and one with no significant internal reinforcement (designated CNIR). Figure 5.1c and Figure 5.1d present the typical cross-sections of CIR and CNIR, both of which had an outside dimeter and steel wall thickness of 940 mm (37 in) and 12.5 mm (1/2 in), respectively (Table 5.1). Grade 50 straight-seam steel casing was used for both the cased shafts, specially made to produce the same nominal concrete area in section as the uncased shafts. The steel reinforcement cage placed

Table 5.1. Summary of the Configuration of the Experimental, Instrumented Test Shafts.

Test Shaft and Designation	Nominal Auger Diameter m (in)	Internal Steel Type	External Steel Type	Casing Wall Thickness mm (in)	Internal and External Steel (%)
Mild Internal Steel Reinforcement (MIR)	0.915 (36)	Grade 60	-	0	2.00
High-strength Internal Reinforcement (HSIR)	0.915 (36)	Grade 80	-	0	1.50
Cased, Mild Internal Reinforcement (CIR)	0.915 (36)	Grade 60	Grade 50	12.5 (0.5)	7.20
Cased, No Internal Reinforcement (CNIR)	0.940 (37)	Grade 60*	Grade 50	12.5 (0.5)	5.33

* Only 0.15% of longitudinal steel reinforcement was used to deliver strain gages to the necessary elevations

* The total and embedded length of each shaft is 19.8 m (65 ft) and 18.3 m (60 ft), respectively.

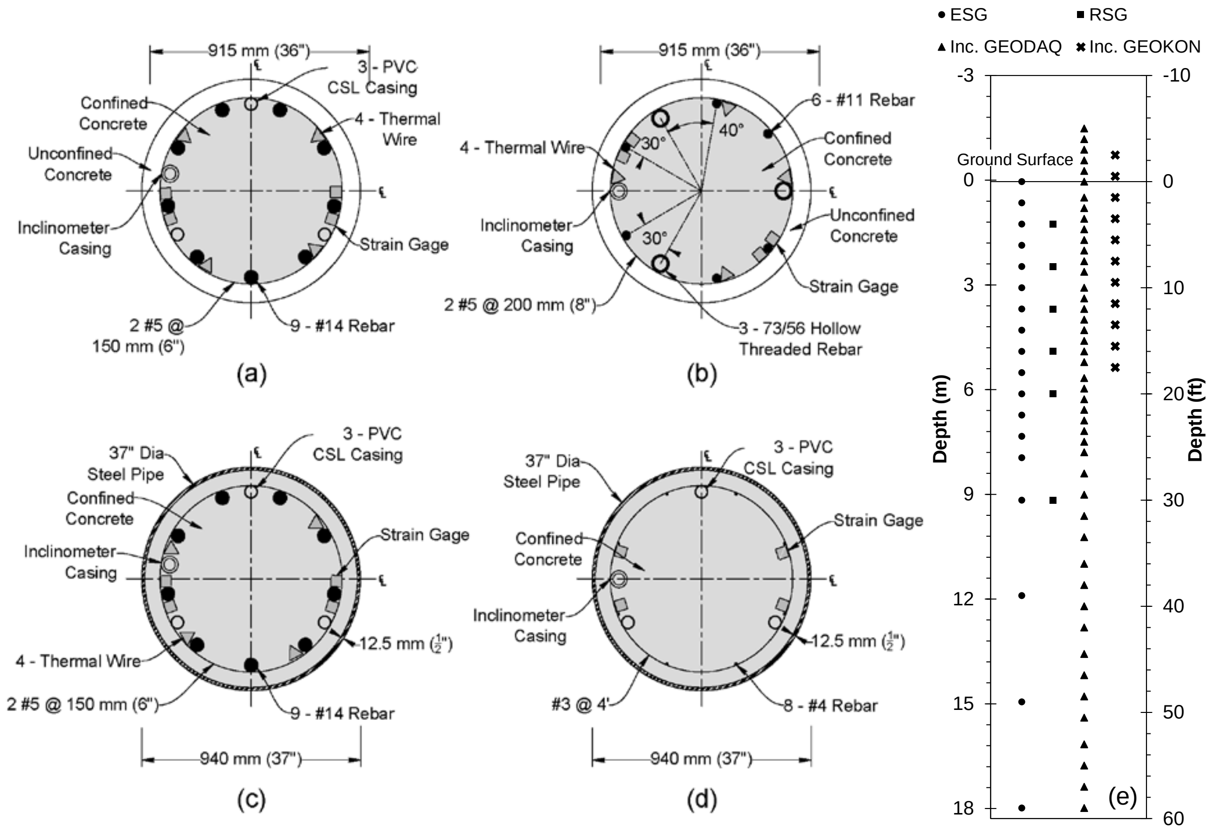

Figure 5.1: Cross-sections of the test shafts: (a) MIR, (b) HSIR, (c) CIR, and (d) CNIR with shaded area indicating the confined concrete used in section analyses, and (e) elevations of the resistance strain gages (RSG), embedded strain gages (ESG), GEODAQ in-place inclinometer (Type I Inc.), and GEOKON in-place inclinometer (Type II Inc.).

Within CIR was identical to that of MIR, whereas the cage for CNIR (with 0.15% longitudinal steel) was selected to facilitate delivery of the strain gages to the required elevations. In practice, shaft CNIR would offer substantially improved constructability of fully-cased shafts should its loading performance exhibit similar characteristics to the CIR due to the lack of internal reinforcement. To compare the effect of subtle construction differences on axial resistance, the auger diameter used for CNIR and CIR was 940 and 915 mm (37 and 36 in), respectively; this subtle difference was found to produce a significant effect on the axial response but little impact on the lateral response. Figure 5.2 show the steel cages for test shafts. It noted that the cages for MIR and CIR were identical so that the cage in Figure 5.2b is used to represent both MIR and CIR.

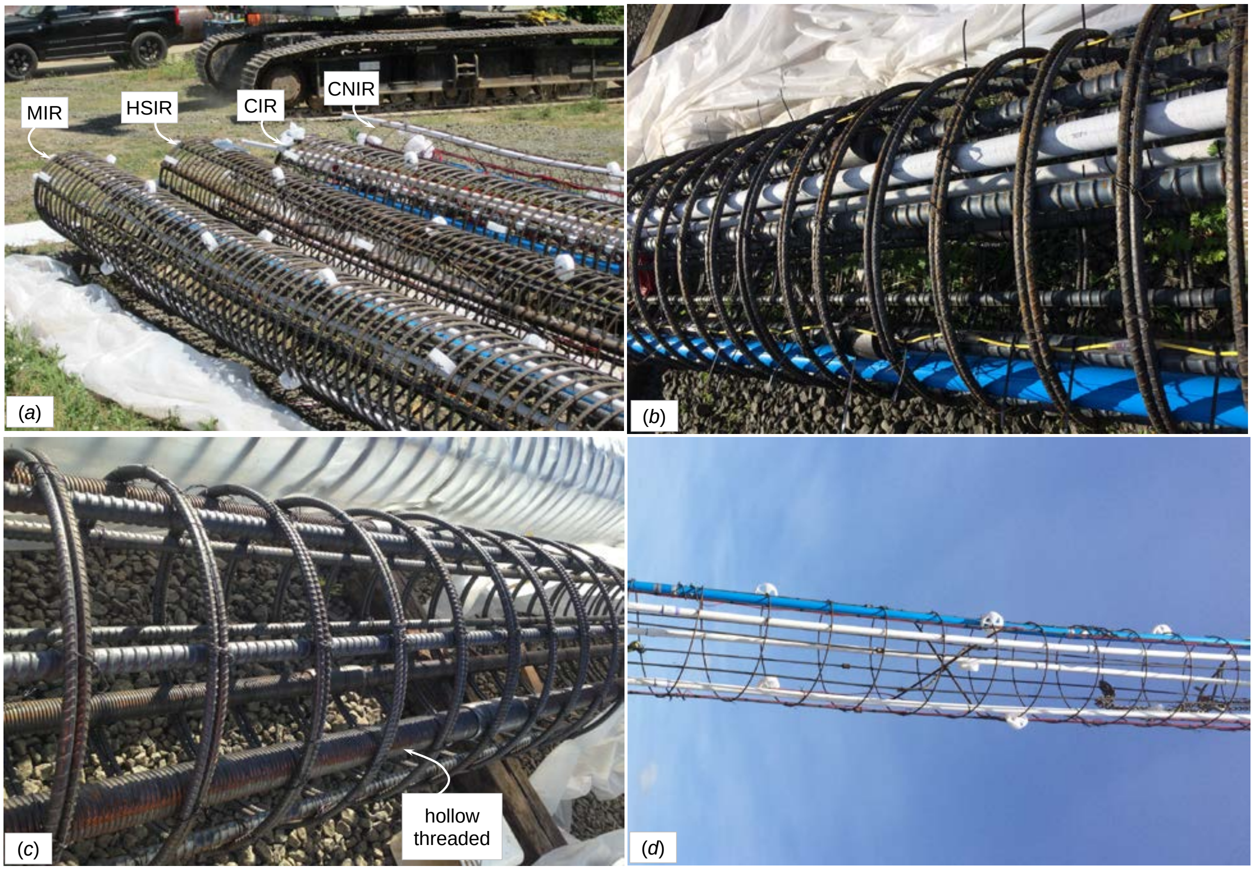

Figure 5.2: Fabricated steel cages of (a) all test shafts, (b) MIR or CIR (*n.b.*, these cages are identical), (c) HSIR, and (d) CNIR.

5.2 CONSTRUCTION OF THE TEST SHAFTS AND THE REACTION PILES

The test shafts were installed on June 16th and 17th, 2015.The wet construction method was used in the construction of the test shafts by introducing polymer slurry into the dry borehole at an excavation depth of approximately 5.5 m (18 ft) before the borehole was excavated to the final depth of 18.3 m (60 ft). Figure 5.3 shows the construction of the uncased shafts, including drilling a hole, lowering the steel cage into the hole, installing sonotube concrete form, and placing the concrete using the tremie method. Sonotube concrete forms were used to form the shafts above ground surface and were pushed 0.46 m (18 in) below ground. For the cased shaft,

Figure 5.4 shows the construction procedure, including drilling a hole, vibrating steel casing into the hole, lowering the steel cage, and placing the concrete.

Because the use of 940 mm (37 in) auger, the installation of the casing for CNIR was much easier than for CIR. The average compressive strength of the concrete on the day of the loading tests of MIR, HSIR, CIR, and CNIR was 69, 72, 65 and 64 MPa (10,500, 10,050, 9,440, and 9,270 psi), respectively. The concrete mix design used for the test shafts is summarized in Table 5.2.

Figure 5.3: Construction of the uncased shafts: (a) drilling a hole, (b) lowering the steel cage into the hole, (c) installing sonotube concrete form, and (d) placing the concrete.

Figure 5.4: Construction of the cased shafts: (a) drilling a hole, (b) vibrating steel casing into the hole, (c) lowering the steel cage for CNIR, and (d) placing the concrete.

Table 5.2 Concrete Mix Design for the Test Shafts

Parameters	Value
Comp. Strength 28 days, MPa (psi)	28 (4,000)
Slump, mm (in)	216 ± 38 (8.5 ± 1.5)
Air Content (%)	1.5% ± 1.5%
Plastic Unit Weight, kg/m^3 (pcf)	2,241 (139.9)
Maximum water/cement (w/c) Ratio	0.50
Water Reducer, mL/m^3 (oz/yd^3)	1,880 (49)
Hydration Stabilizer, mL/m^3 (oz/yd^3)	3,760 (97)
Maximum Aggregate	9.5 mm (3/8")

Twelve continuous flight auger piles (Figure 4.6) were installed to serve as reaction shafts (RS) to provide uplift reaction in axial loading tests. On either side of the shaft, there were two 0.76 m (30 in) diameter by 17 m (55 ft) long RS with 63 mm (2¼ in) diameter solid steel thread bars at center of the RS. Figure 5.5 shows the construction of the continuous flight auger piles, including drilling a hole, simultaneously pumping of the concrete and withdrawing of the auger, lowering the steel bar, and supporting the steel bar.

5.3 INSTRUMENTATION OF THE TEST SHAFTS

An instrumentation program was developed to observe the axial and lateral response of the shafts during testing. The shafts were instrumented, as shown in Figure 5.6, using concrete embedment strain gages (ESGs), resistance strain gages (RSGs), load cells, dial gages and string-potentiometers, and in-place inclinometers to observe the axial and lateral response of the shafts during testing. For each shaft, as shown in Figure 5.1e, ESGs were installed at 18 elevations and RSGs were installed at six elevations; two pairs of each strain gage type were installed at given elevation. The locations of the strain gages and inclinometers at each elevation of each shaft are shown in Figure 5.1a through Figure 5.1d. The RSGs had a strain limit of 50,000 $\mu\varepsilon$, whereas two types of ESGs were used: a low range (3000 $\mu\varepsilon$ limit) and high range (8000 $\mu\varepsilon$ limit) type, the latter of which was placed where the greatest flexural strains were anticipated during the lateral loading tests.

During the axial loading tests, the load applied at the top of each test shaft was measured directly using load cells. Three dial gages and three string-potentiometers were used to measure displacements. The displacements measured from the dial gages and string-potentiometers were nearly identical, and the mean value of the six measurements was used to represent the shaft head displacements. During the lateral loading tests, string-potentiometers and load cells were used to measure the applied displacement and corresponding lateral load. Each test shaft was instrumented with three string-potentiometers at different elevations above the ground surface with 0.3 m (1 ft) apart. The middle string-potentiometers were set at the same elevation of the resultant of the actuator-applied load. The displacements measured from the string-potentiometers and inferred from the in-place inclinometers were nearly identical at the point of load application. The measured displacement from the string-potentiometer was used to represent the deflection at the loading point, and the estimated displacement from the inclinometers was used to present the lateral displacement profiles along the shafts.

Figure 5.5: Construction of the continuous flight auger piles: (a) drilling a hole, (b) simultaneously pumping of the concrete and withdrawing of the auger, (c) lowering the steel bar, and (d) supporting the steel bar.

Given the need for reliable and redundant measurements to be used in the development of the lateral load transfer, inclinometers were used to measure the tilt, or slope, along the test shafts. Two types of in-place inclinometers were used: a GEODAQ model i6 (designated Type I inclinometer) and a GEOKON model 6150 (designated Type II inclinometer). The sensor resolution of Type I and II inclinometers is 0.004° and 0.0006°, respectively. The Type I inclinometer consisted of eight modules, connected together in series, where each module had a length of 2.4 m (8 ft). The top four modules had eight tilt sensors each (spaced 0.3 m or1 ft), whereas the bottom four modules had four tilt sensors per module (spaced 0.6 m or 2 ft). The Type II inclinometer had 11 tilt sensors placed 0.6 m (2 ft) apart starting from the loading point (Figure 5.1e). The Type II inclinometer was used in shafts MIR and CNIR, whereas the Type I inclinometer was used in shafts HSIR and CIR.

5.4 NON-DESTRUCTIVE INTEGRITY TESTS

Non-destructive tests (NDTs) provide a set of critical tools for the evaluation of the integrity of constructed deep foundations, particularly for cast-in-place foundation elements. Construction defects may require the rejection of the foundation element by the owner's representative, resulting in costly repairs or replacements and delays to the project schedule. The use and appropriate interpretation of the results from the NDTs provide the information required when evaluating the integrity of these constructed elements. A cooperative research program was conducted to assess the effects of various construction variables on the axial and lateral performance of drilled shaft foundations, which provided an opportunity to compare the established Crosshole Sonic Logging (CSL) test method to the newer Thermal Integrity Profiling (TIP) Thermal Wire method. Owing to the use of fully-threaded longitudinal steel hollow bars, the experimental program also allowed the assessment of the use of the hollow bars as access tubes for the CSL tests.

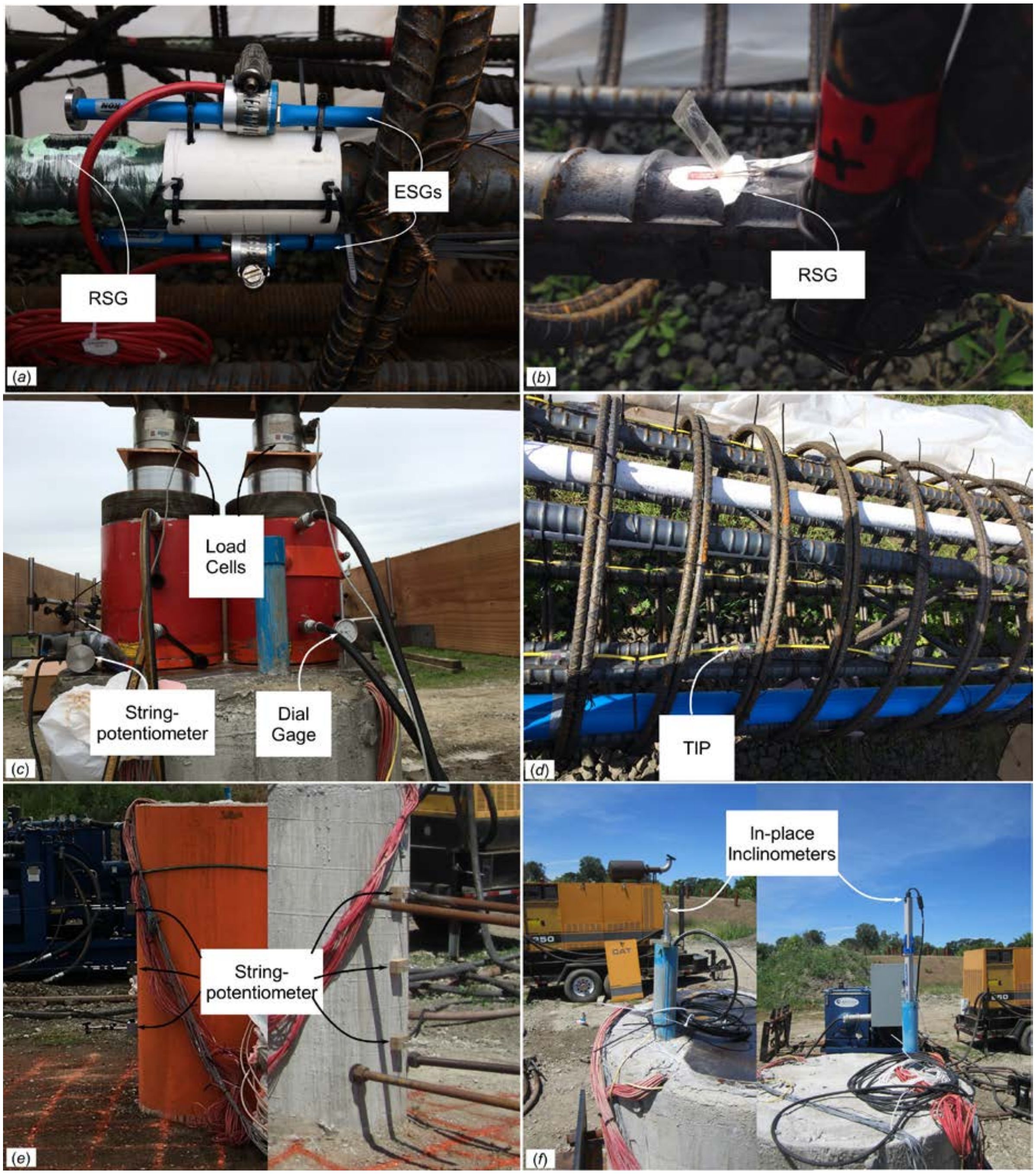

Figure 5.6: Instrumentation of the test shafts, including (a) concrete embedment strain gages (ESGs), (b) resistance strain gages (RSGs), (c) load cells, dial gages and string-potentiometers for axial loading tests, (d) string-potentiometers for lateral loading tests, (e) in-place inclinometers, and thermal wires used for thermal integrity profiling (TIP).

5.4.1 Non-Destructive Test (NDT) Methods Evaluated

The Crosshole Sonic Log (CSL) method is a downhole testing technique using ultrasonic pulse velocity (UPV), which is standardized in ASTM Standard D6760 (ASTM, 2014a). The UPV through concrete is a function of the density, age, and Young's modulus of the material, and can therefore be used to assess the as-constructed quality of the material. In this bottom-up method, a transmitter and receiver are simultaneously raised upward along the shaft within the access tubes, thereby allowing the measurement of the UPV along the ray path of the compressive *p*-wave signal. A series of velocity measurements made at uniform spacing (between transmitter and receiver) along a uniform path length can be plotted together in what is a termed a "waterfall" plot to quickly to permit a rapid visual assessment of material uniformity. It is critical that the access tubes be installed at uniform spacing along the entire length of the shaft. A rule of thumb for the minimum number of access tubes in a shaft is one tube per 0.3 m (1 ft) of shaft diameter but no less than 3 tubes (Brown et al., 2010), and this approach was followed for the test specimens evaluated in this study.

Access tubes are typically 51 mm (2 inch) in inside diameter, are either PVC or steel pipe, and are fixed to the reinforcement cage prior to placement in the excavated shaft cavity. Prior to concreting, the access tubes are filled with water to counter buoyancy, to facilitate maintaining uniform temperatures during the curing of the shaft concrete (which the potential of debonding of the pipe from the concrete), and to assist with the transmission and receiving of the UPV signal. *P*-wave velocities in good quality concrete will range from 3,600 to 4,400 m/s (11,800 to 14,400 ft/s) depending on the density, age, and Young's modulus of the concrete. One can identify anomalies by comparing the measured *p*-wave velocity to the expected velocity for the given concrete mix design and stiffness. Zones of concrete that have voids, contaminated concrete, segregation of aggregate from the paste, soil inclusions, or other possible anomalies will yield slower UPVs. The CSL method has been widely accepted as a NDT for integrity assessment and quality assurance of drilled shaft construction due to its relatively inexpensive cost and relatively rapid execution. Unfortunately, CSL testing can only measure the velocity of the material in a straight line between the transmitter and receiver, cannot test the material between the soil-shaft interface and the reinforcement cage, and cannot give, therefore, an indication of the thickness or quality of the concrete cover.

The CSL access tubes used in the test shafts were constructed using PVC pipes, which, as discussed above, are subject to debonding. To mitigate the risk of debonding, the surface of each segment of PVC pipe was scored and roughened along its entire length by rotating and advancing the pipe through a scoring box. This approach produced a very rough surface intended to improve the bond strength of the pipe to the concrete. In general accordance with established best practices, each of the PVC pipes were filled with water soon after the installation of the reinforcement cages. Based on the results of the CSL tests, described below and conducted by the leading international expert in the field, no debonding was suspected in the test shafts.

Thermal integrity profiling uses the heat generated by the curing cement (i.e., hydration energy) to assess the quality of cast-in-place concrete foundations, such as drilled shafts, bored piles, augered cast-in-place piles, continuous flight auger piles, and drilled displacement piles. The expected temperature at any location depends on the shaft diameter, mix design, time of measurement, and distance from the center of the shaft. Anomalies such as soil inclusions, voids, segregated concrete, and alignment of the reinforcement cage can be determined by measuring the hydration temperatures during the curing phase. The relationship between the shaft diameter and hydration temperature tends to be linear in the region near the cage; therefore, the actual shape of the shaft can be estimated (Mullins, 2010). Because this method relies on the heat of hydration, TIP testing is performed near the time of peak temperature, generally taken between 12 and 48 hours after concrete placement, depending on the shaft diameter and mix design, and in accordance with ASTM D7949 (ASTM, 2014b).

For the test shafts, data was acquired using full length Thermal Wires® that were tied to the reinforcement cage (e.g., yellow wires in Figure 5.6f). Typical practice requires one wire for each foot of shaft diameter but with a minimum of four wires, which are installed prior to placement of the reinforcement cage and prior to concreting. Data loggers are attached to each wire at the top of the shaft and collect temperature measurements in 15 minute increments, typically until after the peak temperature has been reached and has begun to decay. TIP measurements that are cooler than the average indicate necking, inclusions, or poor quality concrete, whereas warmer than average measurements are indicative of bulges. In general, temperature variations of +/- 2 °C are within the normal range for TIP results due to variations in the cable location and unavoidable shifting or movement of the reinforcement cage during installation in the shaft excavation and during concreting. Anomalies are indicated by abrupt changes in temperature at a particular depth. Diametric variations of temperature across the shaft reveal misalignments of the cage. The recorded measurements are interpreted in consideration of the actual volume of concrete poured to produce an estimate of shaft geometry, in addition to integrity.

5.4.2 CSL Test Results

The drilled shafts were constructed on June 16 and 17, 2015, and the CSL tests were performed approximately 3 weeks later on July 6, 2015. All of the CSL test results can be found in Appendix C. The results from the CSL testing performed on shaft MIR indicated two thin zones of reduced pulse energy and velocity reductions on all three profiles at depths of about 1.2 m (4 ft) and 4.3 m (14 ft) below the top of the concrete. As shown on Figure 5.7a, profiles 1-2 and 1-3 also revealed reduction in the velocity and energy at depths of about 0.6 m (2 ft) and 1.07 m (3.5 ft) below top of concrete. These velocity reductions were attributed to the horizontal, full penetration PVC pipes that were added to the shaft for connection of the hydraulic actuator for the lateral loading test. Some electrical interference was apparent as denoted by the horizontal streaks in the lower portions of profiles 1-2 and 1-3. The typical CSL pulse velocity was about 3,760 m/s (12,320 ft/s), and no significant anomalies were detected for the MIR shaft.

For shaft HSIR, the CSL test results indicated thin zones of reduced pulse amplitude and velocity reduction at multiple locations recurring at intervals of about 3 m (10 ft), starting at a depth of about 1.5 m (5 ft) below top of concrete, but there was no evidence of any significant anomalies (Figure 5.7b). These regular indications of reduced UPV correlate to the location of couplers used to connect the segments of the 3 m (10 ft) long hollow fully threaded bars. Couplers have contributed to the partial segregation of the aggregate from the cement paste and/or to the partial consolidation of the concrete. The typical CSL pulse velocity for the HSIR shaft was about 3,770 m/s (12,360 ft/s).

For the CIR shaft, the CSL profiles (Figure 5.8a) indicated minor variation in the first arrival time (FAT) of the pulse and in the pulse energy from a depth between about 0.6 m (2 ft) and 1.38 m (4.5 ft) below the top of concrete. Local, random electrical noise appeared to disturb the UPV signal in one of the profiles; however, no evidence of any significant anomalies was noted in the

CIR shaft. The typical CSL pulse velocity for this shaft was approximately 3,910 m/s (12,830 ft/s).

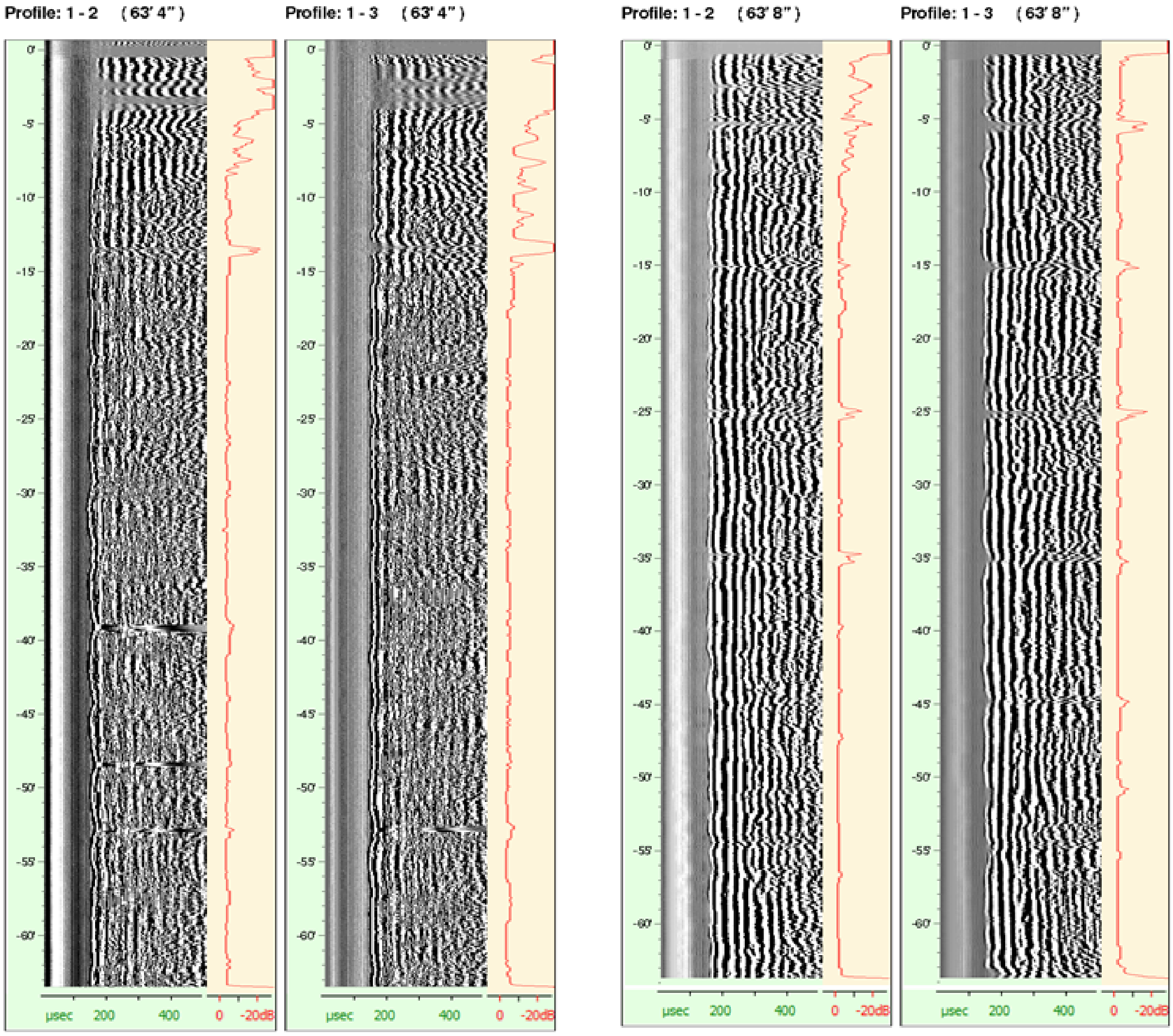

(a) (b)

Figure 5.7: Full depth sample CSL test results for (a) MIR, and (b) HSIR.

Based on the CSL test results for the CNIR shaft (Figure 5.8b), there was a thin zone located around a depth of about 1.07 m (3.5 ft) below the top of concrete where both the pulse energy and the velocity were diminished by as much as 50% of the pulse energy and velocity outside of this zone. Similar small zones were observed at multiple locations recurring at intervals of about 3 m (10 ft) along the length of the shaft, but these zones produced progressively less velocity reduction with increasing depth. These observations were attributed to localized zones of partial segregation or lack of consolidation associated with the PVC tube couplers. The typical CSL pulse velocity for the CNIR shaft was about 3,820 m/s (12,770 ft/s).

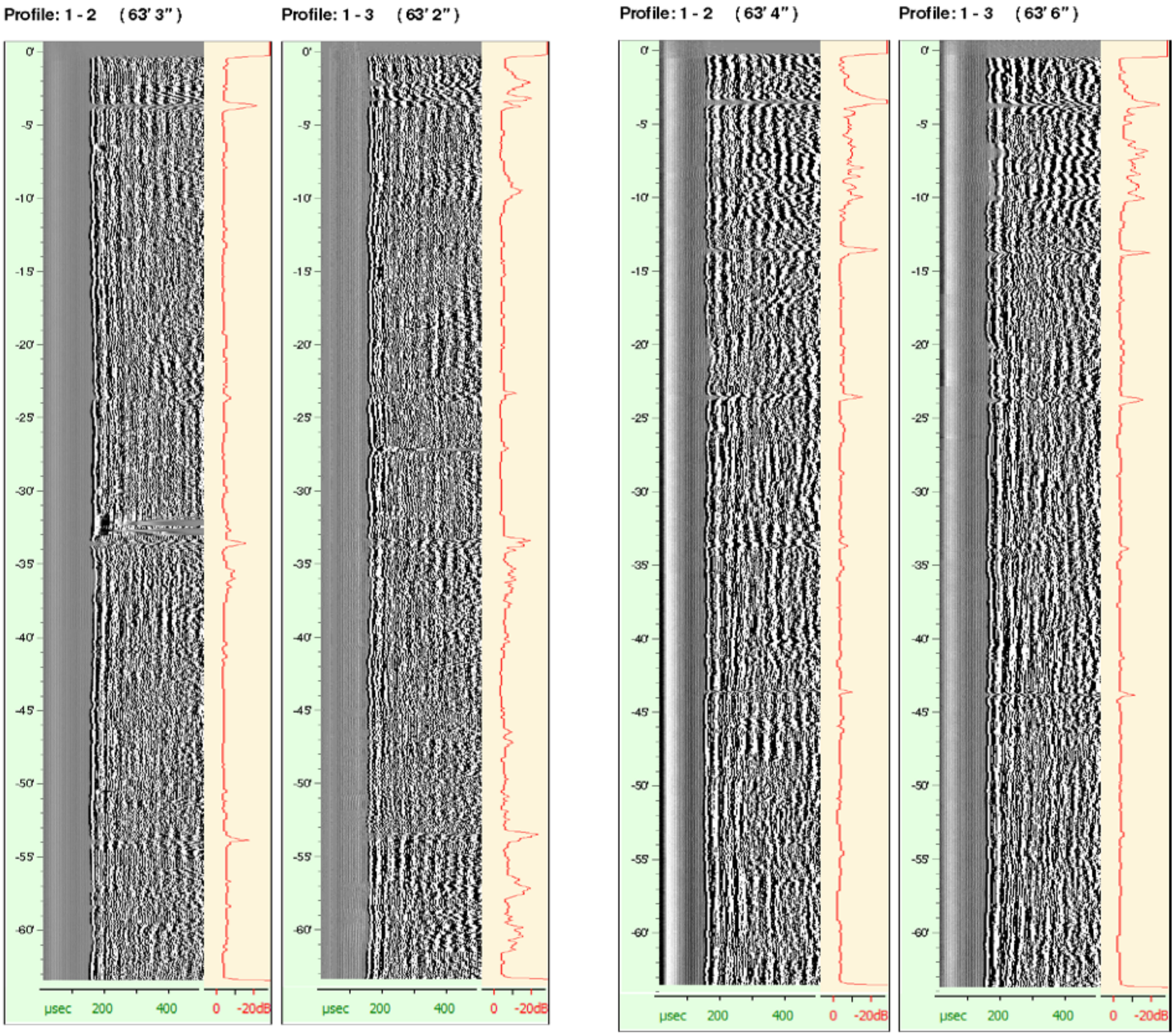

(a) (b)

Figure 5.8: Full depth sample CSL test results for (a) CIR, and (b) CNIR.

Of interest is the comparison of the signals from the CSL test results obtained using the PVC tubes and the hollow threaded bars. Representative wave forms obtained from within MIR and HSIR shafts are shown in Figure 5.9. The signal generated within shaft MIR is erratic, complex, of higher frequency, and low amplitude; furthermore, such signals are more difficult to interpret. Conversely, the signal generated within shaft HSIR produced very clean, crisp, and well-defined waveforms that are clear and easy to interpret. The advantage of receiving clean signals may be observed in the comparison of waterfall plots, where the stacked signals are separated by thick, well-spaced parallel lines indicative of good signals for shaft HSIR (Figure 5.7b) compared to muddled signals for shaft MIR (Figure 5.7a). Thus, the use of hollow threaded bars appears well suited as a quality control component, which could help alleviate congestion within the reinforcement cage and could minimize the potential for anomalies or defects in a completed shaft.

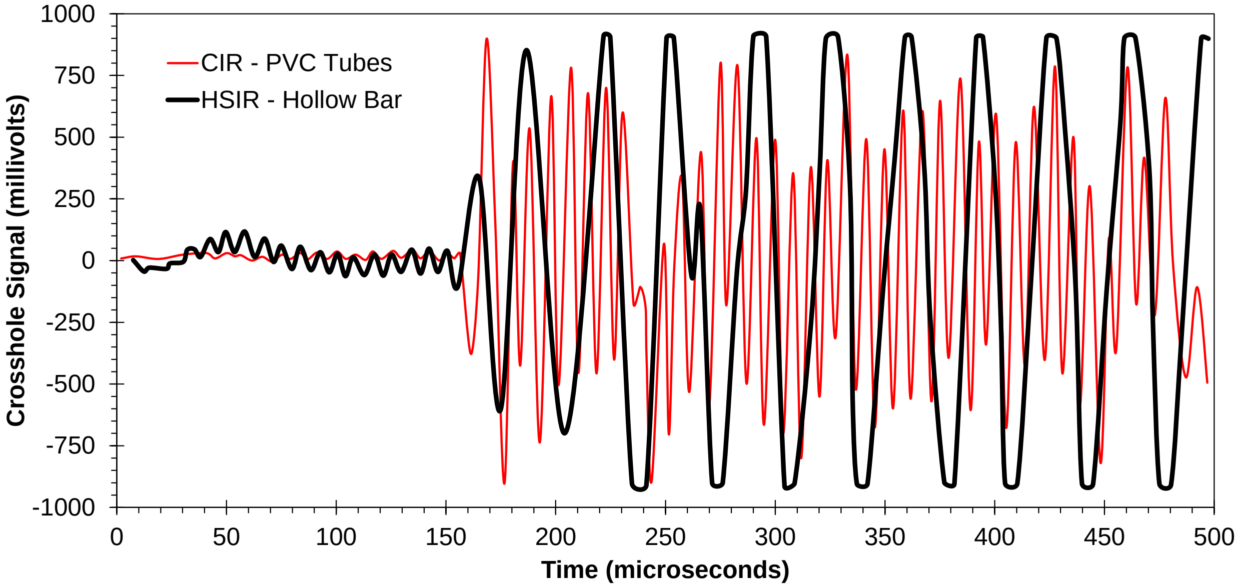

Figure 5.9: Comparison of typical wave forms developed within PVC and hollow threaded bar.

5.4.3 TIP Test Results

The collection of thermal data using the TIP Thermal Wires® commenced several hours following the completion of construction on June 16 and 17, 2015, for shafts MIR and HSIR, and for shaft CIR, respectively. No TIP thermal data was collected for shaft CNIR due to the weak cage used for this shaft. TIP Thermal Wires®, data was collected at 15 minute intervals for approximately five days. In general, the results from TIP included profiles of measured temperature and calculated shaft radius versus depth. The calculated shaft radius incorporates the measured thermal profile, the reported shaft length, and the actual volume of concrete used (Table 1). Given sufficient thermal measurement points, the calculated radius can be interpolated from the four Thermal Wires distributed around the perimeter of the reinforcement cage. Shafts MIR, HSIR, and CIR reached peak temperature approximately 46, 49, and 46 hours, respectively, after placement. The presence of the permanent casing in shaft CIR did not appear to affect the time required to obtain peak heat of hydration temperature.

Representative results from the TIP measurements obtained for shaft MIR are presented in Figure 5.10, as the full results can be found in Appendix D. The reinforcement cage for shaft MIR is overlain on a 2D color spectrum map to improve the visualization of the estimated radius profile (Figure 5.10a). The average calculated radius is consistently larger than the design shaft radius of 0.45 m (18 inches) and associated with the 915 mm (36 in) auger diameter, with a generally decreasing radius with depth. The shaft radius generally increases to a maximum of 0.58 m (23 inches) for depths between 6 to 7.5 m (20 to 25 ft), which is consistent with the location of the lower sand layer. The thermal results also indicate that the reinforcement cage is slightly shifted along the instrumented length of the shaft; however, the concrete cover provided to the cage was not smaller than 75 mm (3 inches). The alignment of the reinforcement cage is shifted such that Wires 1 and 2 are closer to the center of the shaft (and therefore exhibit higher temperatures) and Wires 3 and 4 are closer to the shaft-soil interface (indicated by lower temperatures).

Temperature reduction (termed “roll-off”) for MIR was observed to begin at a depth of approximately 1.5 m (5 ft) below the top of the shaft, which is caused by heat loss due to the exposure of the concrete to ambient air temperatures. However, the high temperature above the ground surface was attributed to the insulating-effect of the cardboard sonotube form used to temporarily support the fresh concrete. Shaft HSIR also exhibited this temperature signature (Figure 5.11), whereas shaft CIR did not, indicating that the heat-conductive steel casing did not produce an insulating effect. Temperature roll-off also occurred at the bottom of shaft MIR, which was caused by heat loss at the shaft-soil interface at the base of the shaft. The shaft bottom temperature roll-off begins at a depth of approximately 1.5 m (5 ft) above the shaft base (Figure 5.10b). No anomalies were identified around the base of the shaft.

The TIP results (i.e., average temperature- and radius-vs.-depth profiles) for the three TIP-instrumented shafts are compared in Figure 5.11. Slight variations in temperature are noted between shafts MIR and HSIR, which can be due to slight differences in the concrete mix; however, the profiles are quite similar resulting in a similar estimate of radius with depth. Localized increases in radius in the sandy seams are consistent with caving susceptibility that was observed in other shaft construction at the OSU test site. The profile of the estimated radius provides excellent guidance for the back-calculation of unit shaft and lateral resistance derived from the axial and lateral loading tests. The accuracy of the radius calculation can be observed in the computed radius for the cased shaft, as shown in Figure 5.11b, which has a known, full-depth inner radius of 0.45 m (18 inches). Comparing the measurements of the individual thermal wires in shafts HSIR and CIR indicated that the cages were very well centralized within the casing. Shaft HSIR had, on average, more than 75 mm (3 inches) of cover along the entire depth, whereas shaft CIR yielded an even 75 mm of cover due to the permanent casing (Figure 5.11b).

Important Note: Comparing the average temperature profiles between the cased and uncased shafts (Figure 5.11 a), significant differences are observed above a depth of about 8 m (26.5 ft), whereas similarities are noted for depths below 8 m. Of particular note at a depth of about 5 m (16.4 ft) and corresponding to the interface between the first and second (a water bearing) soil layers, the shaft became somewhat belled. The drilling protocols were identical for all shafts and therefore the variation in diameter of the excavation should be similar. However, this is not observed in the temperature profile due to the presence of the casing, which would have been surrounded by flowing groundwater that could act to cool the shaft. The temperature profile indicated the presence of significant gaps between the casing and the sidewalls of the shaft cavity from depths of 3 to 8 m. The presence of gaps seemed to be confirmed upon axial loading (described below). In addition, the temperature-based inference of shaft radius appeared slightly smaller than the actual (and known) radius, perhaps due to the cooling effect of the groundwater.

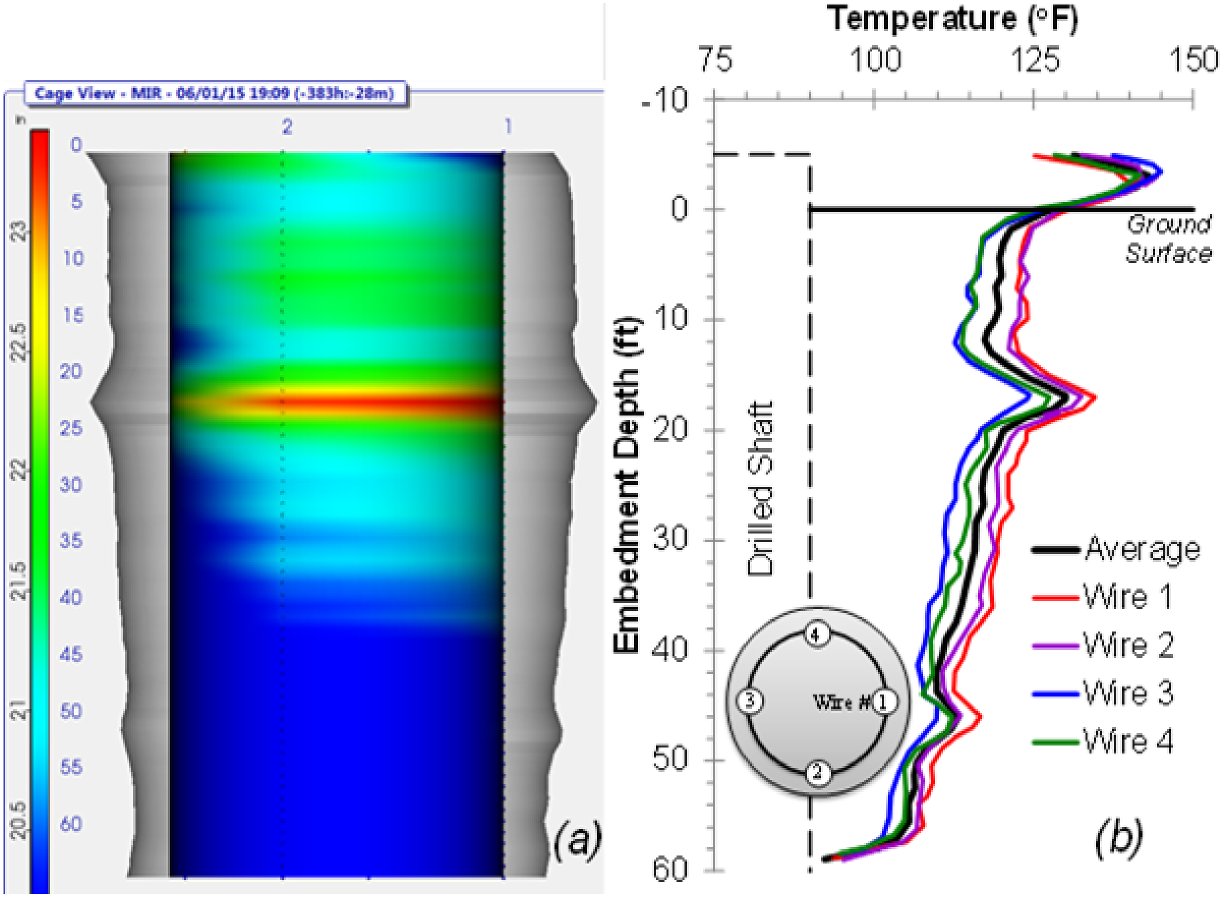

Figure 5.10: TIP results for shaft MIR (a) variation of radius map with depth inferred from thermal measurements, and (b) actual depth profiles of temperature measured along four points on reinforcement cage. Note: figure (a) shows depth beginning at the top of shaft (1.5 m above ground surface).

5.5 AXIAL LOADING TEST SETUP

Axial loading tests were conducted on April 8th, 15th, 21st, and 26th, 2016 for CNIR, CIR, HSIR, and MIR, respectively, approximately 10 months after the shafts were constructed. Conventional top-down axial compression load tests were conducted by inducing a load into the test shaft using hydraulic jacks and by reacting against a large, 18 MN (4,000 kip) capacity cross beam with two saddle beams tied to reaction piles, as shown in Figure 5.12. Axial displacements were applied to the test shafts using two jacks with the combined capacity of 7,120 kN (1,600 kips) at 70 MPa (10 ksi). Four 63 mm (2¼ in) diameter solid steel thread bars connected the reaction frames to four 0.76 m (30 in) diameter by 17 m (55 ft) long continuous flight auger piles, two on either side of the test shaft, to provide the necessary tiedown resistance to the uplift reaction generated by the jacking force.

Axial loads were applied in increments of 267 kN (60 kips) until failure or until the limit of available pressure with the hydraulic pump was reached. The loading increments were deemed too large for the cased shafts, but were used nonetheless to facilitate the comparison of load-displacement behavior among the test shafts. At each load increment, the applied axial loads were maintained for 10 minutes to allow sufficient sampling of the ESGs, which required 3 seconds/sample.

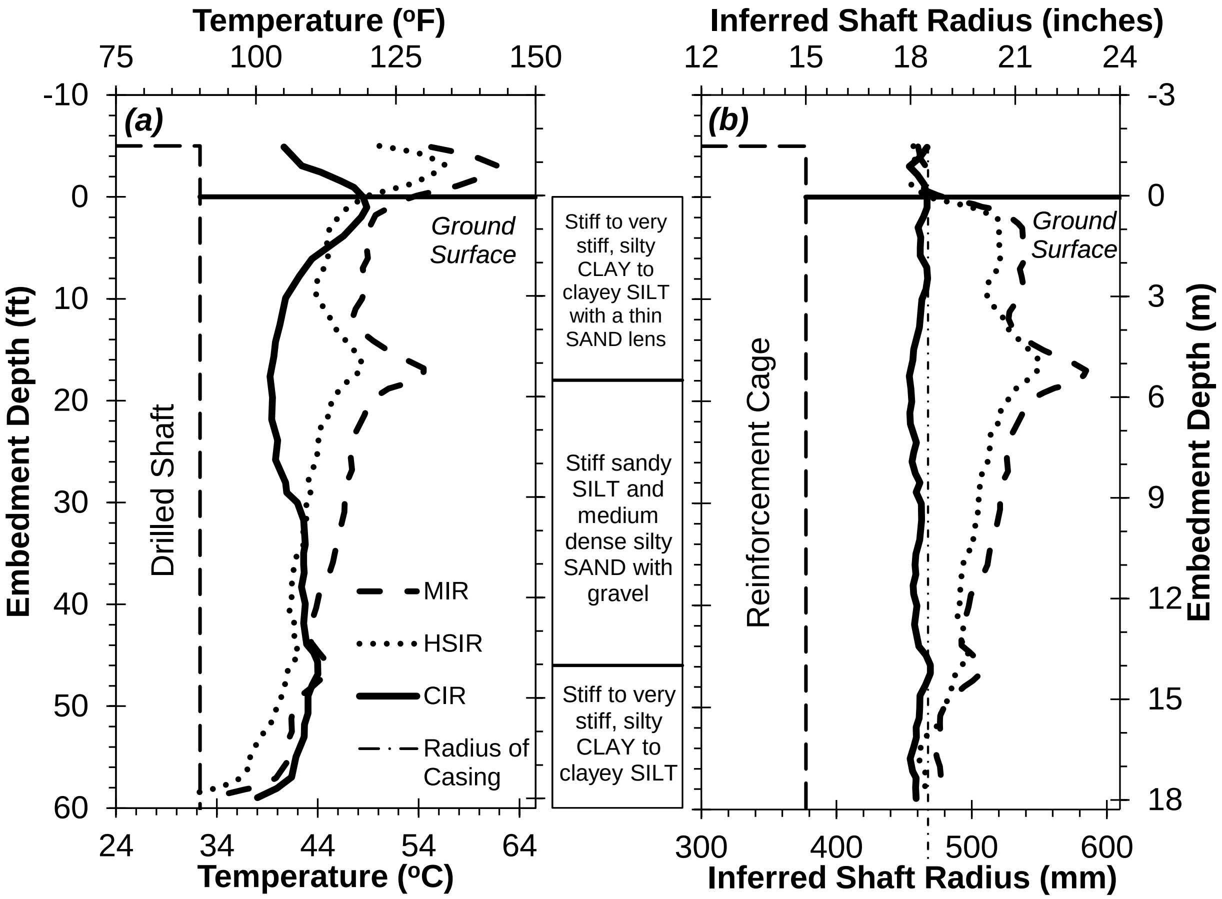

Figure 5.11: Comparison of (a) average temperature-depth profiles, and (b) average radius-depth profiles for shafts MIR, HSIR, and CIR.

5.6 LATERAL LOADING TEST SETUP

Lateral loading tests were conducted by displacing two test shafts at a resultant point located approximately 760 mm (2.5 ft) above the ground surface using a hydraulic actuator (Figure 5.13). Owing to the need to displace each shaft to large displacements, the loading tests were paired with shafts of similar flexural rigidity; therefore, shaft MIR provided the reaction for HSIR, whereas CIR provided the reaction for CNIR (and vice versa). Lateral loading tests were conducted on June 4th and 14th, 2016 for uncased and cased shafts, respectively.

The loading tests commenced with a target of 2.54 mm (0.1 inch) of incremental displacement until the displacement reached 12.7 mm (0.5 inch). The incremental lateral displacement increased to 6.35 mm (0.25 inch) until total displacement of 25.4 mm (1.0 inch). Then, the incremental lateral displacement of 12.7, 25.4, and 50.8 mm (0.5, 1.0, and 2.0 inch) were applied when the total displacement reached at 50.8, 101.6, 304.8 mm (2.0, 4.0, and 12.0 inch), respectively. The displacement recorded at the resultant point of load application at HSIR and CIR was used to control the applied displacements; accordingly, displacements of the reacting shafts were alternately smaller, equal, and larger than the specified displacements due to compliance in the experimental setup and the spatial variability of the soil. Lateral loads, V_h, were held at 18-minute time intervals at each target load to allow sufficient sampling of ESG data. Table 5.3 summarizes the load schedule of applied displacement, y_h, at the loading points.

For the cased shafts, the final applied displacement was approximately 203 mm (8 in) due to the limitation of the available pressure possible with the hydraulic actuator.

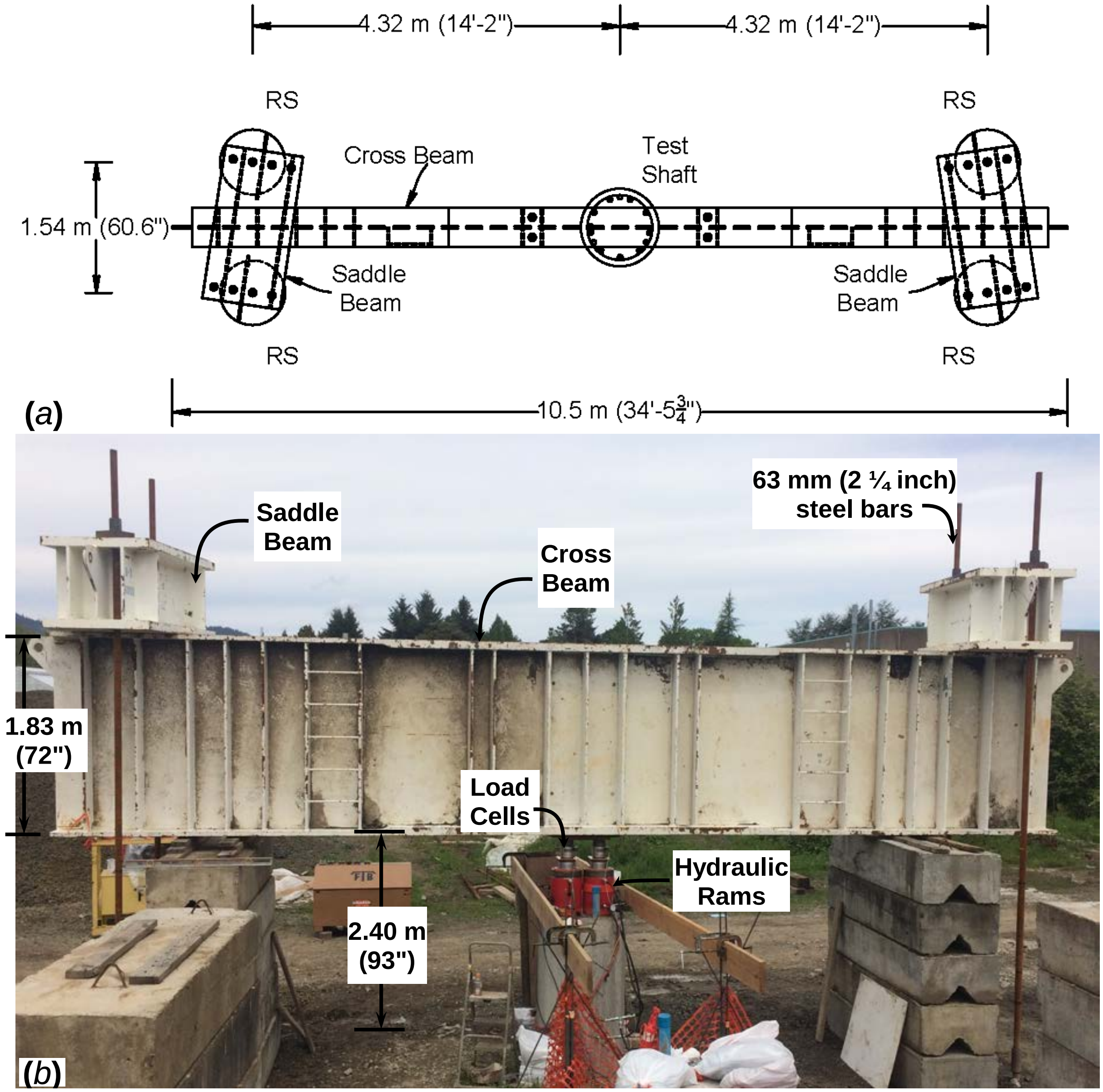

Figure 5.12: Experimental setup for the axial loading tests: (a) top view and (b) plan view.

Figure 5.13: Lateral loading tests setup for (a) uncased shafts and (b) cased shafts. Note, the photos were taken at the applied displacement of 447, 206, 213, and 205 mm (17.6, 8.11, 8.39, and 8.07 in) for MIR, HSIR, CIR, and CNIR, respectively.

Table 5.3. Summary of Loading Protocol and Measured Lateral Displacement, y_h, and Lateral Shear Force, V_h, for the Four Test Shafts.

Increment	Scheduled y_h, mm (inch)	Measured y_h, mm (inch)				Measured V_h, kN (kip)	
		MIR	HSIR	CIR	CNIR	uncased	cased
0	0	0	0	0	0	0	0
1	2.5 (0.1)	2.6 (0.1)	3.3 (0.1)	4.3 (0.2)	3.8 (0.1)	170 (38)	130 (29)
2	5.1 (0.2)	4.3 (0.2)	5.5 (0.2)	8.0 (0.3)	6.4 (0.3)	210 (47)	180 (40)
3	7.6 (0.3)	6.0 (0.2)	8.8 (0.3)	11.7 (0.5)	8.1 (0.3)	260 (58)	225 (50)
4	10.2 (0.4)	7.5 (0.3)	10.8 (0.4)	17.6 (0.7)	11.1 (0.4)	280 (63)	275 (62)
5	12.7 (0.5)	9.7 (0.4)	13.5 (0.5)	20.7 (0.8)	13.1 (0.5)	310 (70)	310 (69)
6	19.1 (0.8)	16.0 (0.6)	19.9 (0.8)	29.0 (1.1)	19.9 (0.8)	370 (83)	415 (93)
7	25.4 (1.0)	20.7 (0.8)	25.7 (1.0)	35.1 (1.4)	25.6 (1.0)	425 (95)	495 (111)
8	38.1 (1.5)	34.5 (1.4)	38.9 (1.5)	50.0 (2.0)	38.9 (1.5)	530 (119)	630 (142)
9	50.8 (2.0)	46.6 (1.8)	51.4 (2.0)	65.2 (2.6)	51.8 (2.0)	605 (137)	745 (167)
10	76.2 (3.0)	68.7 (2.7)	77.1 (3.0)	91.5 (3.6)	77.7 (3.1)	720 (162)	925 (208)
11	102 (4.0)	92.0 (3.6)	103 (4.0)	115 (4.5)	103 (4.0)	800 (179)	1,085 (244)
12	152 (6.0)	183 (7.2)	151 (6.0)	164 (6.5)	155 (6.1)	860 (194)	1,350 (304)
13	203 (8.0)	446 (17.5)	206 (8.1)	213 (8.4)	205 (8.1)	885 (199)	1,540 (346)
14	254 (10.0)	477 (18.8)	255 (10.0)	-	-	910 (204)	-
15	305 (12.0)	523 (20.6)	305 (12.0)	-	-	920 (207)	-

6.0 AXIAL LOADING TEST RESULTS AND DISCUSSION

This chapter provides the specific details regarding the axial loading tests on the four test shafts, including the interpretation of measured axial strains, the global load-displacement performance of the test shafts, and the axial load transfer profiles. Based on these measurements, the data is interpreted to provide the unit shaft and toe resistances, where appropriate, and which are used to propose a CPT-based approach to estimate the axial capacity of drilled shafts in similar Willamette Valley soils. Thereafter, the suitability of the FHWA load transfer method outlined in O'Neill and Reese (1999) is evaluated. Finally, the effect of casing installation and construction sequence on the unit shaft resistance of drilled shaft foundations is summarized based on this and previously-reported loading tests.

See Chapter 4.0 for details regarding the subsurface conditions that contribute to the observed axial loading performance. Refer to Chapter 5.0 for details regarding the construction and configuration of the test shafts and corresponding instrumentation used to observe the axial load transfer.

6.1 INTERPRETATION OF MEASURED AXIAL STRAINS

At the same elevation, the concrete embedment strain gauges (ESGs) and resistance strain gauges (RSGs) recorded similar values of axial strain. Therefore, only the axial strains measured using the ESGs, which were installed at more elevations, were used to interpret the axial load transfer. The axial load, Q, at a depth, z, was evaluated using:

$$Q(z) = E_s(z) \cdot A(z) \cdot \varepsilon(z) \tag{6.1}$$

where $E_s(z)$ = composite secant modulus of the shaft, $A(z)$ = cross-sectional area of the shaft, and $\varepsilon(z)$ = recorded axial strain. The cross-sectional area of the shaft at each depth of interest was estimated using the inferred shaft radius back-calculated using the TIP results (Figure 5.11b). The secant modulus of the shaft is a function of strain level; therefore, the secant modulus varies along the length of the shafts during loading and varies according to the applied load and resulting strain even at the same elevation. The relationship between E_s and ε was evaluated for each shaft using the method presented by Fellenius (1989, 2017). First, the tangent modulus, E_t, for different strain levels was estimated using the applied loads and strains at the ground level, where shaft resistance is the smallest, using:

$$E_t(\varepsilon) = \frac{\Delta Q(\varepsilon)}{A \cdot \Delta\varepsilon} \tag{6.2}$$

where $\Delta Q(\varepsilon)$ and $\Delta\varepsilon$ = change of load and strain, respectively, from one load increment to the subsequent increment. The linear relationship between tangent modulus and corresponding strain was obtained using the ordinary least squares (OLS) method, and is expressed by:

$$E_t(\varepsilon) = a \cdot \varepsilon + b \tag{6.3}$$

where a = slope of the tangent modulus line and b = initial tangent modulus. An example of the evaluation of the strain-dependence of tangent modulus using the data from MIR is shown in Figure 6.1. Then, the secant modulus was obtained by (Fellenius 2017):

$$E_s = 0.5a \cdot \varepsilon + b \tag{6.4}$$

The axial load, Q, at the depth z, was then be computed as a function of strain:

$$Q(z) = \left[0.5a \cdot \varepsilon(z) + b\right] \cdot A(z) \cdot \varepsilon(z) \tag{6.5}$$

The small slope shown in Figure 6.1 is representative of large diameter, axially stiff shafts; smaller, more slender elements, such as augercast piles, exhibit significantly greater variation in tangent modulus with strain level (Stuedlein et al., 2012).

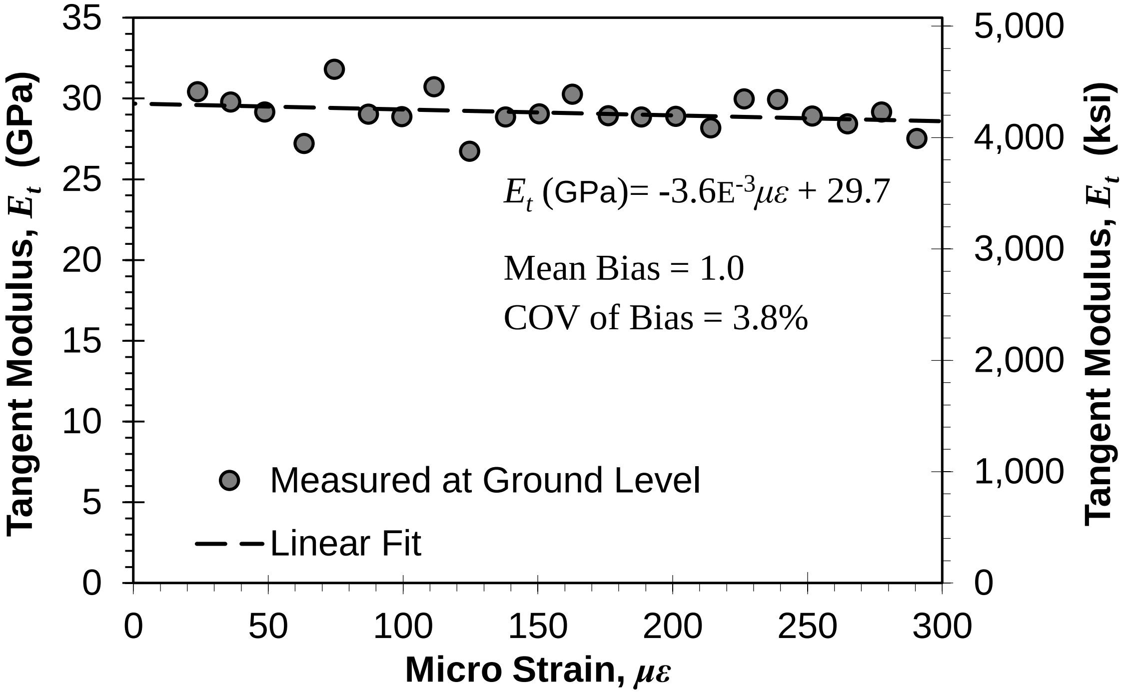

Figure 6.1: Example of evaluation of the strain-dependence of tangent modulus for MIR.

6.2 LOAD AND DISPLACEMENT OBSERVED AT SHAFT HEAD

The measured load-displacement response at the top of the shaft is shown in Figure 6.2 for each test shaft. The axial resistance of the cased test shafts CIR and CNIR was fully mobilized (i.e., achieved an ultimate resistance) since plunging was observed at final displacements of 84 and 74 mm (3.3 and 2.9 in) at maximum applied load of approximately 1,960 kN (440 kips) and 1,330 kN (300 kips), respectively, prior to termination of the tests. The subtle change in auger diameter between CIR and CNIR (915 vs. 940 mm, respectively) resulted in about 47% greater axial resistance for CIR. Shafts MIR and HSIR could not be loaded to an ultimate axial resistance, as the available hydraulic pressure capacity of the hydraulic pump limited the application of higher loads (specifically, the pressure was limited to 65 MPa or 9,500 psi for safety purposes).

The load-displacement response at the top of the uncased shafts was nearly identical to one another, as shown in Figure 6.2. The maximum load applied to MIR and HSIR was 6,125 kN (1,377 kip) and 6,380 kN (1,435 kip), respectively, with corresponding displacements of 4.3 mm (0.17 in) and 3.8 mm (0.15 in), or about one order of magnitude smaller than for the cased test shafts. For example, although the axial resistance of MIR was not fully mobilized by the end of the test, MIR still exhibited about 210% greater resistance compared to the fully-mobilized axial resistance of CIR. The resulting improvement in axial load transfer is due to the rougher soil-concrete interface and larger as-built diameter of the uncased test shafts, and to the presence of gaps between the soil and casing for the cased shafts. In a production setting, the TIP data could have been used to establish a basis for remedial grouting at the soil-shaft interface to ensure intimate contact between the soil and the casing to improve its load transfer characteristics.

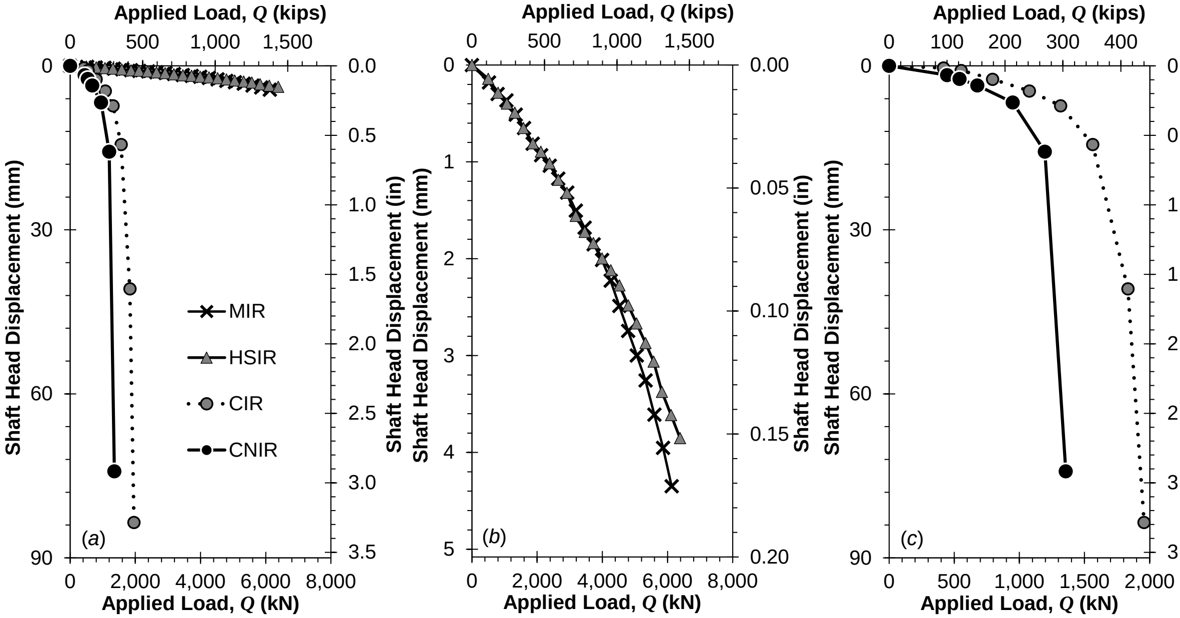

Figure 6.2: Relationship between the measured load and displacement for (a) each of the test shaft, (b) uncased shafts, and (c) cased shafts.

6.3 AXIAL LOAD TRANSFER

Load transfer distributions for the test shafts at selected load increments and for the cased test shafts for all of the load increments are shown in Figure 6.3. Each of the test shafts exhibited bending during axial loading, which may have resulted from the following: (1) differences in shaft geometry and resistance with azimuthal direction and depth, (2) differences in the axial load applied by the two jacks (arising from differences in surface topography of the shaft head and energy losses in the hydraulic lines), (3) imperfect alignment of the reaction frame, and/or (4) differential mobilization of uplift load transfer among the four reaction piles (observed from optical survey). In view of the observed bending, the load transfer data were interpreted following fitting of the observed load transfer to the continuous function:

$$Q = \frac{a_1}{\cosh\left[(z/a_2)^n\right]} + a_3 \tag{6.6}$$

where a_1, a_2, a_3 and n = fitting parameters, determined using OLS regression. The constraint applied in curve fitting was that load at the shaft head equaled the load measured using the load cells. In addition, the measured data from the depths of 0.6 to 3.0 m (2 to 10 ft) for MIR were omitted in the curve fitting due to the significant influence of bending at this section along the shaft. Since the bending effects were negligibly small at deeper portions of the test shafts, the measured loads at the depths below 9.1 m (30 ft) were used for all further analyses of load transfer. The measured and fitted load distribution for the two uncased test shafts, MIR and HSIR, is shown in Figure 6.3a and Figure 6.3b, respectively. The soil provided relatively small shaft resistance near the ground surface to depths of 3.0 m (10 ft) and 1.2 m (4 ft) for MIR and HSIR, respectively. Low shaft resistance in near-surface soils is typical in plastic soils owing to the seasonal moisture changes that occur and result in shrinkage (contraction) of soil away from the shaft (Brown et al. 2010). For MIR, the relatively small shaft resistance observed from the ground surface to the depth of 3.0 m (10 ft) may have also resulted from bending effects in addition to seasonal moisture changes. The toe resistances of the uncased test shafts were not mobilized significantly during the loading tests.

For the two cased test shafts, the loads observed at a depth of 18.0 m (59 ft) were not consistent with the loads recorded above this location, perhaps due to misalignment of the gages during installation and construction. The tip resistance determined using SCPT2 (Figure 4.8) was very similar from a depth of about 11.9 to 18.0 m (39 to 59 ft); therefore, it was assumed that the mobilized unit shaft resistance at depths from 11.9 to 14.9 m (39 to 49 ft) for each load increment was the same as that at depths from 14.9 to 18.0 m (49 to 59 ft). However, it was reasonably assumed that the first two load increments applied to CIR produced unit resistances at the bottom of the shaft that were approximately half of those observed for the tributary area immediately above the base of the shaft. Furthermore, it appears that the shaft resistance was very small from the ground surface to the depth of about 7.9 m (26 ft) and/or mobilized with very little relative displacement, which may be attributed, in part, to the gaps that formed between the casing and the soil.

6.3.1 Unit Shaft Resistance-Relative Displacement Relationships (*t-z* curves)

To generalize the results of the two loading tests of the uncased shafts specifically for similar soils in the Willamette Valley, and to evaluate various design models, unit shaft resistance-relative displacement relationships were developed. The unit shaft resistance, t, was computed by considering the representative tributary area for each portion of the instrumented shaft using the following approach:

$$t = \frac{\Delta Q}{\pi D \cdot \Delta L} \tag{6.7}$$

where ΔQ =the change of axial load along the tributary area, D = the average as-built diameter along the tributary area, and ΔL = the height of tributary area. The relative displacement was calculated by subtracting compression of the shaft at the depth of interest due to axial loading from the displacement induced in the shaft at the depth of the section above. The axial compression of the shaft, δ, was estimated by:

$$\delta = \frac{Q \cdot \Delta L}{A \cdot E_s} \tag{6.8}$$

where Q = the average axial load along the tributary area and A = the average area of the cross-section along the tributary area. The relationship between unit shaft resistance and relative displacement, known as a *t-z* curve, was thus constructed to represent the mobilization of shaft resistance along a unit tributary area of a deep foundation element. Since the axial load transfer data for MIR from depths of 0.6 to 3.0 m (2 to 10 ft) were omitted in the curve fitting, the unit shaft resistance was calculated considering this portion of the shaft as one tributary area. For comparison purposes, one *t-z* curve from depths of 0.6 to 3.0 m (2 to 10 ft) was also calculated for HSIR. The *t-z* responses for the cased test shafts were evaluated at those elevations from where a gap between the casing and soil was not suspected (i.e., from depths of 7.9 to 18.0 m).

The *t-z* curves for the various tributary depths are shown in Figure 6.4 for each test shaft. It appears that the maximum unit shaft resistance of the uncased test shafts ranged from 6 to 300 kPa (120 to 6,200 psf), whereas the maximum unit shaft resistance for the cased test shafts ranged from 8 to 35 kPa (175 to 700 psf). Shaft CIR exhibited greater unit shaft resistances than CNIR below a depth of about 12 m (39 ft), a result stemming from the use of the smaller auger. As relative displacement increased, the interface of CIR softened to reduce to a residual resistance that corresponded to the ultimate resistances observed for CNIR, equal to 12 to 17 kPa (240 to 360 psf).

The back-calculated *t-z* curves for MIR and HSIR are compared in Figure 6.5 through Figure 6.7 to those obtained by fitting to a hyperbolic model using OLS and those computed from a model proposed below. Relatively large differences in the *t-z* responses of MIR and HSIR were observed from the ground surface to a depth of about 6.7 m (22 ft); however, below a depth of 6.7 m (22 ft), similar *t-z* responses were observed. The difference in the upper portion (to a depth of about 4.3 m) may be attributed to bending effects, differences in the as-built shaft geometry, and different water contents in the soil near the ground surface. Based on data from a weather station at the test site, a rain event with an accumulated rainfall of 21 mm (0.84 in) was observed seven days prior to testing HSIR. During testing of HSIR, the groundwater table was located at a depth of 1.8 m (5.9 ft). However, a four-day rain event ended two days prior to testing MIR, which produced an accumulated rainfall of 37 mm (1.47 in) and resulted in the groundwater rising to a depth of 1.6 m (5.2 ft). Thus, changes in water content and effective stresses in the near-surface vadose zone were likely between the time that MIR and HSIR were tested.

For the uncased test shafts, the distribution of the measured peak and extrapolated ultimate unit shaft resistance, $r_{s,m}$ and $r_{s,ult}$, respectively, are shown in Figure 6.8. The hyperbolic model (Kondner 1963) was used to simulate the *t-z* curves for each tributary area of the uncased shafts since they did not exhibit plunging. The model was then used to estimate the ultimate unit shaft resistance, which was assumed equal to the asymptotic, extrapolated resistance. On average, $r_{s,ult}$ determined from extrapolation was 21% larger than $r_{s,m}$. Note: these figures also present the results of a proposed model, described in detail in the sections that follow.

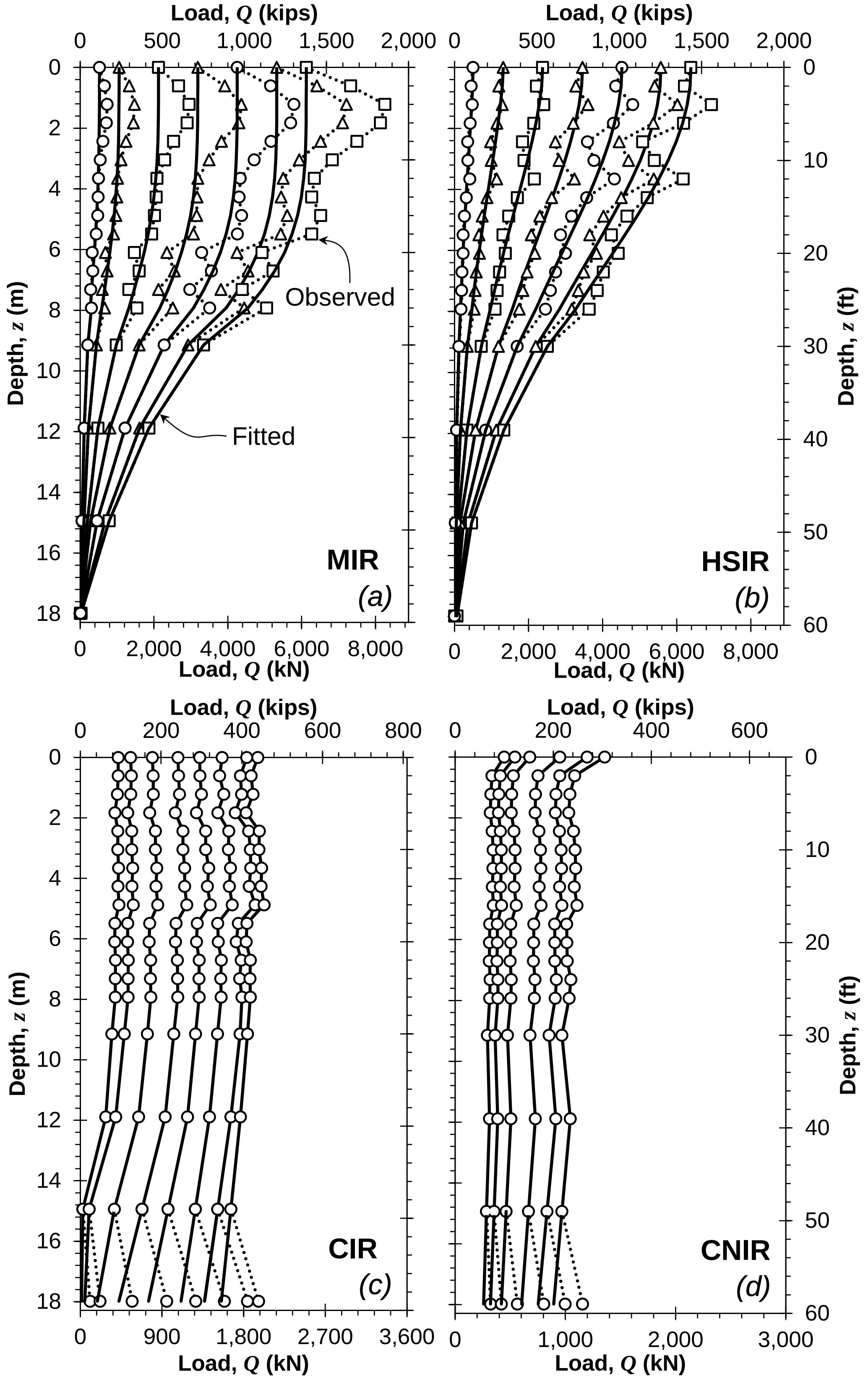

Figure 6.3: Measured and fitted load transfer distributions of shafts (a) MIR and (b) HSIR (c) CIR, and (d) CNIR.

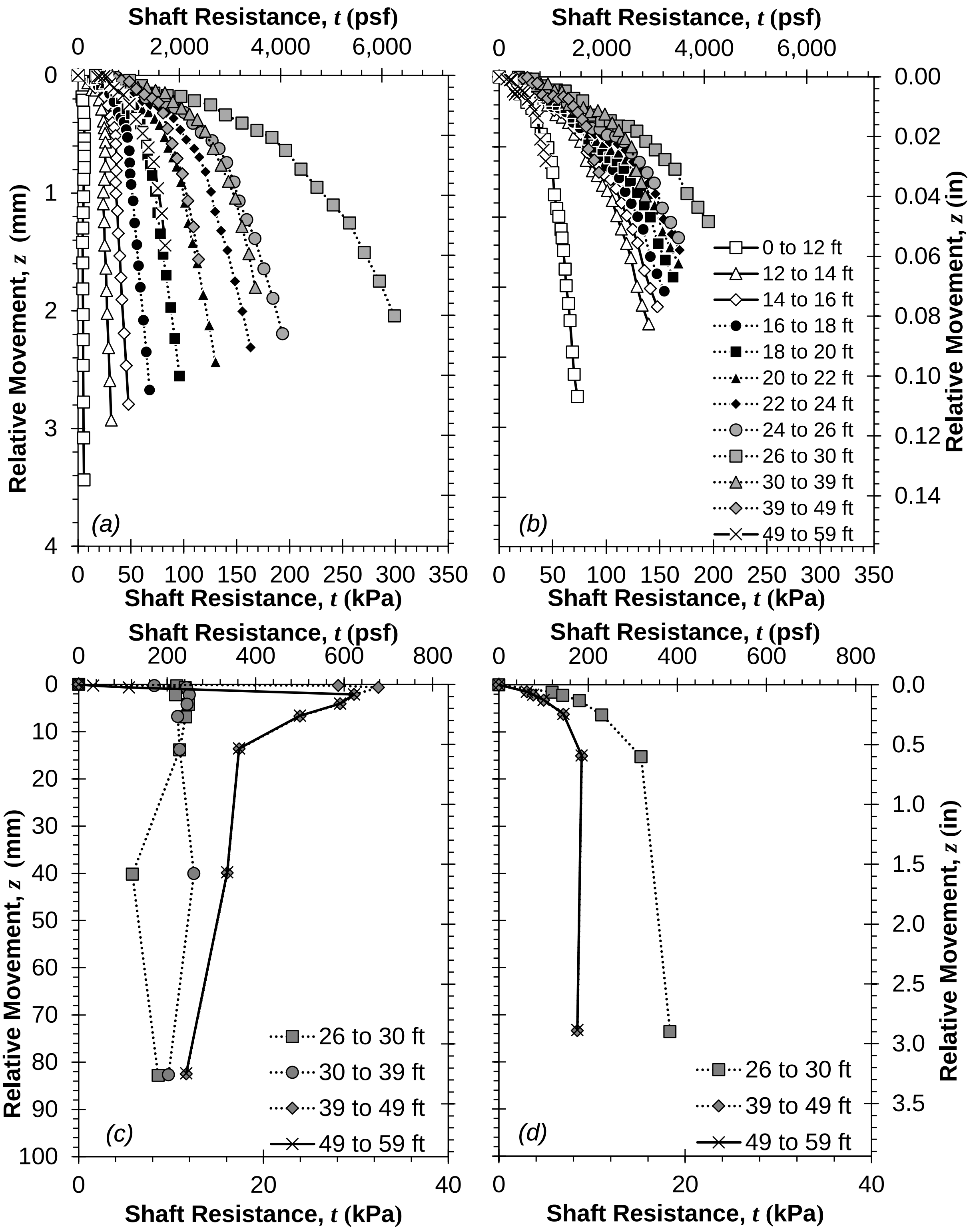

Figure 6.4: Measured *t-z* responses for (a) MIR, (b) HSIR, (c) CIR, and (d) CNIR at different depths.

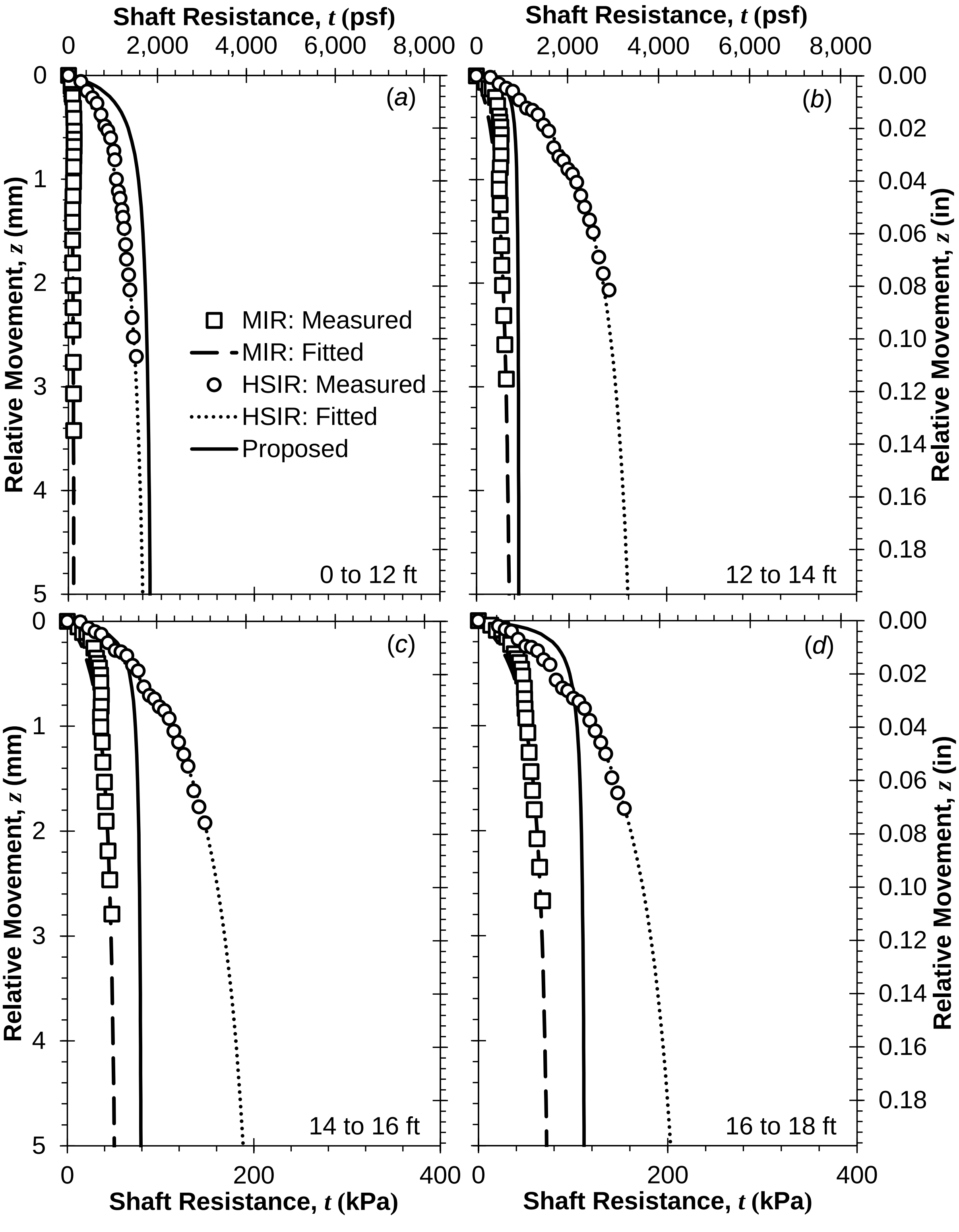

Figure 6.5: Measured, fitted, and proposed *t-z* responses at each tributary area for the two uncased test shafts for load increments from 0 to 5.5 m (0 to 18 ft).

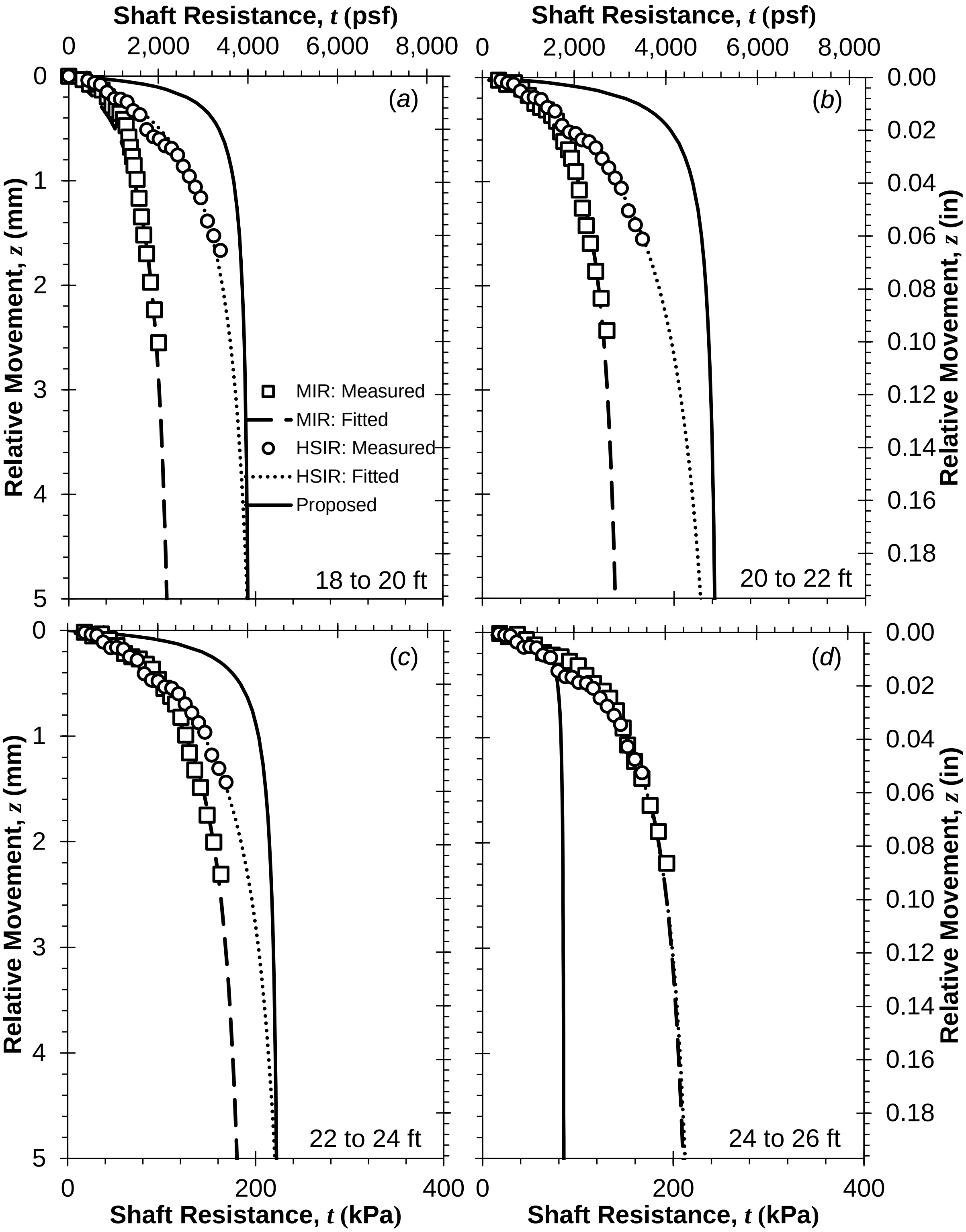

Figure 6.6: Measured, fitted, and proposed *t-z* responses at each tributary area for the two uncased test shafts for load increments from 5.5 to 7.9 m (18 to 26 ft).

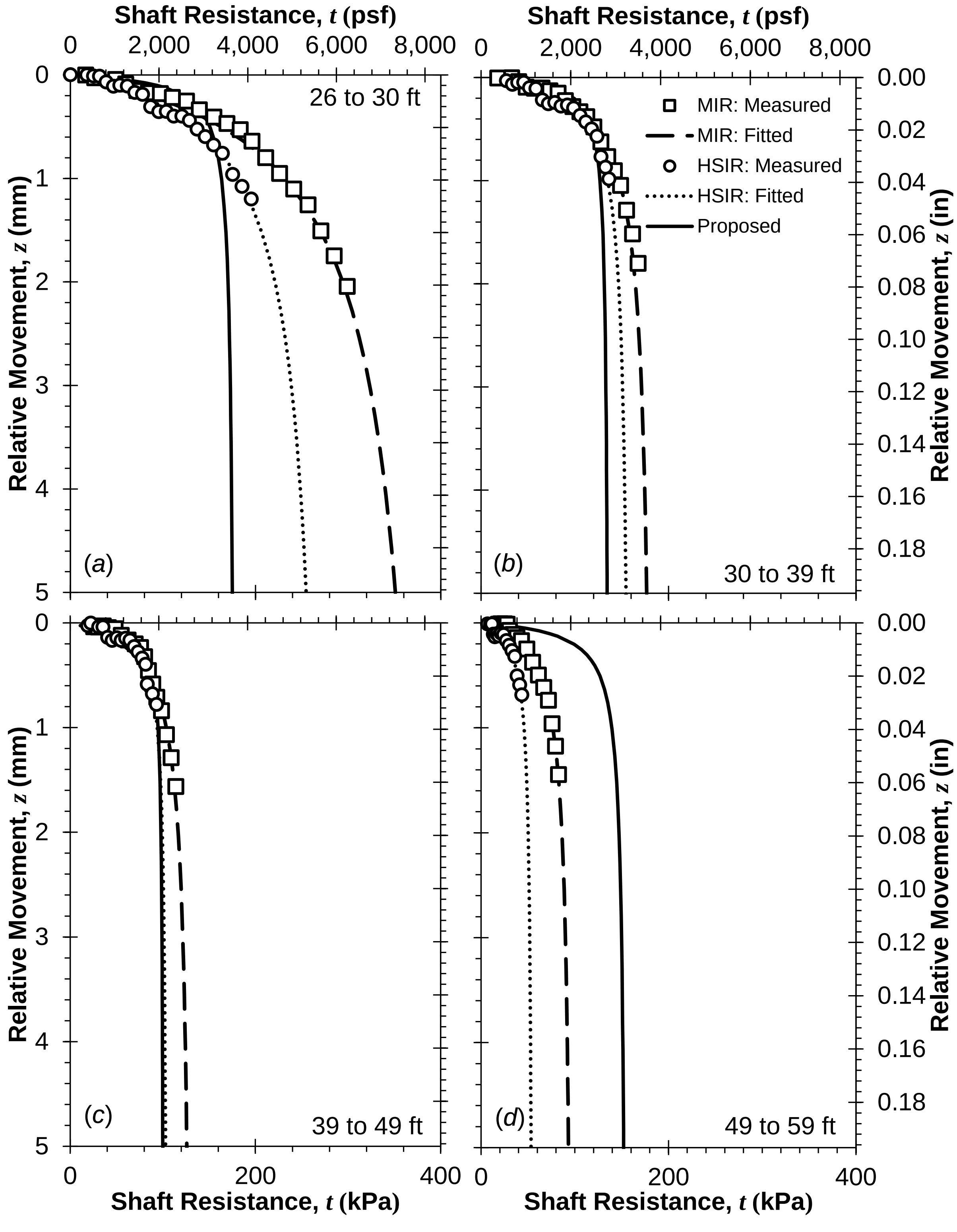

Figure 6.7: Measured, fitted, and proposed *t-z* responses at each tributary area for the two uncased test shafts for load increments from 7.9 to 18.0 m (26 to 59 ft).

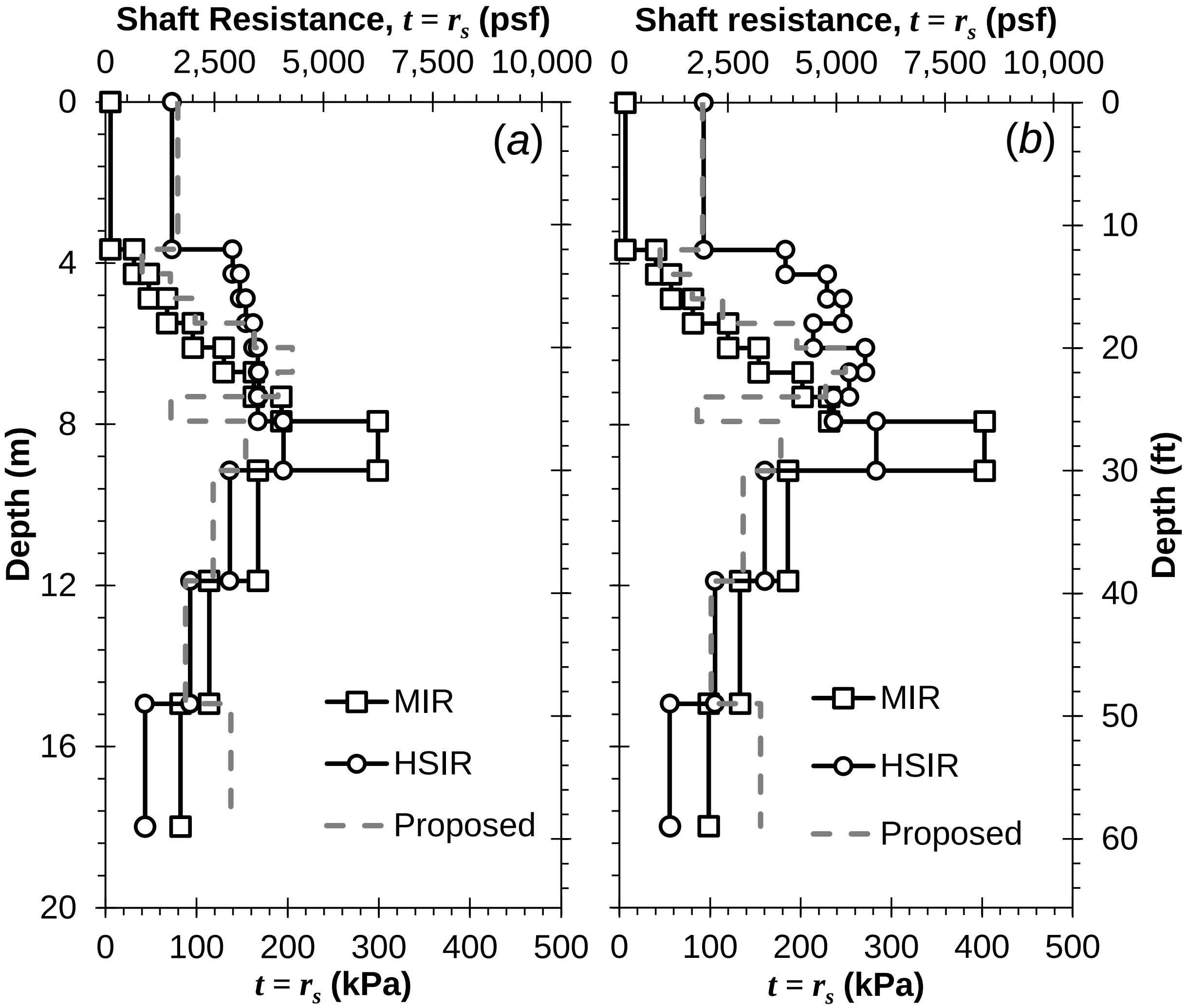

Figure 6.8: Shaft resistance profile of (a) measured peak shaft resistance, $r_{s,pm}$, and corresponding proposed model and (b) extrapolated ultimate shaft resistance, $r_{s,pult}$, and corresponding proposed model.

6.4 UNIT TOE RESISTANCE-TOE DISPLACEMENT RELATIONSHIPS (*Q-Z* CURVES)

The load-displacement curves in Figure 6.3 imply that the toe resistance of the uncased test shafts was not significantly mobilized during the loading tests. However, the cased test shafts did demonstrate an ultimate toe resistance was mobilized during the testing. Therefore, the unit toe resistance and toe displacement relationships (i.e., *q*-*z* curves) could be evaluated, as shown in Figure 6.9, and used to interpret the ultimate resistance of the uncased shafts. The toe resistance for the cased shafts essentially became fully-mobilized at displacements ranging from 20 to 40 mm (0.8 to 1.5 in), or about 2 to 4% of the shaft diameter. The measured peak unit toe resistance, $r_{t,m}$, for CIR and CNIR was 2,240 and 1,290 kPa (47 and 27 ksf), respectively (note, a model proposed to estimate the toe resistance in similar soils is also shown in Figure 6.9, and is described in detail in subsequent sections.

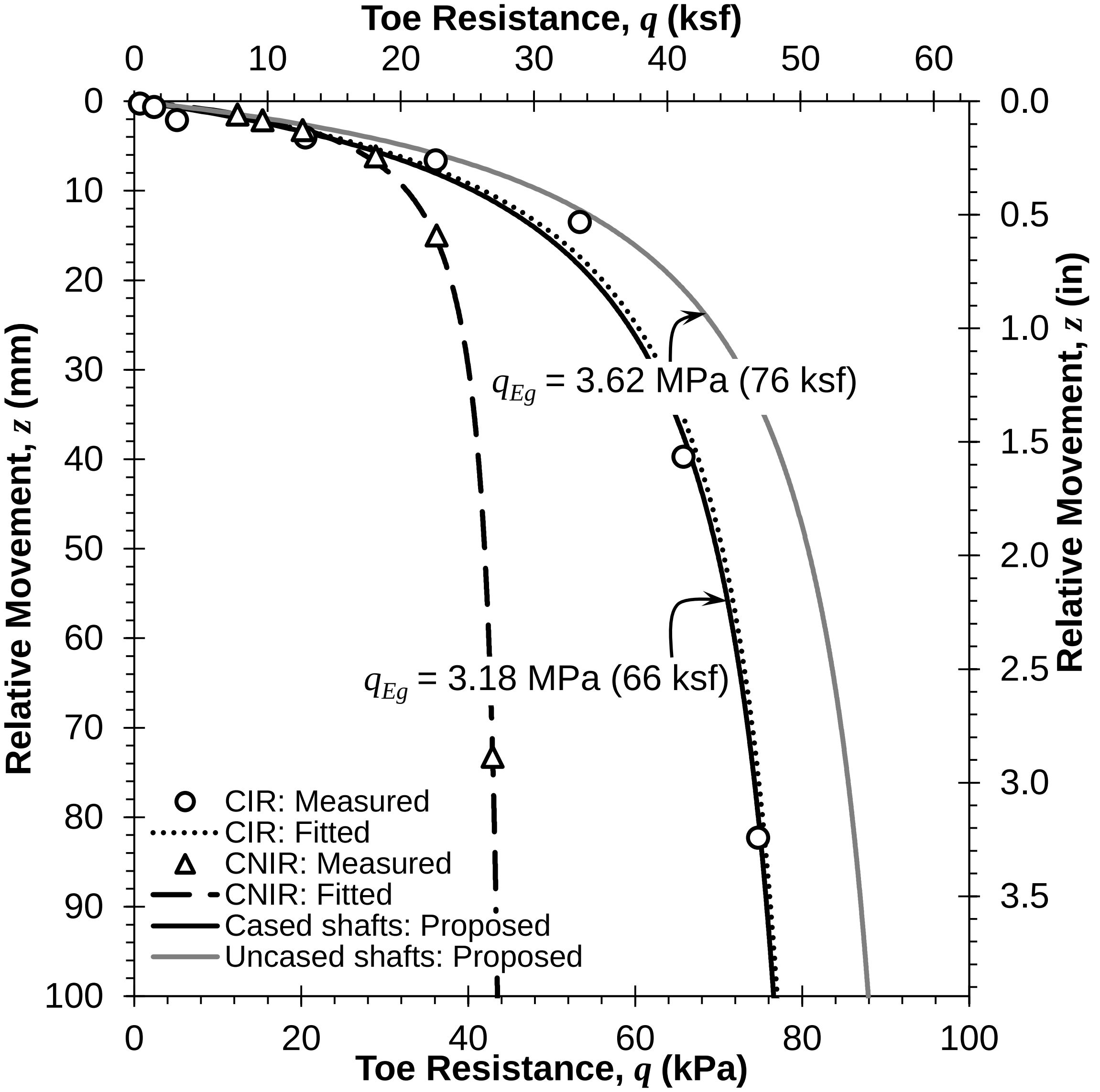

Figure 6.9: The measured, fitted, and proposed *q-z* responses for the test shafts.

The hyperbolic model was used to fit the *q*-*z* curves for CIR and CNIR to extrapolate the ultimate unit toe resistance, $r_{t,ult}$, for each shaft, which was 2,550 and 1,380 kPa (53 and 29 ksf), respectively. The difference between the *q*-*z* response of CIR and CNIR may be due to the differences in drilling protocols used to construct the two shafts. In general, an auger will bore a hole larger than the tool's outside diameter due to various factors such as flexure of the Kelly bar, misalignment of the drill string upon reentry into the hole, and inclination (causing a deviation in verticality) of the Kelly bar. Therefore, the use of an auger diameter equal to the outside diameter of the casing likely resulted in over-drilling or enlarging the diameter of shaft CNIR sufficiently to allow groundwater to flow between the casing and the borehole downward to the toe of the shaft, possibly resulting in a swelling and softening of the near-toe soils before the concrete cured.

6.5 PROPOSED AXIAL LOAD TRANSFER MODEL

To aid in the design of bridge foundations in the Willamette Valley, region-specific *t-z* and *q-z* curve models were developed for the uncased drilled shafts for use in similar soils. The hyperbolic model was selected as the appropriate functional form for the proposed load transfer models given its conservative and asymptotic nature. The hyperbolic model was implemented using direct SCPT measurements, specifically q_t, f_s, u_2, and V_s, from the test site. The proposed model was then used to simulate the axial load transfer for the uncased test shafts at large displacements.

6.5.1 Proposed *t-z* Curve Model

The hyperbolic model has been used to simulate the stress-strain and load transfer response for a variety of engineering applications (e.g., Kondner, 1963; Duncan and Chang, 1970; and Huffman et al., 2015) and has been used extensively for soil-structure interface analyses (e.g., Chin, 1970, 1971; Clemence and Brumund, 1975; Wong and Teh 1995; Kim et al., 1999; Cao et al., 2014; Stuedlein and Reddy, 2014; Li et al., 2017; and Li and Stuedlein, 2017). The hyperbolic model proposed by Clough and Duncan (1971) for soil-structure interfaces, adapted herein for constructing the *t-z* curves, is given by:

$$t = \frac{z}{\frac{1}{K_{t,si}} + \frac{z}{t_{ult}}} \tag{6.9}$$

where $K_{t,si}$ = initial stiffness of a given *t-z* curve and t_{ult}= asymptotic unit shaft resistance of the hyperbola. The asymptotic unit shaft resistance, t_{ult}, can be estimated from CPT measurements, as described below.

6.5.2 Evaluation of the Asymptotic Unit Shaft Resistance

Although the axial resistance of the uncased test shafts was not fully mobilized (Figure 6.2), the measured peak resistance can be considered representative of a lower-bound capacity (Eslami and Fellenius, 1997). Therefore, both the measured peak ($r_{s,m}$) and the extrapolated ultimate values ($r_{s,ult}$) of unit shaft resistance were correlated to the CPT data to construct separate region-specific models. The direct CPT method was initially developed by Eslami and Fellenius (1997) based on 102 axial loading tests of mostly driven pile foundations. Niazi (2014) extended the direct CPT method for all deep foundations using a combined database 153 driven, jacked and bored or augered piles. According to Eslami and Fellenius (1997), the unit shaft resistance, r_s, can be correlated to the effective cone resistance, $q_E = q_t - u_2$:

$$r_s = C_s \cdot q_E \tag{6.10}$$

where C_s = shaft coefficient that is estimated using the CPT-based soil classification chart proposed by Eslami and Fellenius (1997) or using the soil behavior type (SBT) classification index, I_c (Niazi, 2014):

$$\log\left(C_s\right) = 0.732 I_c - 3.681 \qquad (6.11)$$

where the SBT classification index I_c is calculated following the procedure by Robertson (2009).

Using this concept, a region-specific linear relationship between I_c and the log-transformed values of C_s was generated by back-calculating C_s for each tributary area of the uncased test shafts. To provide reasonable lower- and upper-bound estimations of unit shaft resistance, $r_{s,m}$ and $r_{s,ult}$ were used to back-calculate C_s, as shown in Figure 6.10. Since the experimental data from the ground surface to a depth of about 3.7 m (12 ft) was significantly affected by bending, these data were excluded in the development of the models. The shaft coefficient for soils with $2.00 \leq I_c \leq 2.67$ can be expressed as:

$$\log\left(C_{s,m}\right) = 0.98 I_c - 3.88 \quad \text{for } r_{s,m} \qquad (6.12)$$

$$\log\left(C_{s,ult}\right) = 0.93 I_c - 3.69 \quad \text{for } r_{s,ult} \qquad (6.13)$$

where $C_{s,m}$ and $C_{s,ult}$ = shaft coefficient back-calculated using measured peak and extrapolated ultimate values of unit shaft resistance, respectively. Therefore, according to Eq. (6.10), the lower- and upper-bound unit shaft resistances, $r_{s,pm}$ and $r_{s,pult}$, respectively, proposed for use in similar Willamette Valley soils can be estimated using:

$$r_{s,pm} = C_{s,m} \cdot q_E \qquad (6.14)$$

$$r_{s,pult} = C_{s,ult} \cdot q_E \qquad (6.15)$$

The profile of the proposed unit shaft resistances, $r_{s,pm}$ and $r_{s,pult}$, is shown in Figure 6.8a and Figure 6.8b, respectively. The mean bias ($r_{s,m}/r_{s,pm}$) for the proposed lower-bound model is 1.28 and the coefficient of variation (COV) of the sample bias is 62%, whereas the mean bias ($r_{s,ult}/r_{s,pult}$) and the COV are 1.33 and 70%, respectively, for the proposed upper-bound model. These performance statistics indicate that the proposed models under-predict the unit shaft resistances, on average, and exhibit a high degree of variability. Both $r_{s,pm}$ and $r_{s,pult}$ can be used as the asymptotic unit shaft resistance t_{ult} in Eq. (6.9) to estimate axial load transfer. However, $r_{s,pult}$ is used subsequently to extrapolate the global axial response of the uncased test shafts at larger displacements.

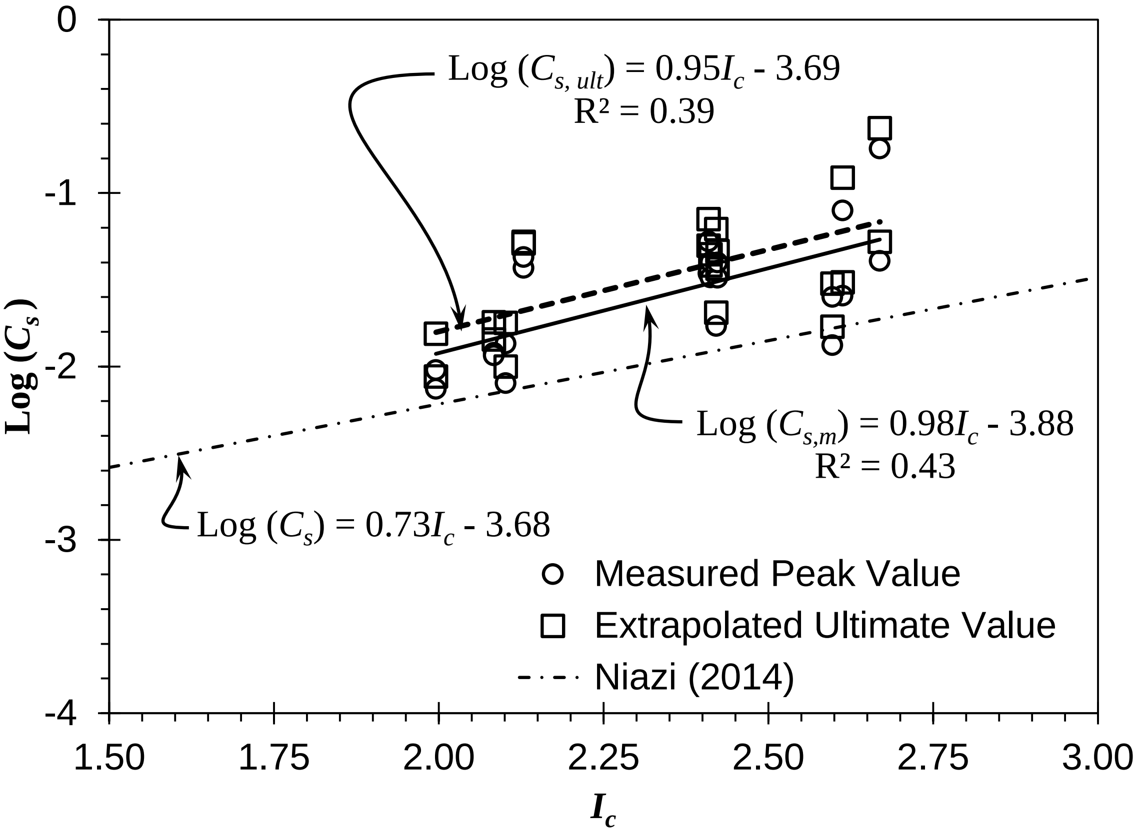

Figure 6.10: Relationship between the SBT classification index I_c and the shaft correlation coefficient $C_{s,m}$ and $C_{s,ult}$ back-calculated using the measured peak and extrapolated ultimate values, respectively.

6.5.3 Evaluation of the Initial t-z Stiffness

The initial stiffness, $K_{t,si}$, of a given *t-z* curve can be estimated using the analytical solution developed by Randolph and Wroth (1978) for axially-loaded deep foundations in linear elastic soil, which is given by:

$$K_{t,si} = \frac{\xi \cdot G_s}{r} \tag{6.16}$$

where G_s = shear modulus of the soil, r = radius of the shaft, and ξ = a function related to the geometry of the deep foundation and to the decay of shear strains away from the shaft interface:

$$\xi = \ln\left(\frac{r_m}{r}\right) \tag{6.17}$$

where r_m = radial distance from the center of the foundation at which shear stresses in the soil become negligible. Although Randolph and Wroth (1978) did not specify the type of shear modulus, G_s, to be used, the maximum shear modulus, G_{max}, is recommended for use herein. Given the general availability of these measurements at bridge sites in the seismically-active Oregon region, G_{max} can be evaluated using shear wave velocity measurements, V_s, and soil density, ρ:

$$G_{\max} = \rho \cdot V_s^2 \tag{6.18}$$

The radial distance, r_m, can be estimated by (Randolph and Wroth, 1978):

$$r_m = 2.5L \cdot \eta \cdot (1 - \nu_{avg}) \tag{6.19}$$

where ν = Poisson's ratio of the soil around the deep foundation, L = length of the deep foundation, and η = inhomogeneity factor:

$$\eta = \frac{G_{\max}(0.5\mathrm{L})}{G_{\max}(L)} \tag{6.20}$$

where $G_{max}(0.5L)$ and $G_{max}(L)$ = maximum shear modulus of the soil at the foundation mid-depth and at the base, respectively. For layered soils, the radial distance $r_m(i)$ at soil layer i can be estimated by (Lee, 1991; and Zhang et al., 2010):

$$r_m(i) = 2.5L \cdot \eta(i) \cdot \left[1 - \nu(i)\right] \tag{6.21}$$

where $\nu(i)$ = Poisson's ratio of the soil around the foundation and $\eta(i)$ = inhomogeneity factor at soil layer i. It was assumed that the $\nu(i)$ was equal to 0.2 for predominantly sandy soils with drained conditions and to 0.5 for predominantly clayey soils with undrained conditions, as suggested by Niazi (2014). The inhomogeneity factor, $\eta(i)$, can be estimated by (Lee, 1991; and Zhang et al. 2010):

$$\eta_i = \frac{G_{\max}(i) \cdot L(i)}{G_{\max}(\max) \cdot L} \tag{6.22}$$

where $G_{max}(max)$ = the largest maximum shear modulus among the soil layers along the length of the deep foundation, $G_{max}(i)$ = maximum shear modulus of soil layer i, and $L(i)$ = length of the deep foundation in layer i.

Table 6.1 summarizes the soil parameters used to model the uncased test shafts as developed from SCPT-3, as well as the hyperbolic parameters $t_{ult} = r_{s,pult}$ and $K_{t,si}$ for each tributary area. Figure 6.5 through Figure 6.7 compare the measured *t-z* curves to those predicted using the proposed CPT-and shear wave velocity-based hyperbolic model. Discrepancies between the proposed and measured *t-z* curves are due to the differences observed between the proposed unit shaft resistance model and the extrapolated ultimate shaft resistance (Figure 6.8b) and due to the discrepancy between the actual and estimated initial stiffness.

6.5.4 Proposed *q-z* Curve Model

Based on the observed *q-z* response of the cased shafts, a hyperbolic *q-z* curve was used to model the response of the toe resistance. To estimate the response of the uncased shafts at large displacements, the observed toe response of shaft CIR was the most appropriate and representative of actual conditions. The hyperbolic *q-z* curve can be expressed as:

$$q = \frac{z}{\frac{1}{K_{q,si}} + \frac{z}{q_{ult}}} \tag{6.23}$$

where $K_{q,si}$ = initial stiffness of the q-z curve, and q_{ult} = asymptotic unit toe resistance that can be computed directly from CPT measurements.

6.5.5 Evaluation of the Ultimate Unit Toe Resistance

Eslami and Fellenius (1997) suggested that the unit toe resistance, r_t, could be estimated by:

$$r_t = C_t \cdot q_{Eg} \tag{6.24}$$

where C_t = toe correlation coefficient and q_{Eg} = geometric average of the effective cone tip resistance over the influence zone around the toe. Eslami and Fellenius (1997) defined the influence zone as from a depth of 4*D* (where *D* = diameter of the deep foundation) below the toe of the deep foundation up to a depth of 8*D* above the toe when the foundation is installed through a weak soil into a dense soil and up to a depth of 2*D* above the toe when the foundation is installed through a dense soil into a weak soil. Fellenius (2017) suggested that the toe correlation coefficient C_t is equal to unity for foundation diameters smaller than 0.4 m (16 in) and equal to 1/(3*D*) for diameters equal to or greater than 0.4 m, where *D* is in meters (or 12/*D* when D is measured in inches). Niazi (2014) proposed a linear relationship between the geometric average of the SBT classification index, I_{cg}, in the influence zone and log-transformed values of C_t, when $1.69 \le I_{cg} \le 3.77$, as given by:

$$\log\left(C_t\right) = 0.325 I_{cg} - 1.218 \tag{6.25}$$

Equation (6.25) does not account for the larger displacements required to mobilize larger diameter piles and shafts, which may need to be adjusted for scale effects at the toe.

Table 6.1: Soil Properties and *t-z* Model Parameters for the Uncased Test Shafts Based on SCPT-3.

Depth, m (ft)	I_c	q_E kPa (ksf)	$t_{ult} = r_{s,pult}$ kPa (psf)	ρ kg/m^3 (lb/ft^3)	V_s m/s (ft/s)	G_{max} MPa (ksf)	$K_{t,si}$ kPa/mm (ksf/in)
0 to 3.7 (0 to 12)	2.40	4839 (101)	92 (1915)	1987 (124)	180 (591)	65 (1349)	421 (223)
3.7 to 4.3 (12 to 14)	2.67	772 (16)	45 (941)	1722 (108)	260 (852)	116 (2427)	737 (391)
4.3 to 4.9 (14 to 16)	2.61	1863 (39)	81 (1683)	1893 (118)	260 (852)	128 (2669)	778 (413)
4.9 to 5.5 (16 to 18)	2.42	3964 (83)	114 (2374)	1991 (124)	325 (1065)	210 (4383)	1243 (659)
2.5 to 6.1 (18 to 20)	2.10	11984 (250)	196 (4088)	2175 (136)	341 (1119)	253 (5284)	1764 (936)
6.1 to 6.7 (20 to 22)	2.00	17535 (366)	249 (5203)	2184 (136)	341 (1119)	254 (5306)	1835 (973)
6.7 to 7.3 (22 to 24)	2.08	14079 (294)	227 (4751)	2169 (135)	345 (1130)	257 (5376)	1888 (1002)
7.3 to 7.9 (24 to 26)	2.13	4521 (94)	86 (1795)	2093 (131)	348 (1140)	253 (5286)	1877 (996)
7.9 to 9.1 (26 to 30)	2.41	5684 (119)	178 (3718)	2145 (134)	348 (1140)	259 (5417)	1941 (1030)
9.1 to 11.9 (30 to 39)	2.41	4190 (88)	137 (2852)	2097 (131)	333 (1091)	232 (4850)	1789 (949)
11.9 to 14.9 (39 to 49)	2.42	2867 (60)	101 (2117)	2034 (127)	302 (989)	185 (3861)	1476 (783)
14.9 to 18.0 (49 to 59)	2.60	3278 (68)	156 (3250)	2044 (128)	302 (989)	186 (3879)	1350 (716)

Since these shafts were not intended to bear on any particular soil layer, the cone tip resistance of the closest CPT (SCPT-2 in Figure 4.8) was used to back-calculate C_t , where the zone of influence was defined as the distance of 4*D* above and below the shaft tip. The corresponding back-calculated lower- and upper-bound toe coefficients for CIR are $C_{t,m} = 0.70$ and $C_{t,ult} = 0.80$ for the measured peak, $r_{t,m}$, and extrapolated ultimate, $r_{t,m}$, toe resistance, respectively, with $I_{cg} = 2.66$ and $q_{Eg} = 3{,}180$ kPa (66 ksf). These toe correlation coefficients may be used to construct the lower- and upper-bound estimates of unit toe resistance using Eq. (6.24) and CPT measurements, as well as the *q-z* curve given by Eq. (6.23). Given the similarity between I_{cg} for the various CPTs at the toe elevation of the test shafts, $C_{t,ult}$ was approximately equal to 0.80, which was used to evaluate the axial load response for the uncased test shafts at large displacements.

6.5.6 Evaluation of the Initial Stiffness

The initial stiffness of a *q-z* curve, $K_{q,si}$, can be estimated assuming that the toe of a deep foundation acts as a rigid punch being forced into an elastic half-space (Randolph and Wroth, 1978; and Guo, 2000), resulting in:

$$K_{q,si} = \frac{4G_{sg}}{\pi r \cdot (1-\nu_{sg}) \cdot \omega} \tag{6.26}$$

where G_{sg} and ν_{sg} = geometric average of the shear modulus and Poisson's ratio of the soil over the influence zone around the toe, respectively, and ω = base load transfer factor. The use of the maximum shear modulus, $G_{max,g}$, is recommended in Eq. (6.26), where $G_{sg} = G_{max,g}$. Guo and Randolph (1998) suggested that $\omega = 1.0$; however, the back-calculated ω was approximately equal to 4.0 (from CIR), which can be attributed to the possible softening effects caused by drilling to compensate the use of G_{maxg}, which was measured without disturbance caused by construction. The *q-z* curves computed using Eq. (6.26) are shown in Figure 6.9. The CPT measurements and model parameters q_{ult} and $K_{q,si}$ are provided in Table 6.2.

Table 6.2: Soil Properties and *q-z* Model Parameters the Test Shafts.

Test Shafts	I_{cg}	q_{Eg}, kPa (ksf)	$q_{ult} = r_{t,pult}$, kPa (psf)	ρ_g, kg/m^3 (lb/ft^3)	V_{sg}, m/s (ft/s)	G_{maxg}, MPa (ksf)	$K_{q,si}$ kPa/mm (ksf/in)
Cased Shafts	2.66	3,180 (66)	2,550 (53)	2,040 (128)	290 (953)	170 (3607)	230 (124)
Uncased Shafts	2.66	3,620 (76)	2,900 (61)	2,060 (128)	330 (1068)	220 (4558)	295 (156)

Note: ρ_g, V_{sg} = geometric average soil density and shear velocity, respectively, in the influence zone.

6.6 PREDICTION OF AXIAL LOAD RESPONSE OF THE UNCASED TEST SHAFTS

Using the commercially available software package TZPile (Reese et al. 2014) and the as-built diameter computed from TIP measurements (see Section 5.4), the fitted and proposed *t-z* curves were used to simulate and compare the axial response of shafts MIR and HSIR at large displacements. The proposed *t-z* curves were developed based on the extrapolated ultimate shaft resistance (Figure 6.8b). Since no *q-z* curves were developed directly from the uncased shafts, the proposed *q-z* curves (Figure 6.9) were used to model the toe resistance.

To evaluate the performance of the proposed axial load transfer models, the proposed *t-z* and *q-z* curves were used to calculate the axial response of MIR and HSIR, shown in Figure 6.11 and Figure 6.12. The simulated global axial load-displacement responses for HSIR and MIR at the shaft head are shown in Figure 6.11. Excellent agreement between the test data and the responses extrapolated using the fitted *t-z* curves is observed in Figure 6.11. The axial resistance for the uncased test shafts at a displacement of 25 mm (1.0 in) would be approximately equal to 7,650 and 8,810 kN (1,720 and 1,980 kips) for MIR and HSIR, respectively, when using *t-z* curves fitted to the observed load transfer characteristics (i.e., "extrapolated"). The load transfer distribution at select head displacements are shown in Figure 6.12, where good agreement with the test data can be observed.

The differences in the axial response between HSIR and MIR in Figure 6.11 and Figure 6.12 are largely due to the variation in the shaft diameter and the resulting composite secant modulus. The deviation between the axial load profiles determined using the proposed model and the profiles determined using the measurements could be attributed to the over- and under-estimation of the *t-z* response for the tributary areas. The proposed *t-z* and *q-z* models sufficiently approximate the test data, with apparent offsetting of error at various depths (see Figure 6.5 through Figure 6.7). At a displacement of 25 mm (1.0 in) and using the proposed model, the predicted axial resistances for the uncased shafts are equal to approximately 8,830 and 8,670 kN (1,985 and 1,950 kips) for MIR and HSIR, respectively.

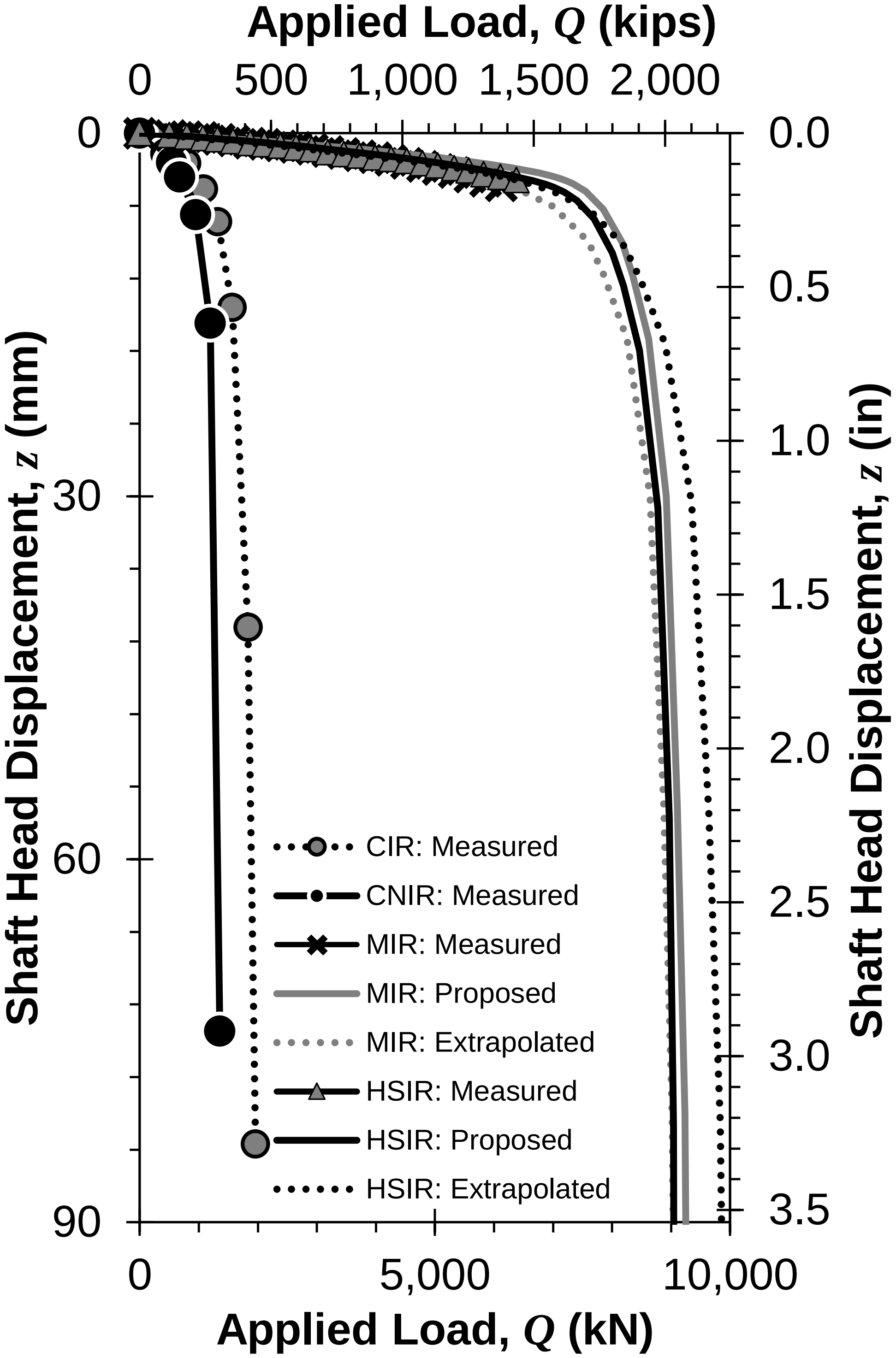

Figure 6.11: Comparison of the proposed and extrapolated global axial load-displacement relationship using proposed and fitted *t-z* curves, respectively, and the measured responses of all test shafts. Note, the proposed *q-z* curves were used in both proposed and extrapolated responses.

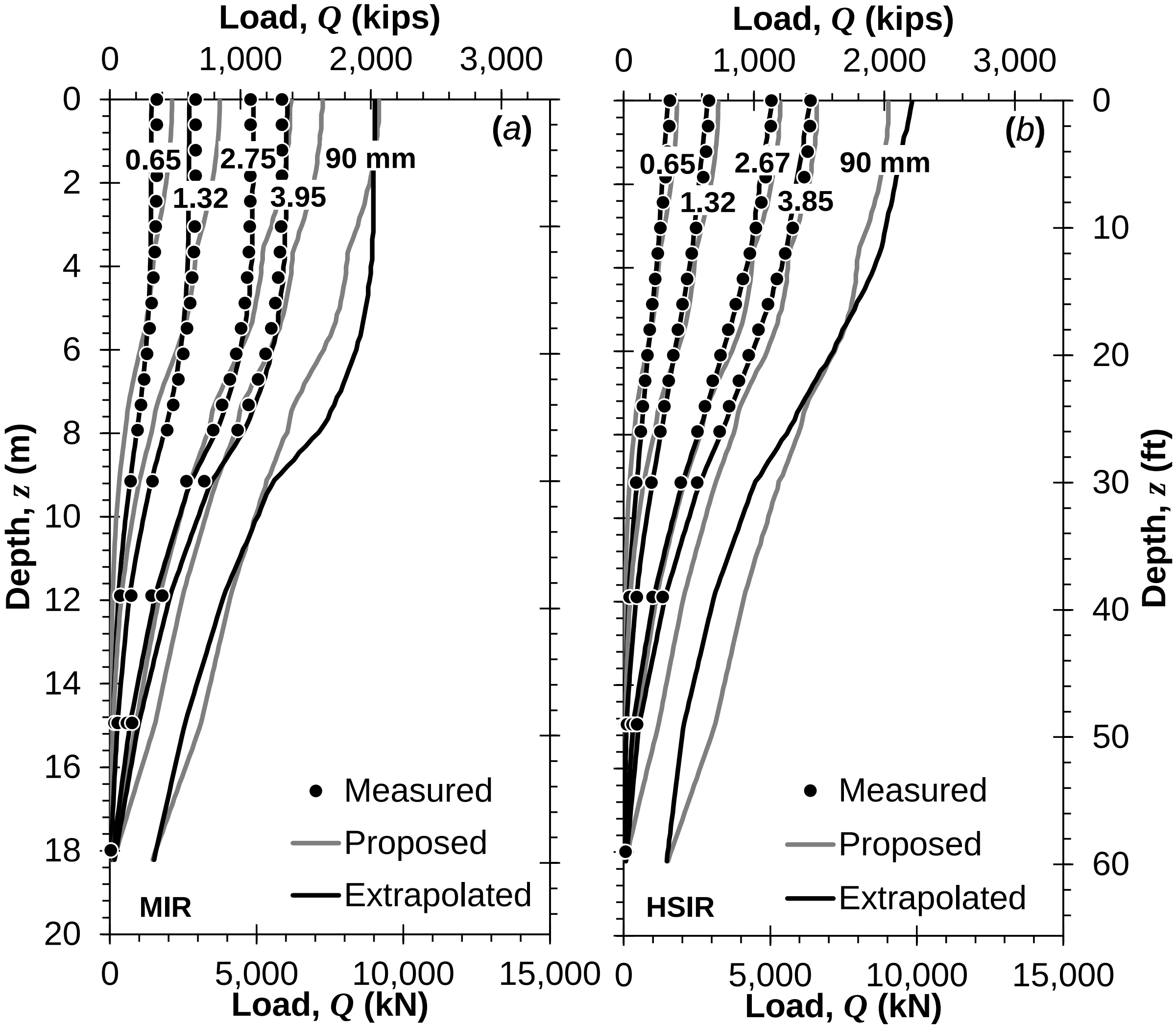

Figure 6.12: Comparison of the proposed and extrapolated axial load profile using proposed and fitted *t-z* curves, respectively, with the measured data of (a) MIR and (b) HSIR. Note, the proposed *q-z* curves were used in both proposed and extrapolated responses.

6.7 EVALUATION OF FHWA METHOD (O'NEILL AND REESE 1999)

The load-displacement response at the head of the drilled shaft can also be estimated using normalized load transfer relations presented by O'Neill and Reese (1999), which is referred as FHWA method herein. Figure 6.13 shows the normalized shaft and toe load transfer for drilled shafts in plastic and granular soils

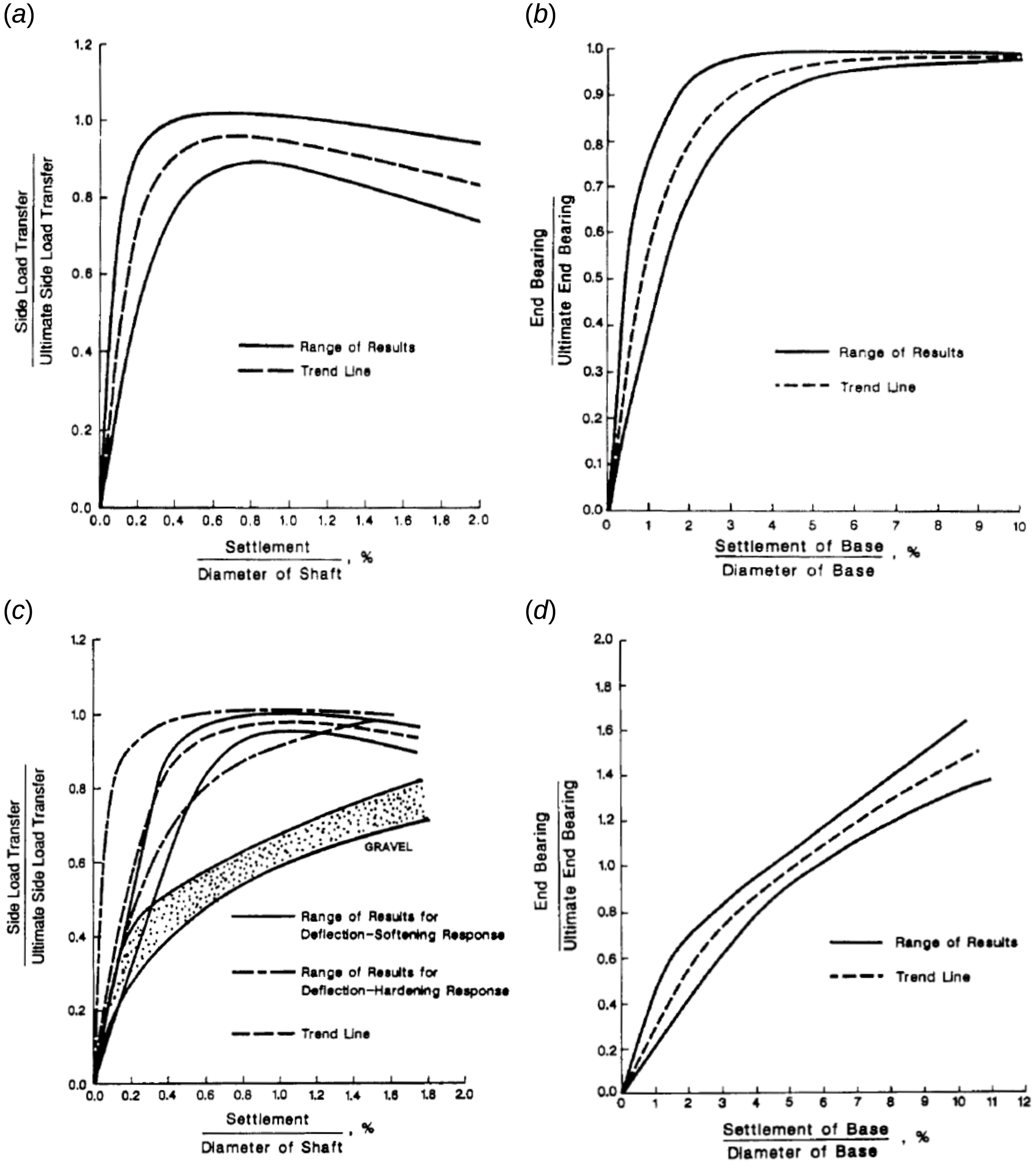

Figure 6.13: Normalized load transfer for drilled shaft for (a) shaft resistance and (b) base resistance in plastic soil, and (c) shaft resistance and (d) base resistance in granular soil (O'Neill and Reese 1999)

Table 6.3 and Table 6.4 summarize the soil and drilled shaft properties for the uncased and cased test shafts, respectively. The average shaft diameter of uncased shafts for each soil layer was estimated based on Figure 5.11. The effective unit weight, *γ'*, of each soil layer was obtained based on the laboratory results described by Dickenson and Haines. (2006) and Nimityongskul

(2010). The undrained shear strength, s_u, for the plastic soil layers was correlated to CPT cone-tip resistance, q_c, (Figure 4.8) using (e.g., Kulhawy and Mayne 1990):

$$s_u = \frac{q_c - \sigma_{vo}}{N_k} \tag{6.27}$$

where σ_{vo} = total overburden stress and N_k = cone factor. The N_k, which varies from 15 when the groundwater table is at its highest (e.g., 0.6 m or 2 ft) in the spring and about 23 when the groundwater table is at its lowest (e.g., 2.5 m or 8 ft), generally in the fall, based on s_u back-calculated from footing loading and consolidated undrained triaxial tests (Martin 2018). The friction angle, ϕ', of the granular soil layers was estimated using correlations to CPT cone-tip resistance (Kulhawy and Mayne 1990). Explorations SCPT-2, SCPT-3, CPT-4, and SCPT-5 were used to estimate the necessary soil parameters.

The shaft resistance was estimated using α and β method for plastic, fine-grained and granular soil, respectively. The unit shaft resistance, r_s, in plastic soil can be estimated by (O'Neill and Reese 1999; and Brown et al. 2010):

$$r_s = \alpha \cdot s_u \tag{6.28}$$

where α = adhesion factor, which is a function of the average s_u for the stratum of interest:

$$\alpha = 0.55 \text{ for } \frac{s_u}{P_a} \le 1.5 \tag{6.29a}$$

$$\alpha = 0.55 - 0.1\left(\frac{s_u}{P_a} - 1.5\right) \text{ for } 1.5 \le \frac{s_u}{P_a} \le 2.5 \tag{6.29b}$$

$$\alpha = 0.45 \text{ for } \frac{s_u}{P_a} > 2.5 \tag{6.29c}$$

where P_a = atmospheric pressure. The unit shaft resistance, r_s, in granular soil was estimated using:

$$r_s = \beta \cdot \sigma'_{v0} \tag{6.30}$$

where and σ'_{v0} = vertical effective stress at the mid-point of the layer of interest and β = shaft resistance coefficient. The β-coefficient was determined using the method recommend by Brown et al. (2010):

$$\beta = (1 - \sin\phi') \cdot \mathrm{OCR}^{\sin\phi'} \tan\phi' \le K_p \tan\phi' \tag{6.31}$$

where OCR = overconsolidation ratio, computed using an empirical estimate of the normalized vertical effective preconsolidation stress, σ'_p :

$$\frac{\sigma'_p}{P_a} = 0.47 \cdot \left(N_{60}\right)^m \tag{6.32}$$

where N_{60} = energy-corrected SPT blow count. The coefficients α and β for different soil layers are summarized in Table 6.3 and Table 6.4. The reduction factor of 0.5 and 0.6 were used for cased shafts in granular and plastic soil, respectively, with the lower bound as recommend by Brown et al. (2010). Since the toe of each test shaft was in plastic soil, the unit toe resistance was estimated by (Brown et al. 2010):

$$r_t = N_c \cdot s_u \tag{6.33}$$

where N_c = bearing capacity factor, which was assumed to be 9.0 with $s_u > 95$ kN (2000 psf). Table 6.3 and Table 6.4 summarize the estimated shaft, R_s, and toe resistance, R_t. The estimated applied load was calculated by:

$$Q = R_{ult} - W = R_s + R_t - W \tag{6.34}$$

where R_{ult} = ultimate axial resistance and W = shaft weight.

Table 6.3: Soil and Drilled Shaft Properties for the Uncased Test Shafts and the Calculation of the Axial Resistance.

Depth m (ft)	Soil Type	MIR D, m (in)	HSIR	γ' kN/m^3(pcf)	s_u kPa (psf)	ϕ' deg	a or β or N_c	MIR R_s, kN (kip)	HSIR
0 to 1.9 (0 to 6.3)	Silty CLAY to Clayey SILT	1.04 (41.1)	1.02 (40.2)	18.1 (115)	110 (2,275)	-	$a = 0.55$	79 (18)	78 (17)
1.9 to 3.4 (6.3 to 11.0)	Silty CLAY to Clayey SILT	1.07 (42.3)	1.03 (40.7)	8.3 (52.6)	65 (1,315)	-	$a = 0.55$	181 (41)	174 (39)
3.4 to 3.7 (11.0 to 12.0)	SAND	1.06 (41.6)	1.05 (41.2)	10.6 (67.6)	-	39	$\beta = 1.86$	89 (20)	88 (20)
3.7 to 5.0 (12.0 to 16.5)	Silty CLAY to Clayey SILT	1.10 (43.4)	1.08 (42.4)	8.3 (52.6)	60 (1,225)	-	$a = 0.55$	149 (33)	145 (33)
5.0 to 12.2 (16.5 to 40)	Silty SAND	1.07 (42.1)	1.02 (40.3)	10.6 (67.6)	-	38	$\beta = 1.26$	3,021 (679)	2,892 (650)
12.2 to 18.3 (40.0 to 60.0)	Silty CLAY to Clayey SILT	0.98 (38.5)	0.96 (37.9)	7.5 (47.6)	290 (5,990)	-	$a = 0.42$	2,283 (513)	2,247 (505)
Toe	Silty CLAY to Clayey SILT	0.98 (38.5)	0.96 (37.9)	7.5 (47.6)	290 (5,990)	-		1,960 (441)	1900 (427)
R_{ult}								7762 (1,745)	7524 (1,691)

Table 6.4: Soil and Drilled Shaft Properties for the Cased Test Shafts and the Calculation of the Axial Resistance.

Depth, m (ft)	Soil Model	D, m (in)	γ' kN/m3 (pcf)	s_u kPa (psf)	ϕ' deg	a or β or N_c	R_s kN (kip)
0 to2.0 (0 to 6.6)	Silty CLAY to Clayey SILT	0.94 (37)	18.1 (115)	85 (1,800)	-	$a = 0.55$	34 (8)
0 to 3.5 (6.6 to 11.5)	Silty CLAY to Clayey SILT	0.94 (37)	8.3 (52.6)	75 (1515)	-	$a = 0.55$	91 (20)
3.5 to 3.8 (11.5 to 12.5)	SAND	0.94 (37)	10.6 (67.6)	-	40	$\beta = 1.98$	54 (12)
3.8 to 5.5 (12.5 to 18.0)	Silty CLAY to Clayey SILT	0.94 (37)	8.3 (52.6)	70 (1,420)	-	$a = 0.55$	95 (21)
5.5 to 18.3 (18.0 to 40)	Silty SAND	0.94 (37)	10.6 (67.6)	-	39	$\beta = 1.39$	1674 (376)
12.2 to 18.3 (40.0 to 60.0)	Silty CLAY to Clayey SILT	0.94 (37)	7.5 (47.6)	285 (5,930)	-	$a = 0.42$	1075 (242)
Toe	Silty CLAY to Clayey SILT	0.94 (37)	7.5 (47.6)	285 (5,930)	-	$N_p = 9$	1779 (400)
R_{ult}							4801 (1,079)

The trend lines for the mobilization of shaft and toe resistance shown in Figure 6.13 were used to evaluate the axial response of each shaft. Since the cased shafts have the same diameter, the axial response for each cased shaft is the same. Figure 6.14 compares the measured and estimated load-displacement response at the head of the drilled shafts. The difference between MIR and HSIR in the estimated response is due to the variation in diameter between the two shafts. To facilitate the evaluation of the FHWA method, the bias in axial load (i.e., the ratio of the observed and computed load at the shaft head) at each displacement was calculated for displacements smaller than or equal to a diameter-normalized displacement of 2% (See Figure 6.13) which is summarized in Table 6.5.

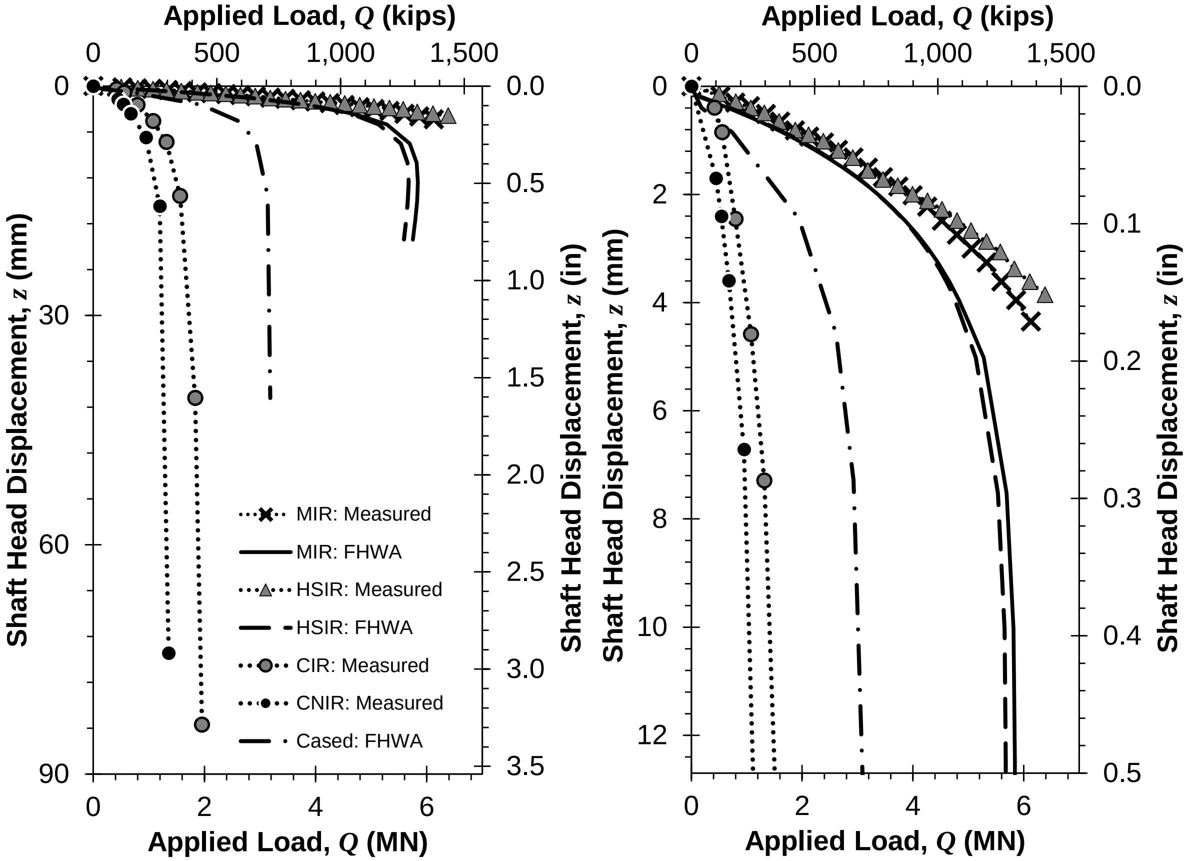

Figure 6.14: Comparison of the predicted global axial load-displacement relationship using FHWA method, and the measured responses of all test shafts for at (a) large range of scale and (b) for the initial response with displacement up to 12.7 mm (0.5 in).

It appears that the FHWA method under-predicts the axial load for the uncased shafts and over-predicts that the axial load for the cased shafts. The FHWA method was developed in consideration of numerous tests on uncased production shafts, which were likely tested shortly (within several weeks) following construction. Owing to the short soil “recovery” period near the soil-shaft interface, the observed shaft resistance was likely smaller than a long-term shaft resistance. The lower-bound casing reduction factor of 0.5 and 0.6 for cased shafts in granular and plastic soil, respectively, appears unconservative; this is explored in greater detail below.

The effect of casing reduction factors is addressed subsequently. The FHWA Method suggested that fully-mobilized resistance for MIR and HSIR was equal to approximately of 5,800 and 5,600 kN (1,300 and 1,250 kip), respectively. However, MIR and HSIR were not full-mobilized with the maximum load of 6,125 and 6,380 kN (1,377 and 1,435 kip), respectively, as measured during the loading tests.

Table 6.5: Comparison of the measured axial load-displacement responses of the test shafts to the calculated responses using FHWA method for diameter-normalized displacement less than or equal to 2%.

Test Shaft	Maximum *z* considered mm (in)	FHWA	
		Mean Bias	COV (%)
MIR	0 to 4 (0 to 0.17)	1.27	16%
HSIR	0 to 4 (0 to 0.15)	1.28	13%
CIR	0 to 14 (0 to 0.57)	0.81	94%
CNIR	0 to 16 (0 to 0.62)	0.31	13%

6.8 EFFECT OF PERMANENT CASING ON AXIAL LOAD RESPONSE

The effect of permanent casing on axial load transfer is compared in Figure 6.15 using the *t-z* curves for different tributary areas for the cased and uncased shafts. The uncased shafts exhibited significantly larger unit shaft resistances than did the cased shafts. The differences, which were more pronounced at shallower depths, were attributed to the enhanced load transfer characteristics at the soil-concrete interface. The comparison between the fitted ultimate unit shaft resistance for the uncased test shafts and the measured resistance for the cased shafts is at relative soil-shaft movements of 2 and 12.5 mm are summarized in Table 6.6 using the shaft resistance ratio, defined as the ratio of unit shaft resistance for the cased shafts and that of the uncased shafts at given relative soil-shaft movements. Since the shaft resistance ratio depends on the specific installation procedure, it assigned the variable of $R_{d\text{-}vc,d}$ to represent construction sequence in the ratio: ratio of a shaft that was drilled and casing vibro-installed, to that of a drilled, uncased shaft. At small relative soil-shaft movements, CIR exhibited $R_{d\text{-}vc,d}$ ranging from 4 to 44%, and then decreased as the interface softened to produce $R_{d\text{-}vc,d}$ ranging from 3 to 23% at 12.5 mm. Shaft CNIR exhibited hardening, but with substantially smaller $R_{d\text{-}vc,d}$ given the use of the slightly larger auger, with $R_{d\text{-}vc,d}$ ranging from 3 to 5% and 4 to 11% for relative movements of 2 and 12.5 mm, respectively. The subtle difference in auger diameter (0.91 vs. 0.94 m, or 36 vs. 37 in) produced significantly different shaft load transfer characteristics.

Table 6.6: Comparison of shaft resistance ratios, $R_{d\text{-}vc,d}$, between the cased and uncased shafts.

Depth m (ft)	Predominant Soil Type	Shaft Resistance Ratio at 2 mm (0.1 in)		Shaft Resistance Ratio at 12.5 mm (0.5 in)	
		CIR	CNIR	CIR	CNIR
7.9 to 9.1 (26 to 30)	Stiff sandy silt	4%	3%	3%	4%
9.1 to 11.9 (30 to 39)	Dense silty sand	8%	-	6%	-
11.9 to 14.9 (39 to 49)	Stiff sandy, clayey silt	28%	3%	15%	7%
14.9 to 18.0 (49 to 59)	Stiff sandy, clayey silt	44%	5%	23%	11%

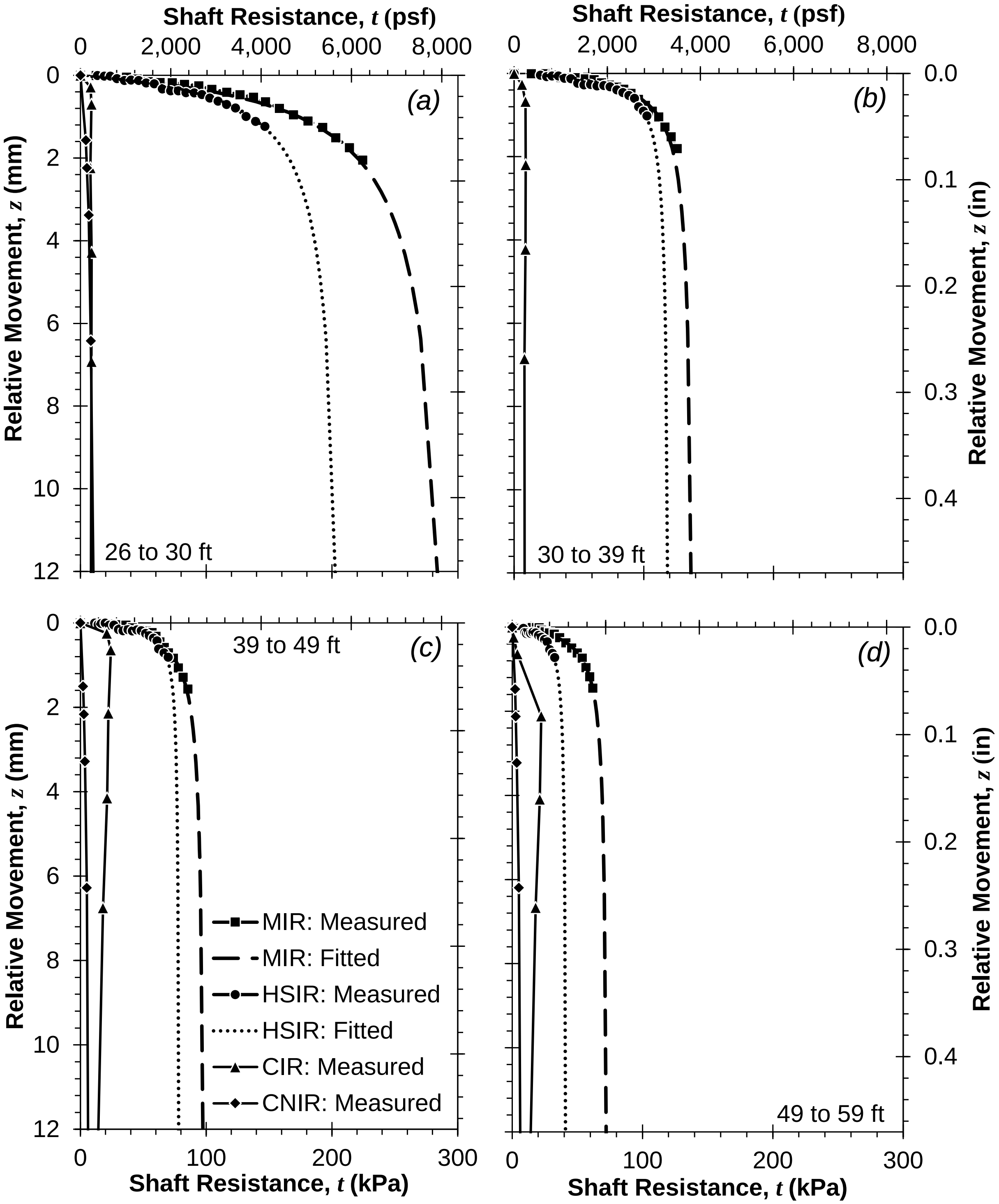

Figure 6.15: Comparison of the proposed and extrapolated axial load profile using proposed and fitted *t-z* curves, respectively, with the measured data of (a) MIR and (b) HSIR. Note, the proposed *q-z* curves were used in both proposed and extrapolated responses.

The unit shaft resistance ratios from full-scale tests conducted by Owens and Reese (1982), Camp et al. (2002), and this study are summarized in Table 6.7. Owens and Reese (1982) studied the effects of casing on shaft resistance at a site in Galveston, Texas where the test shafts were designated G-1 and G-3, and at a site in eastern Texas where the shafts were designated E-1 and E-2. The diameter and length of the steel casing used in shaft G-3 was 0.91 m (36 in) and 18.3 (60 ft), respectively. After the borehole was drilled to a depth of 10.7 m (35 ft) using a 0.91 m (36 in) diameter auger, the steel casing was installed to a depth of 12.2 m (40 ft) using the torque and crowd supplied by the drill rig. Then, a 0.86 m (34 in) diameter auger was used to drill the borehole to a depth of 18.3 m (60 ft). The diameter and length of test shaft G-1 was 1.21 m (48 in) and 18.3 m (60 ft), respectively. Prior to drilling, a steel casing 1.21 m (48 in) in diameter was vibrated to a depth of 15.8 m (52 ft); a 1.17 m (46 in) diameter auger was used to drill the borehole the final depth of 18.3 m. The effect of casing installation methods on the unit shaft resistance was substantial. The unit shaft resistance for G-3 (drill then twist in casing) compared to G-1 (vibrate casing then drill) reduced by an amount ranging from $R_{d\text{-}tc,vc\text{-}d}$ = 9 to 30%, with the largest variability occurring in the sand deposits and with very little variability in the plastic, fine-grained soils (Table 6.7). The reduction of the unit shaft resistance was greater in the loose, saturated sands (average $R_{d\text{-}tc,vc\text{-}d}$ = 13%) than in the dense to very dense sands (average $R_{d\text{-}tc,vc\text{-}d}$ = 23%). On the other hand, on average, the unit shaft resistance of the vibro-cased portion of G-1 within the soft clay layer from a depth of 12.8 to 15.9 m (42 to 52 ft) was about 89% of the unit shaft resistance for the uncased portion of G-3. Vibro-installation of steel casing results in densification and in an increase in unit shaft resistance if the casing is installed prior to drilling as compared to drill-then-install casing in sandy soil, whereas the vibro-installation of casing prior to drilling in the deep, soft clay layer resulted in a reduction in unit shaft resistance compared to that of an uncased shaft.

The diameter and length of the shafts E-1 and E-2 were 0.91 m (36 in) and 18.3 m (60 ft), respectively. Prior to drilling, the casing for shaft E-1 was vibrated to a depth of only 12.2 m (40 ft) because densification of the very loose to medium dense sand prevented further penetration. To reduce shaft resistance on the inside of the casing, the soil was excavated to the same depth as the tip of the casing; the casing was then advanced to 18.3 m using a vibratory hammer. On the other hand, shaft E-2 was constructed using a temporary casing that was vibrated to the full depth, the soil inside of the casing was excavated, and then the casing was extracted during placement of the concrete. Considering the densification of the sand that resulted from the vibratory installation of the permanent steel casing to 10.7 m depth for shaft E-1, $R_{vc\text{-}d\text{-}cr,dc}$ was about 33% on average. On the other hand, considering depths of 13.8 to 18.3 m, where the comparison relates a vibro-cased and drilled and cast shaft interface to a vibro-cased, drilled, and the casing removed, $R_{vc\text{-}d,vc\text{-}d\text{-}cr}$, indicating the benefit of a concrete-soil interface, the reduction in shaft resistance averaged 14%.

Table 6.7: Reduction in Unit Shaft Resistance as a Function of Construction Sequencing.

Reference	Definition of Shaft Resistance Ratio	Range in Depths m (ft)	Shaft Resistance Ratio	Soil Type	Range in Displacements mm (in)	Shaft resistance ratio, R_r	
						Range	Average
Owens and Reese (1982)	Shaft G-3 (drilled to a depth of 35 ft then twist-cased to a depth of 40 ft) to G-1 (vibro-cased to a depth of 52 ft then drilled to a depth of 60 ft, followed by casing removal).	0 to 6.4 (0 to 21)	$R_{d-tc,vc-d}$[1]	Loose to medium dense silty fine sand	23 to 45 (0.90 to 1.75)	9.0 to 17%	13%
		6.4 to 7.9 (21 to 26)	$R_{d-tc,vc-d}$	Very soft to medium stiff clay	23 to 45 (0.90 to 1.75)	17 to 18%	17%
		7.9 to 10.7 (26 to 35)	$R_{d-tc,vc-d}$	Dense to very dense silty fine sand	23 to 45 (0.90 to 1.75)	18 to 30%	23%
Owens and Reese (1982)	Shaft G-1 (vibro-cased then drilled) to G-3 (uncased, drilled from a depth of 40 to 60 ft).	12.8 to 15.9 (42 to 52)	$R_{vc-d,d}$[2]	Soft clay with thin lenses of silty sand	23 to 45 (0.90 to 1.75)	85 to 100%	89%
Owens and Reese (1982)	Shaft E-2 (vibro-cased to a depth of ~57 ft prior to drilling inside the casing then vibro-cased to a depth of 60 ft, followed by casing removal) to E-1 (vibro-cased to a depth of 40 ft prior to drilling inside the casing, then vibro-cased to a depth of 60 ft).	0 to 10.7 (0 to 35)	$R_{vc-d-cr,dc}$[3]	Very loose to medium dense sand	23 to 38 (0.9 to 1.5)	21 to 70%	33%
Owens and Reese (1982)	Shaft E-1 (vibro-cased from a depth of 40 to 60 ft then drilled inside the casing) to E-2 (vibro-cased then drilled, followed by casing removal)	13.8 to 18.3 (45 to 60)	$R_{vc-d,vc-d-cr}$[4]	Very loose to loose sand	23 to 38 (0.9 to 1.5)	8.2 to 20%	14%
Camp et al. (2002)	Vibro-cased portion to uncased portion of shafts (vibro-cased then drilled)	(varies)	$R_{vc-d,d}$	Cooper Marl	$\lesssim$ 12.5 ($\lesssim$ 0.5)	20 to 58%	34%
This Study	Cased shafts (drilled then vibro-cased) to uncased shafts	7.9 to 14.9 (26 to 49)	$R_{d-vc,d}$[5]	Stiff sandy silt and dense silty sand	12.5 (0.5)	3% to 15%	7%
This Study	Cased shafts (drilled then vibro-cased) to uncased shafts	14.9 to 18.3 (49 to 60)	$R_{d-vc,d}$	Stiff sandy clayey silt	12.5 (0.5)	11% to 23%	17%

Notes: [1] $R_{d-tc,vc-d}$ = drilled then twist-installation of casing compared to vibro-cased then drilled;[2] $R_{vc-d,d}$ = vibro-cased then drilled compared to drilled; [3] $R_{vc-d-cr,dc}$ = vibro-cased then drilled and cast followed by removal of casing to driven casing; [4] $R_{vc-d,vc-d-cr}$ = vibro-cased then drilled to vibro-cased then drilled and cast following removal of casing; [5] $R_{d-vc,d}$ = drilled then vibro-cased to drilled

Camp et al. (2002) reported results from loading test of three partially-cased drilled shafts that incorporated permanent casing through weak sediments overlying Cooper Marl, within which the shafts were founded. The steel casing for each shaft was vibrated into place prior to the excavation of the shafts, allowing for a comparison of the effect of casing in the Cooper Marl. Load transfer data obtained during the bidirectional loading tests indicated that the unit shaft resistance was fully-mobilized at relative soil-shaft displacements generally less than about 12.5 mm ($\lesssim$ 0.5 in; Camp 2017). The shaft resistance ratio, $R_{vc\text{-}d,d}$, defined in this ratio of vibro-cased and drilled to the uncased shaft resistance, ranged from about 20 to 58%, with an average of about 34%.

Clearly, construction procedures and sequencing, as well as the type of soil conditions, control the magnitude of shaft resistance reduction that is possible. Table 6.7 may be used as a reference to aid practitioners in estimating possible reductions.

6.9 SUMMARY AND CONCLUSIONS

Four full-scale, instrumented drilled shafts were constructed as part of a study to evaluate various performance characteristics of cased and uncased shafts, with and without internal reinforcement consisting of either Grade 60 or Grade 80 steel reinforcement bars. This paper explored the effects of the steel casing and the effects of auger diameter (relative to the casing diameter) on the axial load transfer characteristics of the cased shafts relative to the uncased shafts. For the shafts incorporating permanent casing, the shafts were drilled to depth using slurry, and then the casing was vibrated into place. The thermal integrity profiling (TIP) method using thermal wires was used as part of the nondestructive testing (NDT) program to provide an estimate of the actual shape of the shaft. For the cased shafts, the results from the TIP profiling indicated that potential gaps existed between the steel casing and the sidewall of the drilled borehole. As deduced from the results of the NDT and load testing, the use of thermal wires with shafts that incorporate steel casing can prove helpful in determining whether voids are present between the steel casing and the sidewalls of the shaft.

Despite similar depth of embedment and nominally similar as-constructed diameter, comparison of the load-displacement curves for the cased and uncased shafts indicated significant differences in their axial response. The load transfer curves developed from the results of the load tests confirmed that the use of steel casing and the method used to install the casing resulted in substantial differences in the load transfer behavior between the cased and uncased shafts. In addition, the shafts constructed with an auger that was nominally the same diameter as the casing resulted in less effective load transfer characteristics as compared to shafts constructed with an auger that was slightly smaller in diameter than the casing.

Empirical *t-z* (shaft resistance) and *q-z* (toe resistance) curves were developed based on the results of the load tests. A direct CPT-based method for estimating load transfer curves for uncased shafts in similar soils was proposed and used to extend the results of the load test program. Finally, to provide a useful reference for practitioners considering the use of casing in drilled shaft foundations the effect of casing on axial load transfer characteristics was evaluated based on load test data reported in the literature as well as with the load testing results from this study.

7.0 LATERAL LOADING TEST RESULTS AND DISCUSSION

This chapter provides the specific details regarding the lateral loading tests on the four test shafts, including the interpretation of measured flexural strains, the global shear load-lateral displacement performance of the test shafts, and the lateral load transfer and displacement profiles. Based on these measurements, the data is interpreted to provide the unit soil reaction-soil-shaft displacement, or *p-y*, curves for each of the shafts. The following chapter explores the importance of using region-specific lateral load transfer models and in consideration of scale (diameter) effects. See Chapter 4.0 for details regarding the subsurface conditions that contribute to the observed lateral loading performance. Refer to Chapter 5.0 for details regarding the construction and configuration of the test shafts and corresponding instrumentation used to observe the lateral load transfer characteristics.

7.1 OVERVIEW OF TESTS AND DISCUSSION

The lateral loading tests were conducted using the protocol discussion in Chapter 5.0 and summarized in Table 7.1. During the loading tests, gaps developed behind the shafts and the soil at the ground surface heaved and cracked in front of the shafts to form a radial cracking pattern in front of the shafts that indicated the formation of passive wedges. Figure 7.1 and Figure 7.2 show the cracks, gaps, and ground heaving at the end of the loading tests for uncased and cased shafts, respectively, which may be interpreted using the 0.3 m (1 ft) by 0.3 m (1 ft) spaced grid. Table 7.1 summarizes the displacement at ground level, y_{gl}, the approximate maximum gap width, w_{gap}, the maximum distance of cracking emanating from the front and edges of the shaft, $d_{c,f}$ and $d_{c,s}$, respectively, and y_h. Comparison of y_{gl} from the inclinometers to w_{gap} indicates similarity in magnitudes. Based on the distance of crack propagation, CIR appeared mobilized a larger volume of soil during the loading test as compared to the uncased shafts, attributed to deeper extent of load transfer; this is confirmed in the lateral displacement profiles described subsequently. Owing to the use of a slightly larger auger and the development of larger gaps between the shaft from depths of 3 to 8 m (9.8 to 26.5 ft) (see Chapter 5.0), CNIR produced less surface expression of mobilized soil volume as compared to CIR.

Table 7.1. Comparison of the Displacement at Ground Level, y_{gl}, the Approximate Maximum Gap Width, w_{gap}, the Maximum Distance of Cracking Emanating from the Front and Edges of the Shaft, $d_{c,f}$ and $d_{c,s}$, Respectively, for Lateral Head Displacement, y_h, of about 200 mm (8 in).

Test Shaft	y_h mm (in)	y_{gl} mm (in)	Approximate w_{gap}, mm (in)	$d_{c,f}$ m (ft)	$d_{c,s}$ m (ft)
MIR	183 (7.2)	142 (5.6)	150 (6.0)	1.5 (5)	1.2 (4)
HSIR	205 (8.1)	152 (6.0)	165 (6.5)	1.8 (6)	1.2 (4)
CIR	213 (8.4)	183 (7.2)	190 (7.5)	3.4 (11)	1.5 (5)
CNIR	205 (8.1)	186 (7.3)	190 (7.5)	1.8 (6)	1.5 (5)

Figure 7.1: Photos at the end of the loading tests showing: (a) crack patterns, (b) gap behind the shaft, and (c) side view of the shaft for MIR with applied displacement of 523 mm (20.6 in), and (d) crack patterns, (e) gap behind the shaft, and (f) side view of the shaft for HSIR with applied displacement of 305 mm (12.0 in).

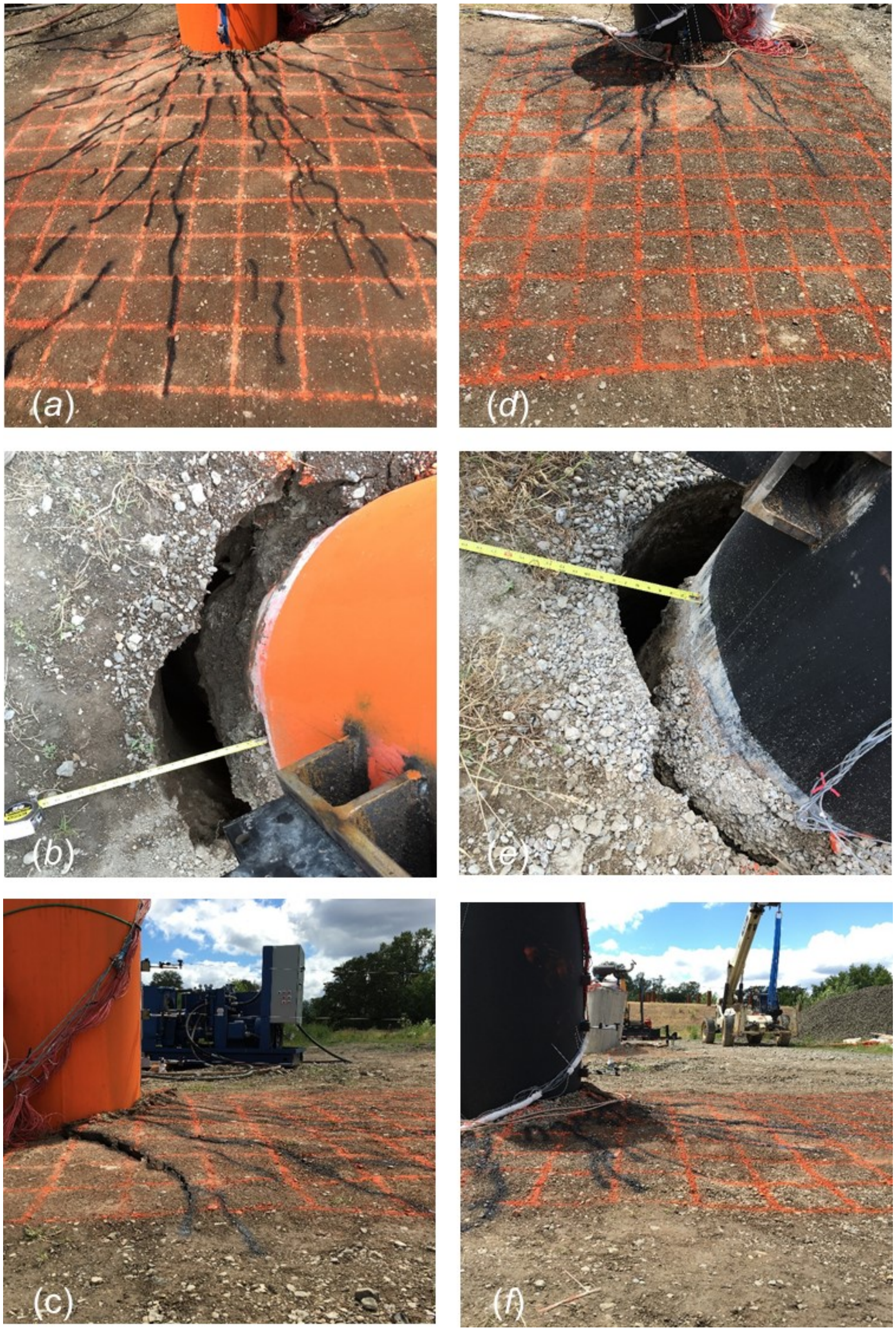

Figure 7.2: Photos at the end of the loading tests for (a) crack patterns, (b) gap behind the shaft, and (c) side view of the shaft for CIR with applied displacement of 213 mm (8.4 in),, and (d) crack patterns, (e) gap behind the shaft, and (f) side view of the shaft for CNIR with applied displacement of 205 mm (8.1 in).

7.2 SECTION ANALYSES FOR THE TEST SHAFTS

In order to estimate the bending moment, M, distribution along the test shafts based on the measured section curvature, ϕ, through strain gages and inclinometers, section analyses, described by Stuedlein et al. (2015), were conducted to evaluate the moment-curvature (M-ϕ) relationship for each test shaft. Both the finite element platform OpenSees (McKenna et al. 2010) and the finite difference platform LPILE (Isenhower and Wang 2015) were used to perform section analyses and compare to the response observed during the loading tests.

For the OpenSees model, the steel material was simulated using the uniaxial bilinear material model, *Steel01* (Mazzoni et al. 2006), considering strain hardening and assuming similar tensile and compressive stress-strain responses (Figure 7.3a). The initial stiffness, E_{steel}, and strain-hardening ratio, b, were assumed equal to be 200 GPa (29,000 ksi) and 0.01, respectively. The actual geometry of the hollow bars were modeled directly in the OpenSees model. The concrete was simulated using the modified Kent and Park (Kent and Park 1971; Yassin 1994; Mazzoni et al. 2006) material model, *Concrete02*, considering linear tension softening. As shown in Figure 7.3b, the compressive strength of concrete, f_c, is calculated as:

$$f_c = f_c' \cdot \left[2\frac{\varepsilon_c}{\varepsilon_{c0}} - \left(\frac{\varepsilon_c}{\varepsilon_{c0}} \right)^2 \right] \text{ for } 0 \le |\varepsilon_c| \le |\varepsilon_{c0}| \qquad (7.1a)$$

$$f_c = \frac{(\varepsilon_c - \varepsilon_{c0}) \cdot (f_{cu} - f_c')}{\varepsilon_{cu} - \varepsilon_{c0}} + f_c' \text{ for } |\varepsilon_{c0}| \le |\varepsilon_c| \le |\varepsilon_{cu}| \qquad (7.1b)$$

$$f_c = f_{cu} \text{ for } |\varepsilon_c| \ge |\varepsilon_{cu}| \qquad (7.1c)$$

where f'_c = compressive strength, ε_c and ε_{c0} = compressive strain and strain at the maximum compressive strength, f_{cu} = crushing strength, and ε_{cu} = strain at crushing strength. The effect of confinement on the concrete in the cased shafts and the core concrete within the transverse reinforcement of the uncased shafts, as indicated by the shaded area in Figure 5.1a to Figure 5.1d, was incorporated into section analyses following the approach of Mander et al. (1988). The compressive strength, f'_c, of the unconfined concrete was determined on the day of each loading test as described above. The modulus of elasticity of concrete, E_c, was estimated through 4,700 $\sqrt{f_c'}$ (MPa) based on ACI 318-14 (ACI 2014). The ε_{c0} of unconfined concrete was assumed to be $2f'_c/E_c$ in the modified Kent and Park material model. The parameters of f_{cu}, and ε_{cu} were assumed to equal $0.85f'_c$ and 0.38%, respectively, for unconfined concrete (Hognestad 1951). For the confined concrete, the parameters f'_c, ε_{c0}, f_{cu} and ε_{cu} were determined using Mander et al. (1988). The tensile strength, f_t, for both confined and unconfined concrete, was assumed equal to $0.33\sqrt{f_c'}$ (MPa) (e.g., Vecchio and Collins 1986). The tension softening stiffness, E_{ts}, for both the confined and unconfined concrete was assumed equal to f_t/ε_{c0} (e.g., Barbosa 2011; Elgamal et al. 2014). However, the use of $E_{ts} = 10f_t/\varepsilon_{c0}$ appears to better capture the measured M-ϕ relationships (Figure 7.4b), particularly for the uncased shafts at larger curvature. The concrete parameters used in the OpenSees model are summarized in Table 7.2.

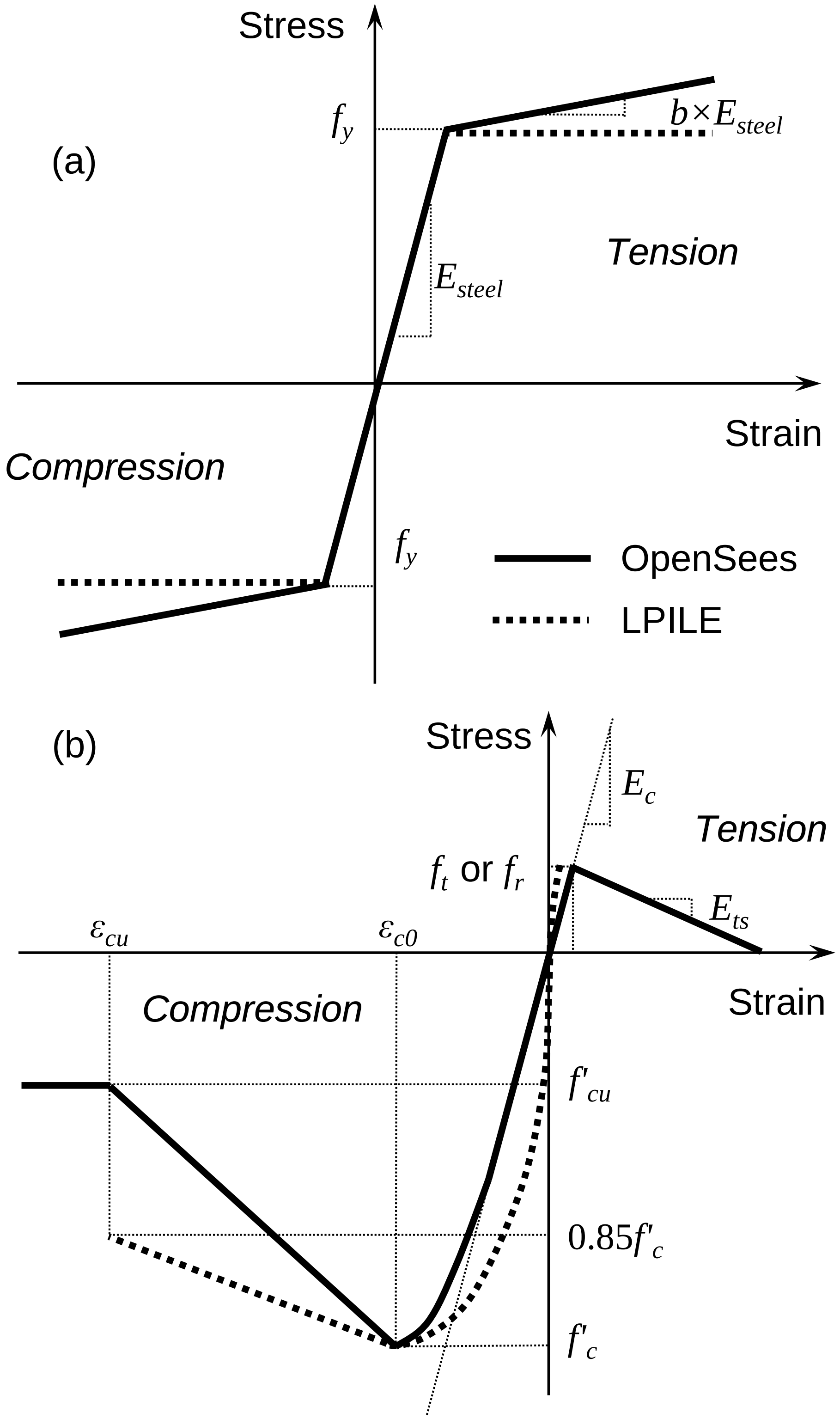

Figure 7.3: Stress-strain relationship of (a) concrete and (b) steel used in the OpenSees and LPILE models.

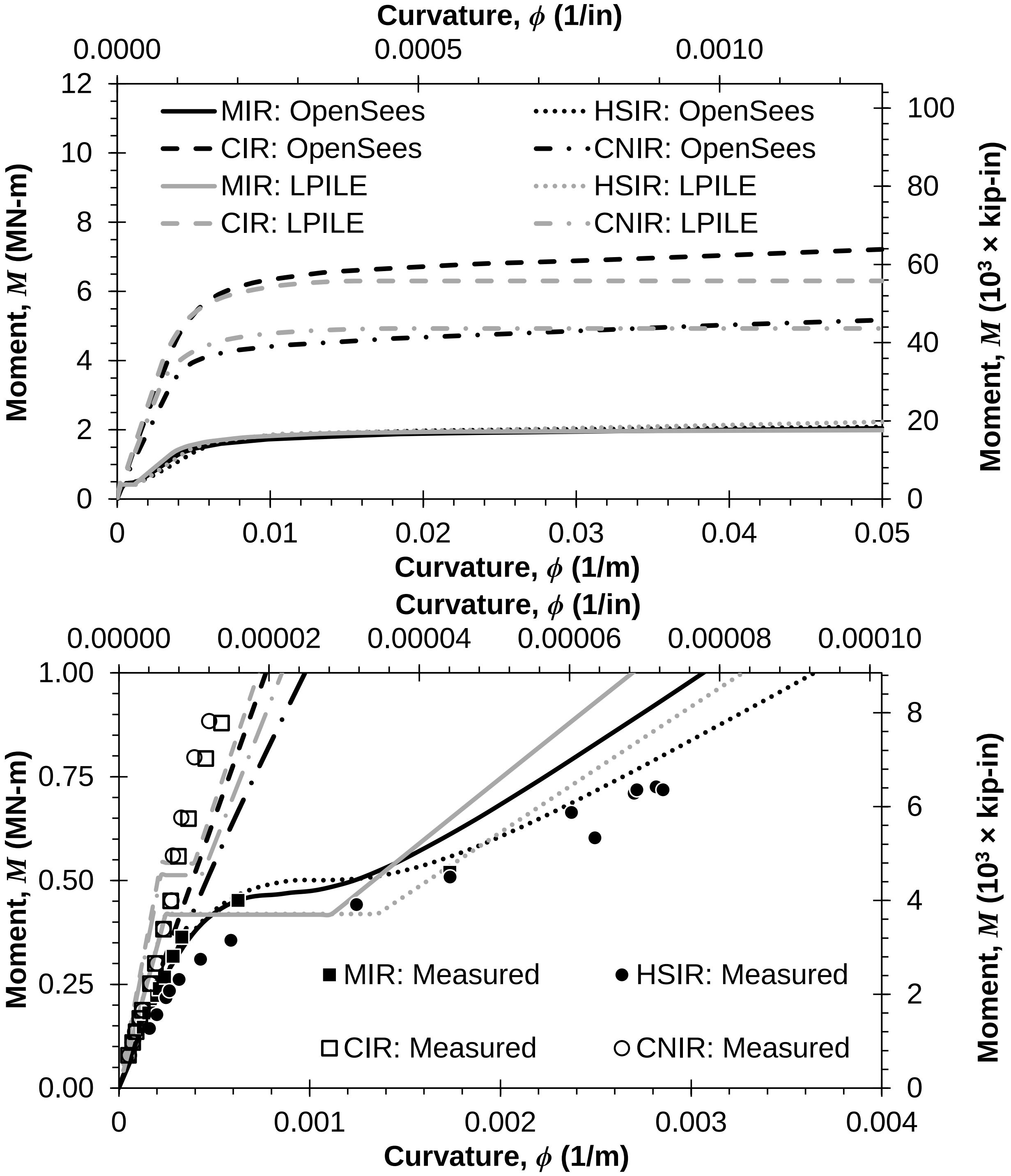

Figure 7.4: Moment-curvature relationships for the test shafts section at the ground level, including (a) the comparison of calculated relationships using OpenSees and LPILE, and (b) comparison of the calculated and measured relationships.

The stress-strain model of concrete and steel implemented in LPILE is slightly different to the OpenSees *Concrete02* model. The LPILE model assumes an elastic-perfectly plastic constitutive response for steel (Figure 7.3a). Since the hollow bars in HSIR could not be modeled in LPILE, solid bars with similar steel area were used, which reduces the local moment of inertia and corresponding flexural rigidity. The concrete stress-strain relationship used in LPILE is shown in Figure 7.3b, and can be calculated through Eqs. (7.1a) and (7.1b) assuming $\varepsilon_{c0} = 1.7f'_c/E_c$, $\varepsilon_{cu} = 0.38\%$, $f_{cu} = 0.85f'_c$, and $f_c = 0$ when $|\varepsilon_c| \geq |\varepsilon_{cu}|$. The modulus of rupture, f_r, was assumed to equal $0.62\sqrt{f'_c}$ (MPa) with the corresponding tensile strain, ε_t, calculated by:

$$\varepsilon_t = -\varepsilon_{c0}\left(1-\sqrt{1+\frac{f_r}{f'_c}}\right) \tag{7.2}$$

The concrete model in LPILE specifies a larger initial compressive stiffness for a given f'_c through the use of $\varepsilon_{c0} = 1.7f'_c/E_c$ as compared to $\varepsilon_{c0} = 2f'_c/E_c$ for OpenSees model. In addition, $f_r = 0.62\sqrt{f'_c}$ (MPa) is used in the LPILE model, which is larger than $f_t = 0.33\sqrt{f'_c}$ (MPa) used in the OpenSees model. The tension softening and the effect of confinement on the concrete are not considered in LPILE.

Table 7.2 Concrete Model Parameters Used to Simulate the Test Shafts in OpenSees.

Test Shaft	Confinement	f'_c, MPa (ksi)	ε_{c0}, %	f_{cu}, MPa (ksi)	ε_{cu}, %	f_t, MPa (ksi)	E_{ts}, GPa (ksi)
MIR	Unconfined, Cover	68.9 (10.1)	0.354	59 (8.5)	0.380	2.76 (0.40)	0.78 (113)
	Confined, Core	86.7 (12.6)	0.807	82.9 (12.0)	1.354	2.76 (0.40)	0.78 (113)
HSIR	Unconfined, Cover	72.1 (10.5)	0.361	61.3 (8.9)	0.380	2.82 (0.77)	0.78 (113)
	Confined, Core	88.9 (12.9)	0.782	84.7 (12.3)	1.314	2.82 (0.77)	0.78 (113)
CIR	Confined	88.1 (12.8)	0.952	72.9 (10.6)	3.407	2.68 (0.39)	0.78 (113)
CNIR	Confined	87.0 (12.6)	0.953	71.9 (10.4)	3.443	2.66 (0.39)	0.78 (113)

Figure 7.4 shows the calculated and measured M-ϕ relationships of the test shafts at the ground surface, corresponding to the location where measuring the M-ϕ relationship directly was possible. The general section performance of MIR and HSIR is similar for the initial and large-curvature responses of the shafts. However, the flexural rigidity of MIR was slightly larger than that of HSIR for the transition from the pre-cracking to post-initial cracking regime, stemming from the larger steel area used with MIR as compared to HSIR. The initial measured M-ϕ response for both the uncased and cased shafts agree quite well with the results estimated using OpenSees (e.g., $\phi \lesssim 2.5\mathrm{E}^{-4}$ m^{-1}), whereas the LPILE models over-estimate the flexural stiffness. The OpenSees model accurately captured the smooth M-ϕ transition following initial concrete cracking for MIR, but did not appear to model the transition for HSIR as accurately. However, at larger curvatures, the effect of smaller steel area for HSIR was compensated by the higher yield

strength, the use of hollow bars (with larger moment of inertia), and the slightly higher compressive concrete strength.

No evidence for concrete cracking was observed in the cased shafts during testing, nor was it computed in the OpenSees model. Rather, the cased shafts appear to remain elastic or slightly harden for the range in curvature induced during the loading tests. Both the OpenSees and LPILE models indicate the significant increase in flexural rigidity and moment capacity for the cased shafts as compared to the uncased shafts, owing to the greater steel area with the use of steel casing and greater confinement of the concrete (Roeder et al. 1999; Roeder et al. 2010; Roeder and Lehman 2012) as considered in OpenSees model. The moment capacity of CIR is approximately 40% larger than that of CNIR due to the use of internal reinforcement based on the OpenSees model. Using MIR as a baseline for comparison, the increase in moment capacity for HISR, CNIR, and CIR is approximately 2, 150, and 250%, respectively, at a curvature of 0.05 m^{-1} (0.00127 in^{-1}) based on the OpenSees model.

In general, the M-ϕ relationships computed using LPILE are similar to those from OpenSees; however, the initial response for each shaft from LPILE are larger than that from the OpenSees models, which is attributed to the larger initial compressive stiffness and tensile strength of the LPILE concrete model. The effect of initial concrete cracking calculated from LPILE is significant for each shaft, a result of neglecting the tension softening of the concrete. Again, no cracking was observed in the cased shafts for curvatures induced, suggesting room for improvement in the concrete models available in LPile. The slight differences between the LPILE and OpenSees models at large curvatures is mainly caused by differences in the stress-strain relationships assumed for the steel reinforcements; LPILE does not consider strain hardening.

Since the M-ϕ relationship obtained using OpenSees exhibited better agreement with the measured responses as compared to the LPILE models, the OpenSees models were used to estimate the moment profiles for each shaft, as described subsequently. To account for the effect of the variation of the as-built diameter along the uncased shafts (Figure 5.11b) on the back-calculated moment and p-y relationships, a series of section analyses were conducted using the as-built diameter at each instrumented elevation. Then, the depth-specific M-ϕ relationship based on the OpenSees model was used to estimate the moment at each instrumented elevation from the curvature obtained from the ESGs or inclinometers, as appropriate at a given strain level.

7.3 LOAD-DISPLACEMENT RESPONSE AT THE SHAFT HEAD

The global lateral response at each shaft head was measured using load cells and string-potentiometers at the resultant loading point (Figure 5.13). Table 5.3 summarizes the imposed and measured displacements, y_h, and shear force, V_h, at the head of each test shaft. At the end of the lateral loading tests, the maximum displacement for MIR and HSIR was 523 and 305 mm (20.6 and 12.0 in), respectively, with a developed shear force, V_h, of 920 kN (207 kip). In comparison, the V_h for CIR and CNIR was 1,540 kN (346 kip) with corresponding y_h of just 213 and 205 mm (8.4 and 8.1 in), respectively.

Figure 7.5 shows the measured lateral load-lateral displacement response at the head of the shaft. The lateral system resistance of the uncased shafts was fully-mobilized at an applied load of approximately 890 kN (200 kips) and at applied displacement of approximately 150 mm (6 in). The shafts exhibited a similar lateral response to applied displacements of approximately 190 mm (7.5 in), with slight differences at small displacements. The initial response for MIR was slightly stiffer than HSIR, consistent with its slightly larger diameter (Figure 5.13) and stiffer M-ϕ relationship described previously. Towards the end of the loading test (discussed below), MIR exhibited larger lateral displacement than HSIR at a given lateral load, possibly due to: (1) the slightly higher moment capacity of HSIR for $\phi \geq 0.2\ \mathrm{m}^{-1}$(Figure 7.4a), and (2) inherent variability of the soil stiffness and strength.

The lateral resistance of the cased shafts was not fully–mobilized during the loading tests. Although the moment capacity of CIR was approximately 40% larger than that of CNIR, the differences in capacity was inconsequential for the displacements imposed. Further, CNIR appeared slightly stiffer than CIR, perhaps due to variability in the soil layer thicknesses and consistency, or due to measurement error. However, the differences are minor and the exhibited responses can be assumed equal for practical purposes.

7.4 LATERAL DISPLACEMENT PROFILES

In order to understand the lateral load transfer for test shafts, the lateral responses, including the profiles of lateral displacement, moment, and soil reaction, were investigated. The distribution of lateral displacement and soil reaction along the shafts were also used to evaluate the lateral soil reaction-displacement relationships (p-y curves) at various depths.

For HSIR and CIR, the lateral displacements, $y(z)$, were calculated by integrating the slope, $s(z)$, along the shaft and obtained directly using the GEODAQ data acquisition system. For MIR and CNIR using the Type II inclinometer, the $s(z)$ was recorded by tilt sensors from the loading point to the depth of 5.3 m (17.5 ft). A seventh order polynomial was fit to the discrete slope measurements along the shaft. Since the Type II inclinometer did not provide measurements below 5.3 m (17.5 ft; Figure 3e), it was assumed that the slope was zero based on the zero curvature measured from the ESGs. Then, the displacement profiles for MIR and CNIR were computed by integration of the rotation polynomial function along the shaft using:

$$y(z) = \int s(z)\,\mathrm{d}\,z \tag{7.3}$$

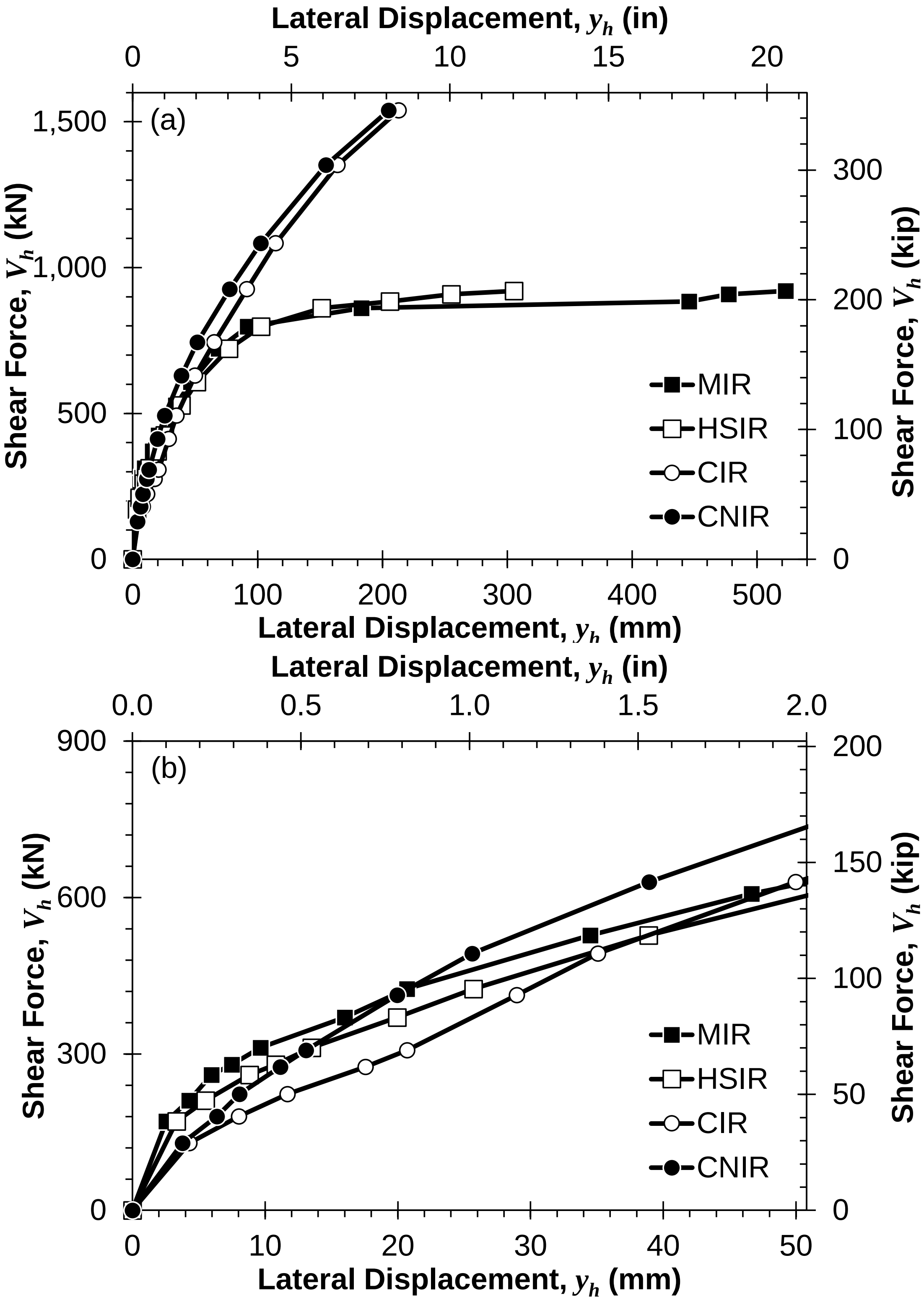

Figure 7.5: Load-displacement response at the shaft head for the test shafts (a) during the loading tests and (b) with lateral displacement up to 50 mm.

Figure 7.6 presents the lateral displacement profile for each test shaft at similar lateral load magnitudes to aid comparison between shafts of similar and different flexural rigidities. The lateral displacement profile for each shaft was similar for relatively small lateral loads (e.g., 275 to 280 kN, or 62 to 63 kips). However, differences between the shafts emerged with increases in lateral load. For example, for V_h = 920 to 925 kN (approximately 208 kips) the displacement at the ground surface for MIR, HSIR, CIR, and CNIR was approximately 411, 229, 79, and 75 mm (16.2, 9.0, 3.1, and 2.9 in), respectively.

The maximum depth of the mobilized soil-foundation displacement for the cased shafts at the highest load is approximately 9.0 m (30 ft), or $10D_n$ (D_n = nominal diameter), whereas it is approximately 3.7 m (12 ft), or $4D_n$, for the uncased shafts. The significant differences in the depth of soil-foundation displacement are due to the differences in the flexural rigidity of the shafts; the significantly larger flexural rigidity of the cased shafts allows deeper soils to participate in the system response.

7.5 LATERAL SOIL REACTION-DISPLACEMENT RELATIONSHIPS (*P-Y* CURVES)

The lateral displacement, *y(z)*, as shown in Figure 7.6, were used to directly construct the lateral resistance-lateral displacement, or *p-y*, curves. The lateral soil reaction, *p*(*z*), was back-calculated using beam theory by double differentiating the bending moment, *M*(*z*), along the test shafts with respect to depth, *z*, using:

$$p(z) = \frac{d^2}{dz^2} M(z) \tag{7.4}$$

The bending moment at depth *z*, *M*(*z*), is a function of section curvature, $\phi(z)$, and nonlinear flexural rigidity, *EI*, given by:

$$M(z) = EI \cdot \phi(z) \tag{7.5}$$

The moment profile was obtained based on the nonlinear $M\text{-}\phi$ relationship, as shown in Figure 7.4. The variation of the as-built diameter along the uncased shafts (Figure 5.11) was considered in the development of the depth-dependent $M\text{-}\phi$ relationship. Then, a sixth order polynomial function was used to fit the discrete *M* at the instrumented level for each test shaft.

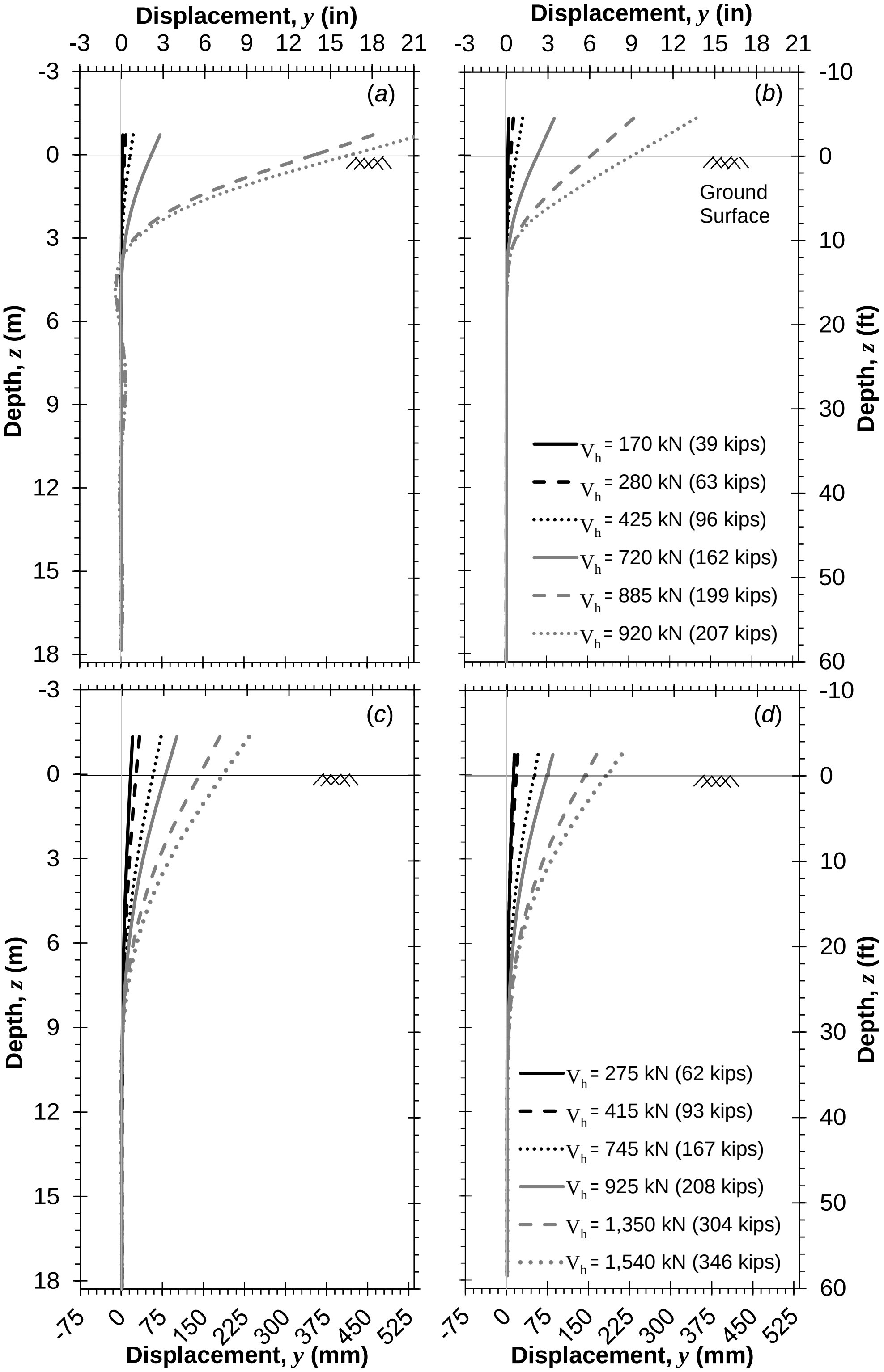

Figure 7.6: Selected lateral deflection profiles for (a) MIR, (b) HSIR, (c) CIR, and (d) CNIR.

The $\phi(z)$ was computed using the measured axial strain, $\varepsilon(z)$, from the ESGs by:

$$\phi(z) = \frac{\varepsilon_T(z) - \varepsilon_C(z)}{h} \tag{7.6}$$

or the slope, $s(z)$, from inclinometers by:

$$\phi(z) = \frac{d}{dz} s(z) \tag{7.7}$$

where $\varepsilon_T(z)$ and $\varepsilon_C(z)$ = measured tensile and compressive strain at depth z, h = horizontal distance between the strain gauges. Seventh order polynomial functions were used to fit the measured slope along the test shafts to perform the numerical differentiation.

The evaluation of $p(z)$ is sensitive to the quality (and quantity) of the discrete measurements along the shaft because of the use of curve fitting techniques and numerical differentiation. The Type II inclinometers (used with MIR and CNIR) provided $s(z)$ from the loading point to the depth of 5.3 m (17.5 ft) and spaced at 0.6 m (2 ft), producing a total of 11 measurements. Thus, the quality of the fitting and numerical differentiation may lead to unreasonable estimation of $p(z)$. Therefore, only the measurements from the ESGs were used to estimate $\phi(z)$ and $p(z)$ for MIR and CNIR, whereas both the measurements from the ESGs and Type I inclinometer were used for HSIR and CIR.

The $\phi(z)$ calculated from the ESGs were considered more reliable than those calculated from the inclinometer measurements for the initial stages of loading. However, as the loading and displacement increased, the ESG measurements became unreliable as the strains in the concrete either exceeded the strain range of the gage or the concrete began to crack in proximity to the gage from the induced flexural strains. Taking CIR as an example as shown in Figure 7.7, the profiles of curvature, displacement, moment, and soil reaction at selected lateral loads are compared. When the loads were smaller than 415 kN (93 kips), the profiles of obtained using the ESG and inclinometer measurements agree fairly well. Measurements of $\phi(z)$ from ESGs (Figure 7.7b) became increasingly unreliable for the estimation of $p(z)$ with increasing loads. The $\phi(z)$ measured from ESGs below a depth of about 14.9 m (49 ft) was negligible throughout the loading tests, as expected, whereas considerable fluctuations in the derived $\phi(z)$ were produced by the fit to the inclinometer-based slope. Therefore, the comparisons that follow below use the $p(z)$ based on the ESGs to construct p-y curves at small lateral displacements and when considered reliable at a given depth, whereas the $p(z)$ derived from the high resolution inclinometer was used for large lateral displacements. Curvature derived from the ESG measurements were used to construct $p(z)$ for all of the near-zero, deeper instrumented sections.

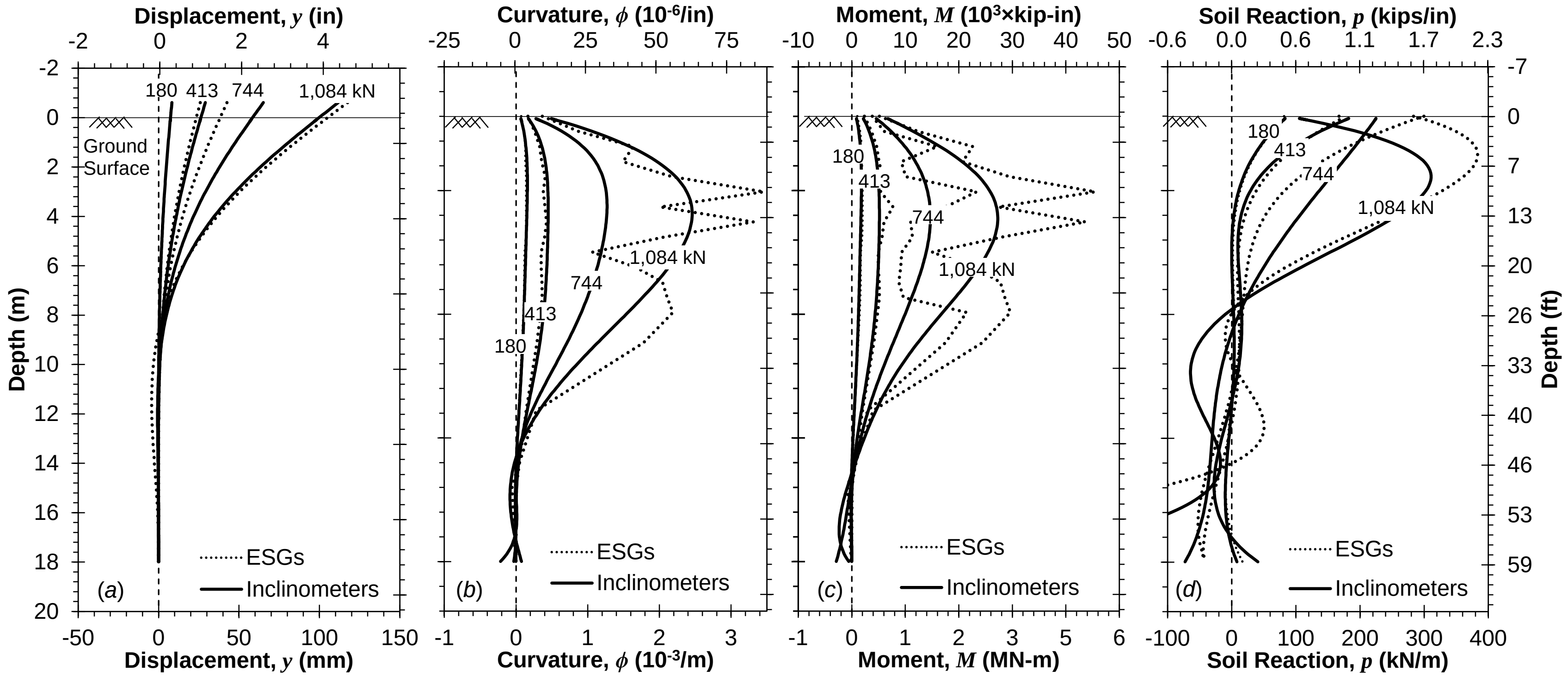

Figure 7.7: Comparison of selected profiles of (a) displacement, (b) curvature, (c) moment, and (d) soil reaction obtained using the measurements from ESGs and the GEODAQ in-place inclinometer for CIR. Note: markers indicates the directly measured data at certain depths, which were not derived using numerical integration or differentiation.

Figure 7.8 compares the *p*-*y* curves at selected depths for the uncased and cased shafts from the ground surface to a depth of $3D_n$ (i.e., 2.7 m or 9 ft) and 7 D_n (i.e., 6.4 m or 21 ft), respectively. The *p*-*y* curves for the two cased shafts are similar to one another, as are those for the uncased shafts at each depth. However, the soil reaction for the uncased shafts are significantly larger than those for cased shafts at a given soil displacement, as shown in the Figure 7.8a through Figure 7.8d. This may be attributed to: (1) the improved roughness of the soil-concrete interface associated with the uncased shafts as compared to the soil-steel interface (Lam and Martin 1986), which provides a larger counteracting moment in the direction of load due to axial shaft resistance, and (2) the as-built diameter of the uncased shafts are significantly larger than those of the cased shafts (Figure 5.11b), which also leads to a larger unit soil resistance (Lam and Martin 1986; Lam 2013). Furthermore, the uncased shafts exhibit a significantly large initial stiffness in the *p*-*y* response, demonstrating excellent coupling with the adjacent soil, perhaps in part due to the stiffening of the surrounding soil during water migration associated with the hydration of the concrete.

Softening in the near-surface *p*-*y* curves was noted, similar to the *p*-*y* curves obtained by Nimityongskul (2010) and Nimityongskul et al. (2018), derived from piling tested 30 m (98 ft) away from the present test site, as well as from loading tests on plastic soils reported by others (e.g., Matlock 1970; Reese and Welch 1975). For the cased shafts, the initial stiffness of the *p*-*y* curves were similar to one another above the depths of 1.2 m (6 ft). However, the initial response transition to a concave-up shape from the depths of 2.7 to 6.4 m (9 to 21 ft), due to the loss of soil-casing coupling and gaps that had formed as observed in Figure 5.11b and in the axial loading response of these shafts described in Chapter 6.

7.6 ASSESSMENT OF BACK-CALCULATED *P-Y* CURVES

The site-specific *p*-*y* curves back-calculated for each shaft were used to compare with the commonly-available (termed “general”, herein) *p*-*y* curve models, which may not be universally suitable for deep foundations with different diameters, installation methods (e.g., drilled shafts versus driven piles) or types of soil-structure interface (e.g., cased versus uncased drilled shafts). In addition, the sufficiency of a selected, commonly-available software package LPILE (Isenhower and Wang 2015) was evaluated using the back-calculated *p*-*y* curves and the M-ϕ response provided by the section analysis available in LPILE to predict the lateral response of each test shaft. An effort was also made to compare the test results to the lateral responses simulated using LPILE with the back-calculated and the general *p*-*y* curve models available in LPILE.

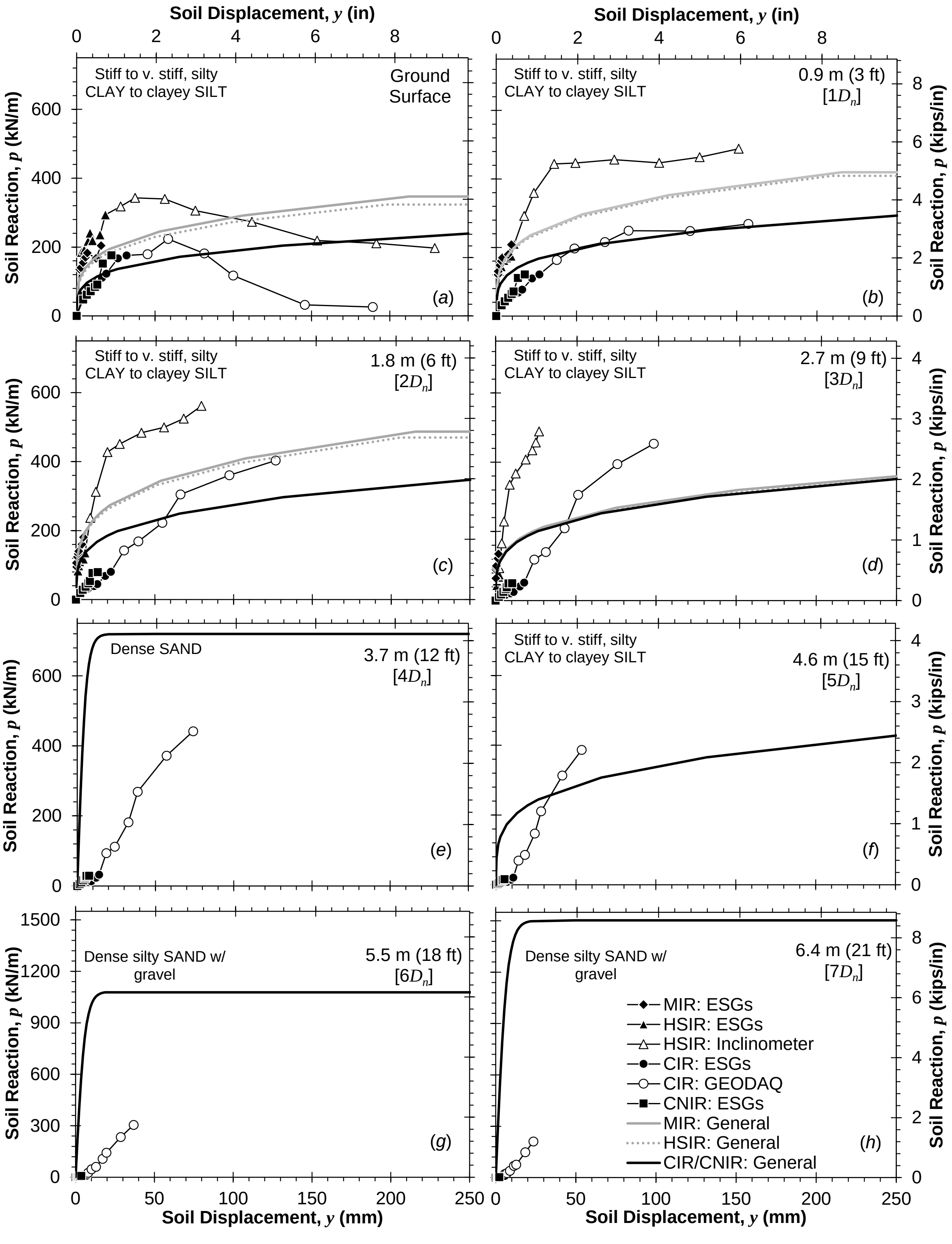

Figure 7.8: Back-calculated *p-y* curves for all of the test shafts at (a) ground surface, (b) 0.9 m (3 ft), (c) 1.8 m (6 ft), and (d) 2.7 m (9 ft), and for only the cased test shafts at (e) 3.7 m (12 ft), (f) 4.6 m (15 ft), (g) 5.5 m (18 ft), and (h) 6.4 m (21 ft).

7.6.1 Comparison of the Back-Calculated and the General *p-y* Curves

The *stiff clay without free water* (Welch and Reese 1972; Reese and Welch 1975) and *API Sand* models (Reese et al. 1974; API 2010) have been proposed and are generally used for plastic and granular soils, respectively. To evaluate the suitability of these general *p-y* curve models for the cased and uncased shafts, comparisons were made between the back-calculated and the general *p-y* curves.

The *p-y* curve models used for the uncased and cased shafts are summarized in Table 7.3 and Table 7.4, respectively. The effective unit weight, γ', of each soil layer was obtained based on the laboratory results described by Dickenson and Haines. (2006) and Nimityongskul (2010). The undrained shear strength, s_u, for the plastic soil layers was correlated to CPT cone-tip resistance, q_c, (Figure 4.8) using (e.g., Kulhawy and Mayne 1990):

$$s_u = \frac{q_c - \sigma_{vo}}{N_k} \tag{7.8}$$

where σ_{vo} = total overburden stress and N_k = cone factor. The N_k, which varies from 15 when the groundwater table is at its highest (e.g., 0.6 m or 2 ft) in the spring and about 23 when the groundwater table is at its lowest (e.g., 2.5 m or 8 ft), generally in the fall, based on s_u back-calculated from footing loading and consolidated undrained triaxial tests (Martin 2018). The friction angle of the granular soil layers was estimated using correlations to CPT cone-tip resistance (Kulhawy and Mayne 1990). Explorations SCPT-2, SCPT-3, CPT-4, and SCPT-5 were used to estimate the necessary soil parameters for the available *p-y* curve models. Exploration CPT-4 and SCPT-5 were performed to a depth of approximately 12 m (40 ft) in between the test shafts one day after the loading tests in zone of soil not likely to be affected by the loading. Explorations SCPT-2 and -3 were conducted five months prior to the loading tests and were used for depths below 12 m (40 ft). Other parameters, including the strain corresponding to a stress of 50% of the peak soil strength of plastic soils, ε_{50}, and the coefficient of subgrade reaction, *k*, were selected based on recommendations provided in Isenhower and Wang (2015).

Figure 7.8 shows the comparison of the back-calculated and the general *p-y* curves at selected depths for the test shafts. The slight difference between the general *p-y* curves for MIR and HSIR are due to the variation of the diameter profile (Figure 5.11). Since the back-calculated *p-y* curves for MIR and HSIR are similar to one another, as are those for CIR and CNIR, the comparison was made quantitatively for HSIR and CIR. The mean bias (i.e., the ratio of the back-calculated and the general soil reaction, *p*) calculated at measured soil displacements at each instrumented depth, and the coefficient of variation (COV), of the sample biases are summarized in Table 7.5. The range of mean bias and COV for HSIR are 1.11 to 1.42 and 20% to 42%, respectively, for depths ranging from the ground surface to 2.7 m (9 ft), whereas for CIR these are 0.04 to 0.86 and 37% to 132%, respectively, for the depths ranging from the ground surface to 6.4 m (21 ft). The differences between the back-calculated and the general *p-y* curves stem from the different deep foundation diameters, installation methods, and types of soil-structure interface. For example, the stiff clay model without free water (Welch and Reese 1972;

Reese and Welch 1975) was derived based on a 0.9-m (3-ft) diameter drilled shaft, which may not be appropriate for driven piles or cased drilled shafts.

Table 7.3 Summary of Selected Soil Models and Corresponding *p-y* curve Parameters Used to Simulate the Uncased Shafts in LPILE.

Soil Model	Depth m (ft)	γ' kN/m^3(pcf)	s_u kPa (psf)	ε_{50}	ϕ' deg	k, MN/m^3(pci)
Stiff Clay w/o Free Water	0 to 1.9 (0 to 6.3)	18.1 (115)	110 (2,275)	0.005	-	-
Stiff Clay w/o Free Water	1.9 to 3.4 (6.3 to 11.0)	8.3 (52.6)	65 (1,315)	0.007	-	-
API Sand	3.4 to 3.7 (11.0 to 12.0)	10.6 (67.6)	-	-	39	40 (150)
Stiff Clay w/o Free Water	3.7 to 5.0 (12.0 to 16.5)	8.3 (52.6)	60 (1,225)	0.007	-	-
API Sand	5.0 to 12.2 (16.5 to 40)	10.6 (67.6)	-	-	38	33 (120)
Stiff Clay w/o Free Water	12.2 to 18.3 (40.0 to 60.0)	7.5 (47.6)	290 (5,990)	0.004	-	-

Note: γ' = effective unit weight, s_u = undrained shear strength, ε_{50} = strain corresponding to a stress of 50% of the peak soil strength, ϕ'= friction angle, and k = coefficient of subgrade reaction.

Table 7.4 Summary of Selected Soil Models and Corresponding *p-y* Curve Parameters Used to Simulate the Cased Shafts in LPILE

Soil Model	Depth, m (ft)	γ' kN/m3 (pcf)	s_u kPa (psf)	ε_{50}	ϕ' deg	*k*, MN/m3 (pci)
Stiff Clay w/o Free Water	0 to2.0 (0 to 6.6)	18.1 (115)	85 (1800)	0.007	-	-
Stiff Clay w/o Free Water	0 to 3.5 (6.6 to 11.5)	8.3 (52.6)	75 (1515)	0.007	-	-
API Sand	3.5 to 3.8 (11.5 to 12.5)	10.6 (67.6)	-	-	40	42 (155)
Stiff Clay w/o Free Water	3.8 to 5.5 (12.5 to 18.0)	8.3 (52.6)	70 (1420)	0.007	-	-
API Sand	5.5 to 18.3 (18.0 to 40)	10.6 (67.6)	-	-	39	40 (150)
Stiff Clay w/o Free Water	12.2 to 18.3 (40.0 to 60.0)	7.5 (47.6)	285 (5930)	0.004	-	-

Table 7.5 Accuracy of the General *p-y* Curves at Selected Depths as Compared to the Observed *p-y* Curves

Depth m (ft)	HSIR		CIR	
	Mean Bias	COV (%)	Mean Bias	COV (%)
0	1.32	29%	0.86	45%
0.9 (3)	1.25	20%	0.75	37%
1.8 (6)	1.11	38%	0.64	71%
2.7 (9)	1.42	54%	0.60	95%
3.7 (12)	-	-	0.17	122%
4.6 (15)	-	-	0.39	121%
5.5 (18)	-	-	0.07	132%
6.4 (21)	-	-	0.04	118%

7.6.2 Load-Displacement Response at the Shaft Head

The back-calculated and general *p-y* curve models were used to simulate the lateral responses of the shafts using LPILE in order to validated the LPILE model framework (by using the back-calculated *p-y* curves) and to evaluate the response when assuming that the generally-available curves are appropriate. For the case of validation, the *p-y* curves back-calculated from ground surface to the depth of $10D_n$ was used for the cased shafts, whereas the back-calculated *p-y* curves from ground surface to the depth of $4D_n$ was used for the uncased shafts, given the negligible response observed below $4\ D_n$. The general *p-y* curve models shown in Table 7.3 and Table 7.4 were used for the soil below these depths. It is noted here that the soil below these depths has little effect on the lateral response given the respective flexural rigidity and moment capacity of each shaft. The as-built diameter of the uncased shafts (Figure 5.11b) was accounted for the purposes of this comparison. Due to the lack of reliability of the inclinometer measurements and corresponding smaller range in displacement for the back-calculated *p-y* curves for MIR and CNIR (Figure 7.8), small lateral displacements were applied to the head of MIR and CNIR up to 35 and 19 mm (1.4 and 0.8 in), respectively, in the LPILE model using the back-calculated *p-y* curves for MIR and CNIR, respectively. To simulate the lateral response of MIR and CNIR at large lateral displacements with the LPILE model using the back-calculated *p-y* curves, the back-calculated *p-y* curves for HSIR and CIR with larger displacement range were used, respectively.

The lateral responses of each test shaft was also simulated using only general *p-y* curve models (Table 7.3 and Table 7.4) to evaluate the sufficiency of the general *p-y* curves available in LPILE. Comparisons of the measured and simulated lateral responses were made.

Figure 7.9 compares the measured load-displacement response at the head of each test shaft to those calculated using LPILE using the general and back-calculated *p-y* curves. The responses of the uncased shafts simulated using the back-calculated *p-y* curves agree well with the measured response at the lateral displacements up to about 25 mm (1 in). The simulation of the uncased shafts then diverges from the measured response to over-estimate the applied shear force, which may have resulted from the limitation of the polynomial fitting method used for the back-calculation following plastic hinging in the shaft. As shown in Figure 7.10e, the inclinometer-based slope measurements could not capture the large curvature at depths near the plastic hinge upon section yielding. The response of the cased shafts simulated using the back-calculated *p-y* curves agree well with the measured load-displacement response across all of the displacements simulated, indicating that LPILE can reproduce the observed response when providing back-calculated *p-y* curves. The under-prediction of the initial stiffness may be caused by the slight under-prediction of the M-ϕ relationships with OpenSees model (Figure 7.4), which were used to back-calculate the *p-y* curves.

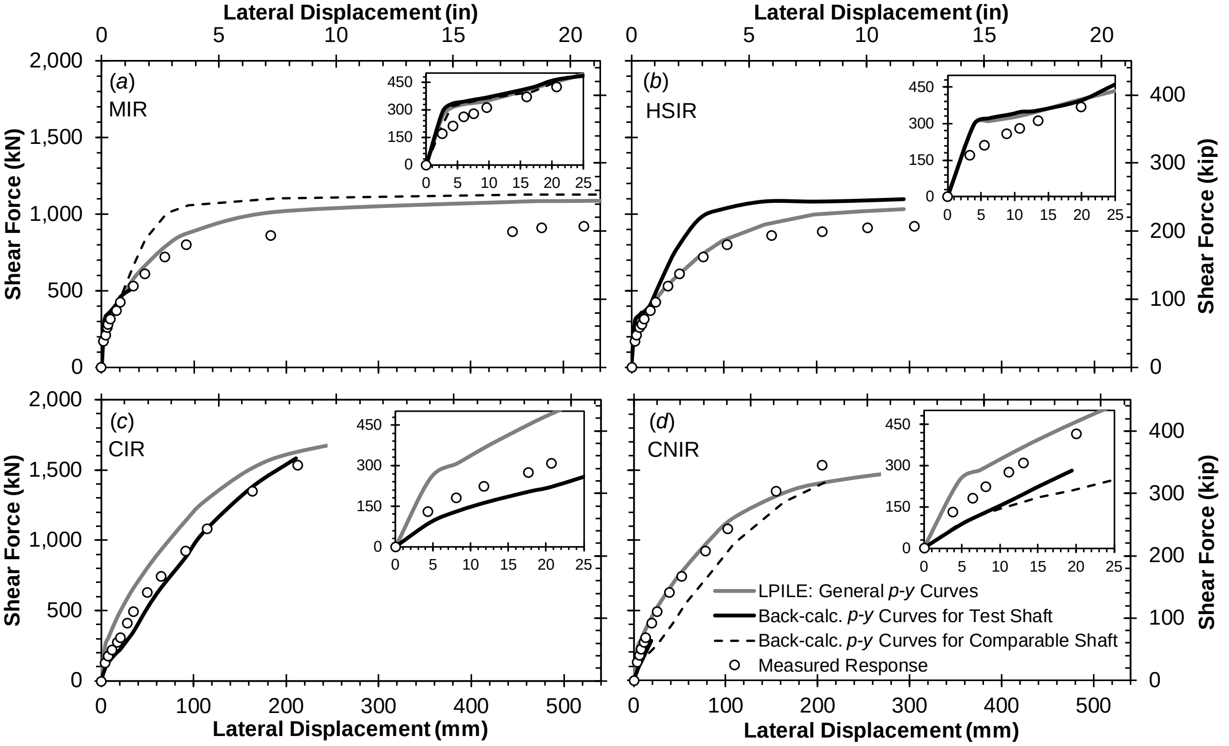

Figure 7.9: Comparison between the measured load-displacement response for the test shafts to the calculated response from LPILE model using general *p-y* curve models and back-calculated *p-y* curves for (a) MIR, (b) HSIR, (c) CIR, and (d) CNIR.

The responses of the uncased shafts simulated using the general *p-y* curves agree well with the measured responses at the lateral displacements up to about 100 mm (4 in). At larger displacement, the simulation using general *p-y* curves over-predicts the shear force. For CIR, the general *p-y* curves over-predict the shear force at shaft head at given applied displacements. The simulated responses for CNIR using general *p-y* curves agree well with the observed responses at the lateral displacements up to about 150 mm (6 in). The general *p-y* curves appear to under-predict the lateral resistance of CNIR at larger displacement.

To facilitate the evaluation of the back-calculated and the general *p-y* curves, the bias of lateral load (i.e., the ratio of the observed and computed shear force at the shaft head) at each applied displacement was calculated and is summarized in Table 7.6. It indicates that both the back-calculated and the general *p-y* curves over-predict the lateral resistance at given displacements within the range of y_h considered. For the cased shafts, the back-calculated *p-y* curves under-predict the lateral resistance at given displacements within the range of y_h considered, whereas the general *p-y* curves over-predict the lateral resistance.

Table 7.6 Comparison of the Measured Load-Displacement Responses of the Test Shafts to the Calculated Responses Using General and Back-Calculated *p-y* Curves.

Test Shaft	Max. y_h considered, mm (in)	General *p-y* curves		Back-calculated *p-y* curves	
		Mean Bias	COV (%)	Mean Bias	COV (%)
MIR	0 to 35 (0 to 1.4)	0.82	13%	0.80	17%
HSIR	0 to 294 (0 to 11.6)	0.88	14%	0.79	12%
CIR	0 to 211 (0 to 8.3)	0.73	19%	1.24	14%
CNIR	0 to 19 (0 to 0.8)	0.72	19%	1.44	5%

7.6.3 Lateral Responses along the Shafts

Figure 7.10 and Figure 7.11 compare the measured and simulated responses of the tests shafts in terms of the depth-varying displacement, curvature, and moment to help evaluate the lateral load transfer simulated using the general and the back-calculated *p-y* curves. These figures present profiles for V_h = 170, 425, 884, and 920 kN (39, 96, 199, and 207 kip) for the uncased shafts, and V_h = 275, 415, 925, and 1,540 kN (62, 93, 208, and 346 kip) for the cased shafts. The corresponding measured y_h for each shaft is indicated in each figure and summarized in Table 5.3 and Table 7.7 through Table 7.10. To facilitate comparison between the two LIPLE simulation cases and the measured data, the comparisons are made at the same magnitude of lateral displacement at the head of the shaft. Therefore, differences between the applied and calculated V_h may be noted in Table 7.7 through Table 7.10.

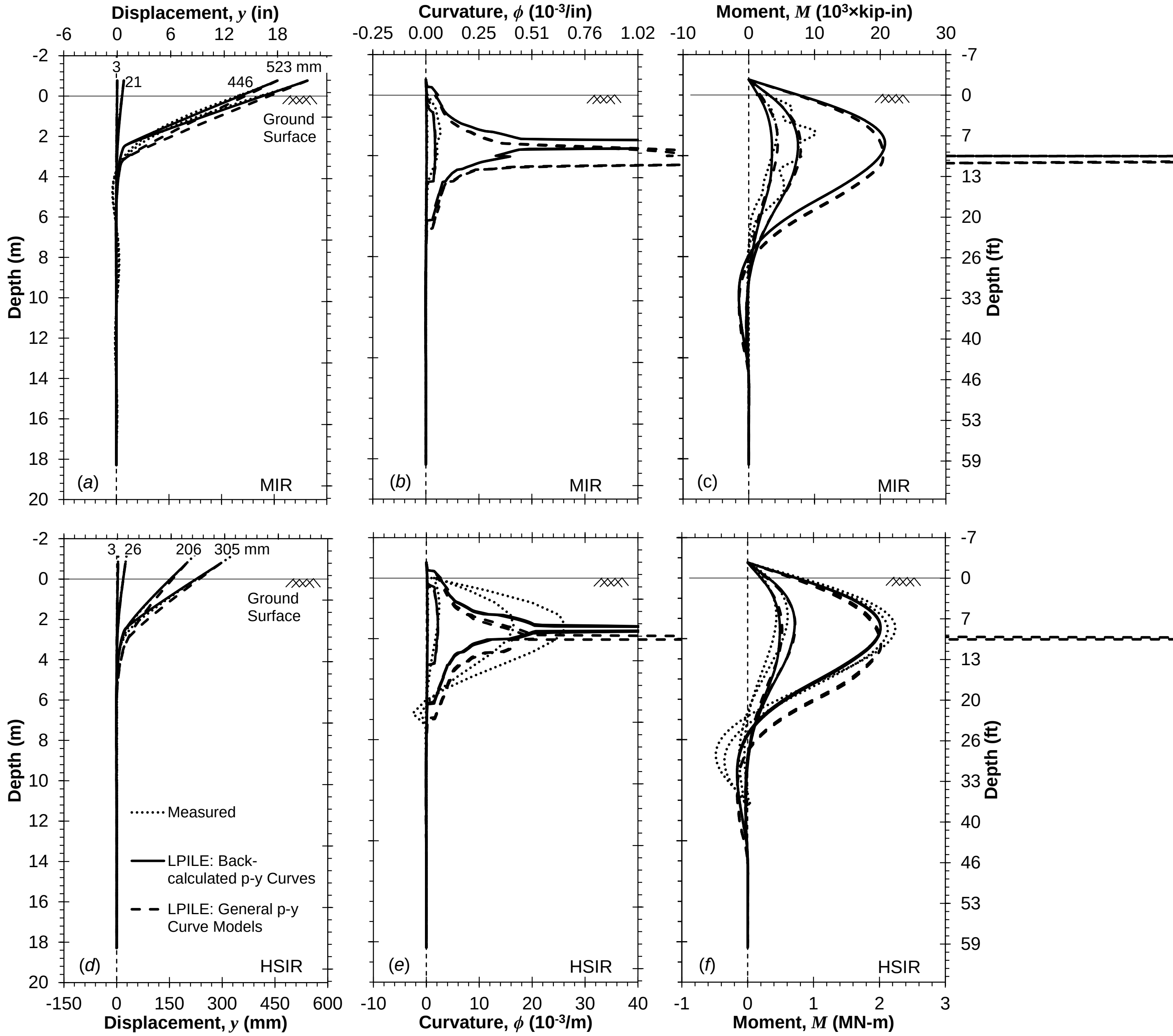

Figure 7.10: Comparison between the measured data and the LPILE model using general *p-y* curve models and back-calculated *p-y* curves on the selected profiles of (a) displacement, (b) curvature, and (c) moment for MIR, and (d) displacement, (e) curvature, and (f) moment for HSIR.

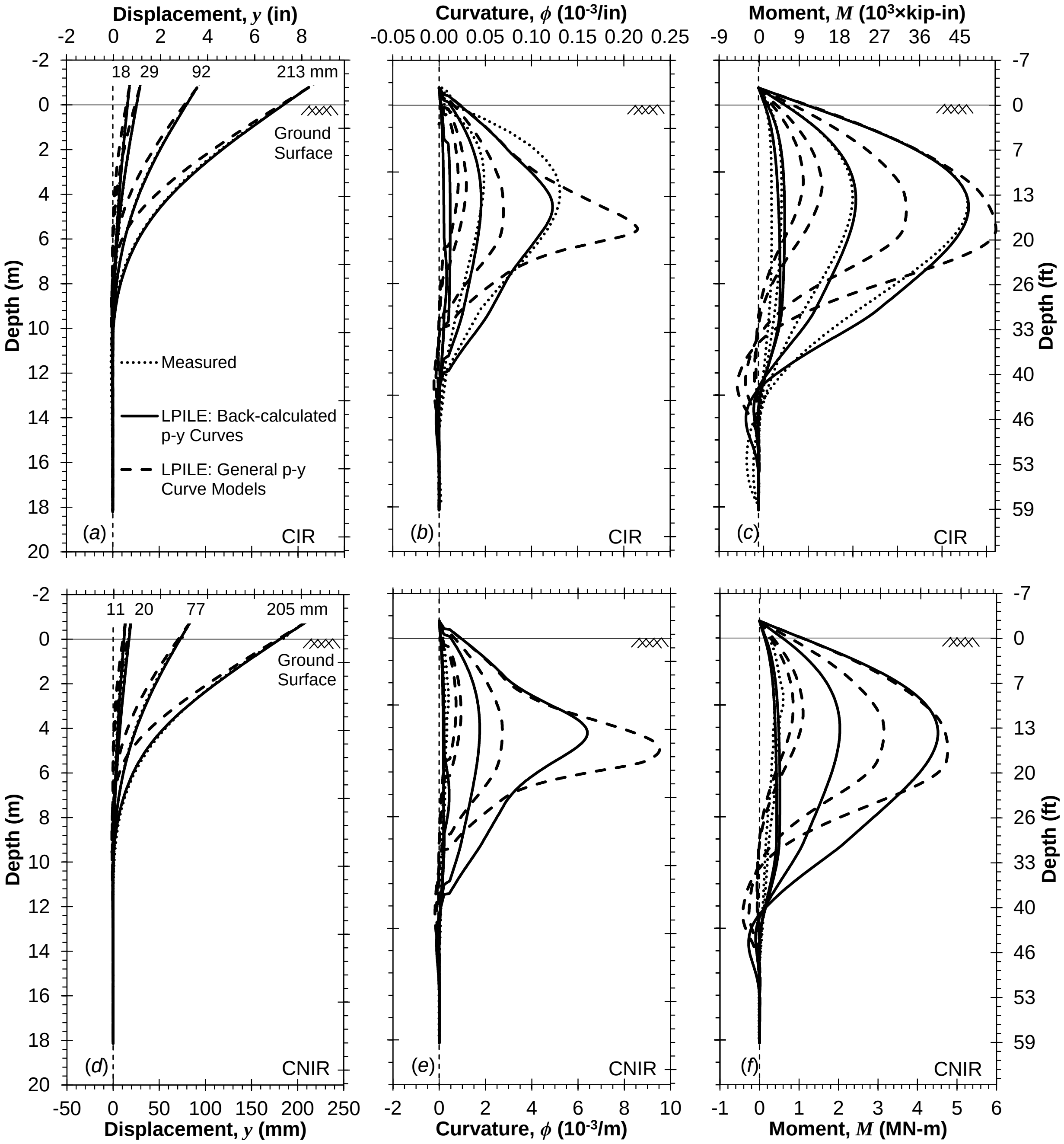

Figure 7.11: Comparison between the measured data and the LPILE model using general *p-y* curve models and back-calculated *p-y* curves on the selected profiles of (a) displacement, (b) curvature, and (c) moment for CIR, and (d) displacement, (e) curvature, and (f) moment for CNIR.

The comparisons in Figure 7.10 and Figure 7.11use the lateral displacement profiles measured using the in-place inclinometers. The profiles of curvature and moment, for CIR and HSIR, were based on the Type I inclinometers measurements, whereas, for MIR and CNIR, those profiles were based on the ESGs measurement at small lateral load. Figure 7.10b, Figure 7.10c, Figure 7.10d and Figure 7.10e only show the measured profiles of curvature and moment with V_h = 170 and 425kN (39 and 96kip) and V_h = 275 and 415kN (62 and 93 kip) for MIR and CNIR, respectively, due to the lack of reliability of the Type II inclinometer and ESGs measurements at large applied displacements. Table 7.7 through Table 7.10 present a quantitative comparison of the lateral responses of the test shafts in terms of the percent difference between observed and computed shear force at the shaft head, V_h, maximum bending moment, M_{max}, and depth-to-maximum bending moment, H_{Mmax}.

For the uncased shafts, the back-calculated *p-y* curves naturally produce better agreement with the lateral displacement profiles than those computed using the general *p-y* curve models. The general shapes and trends of the moment profiles from both LPILE simulations follow those of the test data. In general, the ranges in percent difference between the observed M_{max} and those simulated using the back-calculated and general *p-y* curves are 5 to 30%, and 0.3 to 25%, respectively. The ranges in percent difference between the observed H_{Mmax} and those simulated using the back-calculated and general *p-y* curves are 2 to 39%, and 24 to 34%, respectively. For the comparison of V_h, the ranges in percent difference between the observed and the simulated using the back-calculated and general *p-y* curves are 8 to 54%, and 2 to 55%, respectively. Generally, both simulation cases exhibit similar accuracy for the uncased shafts at small displacements, but the accuracy for H_{Mmax} with the general *p-y* curves is smaller than the back-calculated *p-y* curves, in some cases significantly, as the applied displacement increases.

For the cased shafts, the profiles of displacement, curvature, and moment computed using the back-calculated *p-y* curves agree quite well with the observed profiles. The ranges in percent difference between the observed M_{max} and those simulated using the back-calculated and general *p-y* curves are 0.4 to 49%, and 13 to 109%, respectively. The ranges in percent difference between the observed H_{Mmax} and those simulated using the back-calculated and general *p-y* curves are 2 to 86%, and 6 to 79%, respectively. For the comparison of V_h, the ranges in percent difference between the observed and the simulated using the back-calculated and general *p-y* curves are 3 to 38%, and 6 to 49%, respectively. Generally, the accuracy for the cased shafts using back-calculated *p-y* curves is greater than the general *p-y* curves across all of the displacements simulated. This indicates that the general models are naturally less suitable than the site-specific models. This may be attributed to the use of stiff clay model without free water (Welch and Reese 1972; Reese and Welch 1975), which may not be suitable for cased shafts.

Table 7.7 Comparison of the Measured Lateral Response for MIR with the LPILE Simulations

y_h, mm (in)	Model	V_h, kN (kip)	M_{max}, kN-m (kip-in)	H_{Mmax}, m (ft)
3 (0.1)	Measured	171 (38)	497 (4,397)	1.8 (6.0)
	LPILE w/ back-calculated *p*-*y* curves	289 (65)	400 (3,540)	2.7 (8.9)
	Difference	51%	22%	39%
	LPILE w/general *p*-*y* curves	265 (60)	498 (4,409)	2 (7.6)
	Difference	43%	0%	24%
21 (0.8)	Measured	425 (95)	1,149 (10,170)	1.8 (6.0)
	LPILE w/ back-calculated *p*-*y* curves	466 (105)	846 (7,492)	2.5 (8.3)
	Difference	9%	30%	32%
	LPILE w/general *p*-*y* curves	459 (103)	893 (7,908)	2.6 (8.5)
	Difference	8%	25%	34%

Table 7.8 Comparison of the Measured Lateral Response for HSIR with the LPILE Simulations

y_h, mm (in)	Model	V_h, kN (kip)	M_{max}, kN-m (kip-in)	H_{Mmax}, m (ft)
3 (0.1)	Measured	171 (38)	491 (4,345)	1.8 (6.0)
	LPILE w/ back-calculated *p-y* curves	299 (67)	553 (4,890)	2.6 (8.4)
	Difference	54%	12%	33%
	LPILE w/general *p-y* curves	300 (67)	591 (5,230)	2.6 (8.4)
	Difference	55%	18%	33%
26 (1.0)	Measured	425 (95)	686 (6,068)	1.8 (6.0)
	LPILE w/ back-calculated *p-y* curves	460 (103)	806 (7,138)	2.2 (7.4)
	Difference	8%	16%	20%
	LPILE w/general *p-y* curves	434 (98)	815 (7,213)	2.4 (7.8)
	Difference	2%	17%	25%
206 (8.1)	Measured	884 (199)	2403 (21,266)	2.5 (8.3)
	LPILE w/ back-calculated *p-y* curves	1,078 (242)	2279 (20,168)	2.5 (8.1)
	Difference	20%	5%	2%
	LPILE w/general *p-y* curves	997 (224)	2,284 (20,217)	3.4 (11)
	Difference	12%	5%	29%
305 (12.0)	Measured	920 (207)	2,532 (22,408)	2.4 (8.0)
	LPILE w/ back-calculated *p-y* curves	1,093 (246)	2,278 (20,164)	2.4 (7.9)
	Difference	17%	11%	1.56%
	LPILE w/general *p-y* curves	1,033 (232)	2,285 (20,221)	3.2 (10.6)
	Difference	12%	10%	28%

Table 7.9 Comparison of the Measured Lateral Response for CIR with the LPILE Simulations

y_h, mm (in)	Model	V_h, kN (kip)	M_{max}, kN-m (kip-in)	H_{Mmax}, m (ft)
18 (0.7)	Measured	275 (62)	332 (2,937)	5.7 (18.8)
	LPILE w/ back-calculated *p-y* curves	204 (46)	546 (4,834)	7.8 (25.6)
	Difference	30%	49%	31%
	LPILE w/general *p-y* curves	454 (102)	1,132 (10,020)	3.4 (11.3)
	Difference	49%	109%	50%
29 (1.1)	Measured	413 (93)	584 (5,170)	3.8 (12.6)
	LPILE w/ back-calculated *p-y* curves	294 (66)	661 (5,849)	5.1 (16.8)
	Difference	33%	12%	29%
	LPILE w/general *p-y* curves	593 (133)	1,611 (14,260)	3.6 (11.9)
	Difference	36%	94%	6%
92 (3.6)	Measured	926 (208)	2,384 (21,098)	4.1 (13.6)
	LPILE w/ back-calculated *p-y* curves	872 (196)	2,467 (21,835)	4.2 (13.9)
	Difference	6%	3%	2%
	LPILE w/general *p-y* curves	1,134 (255)	3,747 (33,160)	4.7 (15.4)
	Difference	20%	44%	12%
213 (8.4)	Measured	1,539 (346)	5,303 (46,938)	4.4 (14.6)
	LPILE w/ back-calculated *p-y* curves	1,582 (356)	5,325 (47,134)	4.6 (15.0)
	Difference	3%	0.4%	3%
	LPILE w/general *p-y* curves	1,627 (366)	6,018 (53,261)	5.5 (18.2)
	Difference	6%	13%	22%

Table 7.10 Comparison of the Measured Lateral Response for CNIR with the LPILE Simulations

y_h, mm (in)	Model	V_h, kN (kip)	M_{max}, kN-m (kip-in)	H_{Mmax}, m (ft)
11 (0.4)	Measured	275 (62)	377 (3,337)	3.0 (10.0)
	LPILE w/ back-calculated p-y curves	200 (45)	437 (3,863)	7.7 (25.2)
	Difference	32%	15%	86%
	LPILE w/general p-y curves	370 (83)	517 (4,576)	7.1 (23.2)
	Difference	29%	31%	79%
20 (0.8)	Measured	413 (93)	602 (5,326)	2.4 (8.0)
	LPILE w/ back-calculated *p-y* curves	282 (63)	852 (7,545)	3.1 (10)
	Difference	38%	34%	22%
	LPILE w/general *p-y* curves	450 (101)	1,102 (9,758)	3.4 (11.0)
	Difference	9%	59%	32%

7.7 SUMMARY AND CONCLUSIONS

Drilled shaft foundations have been commonly used to provide significant structural and geotechnical resistance to support bridges, buildings, and other civil infrastructure subjected to lateral loads. In order to account for the seismic demands, the amount of steel reinforcement in drilled shaft foundations has increased over the past several decades. However, the increase of reinforcing steel bar area reduces the clearance between the longitudinal and transverse reinforcement, which may increase the difficulty of concrete flowing through the reinforcement and increase the likelihood for voids and defects within the foundations. Moreover, the use of permanent steel casing can also lead to a decrease in the amount, or the outright elimination, of internal reinforcement since the steel casing is able to provide significant increase of inelastic deformation and flexural capacity of the foundation. However, no literature has reported the study of lateral load transfer between the drilled shafts with and without permanent steel casing and high-strength reinforcement at the same site and soil conditions.

To help address this gap in knowledge, four full-scale drilled shafts were constructed to improve the understanding of the lateral load transfer of cased and uncased shafts, with and without internal reinforcement consisting of either Grade 60 or Grade 80 reinforcing steel bars. With the comparisons of various performance metrics between the test shafts, including the performance at the head of the shafts, the lateral displacement, curvature and moment profiles, and the back-calculated soil reaction-displacement (*p-y*) curves, test results of the cased and uncased shafts indicated significant differences in their lateral responses. The cased test shafts exhibited significantly greater lateral resistance as compared to the uncased shafts. The shaft HSIR showed a similar lateral response at shaft head as MIR at small displacements. As the lateral resistance was getting fully mobilized, HSIR exhibited less lateral displacements as compared to MIR with the same lateral loads. The comparison of the *p*-*y* curves for each test shaft shows that the rougher soil-foundation interface and larger diameter lead to larger unit soil resistances at given soil displacements.

Back-calculated *p*-*y* curves for each shaft were compared and used, along with widely-available *p*-*y* curve models, to evaluate the sufficiency of the commonly used software package LPILE and the use of general *p*-*y* curves for a specific site condition; and it shows that the general models are naturally less suitable than the site-specific models.

8.0 PROPOSED *P-Y* CURVE MODEL FOR WILLAMETTE SILT CONSIDERING SCALE EFFECTS

8.1 BASIS FOR DEVELOPMENT OF THE REGION-SPECIFIC LATERAL LOAD TRANSFER MODEL

To aid in the design of bridge foundations in the Willamette Valley, region-specific *p-y* curve models were developed for deep foundations under lateral loading based on consideration of the widely-used *stiff clay without free water* model (Welch and Reese 1972; Reese and Welch 1975) available in commonly-used software (e.g., LPile, (Isenhower and Wang 2015). Chapter 5 described the identification of possible gaps between the steel casing and the surrounding soil, with confirmation of poor axial interface response in Chapter 6. Chapter 7 showed that the gaps between the steel casing and surrounding soil affected the back-calculated *p-y* curves for the cased shafts. In light of these observations, the back-calculated *p-y* curves for uncased shafts were used to propose the region-specific *p-y* curve model for Willamette Silt. The *p-y* curves back-calculated from the ground surface to a depth of 2.7 m (9 ft) for HSIR, which extend to large displacements, were selected for development of the Willamette Silt-specific lateral load transfer model. The comparison between HSIR and CIR was used to study the interface (i.e., concrete-soil versus steel-soil interface) and installation effects, which caused the formation of gap between casing and soil. Owing to the availability of *p-y* curves back-calculated for a 325 mm (12.75 in) diameter driven pipe pile (designated DPP) and extending from the ground surface to a depth of 2.1 m (7 ft), tested at the same site and reported by Nimityongskul (2010) and Nimityongskul et al. (2018), an assessment of the Willamette Silt *p-y* curves could be made with regard to possible scale (i.e., diameter) effects.

8.2 COMPARISON OF *P-Y* CURVES FOR SMALL- AND LARGE-DIAMETER FOUNDATIONS IN WILLAMETTE SILT

Figure 8.1 compares the back-calculated *p-y* curves for the larger diameter drilled shaft, HSIR and CIR, and the smaller-diameter driven steel pile, DPP, for shallow depths that correspond to the source of significant lateral resistance. Several important observations may be drawn from the comparison:

1. The initial stiffness of individual p-y curves increases with depth, regardless of foundation type or diameter;

2. The “concave up” shape of the initial response for the deeper p-y curves for CIR was caused by the presence of gaps between the casing and shaft borehole, as discussed in Chapters 4, 5 and 6;

3. The *p-y* curves transition from a softening-type response to a hardening-type response with increasing depth, indicative of an over-consolidated plastic soil response, regardless of foundation type or diameter;

4. The peak lateral soil resistance of the shafts HSIR and CIR increases with depth, whereas the peak lateral soil resistance for DPP increases with depth to a depth of about 3 to 4 pile diameters, whereupon it decreases slightly with depth; and,
5. The stiffness and peak lateral soil resistance is significantly larger for the larger diameter drilled shafts than the smaller diameter driven pile, indicative of scale (or diameter) effects, and interface characteristics in comparison of HSIR and DPP.

These observations are fully-consistent with established principles of soil-structure interaction. Accordingly, the development of a region-specific model would adhere to the full-scale observations as well as other soil-structure interaction principles established over decades of experience.

8.3 DEVELOPMENT OF THE REGION-SPECIFIC LATERAL LOAD TRANSFER MODEL CONSIDERING SCALE EFFECTS

The development of a lateral load transfer model for the Willamette Valley region, and specifically the Willamette Silt deposit, requires an assessment of the ultimate lateral soil resistance, the initial stiffness or displacement-dependent response, and the general shape of the *p-y* curves themselves. In the discussion that follows, the analytical methodologies established for stiff plastic soils are assessed for suitability in modeling the deep foundations considered herein and are modified based on the observations to produce improvements in accuracy.

The ultimate lateral soil resistance, p_u, for deep foundations in plastic soils at depth z can be calculated as follows (e.g., Matlock 1970; Welch and Reese 1972; Reese and Welch 1975; Reese et al. 1975):

$$p_u(z) = N_p(z) \cdot s_u(z) \cdot D(z) \tag{8.1}$$

where $N_p(z)$ = depth-dependent ultimate lateral resistance coefficient, which depends on the geometry of the failure mechanism (e.g., shallow, 3D passive wedge mechanism, versus the deep, 2D, flow failure mechanism), size of deep foundations, and soil properties, $s_u(z)$ = depth-dependent undrained shear strength, and $D(z)$ = the depth-dependent diameter. Reese et al. (1975) proposed that the depth-dependent change from the shallow to the deep failure mechanism in stiff clay can be facilitated through $N_p(z)$, by setting the ultimate lateral resistance coefficient to the smaller of:

$$N_p(z) = 2 + \frac{\gamma'_{avg} \cdot D(z) \cdot z}{s_u(z)} + \frac{2.83z}{D(z)} \tag{8.2}$$

$$N_p(z) = 11 \tag{8.3}$$

where γ'_{avg} = average effective unit weight from the ground surface to depth z.

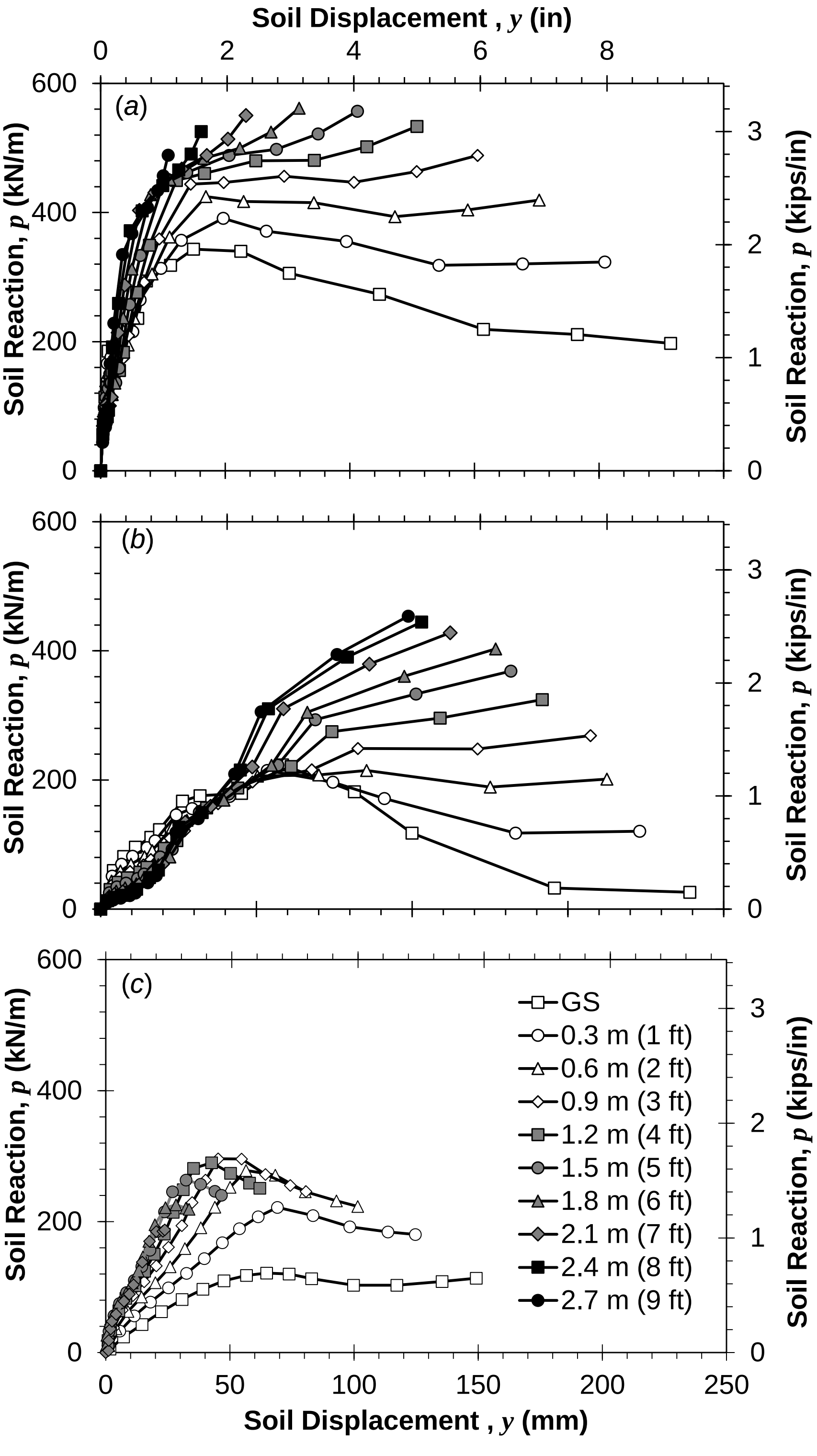

Figure 8.1 Back-calculated p-y curves for (a) HSIR and (b) CIR from ground surface to the depth of 2.7 m (9 ft) and (c) DPP from ground surface to the depth of 2.1 m (7 ft)

The ultimate lateral resistance coefficient, N_p, associated with the full-scale data that was presented in Figure 8.1 was estimated for each *p-y* curve for HSIR and DPP. The s_u corresponding to HSIR and DPP at each depth was estimated using the site-specific N_K factor in Eq. (7.8) with explorations CPT-4 (Figure 4.6, Appendix B.4) and 1997 CPT-1 (Appendix B.8), which is the exploration nearest to DPP. The ultimate lateral resistance coefficient was back-calculated for each depth by assuming that the representative p_u was equal to the observed peak or extrapolated asymptotic value, depending if the soil resistance was partially-mobilized (typically associated with hardening behavior) or if the soil resistance was fully-mobilized and subsequently exhibited post-peak softening behavior. If the lateral resistance was not fully-mobilized, the hyperbolic model was used to fit to the empirical *p-y* curves to extrapolate to the asymptotic p_u. Extrapolation to asymptotic quantities has been shown in numerous geotechnical applications that the extrapolated quantities represent relatively conservative (i.e., less than the likely) quantity estimates (Stuedlein 2008; and Huffman and Stuedlein 2014).

Figure 8.2 shows the variation of N_p with normalized depth *z/D*, which indicates that the back-calculated N_p for HSIR, CIR, and DPP share a similar trend from the ground surface to $z/D \cong 3$. Figure 7.2 also compares the back-calculated N_p to that derived from the stiff clay model from Reese et al. (1975) for a range in *z/D*. The minor differences between the estimates of N_p computed using the Reese et al. (1975) model for each foundation are due to differences in the soil properties (i.e., s_u and γ'_{avg}) and foundation diameters at each *z/D*, as indicated by the second and third terms in Eq. (8.2). The stiff clay model under-estimated N_p by approximately 30%, as the mean bias (i.e., the ratio of the observed and calculated N_p) was determined equal to 1.3.

Based on the full-scale observations reported herein, adjustments to the ultimate soil resistance appear warranted. In order to improve the performance of the Reese et al. (1975) model, it is proposed to modify p_u computed using Eqs. (8.2) and (8.3) using a model factor of 1.3 as follows:

$$p_u(z) = 2.6s_u(z) \cdot D(z) + 1.3\gamma'_{avg} \cdot D(z) \cdot z + 3.7s_u(z) \cdot z \tag{8.4}$$

$$p_u(z) = 14.3s_u(z) \cdot D(z) \tag{8.5}$$

where Eqs. (8.4) and (8.5) are formulated to compute p_u directly, rather than coefficient N_p, for ease of incorporation into software.

In the *stiff clay without free water* model (Welch and Reese 1972; Reese and Welch 1975), *p-y* curves are presented in displacement- and resistance-normalized terms. The displacement equal to that corresponding to one-half of p_u, termed, y_{50}, is used to normalize the lateral soil displacement, *y*, in the *p-y* model. In this approach, y_{50}, is termed the characteristic displacement, and is used to relate the strain within soil to the displacement of the soil-pile or soil-shaft interface. The *stiff clay without free water* model specifies that the characteristic displacement y_{50} be computed using:

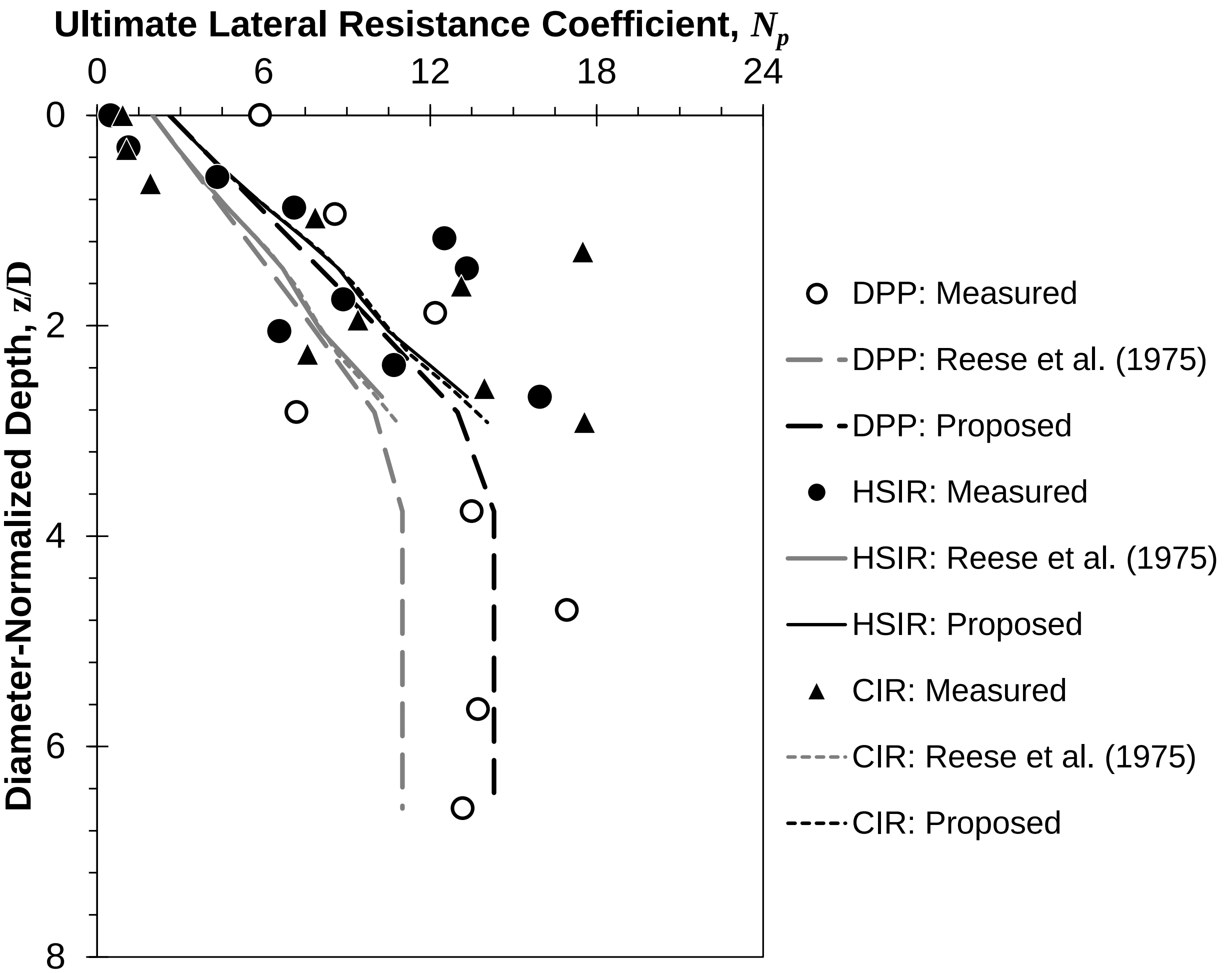

Figure 8.2 Comparison of Measured Ultimate Lateral Resistance Coefficient, N_p, to the Model from Reese et al. (1975) for Stiff Clay and the Corresponding Proposed Model for Willamette Silt

$$y_{50} = 2.5\varepsilon_{50} \cdot D \tag{8.6}$$

where ε_{50} = the strain corresponding to a shear stress equal to 50 percent of the shear strength. In the model proposed herein, the concept of a characteristic displacement was also used, though in a slightly different manner. A characteristic displacement, y_c, was defined in consideration of Eq. (8.6):

$$y_c = 2.5\varepsilon_{50} \cdot D \tag{8.7}$$

However, as described subsequently, y_c may not correspond to the displacement at one-half of the p_u. The p-y data back-calculated for HSIR and DPP at different depths were normalized by p_u and y_c, as shown in Figure 8.3. The normalized p-y data for HSIR exhibit significantly less variability than the normalized p-y data associated with CIR and DPP. When $y/y_c = 1$, the measured $p/p_u \approxeq 0.5$ for HSIR, indicating the y_c is approximately the displacement at one-half of the p_u, whereas $p/p_u \cong 0.05$ to 0.4 for CIR and $p/p_u \cong 0.1$ to 0.3 for DPP. The differences between the stiffer HSIR and softer CIR response are caused by the differences in installation (i.e., gap) effects, whereas the difference HSIR and DPP indicates the scale effects. Furthermore, differences between HSIR and the cased shaft and driven pile exist due to differences in the soil-pile interface (i.e., soil-concrete vs. soil-steel interfaces).

It appears that the normalized *p-y* data in Figure 8.3 could be modeled by a hyperbolic model for the range in displacements that are typically considered for serviceability and strength limit states. The hyperbolic model has been used extensively for soil-deep foundation interface analyses (e.g. Chin 1970, 1971; Clough and Duncan 1971; Clemence and Brumund 1975; Wong and Teh 1995; Kim et al. 1999; Cao et al. 2014; Stuedlein and Reddy 2014). The hyperbolic model is selected herein to represent and simulate the lateral load transfer response of deep foundations in Willamette Silt deposits. The functional form of the proposed region-specific normalized *p-y* curves is given by:

$$\frac{p}{p_u} = \frac{y / y_c}{\dfrac{1}{K} + \dfrac{y / y_c}{\left(p / p_u \right)_{ult}}} \qquad (8.8)$$

where K = the diameter-dependent initial stiffness, and $(p/p_u)_{ult}$ = normalized ultimate soil resistance. Since the maximum value of p/p_u is equal to one, the ratio $(p/p_u)_{ult}$ is also equal to 1.0. The initial stiffness, K_{HSIR}, for HSIR was obtained through fitting to the back-calculated, normalized *p-y* data using the ordinary least squares (OLS) method. The value of initial stiffness thus determined is $K_{HSIR} \cong 1.5$. It is noted that the estimated K_{HSIR} is only suitable for HSIR and other 1,025 mm (40 in) uncased drilled shafts in Willamette Silt; the effects of scale (or diameter) on the initial stiffness for deep foundations with other diameters should be accounted for, as described subsequently. As shown in Figure 8.3, the hyperbolic model sufficiently captures the trend of the observed normalized *p-y* data for HSIR. The mean bias (i.e., the ratio of the observed and calculated p/p_u) and COV of the observed normalized *p-y* curves and the fitted hyperbolic model for HSIR were 1.1 and 18%, respectively.

Studies by Carter (1984) and Ling (1988) proposed that the initial stiffness is proportional to the foundation diameter (Pender 1993; Lam 2013). Therefore, to account for the diameter effects, the initial stiffness of DPP can be modeled using:

$$K_{Design} = K_{ref} \cdot \frac{D_{Design}}{D_{ref}} \qquad (8.9)$$

where D_{Design} = the diameter of the foundation under design consideration, K_{ref} = initial stiffness used as a reference (in this case 1.5), and D_{ref} = the diameter used as a reference (in this case 1,025 mm or 40 in). It is noted that the use of Eq. (8.9) is typically considered as a *y*-multiplier for normalized *p-y* data. Since D_{DPP} = 325 mm (12.75 in) and D_{HSIR} = 1,025 mm (40 in) over depths ranging from the ground surface to 2.7 m (9 ft), K_{DPP} was estimated using Eq. (8.9) (where $K_{DPP} = K_{Design}$) and was equal to 0.48. Figure 8.3a compares the observed normalized *p-y* curves for DPP and the hyperbolic model using $K_{DPP} = 0.48$. The hyperbolic model appears suitable to represent the observed normalized *p-y* curves for DPP. The mean bias and COV of the observed normalized *p-y* curves and the fitted hyperbolic model for DPP were 0.96 and 36%, respectively. Thus, Eq. (8.9) is sufficiently suitable for accounting for scale effects and where HSIR serves as the reference shaft and diameter. However, this study is based on the test data from two deep foundations with average diameter of 325 and 1,025 mm (12.75 and 40 in) in Willamette Silt. Use of Eq. (8.9) for deep foundations larger than 1,025 mm (40 in) should be done cautiously, but will be consistent with previously-reported efforts (Carter 1984; Ling 1988; Pender 1993; and Lam 2013).

If only scale effects were considered for CIR with D_{CIR} = 940 mm (37 in), the initial stiffness $K_{CIR,scale}$ = 1.4 according to Eq. (8.9). The hyperbolic model using Eq. (8.9) for CIR is shown in Figure 8.3b with mean bias and COV of the observed normalized *p-y* data and the fitted hyperbolic model of 0.48 and 63%, respectively. It appears that the consideration of *only* scale effects over-predicts the p/p_u by two times for a given y/y_c. To investigate the combined effect of installation and interface roughness, the fitted initial stiffness, $K_{CIR,}$ was obtained and determined equal 0.3. The ratio of $K_{CIR}/K_{CIR,scale}$ can be considered as a representation of the combined installation and interface effects, appropriate for the use with permanent steel casing when vibrated into an excavated drilled shaft borehole. Therefore, for a cased drilled shaft installed in the same manner as CIR and exhibiting similar borehole-casing gapping, the initial stiffness may be estimated by the following:

$$K_{cased} = \frac{K_{CIR}}{K_{CIR,scale}} K_{uncased} = \frac{0.3}{1.4} K_{uncased} \cong 0.2 K_{uncased} \tag{8.10}$$

Based on the comparison of HSIR and DPP, it is likely that had remedial, post-construction grouting of the gaps between the casing and the soil been conducted, that no casing reduction factor to the initial *p-y* curve stiffness, *K*, would be necessary. This speculation should be confirmed in future research efforts.

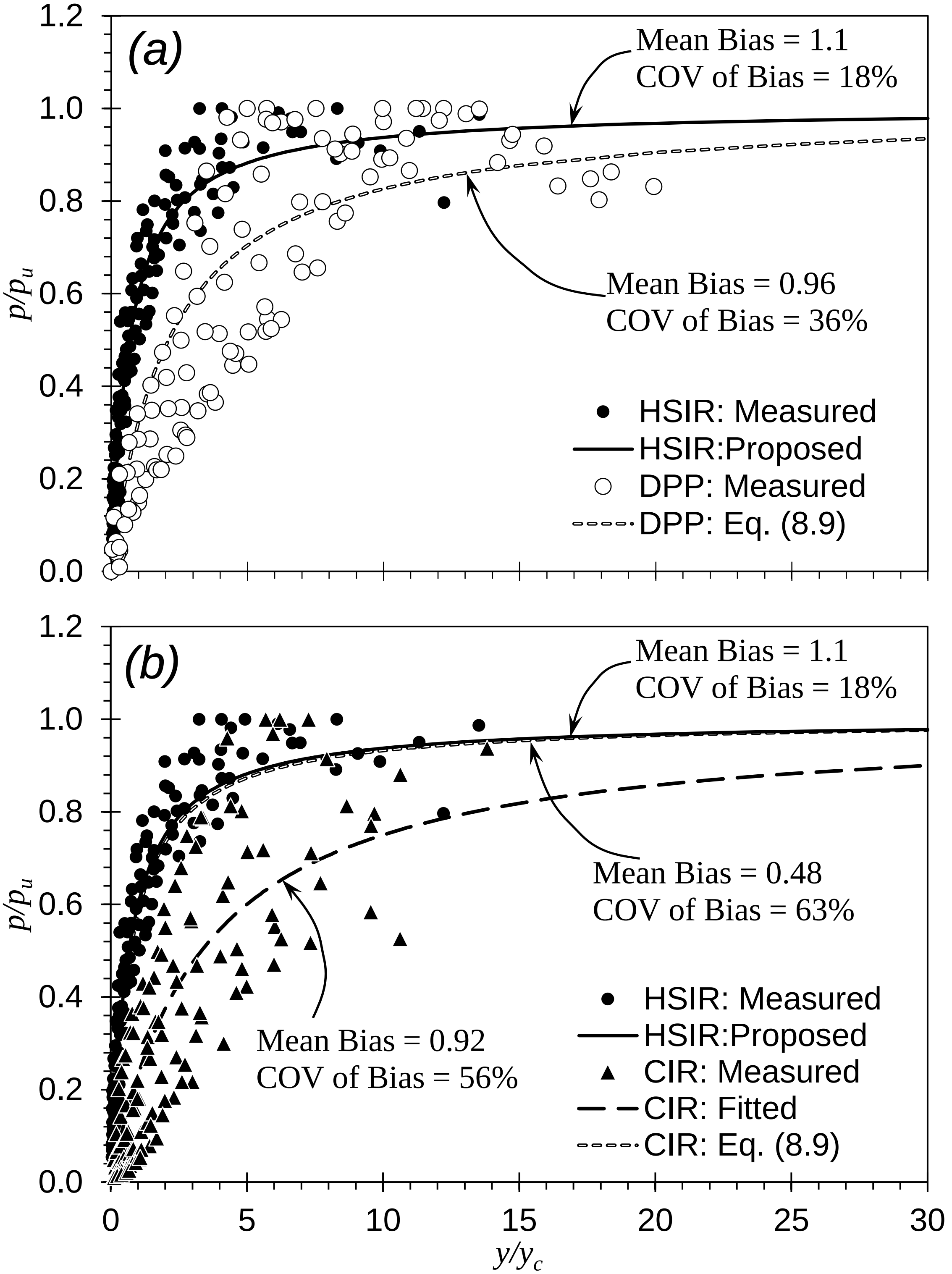

Figure 8.3 Comparison of normalized *p-y* curves for (a) HSIR and DPP, and (b) HSIR and CIR, and the corresponding models proposed for Willamette Valley Silt and adjusted for scale, where appropriate.

8.4 PARAMETRIC STUDY OF SCALE EFFECTS ON THE WILLAMETTE SILT *P-Y* CURVES

A comparison of *p-y* curves for various foundation diameters was conducted to study the role of scale effects using the proposed *p-y* curve model [Eq. (8.9)]. The diameters investigated ranged from 0.3 to 1.2 m (12 to 48 in) at depths ranging from ground surface to 2.4 m (8 ft). It was assumed that the foundations were installed in a uniform deposit of Willamette Silt with s_u = 100 kPa (2,100 psf), γ'_{avg} = 17 kN/m^3 (100 pcf), and ε_{50} = 0.005. The diameter-dependent initial stiffness, *K*, was determined using HSIR as reference with K_{ref} = 1.5. Table 8.1 summarizes the foundation diameters, *D*, and depths with estimated y_c and p_u, computed using Eqs. (8.7) and (8.4) or (8.5), respectively. The characteristic displacement, y_c, is independent of depth for a soil deposit with uniform s_u, and ranges from 3.8 to 15.2 mm (0.15 to 0.60 in) for diameters ranging from 0.3 to 1.2 m (12 to 48 in). The ultimate lateral soil resistance, p_u, depends on both depth and diameter, as discussed above. It is noted that as the failure mode changes from the 3D passive wedge failure mechanism to the 2D flow failure mechanism, the p_u reaches the maximum value as indicated by Eq. (8.5). For example, for *D* = 0.3 m (12 in), the transition depth from passive wedge to flow failure mechanism was at approximately 0.9 m or 3 ft (3*D*).

Figure 8.4 compares the *p-y* curves at selected depths for foundations with various diameters. It appears that at each depth the initial stiffness of the *p-y* curves increases with the increase of diameter as indicated by Eq. (8.9). At shallow depths, the initial stiffness and ultimate lateral soil resistance for a given foundation diameter increases with increases in depth, indicative of the passive wedge failure mechanism. As depths increase, and as the flow failure mechanism controls (e.g., compare *p-y* curves for the 0.3 m diameter foundation at depths of 1.2 and 2.4 m), the *p-y* curve becomes independent of depth.

8.5 SUMMARY AND CONCLUSIONS

The experimentally-derived lateral load transfer data was used to explore the differences between a widely-accepted *p-y* curve model, and differences between three different types of instrumented foundations tested at full-scale a the GEFRS at Oregon State University. The three foundations included the 1,025 mm (40 in) diameter drilled shaft HSIR, the 940 mm (37 in) diameter cased shaft CIR, and the 325 mm (12.75 in) diameter driven steel pipe pile DPP. Significant differences in the observed *p-y* curves was noted between these various deep foundations, however, they all shared similar trends in the ultimate lateral soil resistance. The trends in ultimate lateral soil resistance also differed from that computed using the widely-accepted *p-y* curve model, indicating that the region-specific model for ultimate lateral soil resistance proposed herein will be more suitable for various types of deep foundations constructed in this region.

A methodology to scale the initial stiffness of the region-specific *p-y* curves determined using the proposed model was also developed, based on consideration of previously-reported efforts, to account for differences in foundation diameter. The scaling approach was found to suitably predict the response of the small-diameter driven pipe pile when using the larger diameter HSIR as a reference. Permanently-cased drilled shafts, constructed using the same approach as for CIR, can also be evaluated using the proposed region-specific *p-y* curve model when adding a scale factor to account for the interface roughness and installation effects. Although this option is now available for designers, it is recommended that any suspected anomalies (e.g., gaps) between the casing and drilled shaft borehole be post-grouted to ensure good coupling between the shaft and the soil and to improve the load transfer characteristics.

Table 8.1: Summary of Foundation Diameters, *D*, and Depths with Estimated y_c and p_u Using Proposed Model

Depth	y_c and p_u	*D* = 0.3 m (12 in)	*D* = 0.6 m (24 in)	*D* = 0.9 m (36 in)	*D* = 1.2 m (48 in)
Ground Surface	y_c, mm (in)	3.8 (0.15)	7.6 (0.30)	11.4 (0.45)	15.2 (0.60)
	p_u, kN/m (kips/in)	85 (0.49)	171 (0.97)	256 (1.46)	341 (1.95)
0.6 m (2 ft)	y_c, mm (in)	3.8 (0.15)	7.6 (0.30)	11.4 (0.45)	15.2 (0.60)
	p_u, kN/m (kips/in)	331 (1.89)	421 (2.40)	511 (2.92)	601 (3.43)
1.2 m (4 ft)	y_c, mm (in)	3.8 (0.15)	7.6 (0.30)	11.4 (0.45)	15.2 (0.60)
	p_u, kN/m (kips/in)	469 (2.68)	671 (3.83)	766 (4.37)	860 (4.91)
2.4 m (8 ft)	y_c, mm (in)	3.8 (0.15)	7.6 (0.30)	11.4 (0.45)	15.2 (0.60)
	p_u, kN/m (kips/in)	469 (2.68)	939 (5.36)	1259 (7.19)	1362 (7.78)

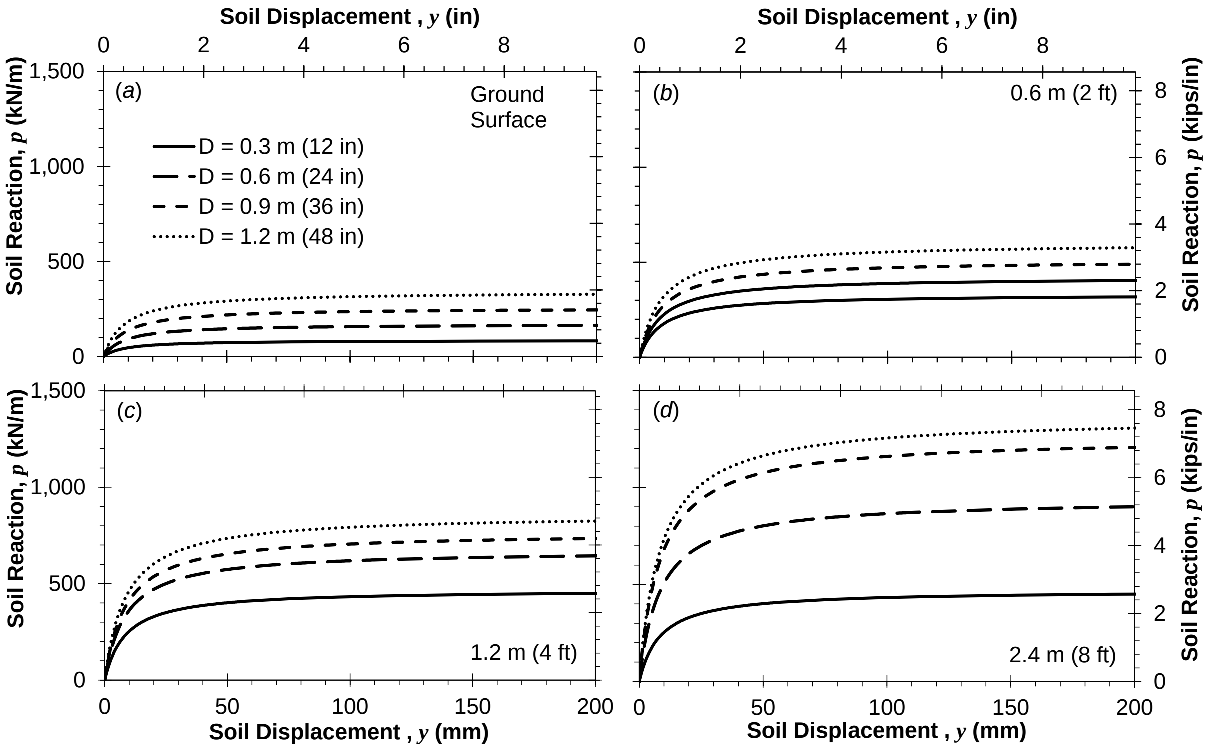

Figure 8.4 Comparison of *p-y* curves derived from the proposed Willamette Valley Silt model at selected depths for deep foundations with various diameters

9.0 SUMMARY AND CONCLUSION

The main objective of this report is to improve the understanding of the axial and lateral load transfer of drilled shaft foundations constructed with high strength steel reinforcement and with steel casing. To accomplish this objective, four full-scale test shafts were instrumented and installed at the Oregon State University (OSU) Geotechnical Engineering Field Research Site (GEFRS). Two uncased shafts were constructed, one using mild steel and one using high strength steel reinforcement, designated MIR and HSIR, respectively, and two shafts with steel casing and with and without internal mild steel reinforcement, designated CIR and CNIR, respectively. The comparison of the cased and uncased shafts was intended to determine differences in axial load transfer. Owing to limited anticipated differences in the axial loading of the two cased shafts if constructed using the same auger diameter, an additional construction variable, that of the auger diameter, was investigated to compare differences in axial load transfer that would result. Accordingly, shaft CNIR was drilled with a 940 mm (37 in) diameter auger (i.e., the same size diameter as that of the casing), whereas CIR was drilled with a slightly smaller, 915 mm (36 in) diameter auger. The comparison of uncased shafts MIR and HSIR was intended to determine if differences in longitudinal steel area (due to the use of high strength bar) would significantly affect the flexural response during lateral loading. The comparison of cased shafts CIR and CNIR was intended to determine whether the presence of internal steel would significantly affect the flexural response during lateral loading. This chapter identifies specific conclusions stemming from the comparison of performance, separated into performance in axial and lateral loading.

9.1 AXIAL LOAD TRANSFER

The axial loading tests were used to compare various performance metrics between the cased and uncased shafts, including the axial load-displacement curves, load transfer distributions, and back-calculated unit shaft resistance-relative displacement relationships (*t-z* curves) and unit toe resistance-toe displacement relationships (*q-z* curves). Specific conclusions include:

1. The effect, of using augers of slightly different diameter was shown to greatly impact the axial resistance of the cased shafts. Shaft CIR, constructed with the smaller, 915 mm (36 in) diameter auger for the 940 mm (37 in) diameter casing, exhibited approximately 45% greater axial resistance than the shaft with the larger diameter. Therefore, when constructing permanently cased drilled shafts, field engineers must confirm that the auger diameter specified for use is actually used prior to commencing the excavation of the borehole.

2. The axial resistance of shafts CIR and CNIR was fully-mobilized at the applied load of approximately 1,960 kN (440 kips) and 1,330 kN (300 kips), respectively. These shafts plunged to final displacements of 84 and 74 mm (3.3 and 2.9 in) prior to termination of the tests.

3. The axial resistance of the uncased shafts was not fully-mobilized during the loading tests. The load applied to shafts MIR and HISR was 6,125 kN (1377 kip) and 6,380 kN (1,435 kip) with corresponding displacement of 4.3 mm (0.17 in) and 3.8 mm (0.15 in).

These shafts, constructed with the same nominal (i.e., auger) diameter as CIR, produced significantly better axial performance than the cased shafts.

4. The uncased shafts exhibited significantly greater axial shaft resistance as compared to the cased shafts due to the rougher soil-concrete interface and larger as-built diameter of the uncased test shafts, and to the presence of gaps between the soil and casing for the cased shafts. For, example, although axial resistance of shaft MIR was not fully mobilized at end of the axial loading test, it still exhibited 210% more axial resistance comparing to the fully-mobilized axial resistance of shaft CIR.

5. Empirical *t-z* (shaft resistance) and *q-z* (toe resistance) curves were developed based on the results of the load tests, appropriate for use in similar soils in the Willamette Valley.

6. A direct CPT-based method for estimating the axial load transfer curves for uncased shafts in similar soils was proposed and can be used to extend the results of the load test program to design of bridge foundations in the Willamette Valley.

7. The effect of casing on axial load transfer characteristics was evaluated based on load test data reported in the literature as well as with the load testing results from this study. The effect of installation method and construction sequence was found to play a critical role in the quality and quantity of axial load transfer. Table 6.7 should be referred to for guidance in determining appropriate casing reduction factors.

9.2 LATERAL LOAD TRANSFER

The results of the lateral loading tests, including the performance at the head of the shaft, the lateral displacement profiles, and the back-calculated curvature, moment, and soil reaction-displacement (*p-y*) curves were compared to form the following findings:

1. The lateral resistance of the uncased shafts was fully-mobilized at the applied load of approximately 890 kN (200 kips) and at applied displacement of approximately 150 mm (6 in).

2. The uncased shafts exhibited a similar lateral response to applied displacements of approximately 190 mm (7.5 in), with minor differences at small displacements.

3. Towards the end of the lateral loading test, MIR exhibited larger lateral displacement than HSIR, possibly due to: (1) the slightly higher moment capacity of HSIR for $\phi \geq 0.2$ m^{-1}, and (2) inherent variability of the soil stiffness and strength. Both test shafts exhibited plastic hinging at large displacements, indicating loss of flexural resistance.

4. Based on the results of the loading test program, it appears that there is no evidence to suggest that the use of high-strength (Grade 80) reinforcement will result in detrimental or poorer lateral performance as compared to a shaft constructed to the same axial and flexural capacity with Grade 60 steel.

5. Due to the significantly greater flexural resistance, the cased shafts transferred load to significantly greater depths than the uncased shafts. The maximum depth of the

mobilized soil-foundation displacement for the cased shafts at the highest load is approximately 9.0 m (30 ft), or $10D_n$ (D_n = nominal diameter), whereas it is approximately 3.7 m (12 ft), or $4D_n$, for the uncased shafts.

6. The lateral resistance of the cased shafts was not fully-mobilized during the loading tests, despite reaching significantly greater loads than the uncased shafts. The maximum load applied to shafts CIR and CNIR was 1,540 kN (346 kip) with corresponding displacement of 213 and 205 mm (8.4 and 8.1 in), respectively. Cased shafts will respond in a more resilient manner than uncased shafts at the same nominal diameter due to their significantly greater flexural rigidity.

7. Although the moment capacity of CIR was approximately 40% larger than that of CNIR, the differences in capacity did not result in significant differences in performance for the displacements imposed.

8. The results of the lateral loading test program were used to develop empirical soil reaction-displacement (*p-y*) curves appropriate for use in Willamette Silt soils.

9. The comparison of the *p-y* curves for each test shaft shows that the rougher soil-foundation interface and larger diameter lead to larger unit soil resistances at given soil displacements.

10. A *p-y* curve model suitable for Willamette Silt was proposed and can be readily implemented into commonly used software.

11. Recommendations to account for pseudo-scale effects due to the increasing contribution of shaft resistance to lateral resistance with increased diameter were proposed. The recommendations can be seamlessly incorporated into the proposed *p-y* curve model for Willamette Silt. The scaling relationship is appropriate for foundations with diameters ranging from 325 to 1,025 mm (12.75 to 40 in), but should be used cautiously for larger diameters until data from larger diameter foundations can be obtained.

9.3 SUGGESTIONS FOR FURTHER STUDY

The results of this study can be used as a basis for specifying high-strength steel and permanent casing in drilled shaft design and construction practice. However, several new questions arose over the course of this research. Suggestions for further study include

1. The investigation of the performance of drilled shafts with Grade 97 bar to further open the reinforcement cage and reduce the rate of suspected anomalies. Such a study could identify the limiting yield stress that would cause a significant softening of the moment-curvature relationship and result in less desirable displacement performance of test shafts.

2. The investigation of casing reduction factors for shaft resistance that focuses on the effect of construction sequence and installation method at the GEFRS site. Examples include vibro-installation followed by shaft excavation, impact driven-installation followed by excavation, and oscillation-installation followed by excavation. These additional three

studies would complete the picture regarding method and sequence of installation on the magnitude of shaft resistance along soil-steel interfaces.

3. The investigation of the lateral response of larger diameter shafts to improve the empirical basis for the scaling law recommended herein. To augment the data derived from the 325 mm (12.75 in), 940 mm (37 in) and 1025 mm (40 in) diameter foundations studied herein, instrumented shafts with diameters of 1,830 mm (72 in) and 3,660 (144 in) could be constructed and tested laterally as done herein and corresponding *p-y* curves determined. The scaling relationship could then be evaluated and adjusted as necessary.

4. Sophisticated three-dimensional (3D) numerical models could be developed by calibrating to the model response to the full-scale data developed as part of this research and then used to investigate scale effects on the lateral load responses of drilled shafts until larger diameter shafts become available for testing.

10.0 REFERENCES

Abendroth, Robert E.; Greimann, Lowell F.; & Ebner, Patrick B. (1989, November). Abutment pile design for jointless bridges, *Journal of Structural Engineering*, 115 (11), 2914-2929.

Alsamman, O.M. (1995). *The use of CPT for calculating axial capacity of drilled shafts* (Doctoral dissertation). Urbana-Champaign, IL: University of Illinois at Urbana-Champaign, IL.

American Association of State Highway and Transportation Officials (AASHTO). (2007). *LRFD Bridge Design Specifications* (4th ed., 2008–2009 interims). Washington, D.C.

American Association of State Highway and Transportation Officials (AASHTO). (2009). *LRFD Bridge Design Specification*. Washington, D.C.

American Association of State Highway and Transportation Officials (AASHTO). (2014). *LRFD Bridge Design Specifications* (7th ed.). Washington, D.C.

American Concrete Institute (ACI). (2008). Building code requirements for reinforced concrete and commentary. *ACI Committee 318*, Farmington Hills, MI.

American Concrete Institute (ACI). (2014). Building code requirements for structural concrete (ACI 318-14) and commentary (318R-14). *ACI Committee 318*, Farmington Hills, MI.

American Institute of Steel Construction (AISC). (2005). *Specifications for Structural Steel Buildings*. ANSI/AISC Standard 360-05, Chicago, IL: American Institute of Steel Construction.

American Petroleum Institute (API). (1987). Recommended practice for planning, designing, and constructing fixed offshore platforms. *API Recommended Practice 2A* (RP-2A) (17th ed.). Washington, D.C.

American Petroleum Institute (API). (1993). *Recommended practice for planning, designing and constructing fixed offshore platforms - Working stress design* (20th Ed.) (API RP2A-WSD). Washington, D.C.: Errata and Supplement

American Petroleum Institute (API). (2010). *Recommended practice for planning, designing and constructing fixed offshore platforms - Working stress design* (21st Ed.) (API RP 2A-WSD). Washington, D.C.: Errata and Supplement

Armaleh, S., & Desai, C.S. (1987). Load-deformation response of axially loaded piles. *Journal of Geotechnical Engineering*, *113*(12), 1483-1500.

Ashour, M., Pilling, P., Norris, G., & Perez, H. (1996). *Development of a strain wedge model program for pile group interference and pile cap contribution effects* (Publication No. FHWA/CA/TL-96/28).

Ashour, M., Norris, G., & Pilling, P. (1998). Lateral loading of a pile in layered soil using the strain wedge model. *Journal of Geotechnical and Geoenvironmental Engineering*, 124(4), 303-315.

Ashour, M., Norris, G.M., & Elfass, S. (2004, June). *Analysis of laterally loaded intermediate or long drilled shafts of small or large diameter in layered soil*. (Report No. CCEER-06-04). Contract No. 59A0348. Reno, NV: Civil Engineering Dept. University of Nevada.

ASTM International. (2014a) *Standard test method for integrity testing of concrete deep foundations by ultrasonic crosshole testing* [ASTM D 6760]. pp. 7, West Conshohocken, PA.

ASTM International. (2014b). *Standard test methods for thermal integrity profiling of concrete deep foundations* (ASTM D7949). Retrieved from www.astm.org.

Au, S.W.C., & Lo, C.R. (1993, September 5-9). Use of waterhead support in the construction of large diameter bored piles: potential savings and problems. *In Proceedings of the 11th Southeast Asian Geotechnical Conference,* 489–494. Singapore

Baguelin, F., et al. (1975) La capacité portante des pieux. *Annales Institut Technique du Bâtiment et des Travaux Publics*, 330(116). 1-22, France.

Baguelin, F., Jézéquel, J.F., & Shields, D.H. (1978). *The pressuremeter and foundation engineering* (1st ed.). Causthal, Germany: Trans. Tech Publications.

Baldi, G., R. Bellotti, V.N. Ghionna, M. Jamiolkowski, & D.F.C. Lo Presti. (1989). Modulus of sands from CPTs and DMTs. *Proceedings, 12th International Conference on Soil Mechanics Foundations*, I, 165-170. Rio de Janeiro, Brazil.

Barbosa, A.R. (2011). Simplified vector-valued probabilistic seismic hazard analysis and probabilistic seismic demand analysis: Application to the 13-story NEHRP reinforced concrete frame-wall building design example (Doctoral thesis). San Diego, CA: Dept. of Structural Engineering, University of California.

Barbosa, A.R., Link, T., & Trejo, D. (2015). Seismic performance of high-strength steel RC bridge columns. *ASCE J. Bridge Eng*. http://ascelibrary.org/doi/abs/10.1061/(ASCE)BE.1943-5592.0000769

Bierschwale, M.W. Coyle, H.M., & Bartoskewitz, R.E. (1981). Lateral load tests on drilled shafts founded in clay. In M.W. O'Neill (Ed.), *Drilled Piers and Caissons*, 98-113. New York, NY.

Briaud, J.L. &. Shields, D.H. (1979). A special pressuremeter and pressuremeter test for pavement evaluation and design," *Geotechnical Testing Journal*, ASTM 23.

Briaud, J.L., Smith, T.D., & Meyer, B. (1982). Design of laterally loaded piles using pressuremeter test results. *In Proc. Symp. Pressuremeter and its Marine Applications* (pp. 377-395).

Briaud, J., Smith, T., & Meyer, B. (1983). Pressuremeter gives elementary model for laterally loaded piles, *International. Symposium on In Situ Testing of Soil and Rock*, Paris, France.

Briaud, J.L., Smith, T., & Mayer, B. (1984). Laterally loaded piles and the pressuremeter: comparison of existing methods. *Laterally loaded deep foundations: Analysis and performance*, *835*, 97-111.

Brinch J.H. (1961). The ultimate resistance of rigid piles against transversal forces. *Bulletin No. 12*, 5–9, Copenhagen, Denmark: Danish Geotechnical Institute.

Broms, B.B. (1964a). Lateral resistance of piles in cohesive soil. *Journal of Soil Mechanics and Foundation Division*, 90(2), 27-64.

Broms, B.B. (1964b). Lateral resistance of piles in cohesionless soil. *ASCE Journal for Soil Mechanics and Foundation Division*, 90(SM3), 123-156

Brown, D.A. & Camp, W.M. (2002). Lateral load testing program for the cooper river bridge, Charleston, SC. *Deep Foundations 2002*, pp. 95-109, Reston, VA: ASCE.

Brown, D.A., Morrison, C. & Reese, L.C. (1988). Lateral load behavior of pile group in sand. *Journal of Geotechnical Engineering*, 114(11), 1261-1276.

Brown, D., Shie, C., & Kumar, M. (1989). P-y curves for laterally loaded piles derived from three dimensional finite element model. *Proceedings from the 3rd International Symposium on Numerical Models in Geomechanics*. 683-690. Niagara Falls, Canada.

Brown, D.A., Turner, J.P., & Castelli, R.J. (2010). *Drilled shafts: Construction procedures and LRFD design methods* (Report No. FHWA-NHI-10-016). Washington, D.C.: U.S. Department of Transportation, Federal Highway Administration.

Budek. A.M. (1997). *The inelastic behavior of reinforced concrete piles and pile shaft* [Dissertation]. San Diego, CA: University of California.

Burland, J.B. Butler, F.G., & Dunicon, P. (1966, February). The behavior and design of large diameter bored piles in stiff clay, large bored piles. *Proceedings of the Symposium organized by the Institution of Civil Engineers and the Reinforced Concrete Association of the Institution of Civil Engineers,* 51-71. London, U.K.: Institution of Civil Engineers.

Bustamante, M. & Gianeselli, L. (1982). Pile bearing capacity prediction by means of static penetrometer. *Proceedings from the European Symposium on Penetration Testing*, 2, 493-500. Amsterdam, Denmark.

Butterfield, R., & Banerjee, P.K. (1971). The elastic analysis of compressible piles and pile groups. *Geotechnique*, *21*(1), 43-60. London, UK.

Caltrans (1986). *Bridge design specifications manual*. Sacramento, CA: California Department of Transportation.

Camp, W.M., Brown, D.A., & Mayne, P.W. (2002). Construction methods effects on drilled shaft axial performance. *Deep foundations 2002* (Geotechnical Special Publication No. 116), M.W. O'Neil and F.C. Townsend (Eds.), pp. 193-208. Reston, VA: ASCE.

Camp, W.M. (2017, June 28). Personal communication.

Cao, W., Chen, Y., & Wolfe, W.E. (2014). New load transfer hyperbolic model for pile-soil interface and negative skin friction on single piles embedded in soft soils. *Int. J. Geomech*., 14(1), 92–100

Carter, D. (1984). *A nonlinear soil model for predicting lateral pile response* (Report No. 359), Auckland, New Zealand: Civil Engineering Department, University of Auckland.

Chai Y.H. (2002). Flexural strength and ductility of extended pile-shafts. i: analytical model. *Journal of Structural Engineering*, 128(5), 589-594.

Chai. Y.H., & Hutchinson. T.C. (1999). *Flexural strength and ductility of reinforced concrete bridge piles* [Final Report]. Report Xo. UCD-STR-99-2. Davis, CA: Department of Civil & Environmental Engineering. University of California, Davis.

Chen, Y.J. & Kulhawy, F.H. (1994). *Case history evaluation of the behavior of drilled shafts under axial and lateral loading* (TR-104601). 1493-04, Palo Alto, CA: Electric Power Research Institute.

Chen, Y.J. & Kulhawy, F.H. (2002). Evaluation of drained axial capacity for drilled shafts. *Proceedings from Deep Foundations 2002* [Geotech. Spec. Publication] 2(116), 1200–1214. Reston, VA: ASCE.

Chilingarian, G.V., and Vorabutr, P. (1981). *Drilling and drilling fluids,* Elsevier, Amsterdam.

Chin, T.K. (1970). Estimation of the ultimate load of piles from tests not carried at failure. *Proceedings from Second South East Asian Conference Soil Mechanics.* Found. Engrg., Singapore.

Chin, F.K. (1971). Discussion of pile test, Arkansas River project. *Soil Mech. and Found. Div*., 97(6), 930-932.

Chow, Y.K. (1986). Analysis of vertically loaded pile groups. *International Journal for Numerical and Analytical Methods in Geomechanics*, 10, 59-72.

Chow, F.C. (1996) *Investigations into the behaviour of displacement piles for offshore foundations* [Doctoral thesis]. London, UK : Imperial College of Science, Technology, and Medicine, University of London.

Clemence, S.P., & Brumund, W.F. (1975). Large-scale model test of drilled pier in sand. *Journal of Geotech. Engrg. Div*., 101(6), 537–550.

Clough, G.W., & Duncan, J.M. (1971). Finite element analyses of retaining wall behavior. *Journal of Soil Mech. Found. Div.,* 97(12), 1657–1673.

Cooke R.W. (1974). The settlement of friction pile foundations. *Proceedings from the Conference on Tall Buildings,* pp. 7–19. Kuala Lumpur.

Cook, R.D., Malkus, D.S., & Plesha, M.E. (1989). *Concepts and Applications of Finite Element Analysis*. New York, NY: John Wiley & Sons, Inc.

Coyle, H.M., & Reese, L.C. (1966). Load transfer for axially loaded piles in clay. *Journal of Soil Mechanics and Foundations Div*, 92. SM2.

Coyle, H.M., & I.H. Sulaiman. (1967). Skin friction for steel piles in sand. *Journal of the Soil Mechanics and Foundation Division*, 93(SM6), 261-278.

Coyle, H.M., Bartoskewitz, R.E., & Berger, W. J. (1973). *Bearing capacity prediction by wave equation analysis – State of the art* (Report 125-8F), pp 1-118. Texas Transportation Institute, Research

Cox, W.R., Reese, L.C., & Grubbs B.R. (1974). Field testing of laterally loaded piles in sand. *Proceedings from 6th Offshore Technology Conference,* OTC 2079, 2, 459-472.

Darragh, R.D., & Bell, R.A. (1969). Load tests on long bearing piles. *Performance of Deep Foundations*, ASTM STP-444, pp 41-67

Davidson, H.L., Cass, P.G., Khilji, K.H., & McQuade, P.V. (1982). *Laterally loaded drilled pier research* [Report EL-2197]. Palo Alto, CA: Electric Power Res. Institute.

Davisson, M.T. (1970). Lateral load capacity of piles. *Highway Research Record,* No. 333, 104–112.

Davisson, M.T., & Gill, H.L. (1963). Laterally loaded piles in a layered soil system. *J. Soil Mech. Found. Div*., 89~3, 63–94.

Det Norske Veritas. (1980). *Rules for the design, construction, and inspection of offshore structures, Appendix F: Foundations*. Hovik, Norway: Det Norkes Veritas.

Dickenson, S.E. & Haines, B.Z. (2006). *Characterization of the geotechnical engineering field research site at Oregon State University* (3rd Ed.). Corvallis, OR: Oregon State University.

Dordi VI, C. (1977). Horizontally loaded piles in layered soils. Proc. of Specialty Session 10. The Effect of Horizontal Loads on Piles due to Surcharge of Seismic Effects. *Ninth international Conference on Soil Mechanics and Foundation Engineering*. 65-70. Tokyo, Japan.

Dowrick, D.J. (1987). *Earthquake resistant design* (2nd Ed.). New York, NY: Wiley-Interscience.

Duncan, J.M., & Chang, C.Y. (1970). Nonlinear analysis of stress and strain of soil. *J. Soil Mech. and Found*. Div., 96(5), 1629–1653.

Duncan, M., Evans, L.T. & Ooi, P.S.K. (1994). Lateral load analysis of single piles and drilled shafts. *J. Geotech. Engng., Am. Soc. Civ. Engrs.* 120(5), 1018-1033.

Dunnavant, T.W. (1986), *Experimental and analytical investigation of the behavior of single piles in overconsolidated clay subjected to cyclic lateral loads* [Doctoral Dissertation]. Houston, TX : University of Houston.

Dunnavant, T.W. & O'Neill, M.W. (1989). Experimental p-y model for submerged, stiff clay. *Journal of Geotechnical Engineering,* 115(1), 95-114.

East Japan Railway, Co., Tekken Construction Co., & Chiyoda Construction Co. (1996). *Evaluation of bearing capacities of a deep diaphragm wall, final report on load testing.* Rep. No. 7(7). Tokyo, Japan: East Japan Railway, Tokyo Construction Office.

Elgamal, A., Lu, J., & Mackie, K. (2014). *MSBridge: OpenSees pushover and earthquake analysis of multi-span bridges-user manual.* Rep.No. SSRP–14/04. Sacramento, CA California Department of Transportation (Caltrans).

Eslami, A. (2006). Bearing capacity of shallow and deep foundations from CPT resistance. *Proceedings from GeoCongress*, 6. Atlanta, GA.

Eslami, A., & Fellenius, B.H. (1997). Pile capacity by direct CPT and CPTu methods applied to 102 case histories. *Canadian Geotechnical Journal, 34*(6), 886-904.

Fahey, M., & J.P. Carter. A finite element study of the pressuremeter test in sand using a non-linear elastic-plastic model. *Canadian Geotechnical Journal*, 30(2), 1993 pp. 348-362.

Fellenius, B.H. (1989). Tangent modulus of piles determined from strain data. *Proc., 1989 Found. Congr* (Special Technical Publication No. SPT 22). F.H. Kulhawy (Ed.), Vol. 1, 500–510. Reston, VA: ASCE.

Fellenius, B.H. (2017). *Basics of foundation design* [Electronic edition]. Retrieved from www.fellenius.net.

Fioravante, V., Ghionna, V.N., Jamiolkowski, M., & Pedroni, S. (1995). Load carrying capacity of large diameter bored piles in sand and gravel. *Proceedings of 10th Asian regional conference on soil mechanics and foundation engineering, Beijing*, 2, Beijing, China. 3-15.

Fleming, W.G.K., Weltman, A.J., Randolph, M.F., & Elson, W.K. (1992). *Piling engineering*. London, UK: Surrey University Press.

Frank, R. (1974) *Etude théorique du comportement des pieux sous charge verticals: Introduction de la dilatance.* (Dr-Ing thesis). France: Université Pierre et Marie Curie.

Gabr, M. & Borden, R. (1988). Analysis of Load Deflection Response of Laterally Loaded Piers Using DMT, *Penetration Testing 1988*, ISOPT-1., A.A. Balkema, Rotterdam, 513-520.

Gambin, M.P. & Rousseau, J. (1988). The Menard pressuremeter: interpretation and application of pressuremeter test results to foundation design. *ISSMFE Technical Committee on Pressuremeter and Dilatometer Testing, General Memorandum*, Sols Soils No. 26, pp. 50.

Gebman, M., Ashford, S.A, & Restrepo, J.I. (2006). *Axial force transfer mechanisms within cast-in-steel-shell piles* (Report No. SSRP-94/10). La Jolla, CA: Department of Structural Engineering, University of California at San Diego.

Georgiadis, M. (1983). Development of p-y curves for layered soils. *Geotechnical practice in offshore engineering*, 536–545. Reston, VA: ASCE.

Georgiadis, M., Anagonostopoulos, C., & Saflekou, S. (1991). Interaction of laterally loaded piles. *Proceedings from Foundations Profondes*, Ponts et Chaussees, Parus, 177-184.

Georgiadis, K., & Georgiadis, M. (2010). Undrained lateral pile response in sloping ground. *Journal of geotechnical and geoenvironmental engineering*, *136*(11), 1489-1500.

Gray, G.R., Darley, H.C.H., & Rogers, W.F. (1980), *Composition and Properties of Oil Well Drilling Fluid* (4th ed.). Houston, TX: Gulf Publishing Company.

Greimann, L. & Wolde-Tinsae, A.M. (1988, June). Design model for piles in jointless bridges. *Journal of Structural Engineering*, 114(6), 1354-1371.

Grosch, J., & Reese, L. (1980). Field tests of small-scale pile segments in a soft clay deposit under repeated axial loading. *Proceedings, 12th offshore Technology Conference*, 4, Houston, TX, 143-151.

Guo, W.D. (2000). Vertically loaded single piles in Gibson soil. *J. Geotech. Geoenviron. Eng*., 126(2), 189–193.

Guo, W.D., & Randolph, M.F. (1998). Rationality of load transfer approach for pile analysis. *Comp. and Geotechnics*, 23(1–2), 85–112.

Gunaratne, M. (2006). *The foundation engineering handbook*. Boca Raton, FL: CRC Press.

Halang, W.A., Langlais, R., & Kugler, E. (1978). Cubic spline interpolation for the calculation of retention indices in temperature-programmed gas-liquid chromatography. *Analytical Chemistry*, 50(13), 1829-1832.

Hansen, JB. (1970). Revised & extended formula for bearing capacity, *Bulletin 28,* 5-11. Copenhagen, Denmark: Danish Geotech. Institute.

Hassan, T.K., Seliem, H.M., Dwairi, H., Rizkalla, S.H., & Zia, P. (2008). Shear behavior of large concrete beams reinforced with high-strength steel," *ACI Structural Journal*,105(2), 173–179.

Hetenyi, M. (1946). *Beams on elastic foundations*. Ann Arbor, MI: University of Michigan Press.

Hognestad, E. (1951). *A study on combined bending and axial load in reinforced concrete members*. 43–46. Urbana-Champaign, IL: Engineering Experiment Station, University of Illinois, Urbana-Champaign.

Holmquist, D.V. & Matlock, H. (1976). Resistance-Displacements Relationships for Axially Loaded Piles in Soft Clay. *Proceedings, 8th offshore Technology Conference*, Vol. 1, 553-569. Houston, TX

Huffman, J.C., & Stuedlein, A.W. (2014). Reliability-based serviceability limit state design of spread footings on aggregate pier reinforced clay. *J. Geotech. Geoenviron. Eng.,* DOI: 10.1061/(ASCE)GT.1943-5606.0001156, 04014055.

Huffman, J.C., Strahler, A.W., & Stuedlein, A.W. (2015) Reliability-based serviceability limit state design for immediate settlement of spread footings on clay, *Soils and Foundations,* 55(4), 798-812.

Hulsey, J.L., Horzdovsky, J.E., Davis, D., Yang, Z.J., & Li, Q. (2011). *Seasonally frozen soil effects on the seismic performance of highway bridge*s [Final Report]. Report No.: FHWA-AK-RD-12-15. Fairbanks, AK: Alaska University Transportation Center.

Ismael, N.F. (1990). Behavior of laterally loaded bored piles in cemented sands. *Journal of Geotechnical Engineering,* 116(11), 1678-1699.

Isenhower, W.M. & Wang, S.T. (2015). *Technical Manual for LPile 2015*. Austin, TX: Ensoft, Inc.

Jamiolkowski, M. (2003). Deep foundations on bored and auger piles. *Proceedings from the 4th International Geotechnical Seminar on Deep Foundations on Bored and Auger Piles,* Ghent: 83–100.

Janbu, N. (1963). Soil compressibility as determined by oedometer and triaxial tests. *Proceedings from the European Conference for Soil Mech. and Found. Engrg*., 1, 19—25. Wiesbaden, Germany

Joffrion, R.J. (2002). *Drilled shaft foundation construction inspection manual.* Louisiana Department of Transportation and Development.

Josef, K.A. (2011). Hollow threaded rebar for cross hole sonic logging access tubes combined with longitudinal concrete reinforcing in drilled shafts. *DFI Journal: The Journal of the Deep Foundations Institute*, 5(2). 16-22.

Juirnarongrit, T. (2002). *Effect of diameter on the behavior of laterally loaded piles in weakly cemented sand* (Doctoral thesis). San Diego, CA: Department of Structural Engineering, University of California.

Kent, D.C., & Park, R. (1971). Flexural members with confined concrete. *Journal of the Structural Division*. 97(7): 51-93

Khadilkar. B.S. Chandrasekaran. V.S. & Rizvi. I.A. (1973). Analysis of laterally loaded piles in two-layered soils. *Proceedings from 8th International Conference on Soil Mechanics and Foundation Engineering*. 21. 155-158. Moscow, Russia.

Kim, S., Jeong, S., Cho, S., & Park, I. (1999). Shear load transfer characteristics of drilled shafts in weathered rocks. *J. Geotech. Geoenviron. Eng.*, 125(11), 999–1010.

Kim, B.T., Kim, N.K., Lee, W.J., and Kim, Y.S. (2004). Experimental load-transfer curves of laterally loaded piles in Nak-Dong river sand. *Journal of Geotechnical and Geoenvironmental Engineering*, ASCE, 130(4), 416-425.

Kondner, R.L. (1963). Hyperbolic stress–strain response: cohesive soils. *J. Soil Mech. Found. Div.* 89 (1), 115–143.

Koojiman, A. (1989). Comparison of an elastoplastic quasi three-dimensional model for laterally loaded piles with field tests. *Proceedings from 3rd Intl. Symposium on Numerical Models in Geomechanics*, 675-682. Niagara Falls, Canada.

Kraft, L.M., Kagawa, T., & Ray, R. P. (1981). Theoretical t-z curves. *Journal of the Geotechnical Engineering Division*, 107(11), 1543-1561.

Kuhlemeyer (1979). Vertical vibration of piles. *J. Geotech. Eng.*, ASCE, 105(2), 273-287.

Kulhawy, F.H. (1985). Drained Uplift Capacity of Drilled Shafts. *Proceedings 11th International Conference on Soil Mechanics and Foundation Engineering*. Rotterdam, The Netherlands, 3, 1549-1552.

Kulhawy, F.H., & Mayne, P.W. (1990). Manual on estimating soil properties for foundation design. *Rep. EL-6800*. Ithaca, NY: Electric Power Research Institute, Cornell University.

Kulhawy, F.H. (1991). Drilled shaft foundations. *Foundation Engineering Handbook* (2nd Ed.). H.Y. Fang (Ed.), Van Nostrand-Reinhold, NY.

Kulhawy, F.H. (2004). On the axial behavior of drilled foundations. *Proc., GeoSupport 2004: Drilled Shafts, Micropiling, Deep Mixing, Remedial Methods, and Specialty Foundation Systems, GSP 124*, J.P. Turner and P.W. Mayne (Eds.), 34–51. Reston, VA: ASCE.

Kulhawy, F.H. & Chen, J.R. (2007). Discussion of 'Drilled shaft side resistance in gravelly soils' by Kyle M. Rollins, Robert J. Clayton, Rodney C. Mikesell, and Bradford C. Blaise," *Journal of Geotechnical and Geoenvironmental Engineering*, 133(10), 1325-1328.

Lam, I., & Martin, G. (1986). *Seismic design of highway bridge foundations* [Rep. No. FHWA/RD-86/102]. Washington, D.C.: Federal Highway Administration.

Lam, I.P.O. (2013). Diameter effects on p-y Curves. *38th Annual Meeting of the Deep Foundations Institute*, Phoenix, AZ.

Lapos, B., & Moore, I.D. (2002, October 2002). Evaluation of the strength and deformation parameters of Olimag Synthetic Olivine. *Proceedings of the 55th Canadian Geotechnical and 3rd Joint IAH-CNC and CGS Groundwater Specialty Conferences*, Niagara Falls, Ontario.

Lee, S.L., & Karunaratne, G.P. (1987). Laterally loaded piles in layered soil. *Soils Found.*, 27(4), 1–10

Lee, C.Y. (1991) Discrete layer analysis of axially loaded piles and pile groups. *Comput Geotech*; 11(4), 295–313.

Li, Q., Stuedlein, A.W., Barbosa, A. R. (2017). Torsional load transfer of drilled shaft foundations. *J. Geotech. Geoenviron. Eng.*. DOI: http://dx.doi.org/10.1061/(ASCE)GT.1943-5606.0001701.

Li, Q., & Stuedlein, A.W. (2017). Numerical simulation of torsionally-loaded deep foundations. *J. Geotech. Geoenviron. Eng.* (in review).

Li, Q., & Yang, Z. (2017). *P–y* approach for laterally loaded piles in frozen silt. *J. Geotech. Geoenviron. Eng.*, 143(5). DOI: http://dx.doi.org/10.1061/(ASCE)GT.1943-606.0001556.

Liang, R., Yang, K., & Nusairat, J. (2009). p-y criteria for rock mass. *Journal of Geotechnical and Geoenvironmental Engineering*, Vol.135(1), 26-36.

Ling, L. (1988). *Back Analysis of Lateral Load Tests on Piles* [M.E. Thesis]. Auckland, New Zealand: Civil Engineering Department, University of Auckland.

Lo, S.C., & Li, K.S. (2003). Influence of a permanent liner on the skin friction of large-diameter bored piles in Hong Kong granitic saprolites. *Canadian Geotechnical Journal*, *40*(4), 793-805.

Lunne, T., P.K. Robertson, & J.J.M. Powell. (1997). *Cone penetration testing in geotechnical practice*. New York, NY: Blackie Academic and Professional.

Mander, J.B., Priestley, M.J.N, & Park R. (1988). Theoretical stress-strain model for confined concrete. *Journal of the Structural Division*, 114(8):1804-1826.

Mansur, C.I., & Hunter, A.H. (1970). Pile tests—Arkansas River project. *Journal of the Soil Mechanics and Foundations Division*, 96(5), 1545-1582.

Matlock, H. (1970). Correlations for design of laterally loaded piles in soft clay. *Proceedings., 2nd Annual Offshore Technology Conference.* OTC 1204, Vol. 1, 577-594. Houston, TX.

Matlock, H., & Ripperger, E.A. (1956). Procedures and instrumentation for tests on a laterally loaded pile. *Proceedings, Eighth Texas Conference on Soil Mechanics and Foundation Engineering* (Special Publication No. 29). Bureau of Engineering Research, University of Texas.

Marchetti. S. (1977). Devices for In Situ Determination of Soil Modulus Es. *Proc. of 9th ICSMFE,* Tokio. Specialty Session 10: 197.

Martin, C.M., & Randolph, M.F. (2006). Upper-bound analysis of lateral pile capacity in cohesive soil. *Geotechnique* , 56 (2), 141–145.

Martin, J.P. (2018). *Full-scale loading tests of shallow foundations on aggregate pier-reinforced clayey silt* (MS Thesis, under development). Corvallis, OR: Oregon State University.

Mayne, P.W., Kulhawy, F.H., & Trautmann, C.H. (1992). *An experimental study of the behavior of drilled shaft foundations under static and cyclic lateral and moment loading* [Rep. TR-lO0221]. Palo Alto, CA: Electric Power Res. Institute.

Mayne, P.W., & Harris, D.E. (1993). *Axial Load-Displacement Behavior of Drilled Shaft Foundations in Piedmont Residuum* [FHWA Reference Number 41-30-2175]. Atlanta, GA: Georgia Tech Research Corporation.

Mazzoni, S., McKenna, F., & Fenves, G.L. (2006). *Open System for Earthquake Engineering Simulation User Manual*. Berkeley, CA: Pacific Earthquake Engineering Research Center, University of California. Retrieved from http://opensees.berkeley.edu.

Ménard. L. & Rousseau J. (1962) L'evaluation des Tassements, Tendence Nouvelle, *Sol-Soils* 1, 13-30.

Meyerhof, G.G. (1976). Bearing capacity and settlement of pile foundations. *J. Geotech. Eng. Div., Am. Soc. Civ. Eng.*, 102(3), 195–228.

McCammon, N.R., & Golder, H.Q. (1970). Some loading tests on long pipe piles. *Geotechnique*, 20(2), 171-184.

McKenna, F., Scott, M.H., & Fenves, G.L. (2010). Nonlinear finite-element analysis software architecture using object composition. *Journal of Computing in Civil Engineering*, 24(1), 95-107.

McVay, M.C., F.C. Townsend, D.G. Bloomquist, M.O. O'Brien, & J.A. Caliendo. (1989). Numerical analysis of vertically loaded pile groups. *Proceedings, Foundation Engineering Congress: Current Principles and Practices*, 675-690. Evanston, IL.

Mullins, G. (2010) Thermal integrity profiling of drilled shafts. *Journal of the Deep Foundations Institute*, 4(2), 54 – 64.

Murchison, J.M., & O'Neill, M.W. (1984). Evaluation of p-y relationships in cohesionless soil *Analysis and design of pile foundations*, 174-191. New York, NY: ASCE.

Murff, J.D., & Hamilton, J.M. (1993). P-Ultimate for undrained analysis of laterally loaded piles. *Journal of Geotechnical Engineering*, ASCE, 119(1), 91-107.

Naik. T.R. & Peyrot. A. (1976). Analysis and design of laterally loaded piles and caissons in a layered soil system. Methods of Structural Analysis. *Proceedings of the Sational Structural Engineering Conference*, Vol.11, 589-606. Madison, WI: ASCI.

Niazi, F.S. (2014). Static axial pile foundation response using seismic piezocone data [Doctoral thesis]. Atlanta, GA: Georgia Institute of Technology.

Nimityongskul, N. (2010). *Effects of soil slope on lateral capacity of piles in cohesive soils* (Doctoral Dissertation). Corvallis, OR :Civil and Construction Engineering Department, Oregon State University.

Nimityongskul, N., Kawamata, Y., & Rayamajhi, D. (2018). Full-scale tests on effects of slope on lateral capacity of piles installed in cohesive soils. *Journal of Geotech. Geoenviron. Eng.*. DOI: https://doi.org/10.1061/(ASCE)GT.1943-5606.0001805.

Norris, G.M. (1986). Theoretically based BEF laterally loaded pile analysis. *Proceedings, Third International Conference on Numerical Methods in Offshore Piling* (361-386). Editions Technip, Paris, France.

O'Neil, M.W., & Reese, L.C. (1972). Behavior of bored piles in Beaumont clay. *Journal of the Soil Mechanics and Foundations Division*, 98(sm2), 195-213.

O'Neill, M.W., & Reese, L.C. (1978). Load transfer in a slender drilled pier in sand. *Spring Convention and Exposition,* Pittsburgh, PA.

O’Neill, M.W. (1994). Drilled shafts. *Proceedings, International Conference. On Design and Construction of Deep Foundations,*1, 185–206.

O’Neill, M.W., & Reese, L.C. (1999). *Drilled shafts: Construction procedures and design methods* (Publication No. FHWA-IF-99-025). McLean, VA: Federal Highway Administration, Office of Implementation.

O'Neill, M.W. (2001). Side resistance in piles and drilled shafts. *Journal of Geotechnical and Geoenvironmental Engineering*, 127(1), 3-16.

Owens, M.J., & Reese, L.C. (1982). *The influence of a steel casing on the axial capacity of a drilled shaft* [Report No. 255-1F]. Austin, TX: Texas State Department of Highways and Public Transportation Center for Transportation Research, Bureau of Engineering Research, The University of Texas at Austin.

Pando, M.A., Ealy, C.D., Filz, G.M., Lesko, J.J. & Hoppe, E.J. (2006). A laboratory and field study of composite piles for bridge substructures [Report FHWA-HRT-04-04].

Pender, M.J. (1993). Aseismic pile foundation design analysis. *Bull. NZ Nat. Soc. Earthquake Eng*., 26(1), 49–160.

Poulos, H.G., & Davis, E.H. (1968). The settlement behaviour of single axially loaded incompressible piles and piers. *Geotechnique,* 18(3), 351-371. London, England.

Poulos, H.G. & Davis, E.H. (1980). *Pile foundation analysis and design*. New York, N.Y: John Wiley and Sons.

Poulos, H.G. (2001). Pile foundations. *Geotechnical and Geoenvironmental Engineering Handbook*, R.K. Rowe (Ed.), Kluwer Academic Press.

Prakash, S., & Sharma, H.D. (1990). *Pile foundations in engineering practice*. New York, NY: Wiley-Interscience.

Rajashree, S.S., & Sitharam, T.G. (2001). Nonlinear finite element modeling of batter piles under lateral load. *Journal of Geotechnical and Geoenvironmental Engineering*, 127(7), 604-612.

Randolph, M.F. & Wroth, C.P. (1978). Analysis of deformation of vertically-loaded piles. *Journal of the Geotechnical Engineering Division,* 104(GT12), 1465 – 1488.

Randolph, M. (1981). Response of flexible piles to lateral loading, *Geotechnique,* 31(2), 247-259.

Randolph, M.F., & Houlsby, G.T. (1984). The limiting pressure on a circular pile loaded laterally in cohesive soil. *Geotechnique,* 34(4), 613-623.

Randolph, M.F. (1994). Design methods for pile groups and pile drafts. *Proceedings, XIII ICSMFpE,* 61-82. New Delhi, India

Redpath B. (2007). Downhole measurements of shear- and compression-wave velocities in boreholes C4993, C4996, C4997, and C4998 at the waste treatment plant, DOE Hanford Site. *PNNL-16559*, Redpath Geophysics (Eds.). Richland, WA: Pacific Northwest National Laboratory.

Reese, L.C., Cox, W.R., & Koop, F.D. (1974). Analysis of laterally loaded piles in sand. *Proceedings, 6th Offshore Technology Conference, Paper 2080*, 473-483. Houston, TX.

Reese, L., Cox, W., & Koop, F. (1975). Field testing and analysis of laterally loaded piles in stiff clay. *Proceedings. 7th Offshore Technology Conf.*, OTC 2312, 2, 671-690. Houston, TX.

Reese, L.C., & O'Neill, M.W. (1988). *Drilled shafts: Construction procedures and design methods* [Publication No. FHWA-HI-88-042], 564–564. Washington, D.C.: U.S. Department of Transportation.

Reese, L., & Welch, R. (1975). Lateral loading of deep foundations in stiff clay. *Journal of Geotechnical Engineering Div*., 101(GT7), 633-649.

Reese, L.C., & Van Impe, W.F. (2001). *Single piles and pile group under lateral loading*. A.A. Balkema (Ed.), pp. 463

Reese, L.C., Wang, S.T. & Arrellage, J., (2014). Analysis of load versus settlement for an axially loaded deep foundation. *TZPILE v2014 Technical Manual.* Austin, TX: ENSOFT, INC.

Rix, G.J., & K.H. Stokoe. (1991) "Correlation of initial tangent modulus and cone resistance." Proceedings, *International Symposium on Calibration Chamber Testing*, 351-362. Potsdam, NY.

Robertson, P., Davies, M., & Campanella, R. (1989). Design of laterally loaded driven piles using the flat dilatometer. *Geotech. Test. J.*, GTJODJ, 12 (1), 30-38.

Robertson, P.K. & Wride, C.E. (1998). Evaluating cyclic liquefaction potential using the cone penetration test. *Canadian Geotechnical Journal*, 35(3), 442–459.

Robertson, P.K. (2009). Interpretation of cone penetration tests – A unified approach. *Canadian Geotechnical Journal*, 46(11), 1337–1355.

Roeder, C.W., Cameron, B., & Brown, C.B. (1999). Composite action in concrete-filled tubes. *J. Struct. Eng.,* 125(5), 477–484.

Roeder, C.W., Lehman, D.E., & Bishop, E. (2010). Strength and stiffness of circular concrete filled tubes. J. *Struct. Eng.,* 136(12), 1545–1553.

Roeder, C., and Lehman, D. (2012). *Initial investigation of reinforced concrete filled tubes for use in bridge foundations* [Report No. WA-RD 776.1]. Olympia, WA: Washington Department of Transportation.

Salgado, R. (2008). *The engineering of foundations*. New York: McGraw Hill.

Scott, R.F. (1980). Analysis of centrifuge pile tests; Simulation of pile-driving. *Report for the American Petroleum Institute OSAPR Project 13*, Pasadena, CA: California Institute of Technology.

Seed, H.B., & Reese, L.C. (1957). The action of soft clay along friction piles. *American Society of Civil Engineers Transactions*. 122, 731-764

Shahrooz, B.M., Miller, R.A., Harries, K.A., & Russel, H.G. (2011). *Design of concrete structures using high-strength steel reinforcement* [NCHRP Report 679], Washington, D.C.: Transportation Research Board.

Skempton, A.W. (1959). Cast in-situ bored piles in London clay. *Geotechnique*, 9(4), 153-173.

Srivastava, K., Singh, V.K., Yadav, A., Shelke, A., & Patra, N.R. (2008, October). Prediction of load displacement response of single pile under uplift load: A comparative study. *Proceedings, 12th Int. Conf. of International Association for Computer Methods and Advances in Geomechanics (IACMAG)*, 3408-3414. Goa, India.

Stevens, J.B. & Audibert, J.M.E. (1979) Re-examination of p-y curve formulations. *Proceedings, 11th Annual Offshore Technology Conference*, Houston, TX.

Stas, C.V., & Kulhawy, F.H. (1984). *Critical evaluation of design methods for foundations under axial uplift and compression loading*. Electric Power Research Institute

Stuedlein, A.W. (2008). Bearing capacity and displacement of spread footings on aggregate pier reinforced clay [Doctoral thesis]. Seattle, WA: University of Washington.

Stuedlein, A.W., Neely, W.J., & Gurtowski, T.G. (2012) Reliability-based design of augered cast-in-place piles in granular soils. *Journal of Geotechnical and Geoenvironmental Engineering*, 138(6), 709-717.

Stuedlein, A.W. & Reddy, S.C. (2014) Factors affecting the reliability of augered cast-in-place piles in granular soils at the serviceability limit state. *Journal of the Deep Foundations Institute*, Vol. 7, No. 2, 46-57.

Stuedlein, A.W., Li, Q., Arduino, P., & Ganji, A. (2015). *Behavior of drilled shafts with high-strength reinforcement and casing* [Report 2013-M-OSU-0024]. Seattle, WA: Pacific Northwest Transportation Consortium University Transportation Center.

Takesue, K., Sasao, H., & Matsumoto, T. (1998). Correlation between ultimate pile skin friction and CPT data. *Geotechnical Site Characterization*, 2, 1177-1182.

Terzaghi, K. (1955). Evaluation of coefficients of subgrade reaction. *Geotechnique,* 5(4), 297-326.

Thompson, G. (1977). *Application of finite element method to the development of p-y curves for saturated clays* [Thesis]. Austin, TX: University of Texas, Austin.

Ting, J.M. (1987). Full scale cyclic dynamic lateral pile response. *Journal of Geotechnical Engineering*, 113(1), 30-45.

Trejo, D., Barbosa A., & Link, T. (2014). *Seismic performance of circular reinforced concrete bridge columns constructed with grade 80 reinforcement* [Research SRS 500-610]. Corvallis, OR: Oregon State University.

Trochianis, A., Bielak, J., & Christiano, P. (1988). *A three-dimensional nonlinear study of piles leading to the development of a simplified model* [Report R-88-176]. Department of Civil Engineering, Carnegie Institute of Technology.

USGS. *The national map viewer*. Available: http://viewer.nationalmap.gov/viewer/. Accessed September 2, 2015.

Vesic, A.S. (1970). Tests on instrumented piles, Ogeechee River site. *Journal of Soil Mechanics & Foundations Div*. 96(sm2), 561-584

Vesic, A.S. (1975). Bearing capacity of shallow foundations. *Fndn. Eng. Handbook* (Ch. 3, 121-147). Winterkorn, H. & Fang, H.Y. (Eds.), New York, NY: Van Nostrand Reinhold.

Vecchio, F.J., & Collins, M.P. (1986). Modified compression-field theory for reinforced concrete elements subjected to shear. *ACI Journal*, 83(2), 219–231.

Vijayvergiya, V.N., Hudson, W.R., & Reese, L.C. (1969). Load distribution for a drilled shaft in clay shale. *Proceedings, Fourth Annual Offshore Technology Conference*, Vol. II, 865-874. Houston, TX.

Vijayvergiya, V.N. (1971). Discussion on tests on instrumented piles, Ogeechee River site. *Journal of Soil Mechanics & Foundations Div*. 97(sm1), 252-256

Vijayvergiya, V.N. (1977). Load-movement characteristics of piles. *Proceedings, Ports '77: 4th Annual Symposium of the Waterway, Port, Coastal, and Ocean Division*, 269-284. Long Beach, CA,

Wallace, J.W., Fox, P.J., Stewart, J.P., Janoyan, K., Qiu, T., & Lermitte, S. (2001). Cyclic large deflection testing of shaft bridges: Part I-background and field test results. *Report to California Department of Transportation*, University of California, Los Angeles, CA

Wesselink, B.D., Murff, J.D., Randolph, M.F., Nunez, I.L., & Hyden, A.M. (1988). Analysis of centrifuge model test data from laterally loaded piles in calcareous sand. *Engineering for Calcareous Sediments*, 1, 261–270. Balkema, Rotterdam, The Netherlands.

Welch, R.C., & Reese, L.C. (1972). *Lateral load behavior of drilled shafts* [Research Report 89-10]. Austin, Texas: Center for Highway Research, The University of Texas at Austin.

Wilson, D.W. (1998). *Soil-pile-superstructure interaction in liquefying sand and soft clay* [Doctoral dissertation]. Davis, CA: University of California, Davis.

Wong, K.S., & Teh, C.I. (1995). Negative skin friction on piles in layered deposits. *J. Geotech. Engrg.,* 121(6), 457–465.

Yang, K., & Liang, R. (2006) Methods for deriving p-y curves from instrumented lateral load tests. *Geotechnical Testing Journal*, 30, 1-8.

Yang, Z., Li, Q., Horazdovsky, J., Hulsey, J.L., & Marx, E. (2012). Analysis of laterally loaded piles in frozen soils. *State of the Art and Practice in Geotechnical Engineering (GeoCongress2012)* [Geotechnical Special Publication] 225, 215-224.

Yang, Z., Li, Q., Horazdovsky, J., Hulsey, J.L., & Marx, E.E. (2017). Performance and design of laterally loaded piles in frozen ground. *Journal of Geotechnical and Geoenvironmental Engineering*, 143(5). http://dx.doi.org/10.1061/(ASCE)GT.1943-5606.0001642, 06016031.

Yassin, M. (1994). *Nonlinear analysis of prestressed concrete structures under monotonic and cycling loads* [Doctoral dissertation]. Berkeley, CA: University of California, Berkeley

Yegian, M. & Wright, S. (1973). Lateral soil resistance - Displacement relationships for pile foundations in soft clays. *Proceedings, 5th Offshore Technology Conf*., OTC 1893, 2, 663-676. Houston, TX.

Zeno, G.A. (2009). *Use of high-strength steel reinforcement in shear friction applications* [Doctoral dissertation]. Pittsburgh, PA: University of Pittsburgh.

Zhang, L., Silva, F., & Grismala, R. (2005). Ultimate lateral resistance to piles in cohesionless soils. *Journal of Geotechnical and Geoenvironmental Engineering*, 131(1), 78-83.

Zhang, Q-Q., Zhang, Z-M., & He, J-Y. (2010). A simplified approach for settlement analysis of single pile and pile groups considering interaction between identical piles in multilayered soils. *Computers and Geotechnics*. 37(7-8), 969–976.

APPENDIX A QUESTIONNAIRE RESULTS

This appendix presents each question in the survey and the corresponding responses.

1) What is the approximate breakdown of foundation types used in your bridge structures constructed over the last decade?

a) Shallow Foundations ______%

b) Driven Piles ______%

c) Drilled Shafts ______%

d) Others (specify): ______%

RESPONSE:

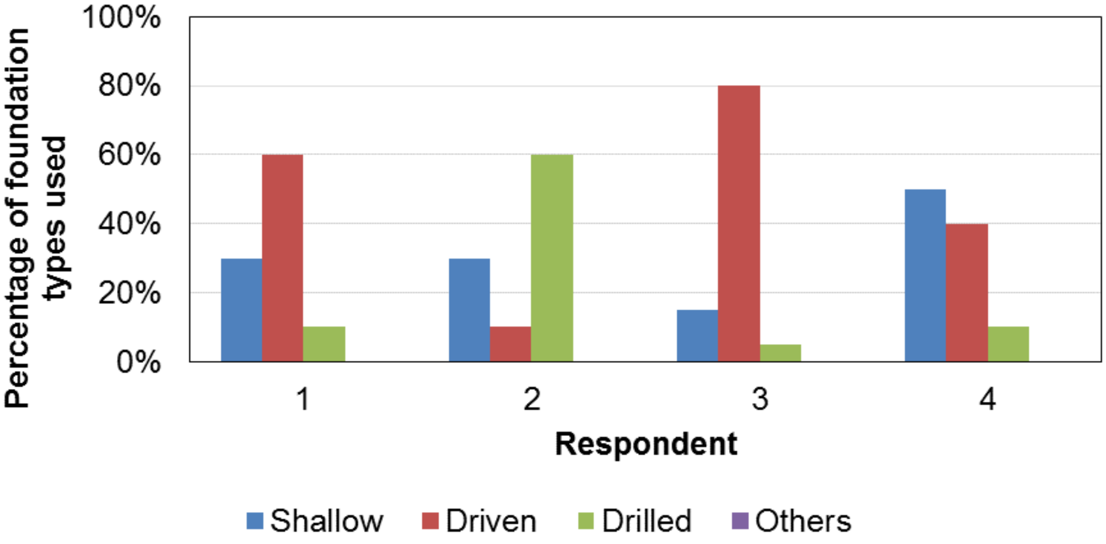

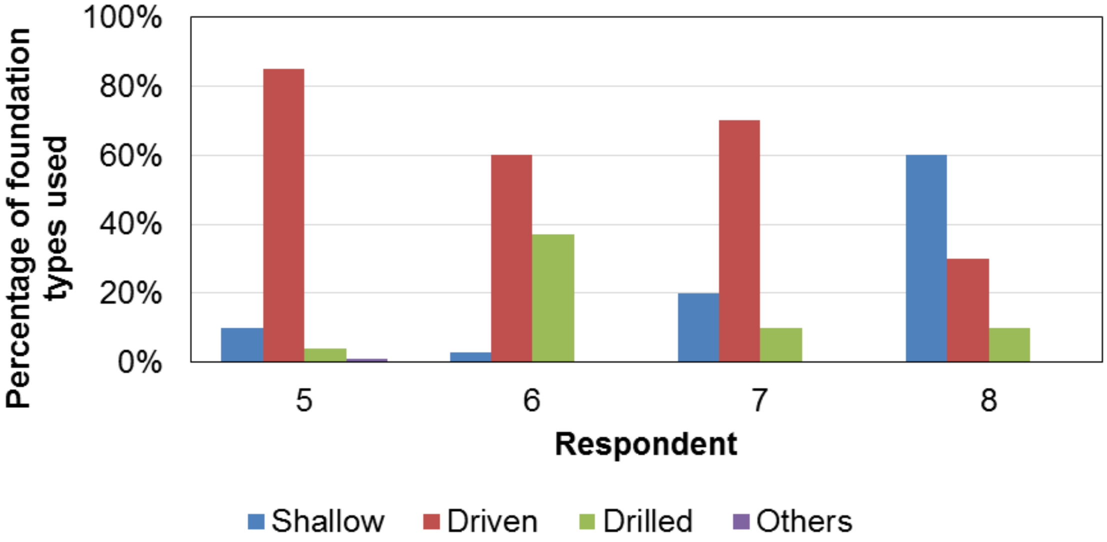

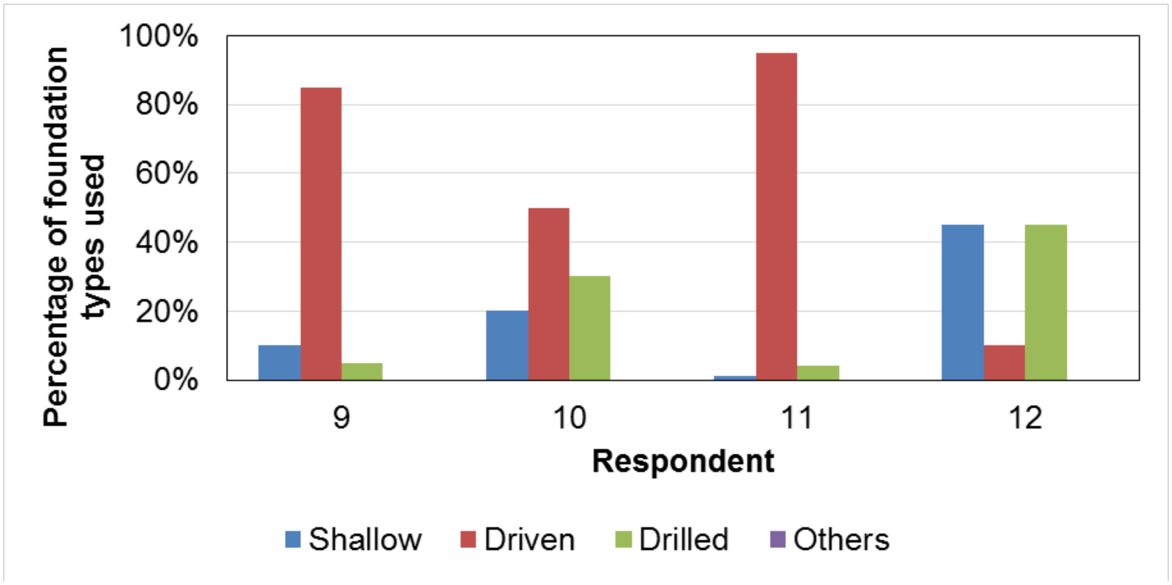
Percentage of foundation types used
100%
80%
60%
40%
20%
0%
9
10
11
12
Respondent
Shallow
Driven
Drilled
Others

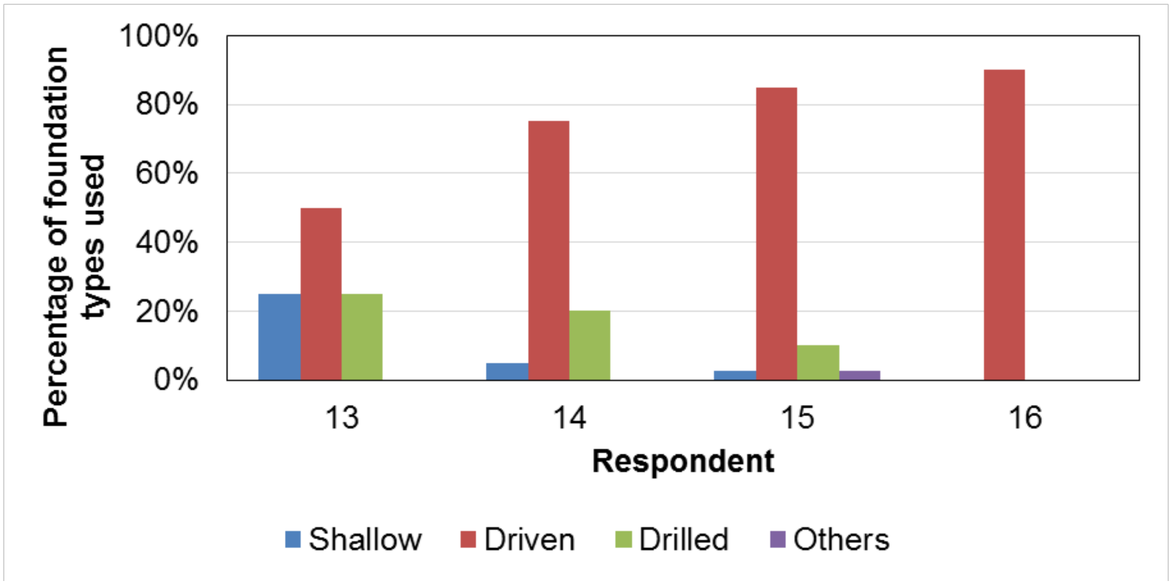
Percentage of foundation types used
100%
80%
60%
40%
20%
0%
13
14
15
16
Respondent
Shallow
Driven
Drilled
Others

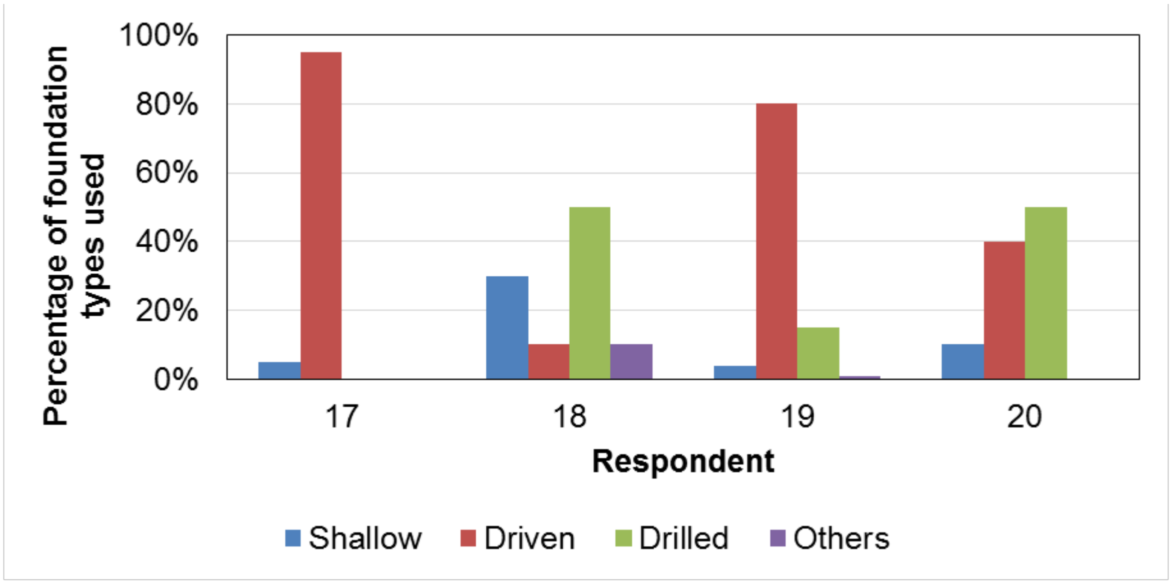

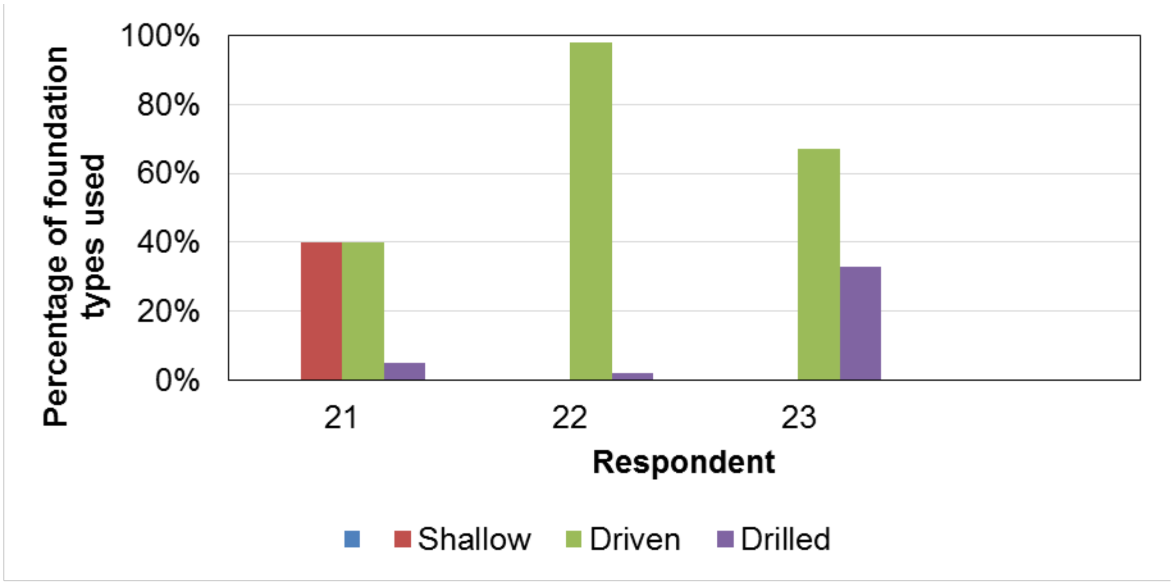

Comments:

There were five respondents had the experience of using micropiles, although the usage of micropiles was less than 5% for all of them. Geosynthetic Reinforced Soil (GRS) foundation was used by one of the respondents.

2) Do you have a preferred type of deep foundation?

   a) Driven Pile

   b) Drilled Shaft

   c) Others (specify): ______________________________________

RESPONSE:

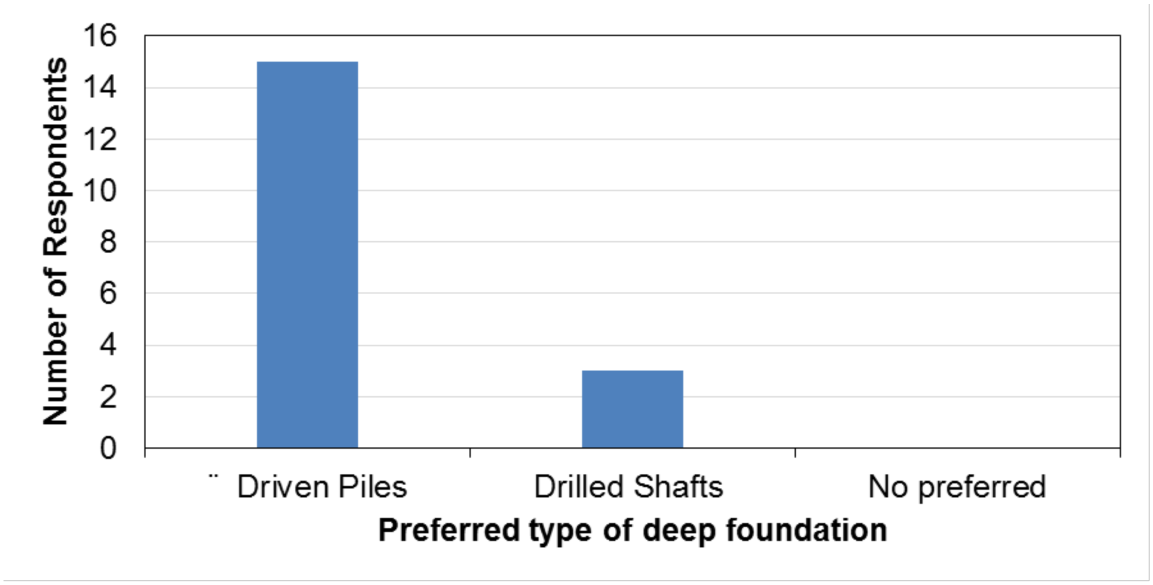

3) How often do you design, specify, and build drilled shaft-supported structures?

   a) 0 to 1 times/year

   b) 1 to 2 times/year

   c) 2 to 4 times/year

   d) 4 to 8 times/year

   e) 8 to 16 times/year

   f) 16+ times/year

RESPONSE:

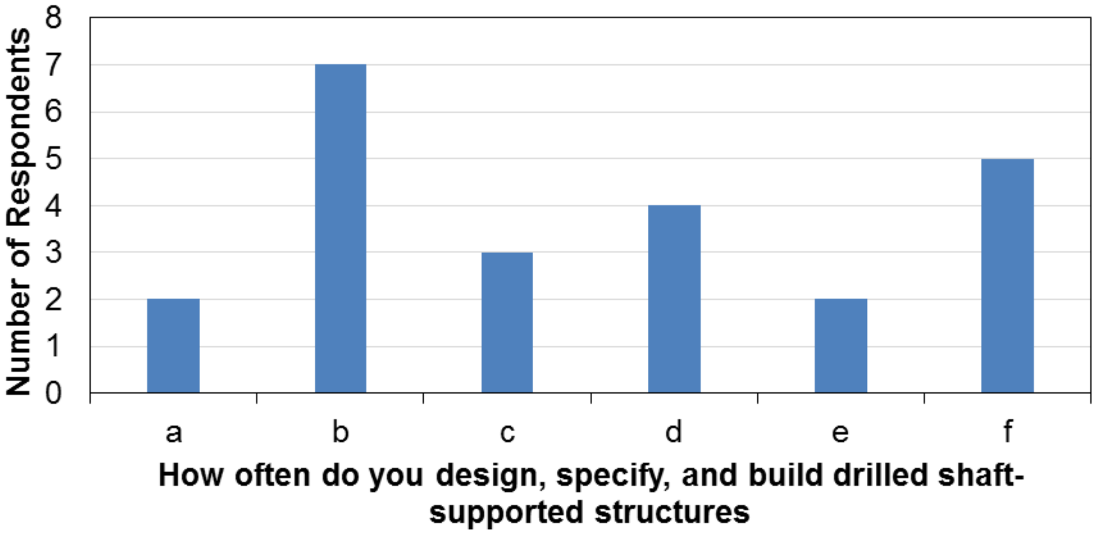

4) What methods does your agency use to characterize the geotechnical conditions of the drilled shaft project site(s) (check all that apply)?

   a) Soil survey/geologic maps
   b) Historical embankment construction documents
   c) Test pits
   d) Borings with split-spoon sampling and SPT blow count
   e) Cone penetration testing
   f) Other (specify): ____________________
   g) No geotechnical investigation performed

RESPONSE:

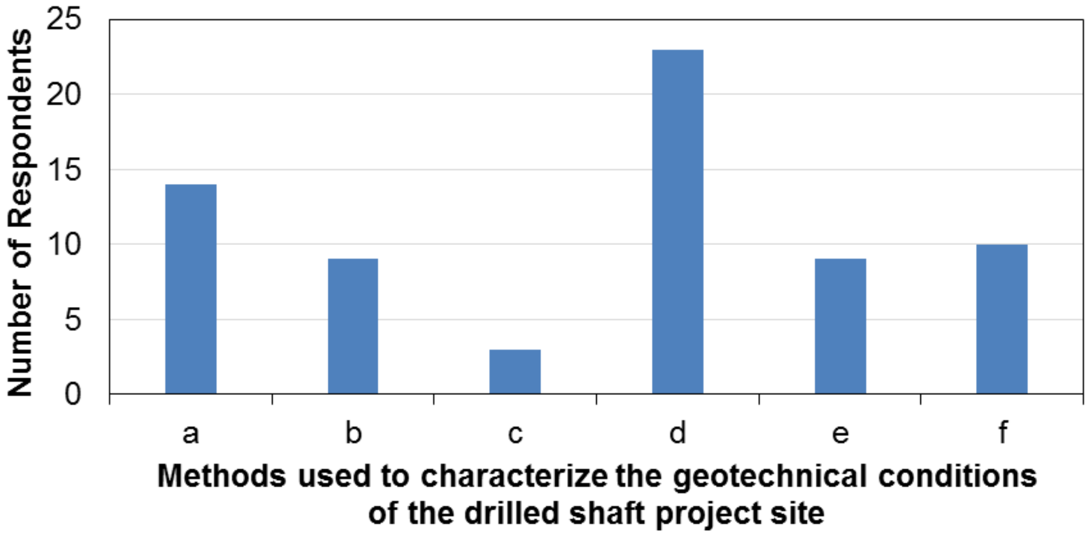

Comments:
There were seven respondents used rock coring, two respondents used geophysical testing, and one respondent used well logs from agency of Natural Resources.

5) What method is your agency's preferred to characterize the geotechnical conditions of the project site (check only one)?

   a) Soil survey/geologic maps

   b) Historical embankment construction documents

   c) Test pits

   d) Borings with split-spoon sampling and SPT blow count

   e) Cone penetration testing

   f) Other (specify): ____

   g) No geotechnical investigation performed

RESPONSE:

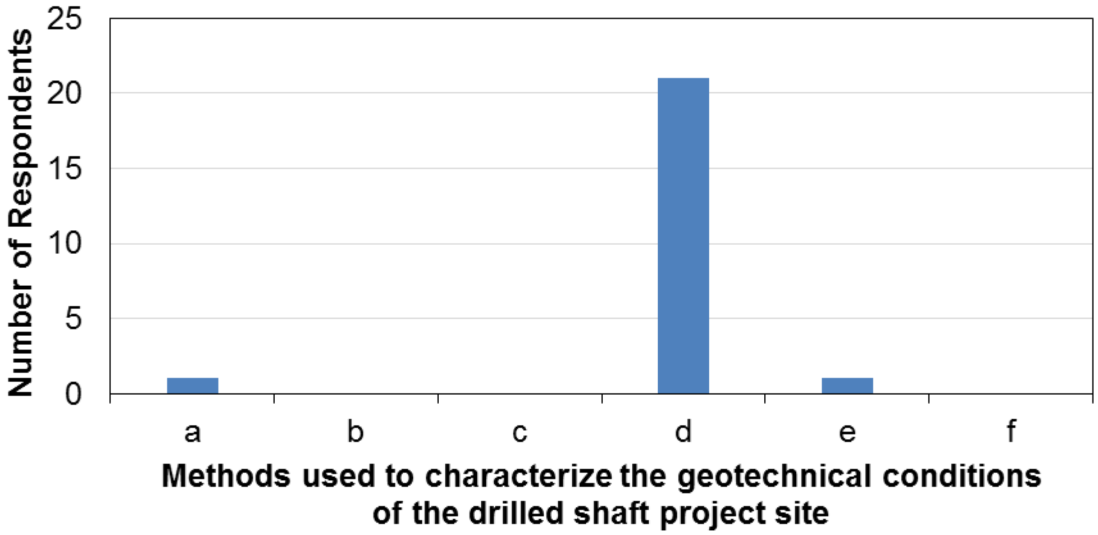

6) What are the primary parameters used in your drilled shaft design analysis (Check all that apply)?

   a) SPT-N Value

   b) CPT Data

   c) Pressuremeter Data

   d) Dilatometer Data

   e) Friction Angle (ϕ') and Cohesion (c)

   f) Other (specify): ____

RESPONSE:

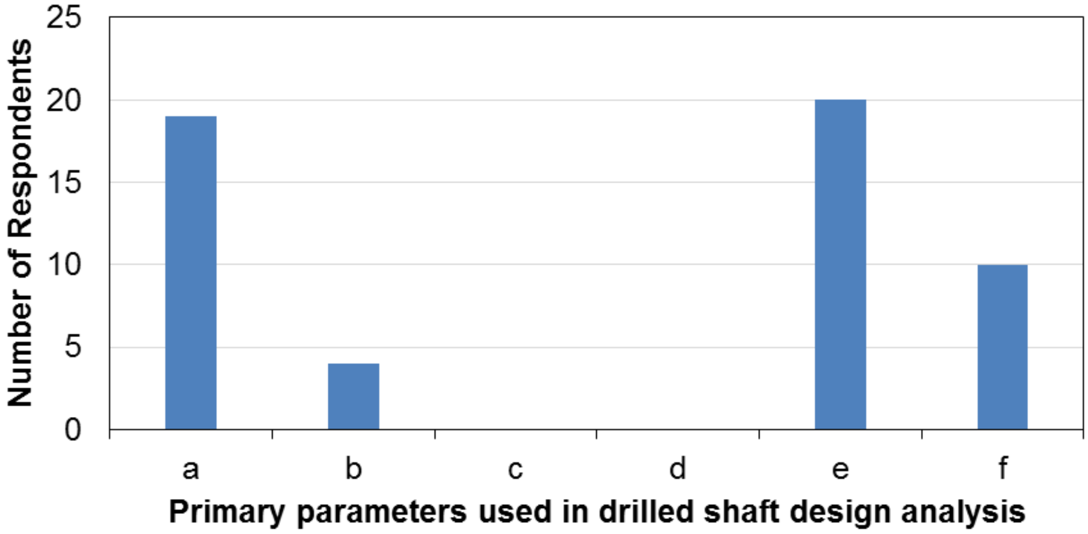

Comments:

There were ten respondents used rock compressive strength (q_u) and one respondent used soil index properties, slake durability index, Rock Quality Designation, and Young's Modulus for Rock.

7) If friction angle (*ϕ*’) and cohesion (*c*) or rock compressive strength (q_u) are used in design, how are these design parameters are determined?

   a) Laboratory tests

   b) Type of test(s): ____

   c) Correlation from in-situ tests

   d) Type of test(s): ____

RESPONSE:

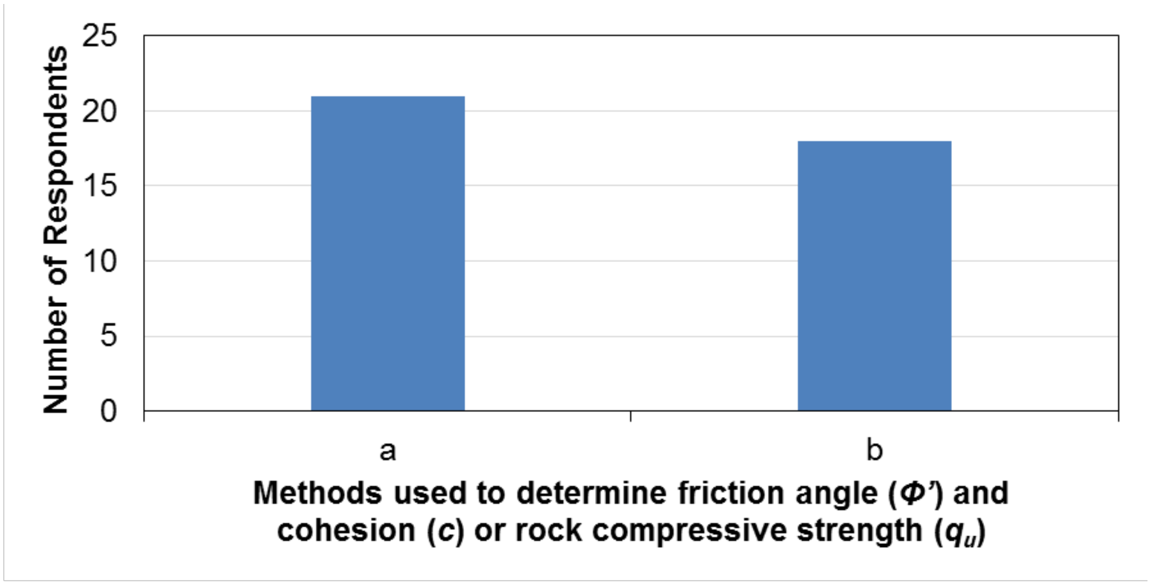

Comments:

The laboratory tests used include direct shear test, unconfined compression test, and triaxial test. In-situ test used for correlation is SPT.

8) What design methods do you use for the design of axial load transfer of drilled shafts?

   a) α-Method (Total Stress Approach; O'Neill and Reese, 1999; Brown et al., 2010)

   b) *β*-Methods (Effective Stress Approach; O'Neill and Reese, 1999[1]; Brown et al., 2010)

   c) Kulhawy et al., (2005) Approach for drilled shafts socketed into rock

   d) Horvath and Kenney, (1979) Approach for drilled shafts socketed into rock

   e) O'Neill and Reese, (1999) Approach for intermediate geomaterials (IGMs)

   f) Brown et al., (2010) Approach for intermediate geomaterials (IGMs)

   g) Others ____

RESPONSE:

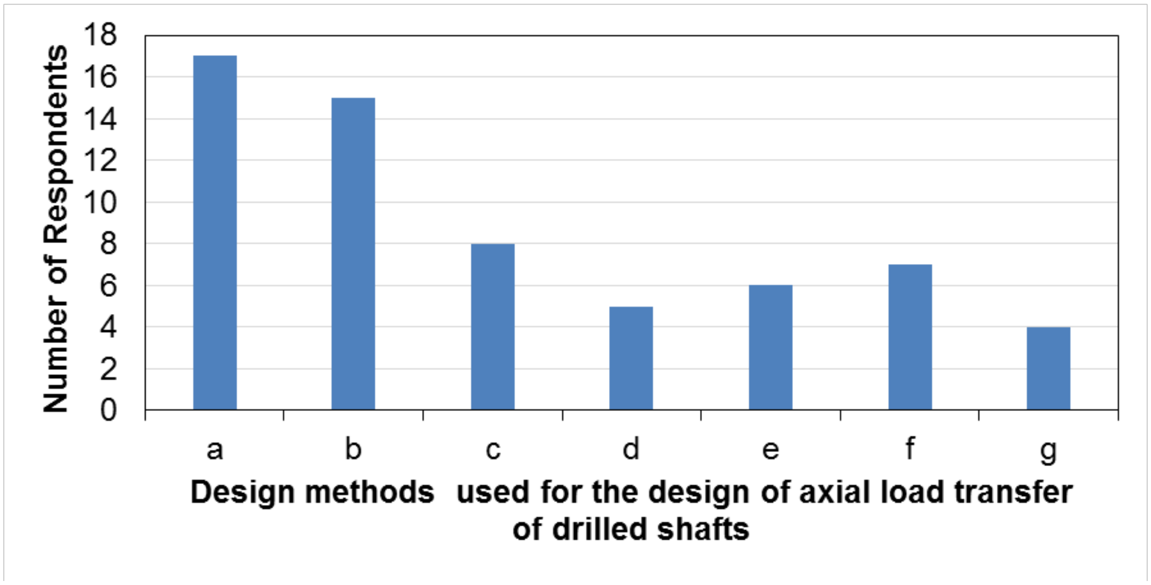

Comments:

Kulhawy and Chen (2007) approach for side resistance of cohesionless soils, Mayne and Harris (1993) approach for weathered rock, Reynolds and Kaderabek (1980) approach for Side shear resistances, and Rowe and Armitage (1987) approach for end bearing were also used by some of the respondents.

9) What design methods does your agency typically use for assessing drilled shafts supporting bridges under lateral loading?

   a) Simplified methods considering a rigid response (e.g., Broms, 1964)

   b) *p-y* curve methods considering a flexible response

   c) Strain wedge approach

   d) Equivalent cantilever approach (Chai 2002)

   e) Other (specify): ______________________

RESPONSE:

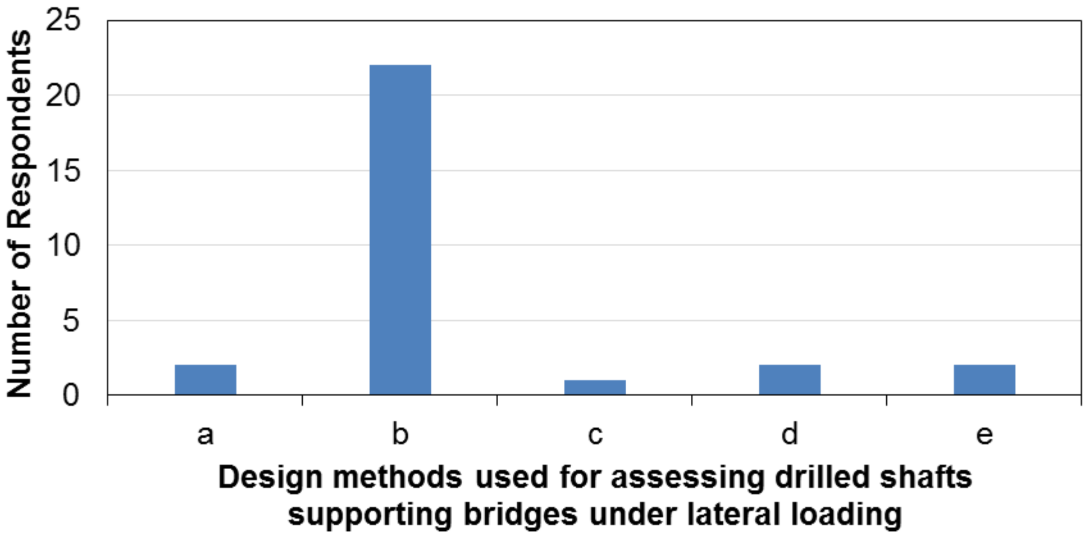

Comments:

Two respondents used elastic continuum approach (Poulos and Davis 1980).

10) What software do you typically use for the axial and lateral design of drilled shafts?

a) FB Pier

b) TZ-Pile

c) LPILE

d) APILE

e) GROUP

f) DFSAP

g) Other (specify): ________________

RESPONSE:

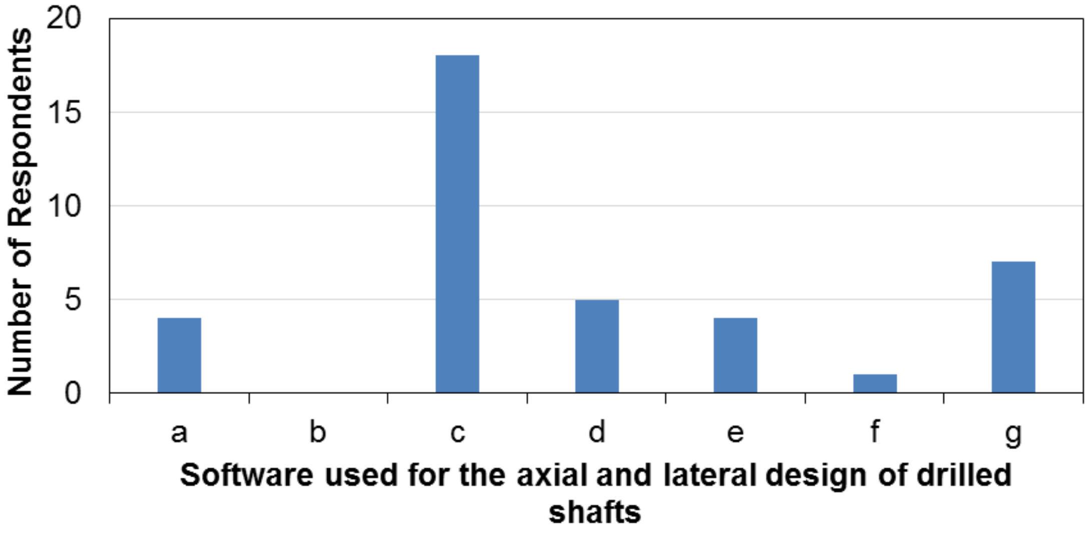

Comments:

Five respondents used in-house programs, including spreadsheets and Mathcad sheets, one respondent used AllPile, and one respondent used SHAFT.

11) If slurry is commonly used to stabilize the drill hole during construction, what type of materials and criteria are used?

a) Mineral Slurry of Processed Attapulgite

b) Mineral Slurry of Bentonite

c) Synthetic Polymers

d) Others (specify): ____

RESPONSE:

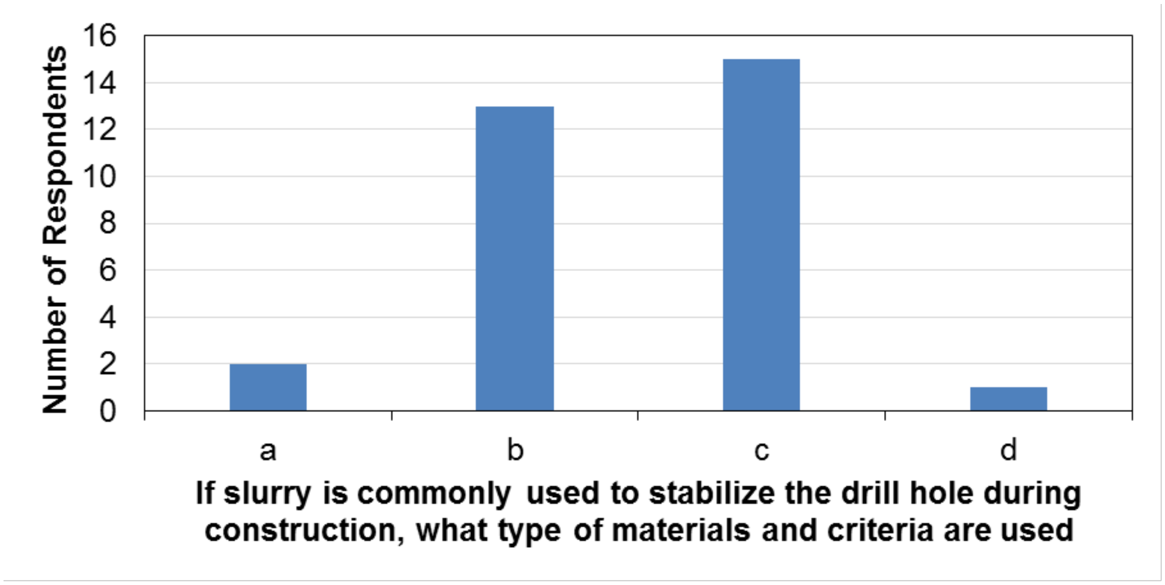

Comments:

The respondent who chose the option of *Others*, did not specify the type of slurry.

12) Do you frequently perform a static loading test during construction?

a) No.

b) Yes. What are the criteria to justify the test?__________

RESPONSE:

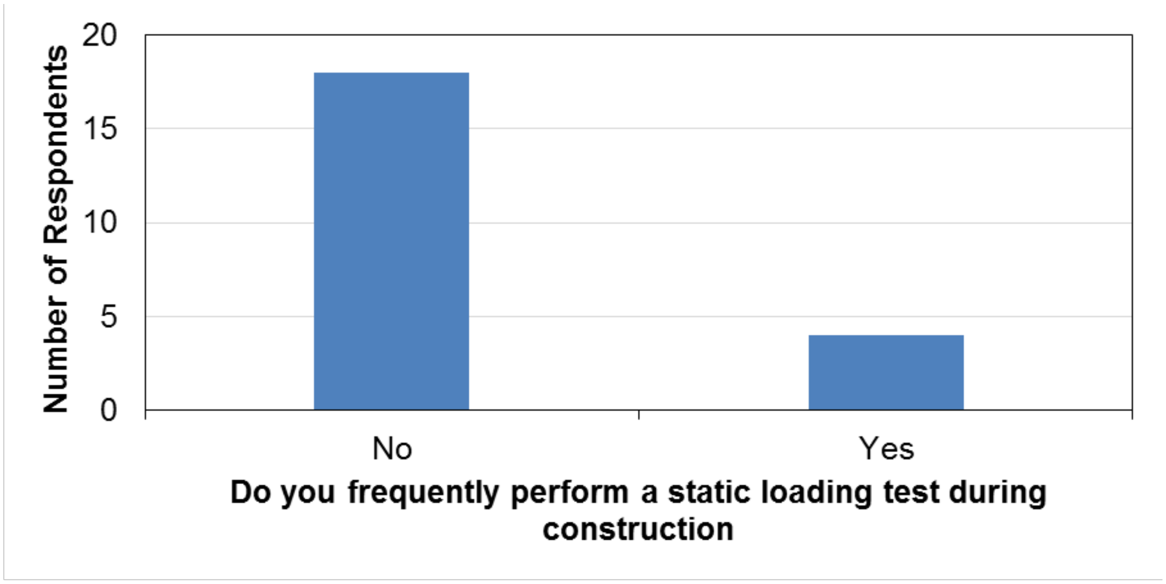

Comments:

The criteria used to justify the test includes size of piles, variations in site geotechnical characteristics, and savings in dimensions or cost from use of higher resistance factor.

13) Regardless of frequency, when a static loading test is performed, what type of test is used?

a) Conventional top-down static loading test

b) Bi-directional Loading Test (e.g., Osterberg cell)

c) Statnamic Loading Test

d) Dynamic Loading test

e) Others ____

RESPONSE:

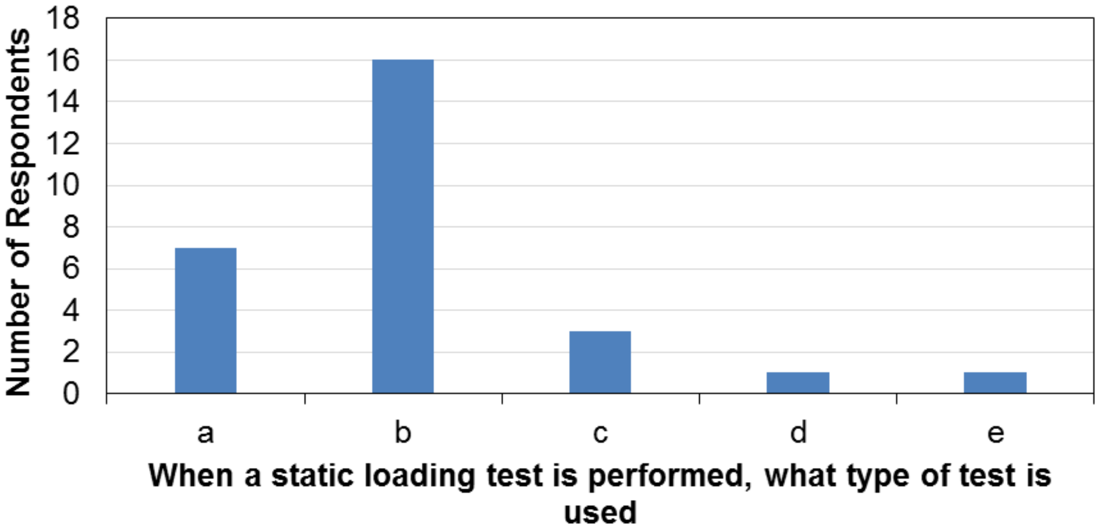

Comments:

The respondent who chose the option of *Others*, did not specify the type of test performed

14) Do you use integrity testing for drilled shafts quality control?

a) No

b) Yes

RESPONSE:

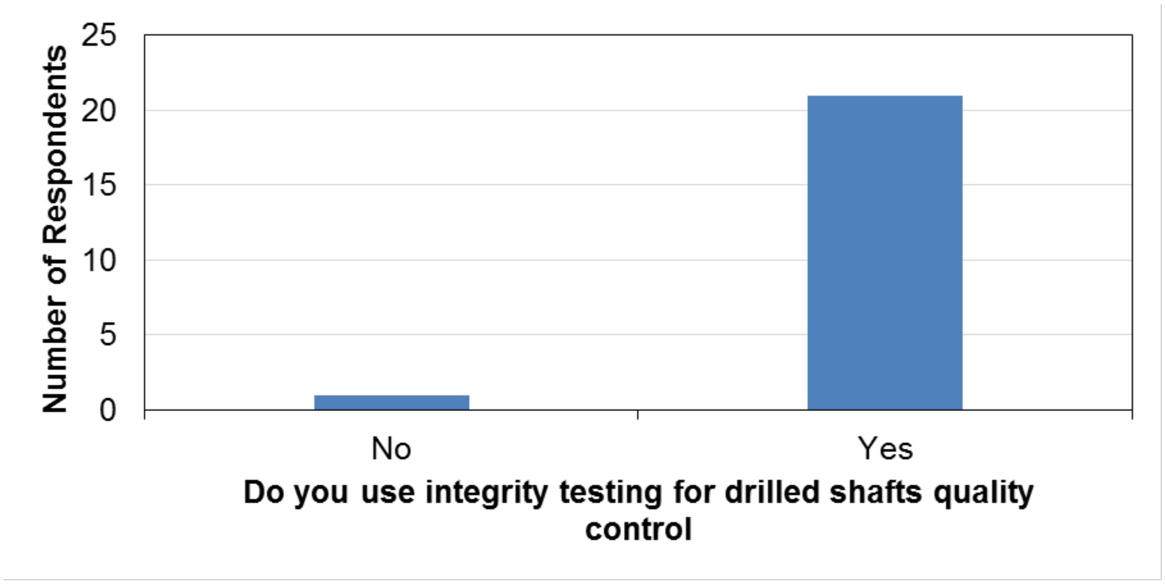

15) If integrity testing is performed, what type of test is used?

a) Cross-hole Sonic Logging (CSL)

b) Gamma-Gamma Density Logging

c) Sonic Echo/Impulse Response (SE/IR)

d) Crosshole Tomography (CT)

e) Others ______________________

RESPONSE:

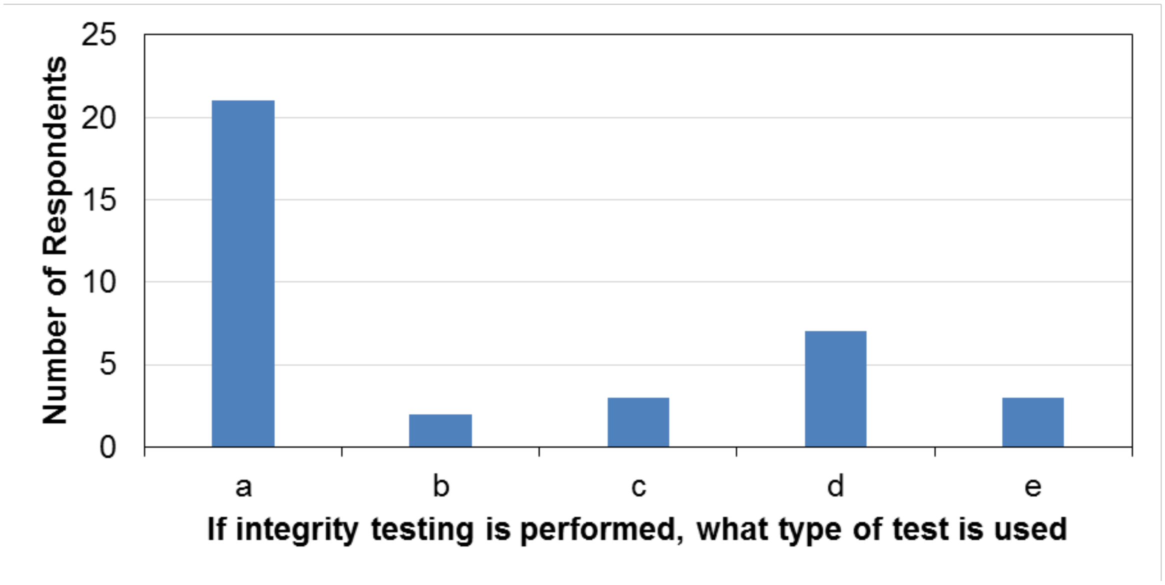

Comments:

Three respondents used Thermal Integrity Profiling (TIP) tests.

16) If integrity testing is performed, approximately what percentage of drilled shafts is tested?

a) 0 to 20%

b) 20 to 40%

c) 40 to 60%

d) 60 to 80%

e) 80 to 100%

RESPONSE:

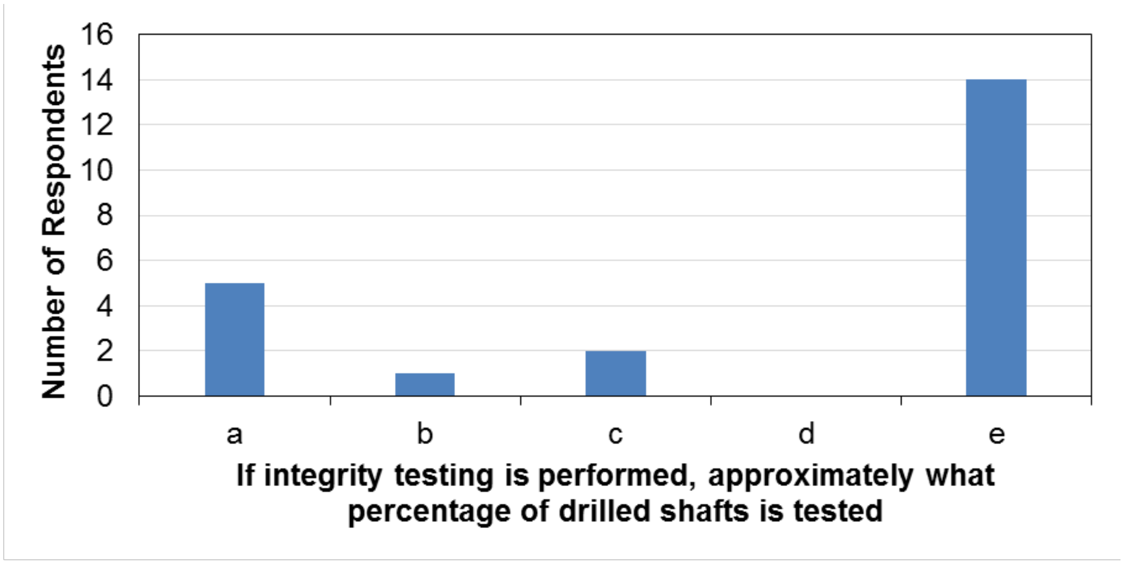

17) Approximately what percent of these drilled shafts employ a permanent steel casing?

a) 0 to 20%

b) 20 to 40%

c) 40 to 60%

d) 60 to 80%

e) 80 to 100%

RESPONSE:

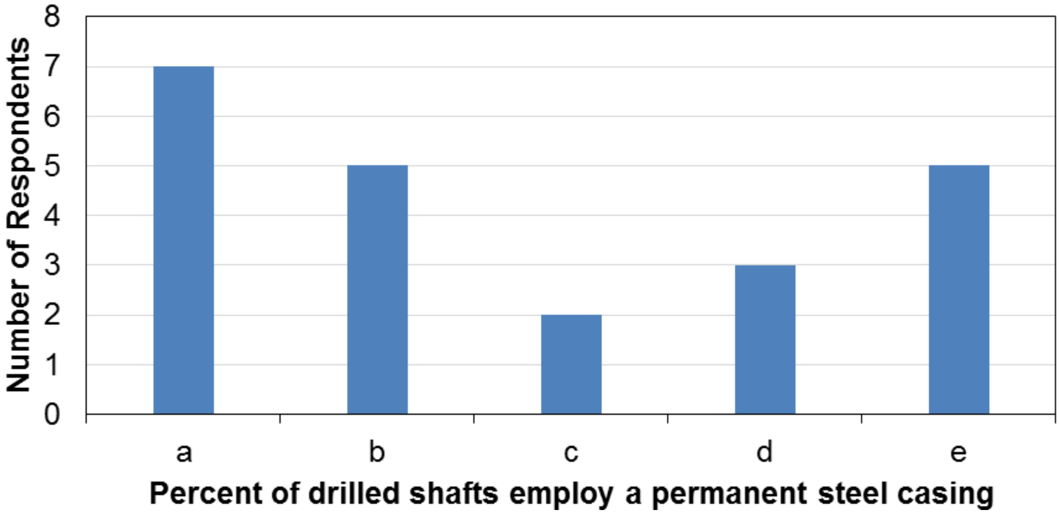

18) When permanent steel casing is used, what purpose is it intended for (check all that apply)?

- a) Constructability in marine environments or karst formations
- b) Soils prone to caving
- c) Preserving the integrity of the concrete placed within very soft and loose materials
- d) Providing significant flexural and shear resistance
- e) Difficulty associated with temporary casing retrieval

RESPONSE:

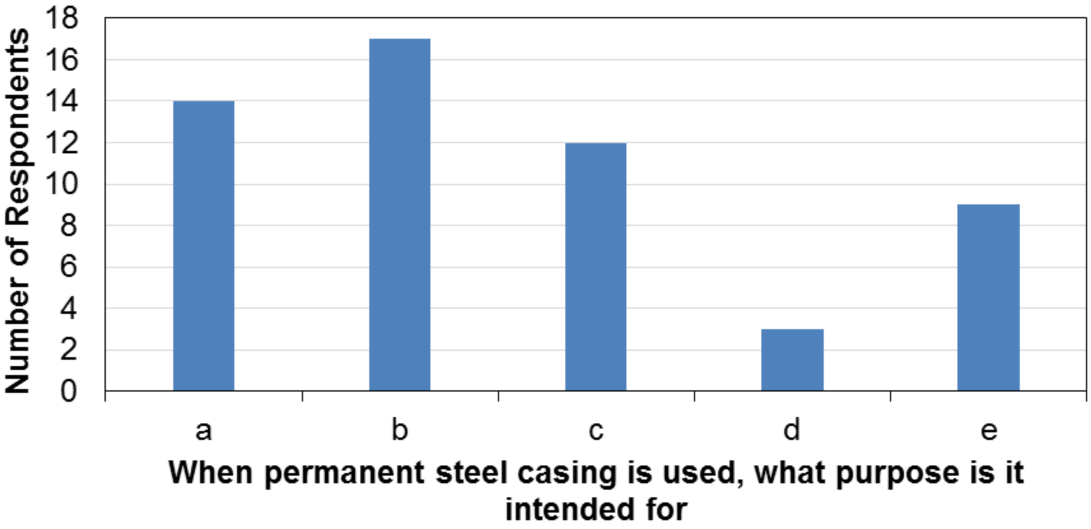

19) If permanent steel casing has NOT been used what are your concerns?

a) Confusion of the design provisions for cased shafts (no unified design code)

b) Difficulty of incorporating structural connections

c) Cost concern

d) Others (specify): ______________________________

RESPONSE:

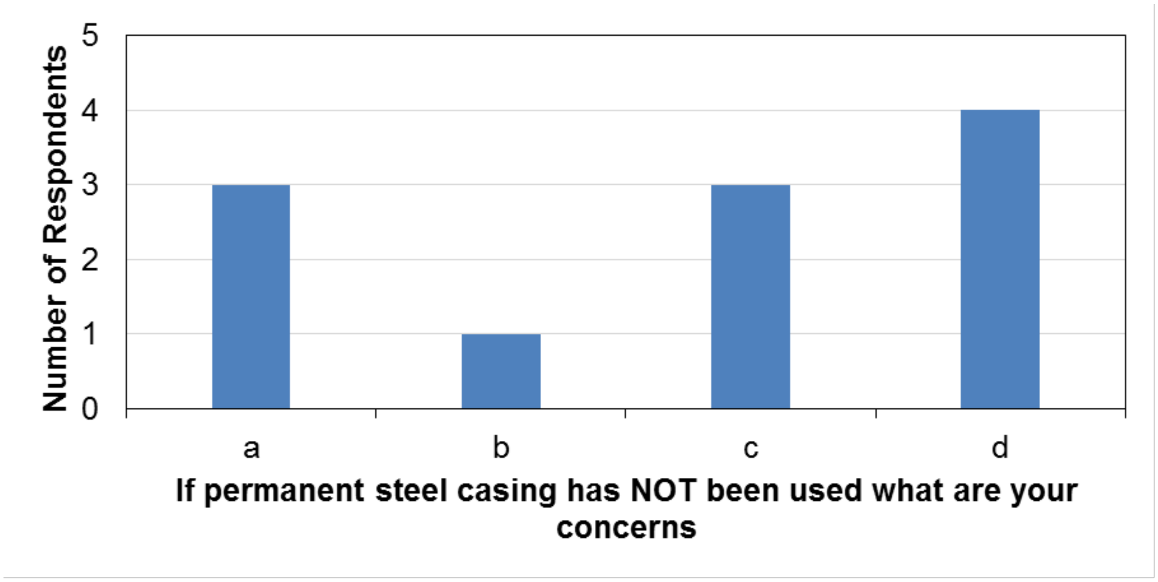

Comments:

Other concerns of using permanent steel casing includes reducing of axial capacity, shaft integrity, and corrosion potential.

20) How many times was casing not specified but was desirable after the fact?

a) 0%

b) 1 to 20%

c) 20 to 40%

d) 40 to 60%

e) 60 to 80%

f) 80 to 100%

RESPONSE:

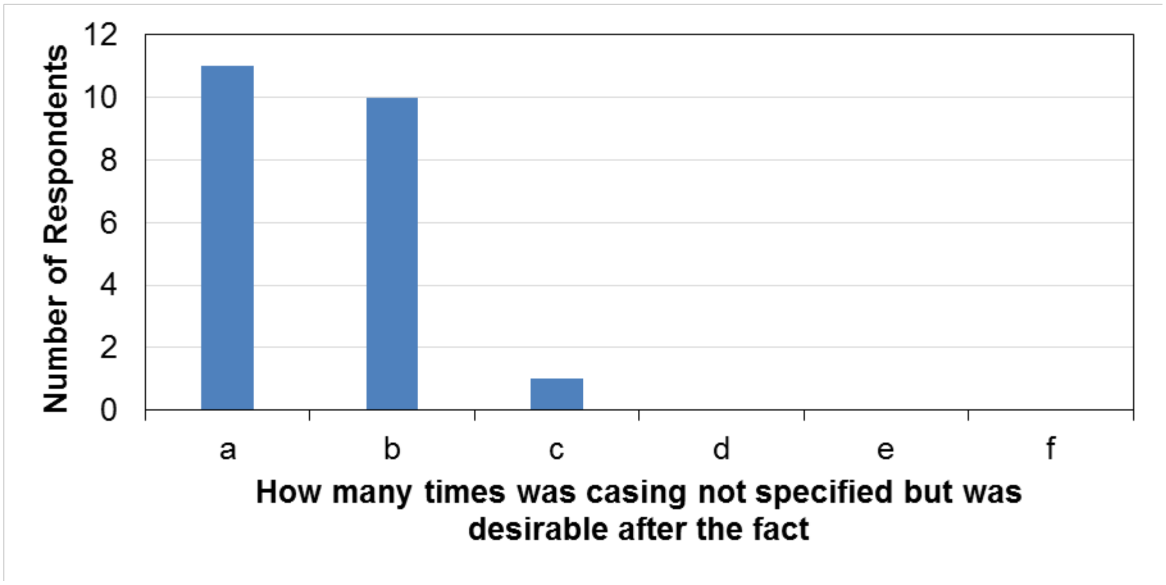

21) If you answered more than zero, why was casing desirable?

RESPONSE:
When casing was desirable, four respondents were due to caving during construction in the site (two of them indicated specifically that the use of slurry alone was not adequate to control some caving layers), two were due to unexpected high water, two were due to the difficulty in extracting temporary casing, one was due to cage support difficulties, one was due to the construction issues related to fluid concrete pressure blowing out into adjacent drill holes

22) When computing shaft displacement, is the axial elastic compression of the steel casing included in the computation?

a) No

b) Yes

RESPONSE:

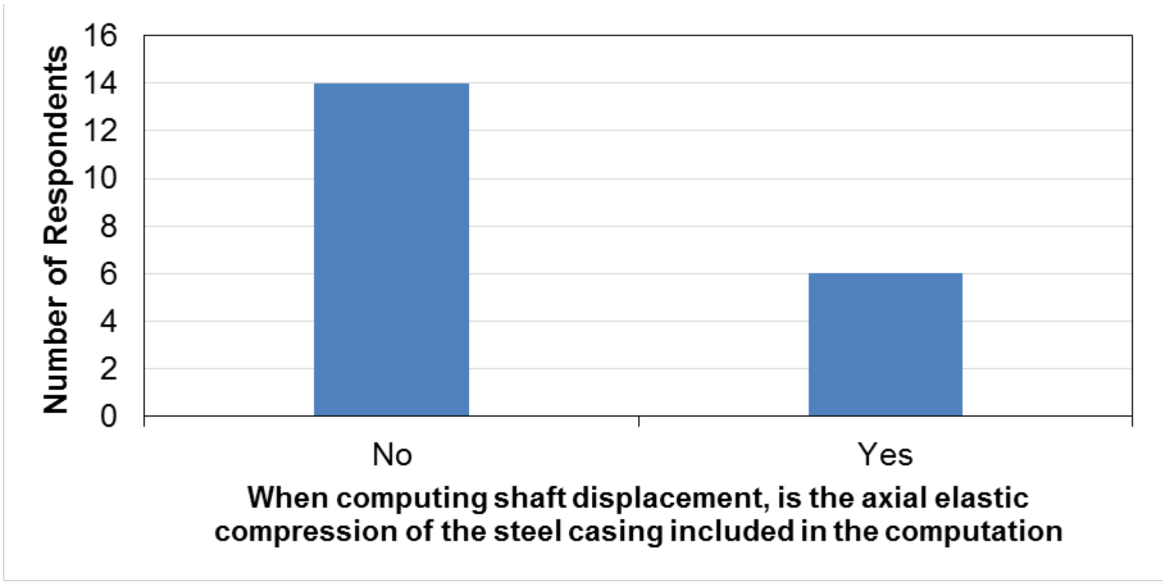

23) When assessing the response of the drilled shaft to lateral loads, is the flexural resistance of the casing incorporated in analysis?

a) No

b) Yes

RESPONSE:

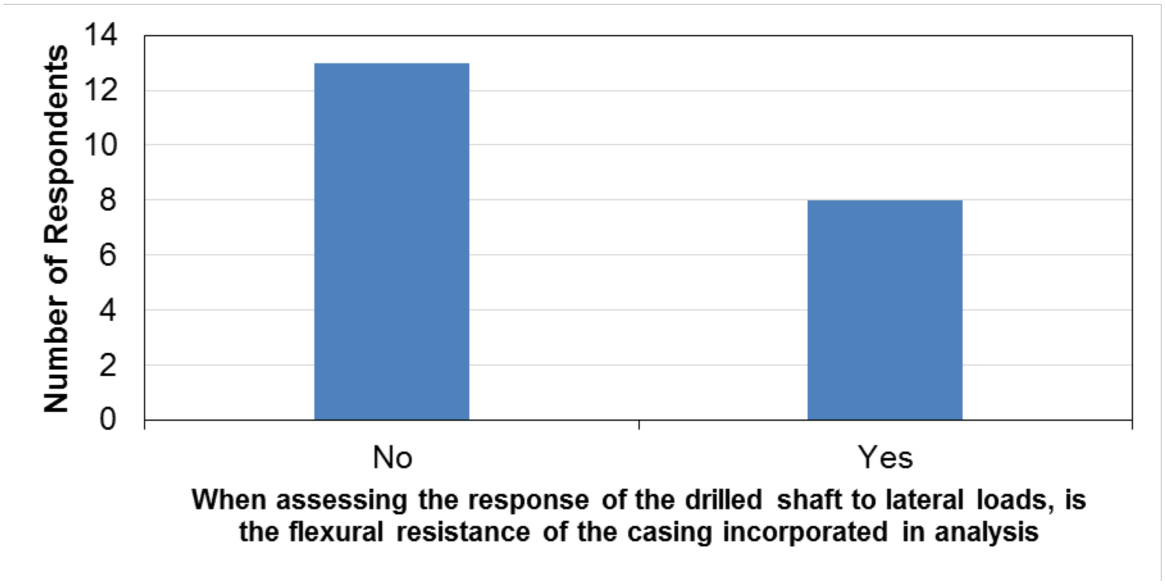

24) In the design of cased drilled shafts (i.e., concrete-filled tubes or CFTs), which codes are used?

a) Does not apply

b) AASHTO

c) ACI

d) AISC

e) Other (specify): ____

RESPONSE:

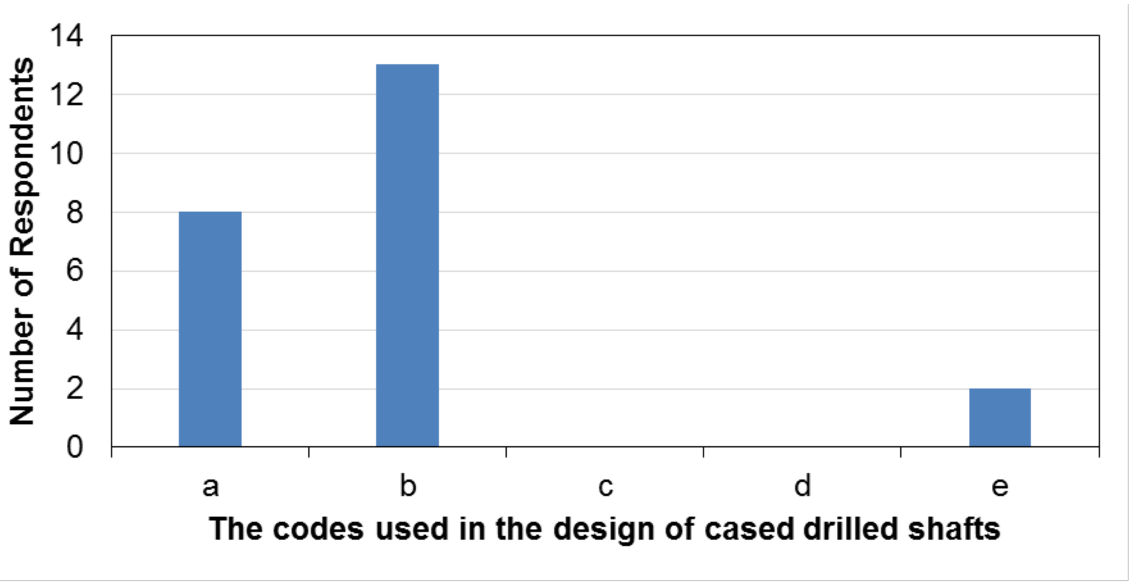

Comment:

One respondent uses FHWA Manual, and one respondent Uses Canadian Foundation Engineering Manual (4th Edition).

25) Which methods do you usually use to estimate the resistance of CFT members subjected to bending and axial load?

a) Does not apply

b) The plastic stress distribution method (AISC Section I1.2a)

c) The strain-compatibility method (AISC Section I1.2b)

d) Other (specify): ____

RESPONSE:

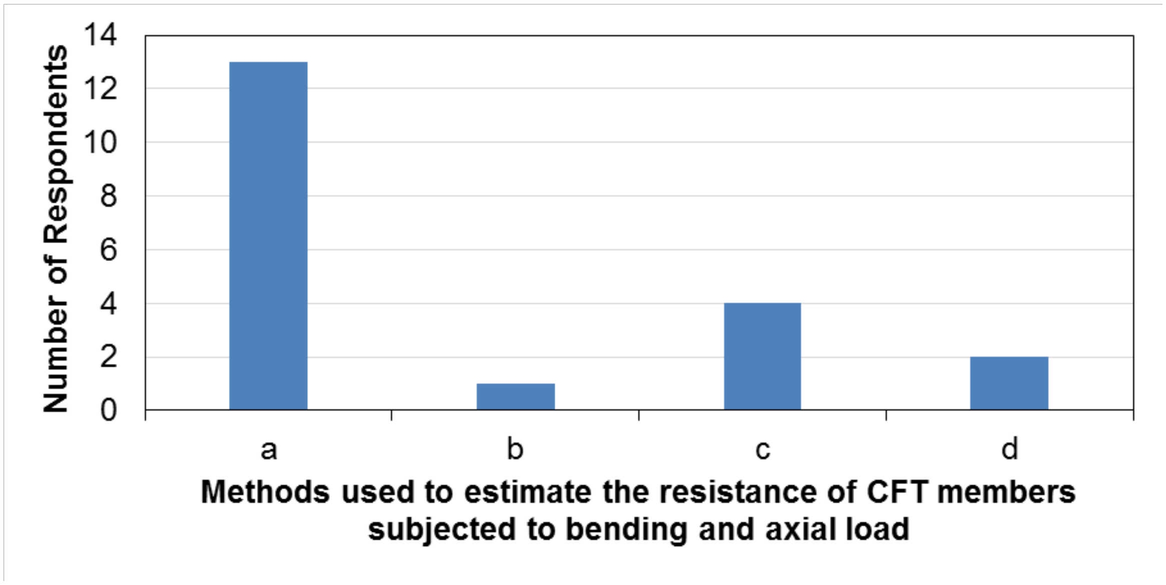

Comments:

One respondent uses Section 7 AASHTO Guide Specifications for LRFD Seismic Bridge Design, and one respondent uses nonlinear moment-curvature analysis.

26) Which type of steel casing is commonly used?

a) Spiral weld

b) Straight weld

c) Other (specify): ____

RESPONSE:

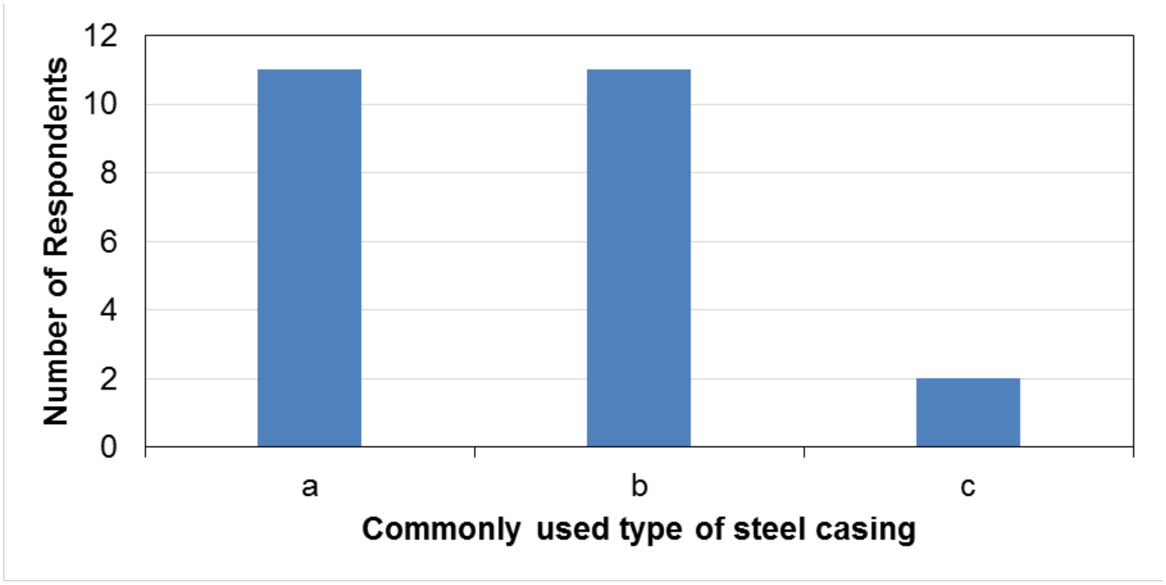

Comments:

One respondent uses steel casing to meet ASTM A252-10, and one uses CGMP as form liner (referred to as double casing method).

27) Relative to traditional reinforced concrete drilled shafts, what is the cost of permanently cased shafts?

a) 0 to 10% less than traditional reinforced concrete drilled shafts

b) 10 to 20% less than traditional reinforced concrete drilled shafts

c) Less than 20%

d) 0 to 10% more than traditional reinforced concrete drilled shafts

e) 10 to 20% more than traditional reinforced concrete drilled shafts

f) Greater than 20%

RESPONSE:

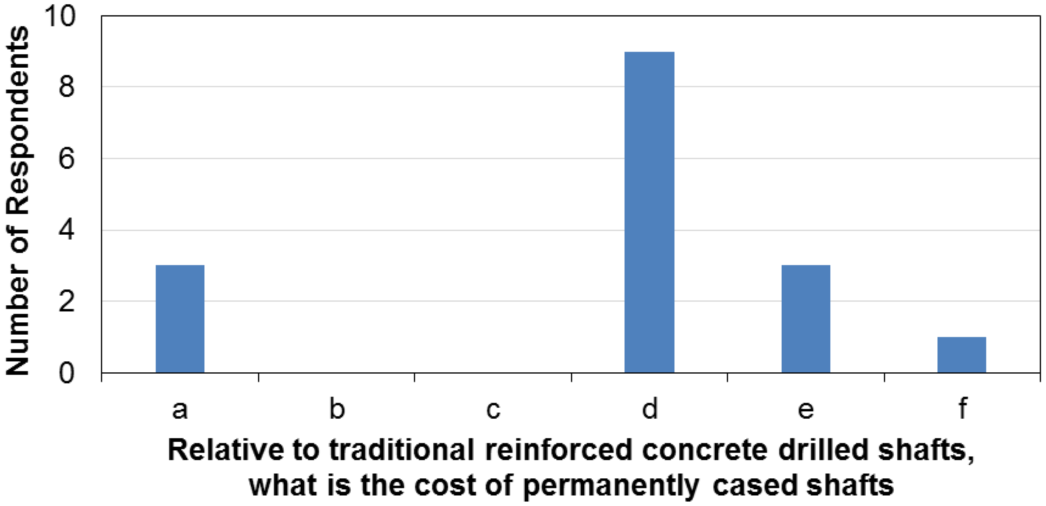

28) How do you evaluate the axial load transfer for shafts with permanent casing?

a) Reduce shaft resistance

b) Increase shaft resistance

c) Design as usual, that is, with concrete interface

d) Ignore all shaft resistance in cased zone

RESPONSE:

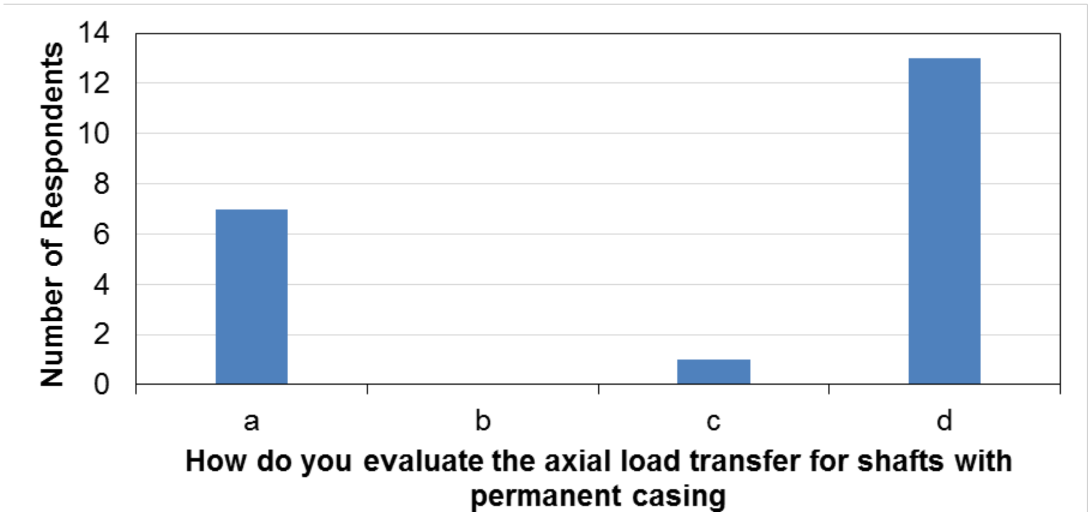

29) How is strain compatibility between the concrete and casing maintained?

a) Welded bar

b) Weld bead

c) Cross bar

d) Tread plate

e) Shear rings

f) Shear stud

RESPONSE:

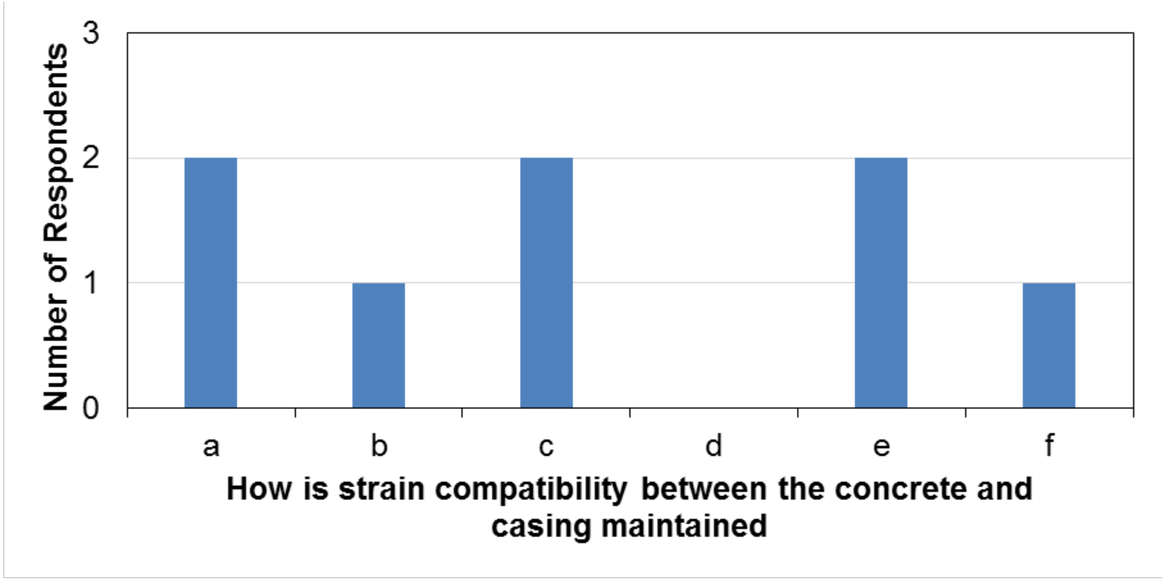

30) How do you deal with a large steel area ratio that may result in a small clearance within the steel cage and construction defects in the design of drilled shafts?

a) Increasing shaft diameter

b) Using high-strength steel (≥ 80 ksi) with the same shaft diameter

c) Using bundled longitudinal reinforcements

d) Changing mix design with smaller aggregate or using concrete additives

e) Other (specify): ____

RESPONSE:

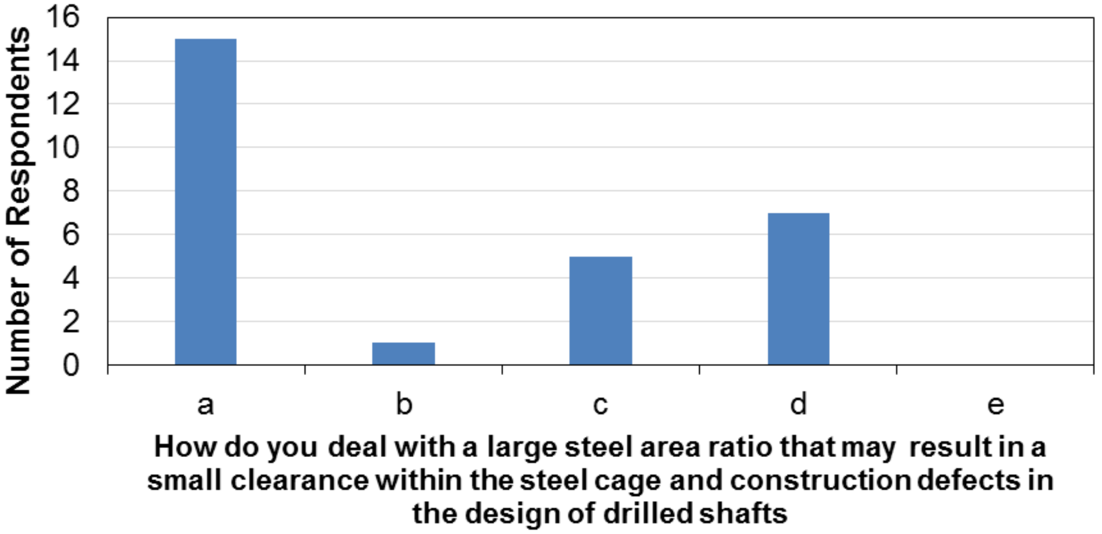

31) What is the highest value of yield strength that has been used by your agency in design?

a) ≤ 60 ksi

b) ≤ 80 ksi

c) ≤ 100 ksi

d) ≥ 120 ksi

RESPONSE:

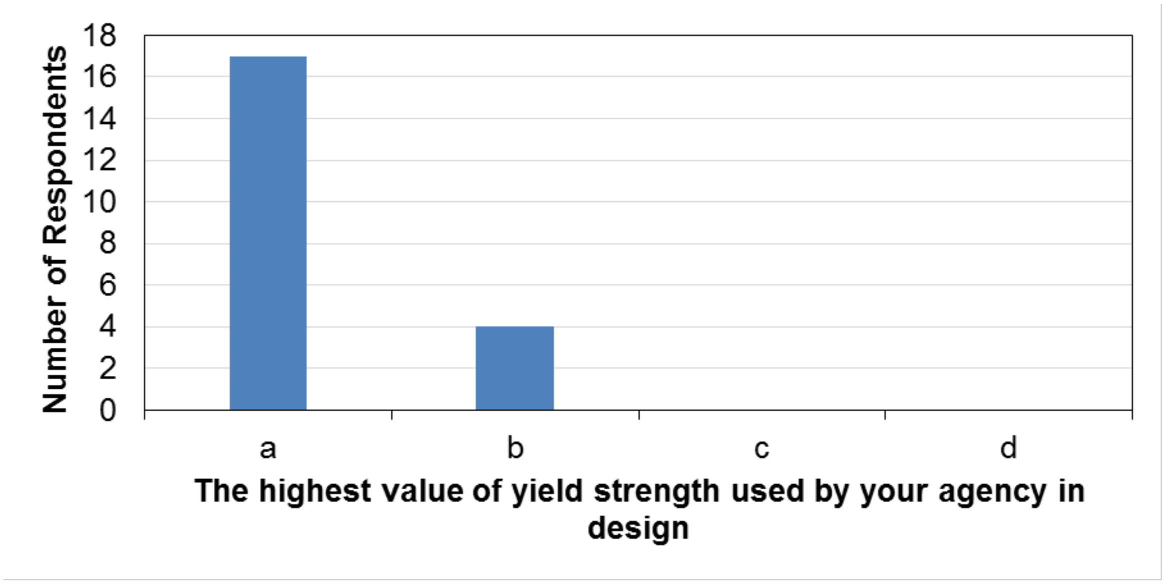

32) If high-strength steel has been used, please explain why it is used

a) Reducing usage of steel and/or member cross sections

b) Increasing the clearance within the reinforcement (Reducing the congestion problems)

c) Having better corrosion resistance

d) Providing better structural performance

e) Other (specify): ______________________________________

RESPONSE:

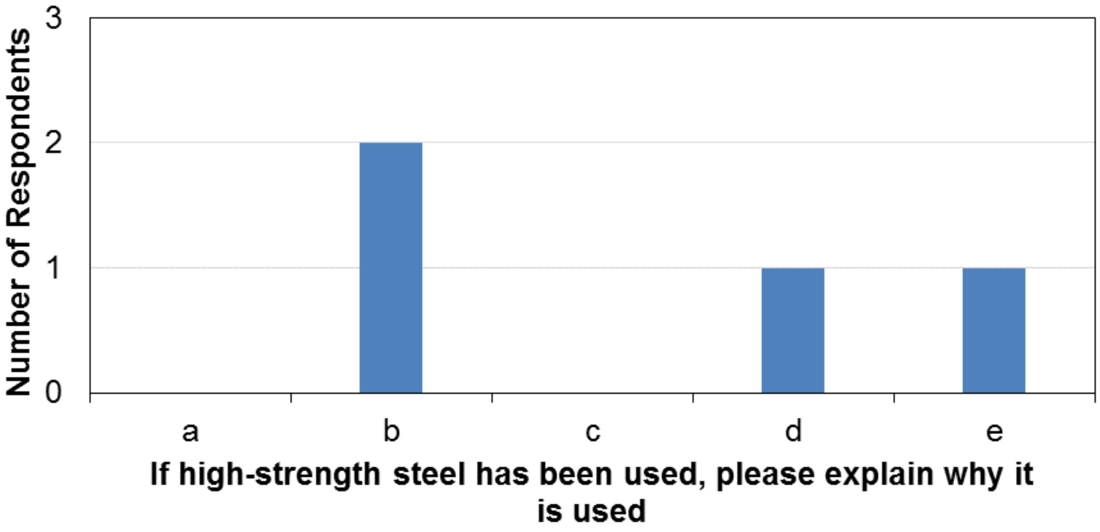

Comments:

The reason for one respondent is to value engineering proposal to improve constructability.

33) If high-strength steel has NOT been used, what are your concerns?

- a) Lower overstrength factors and/or other questions regarding performance
- b) Unknown bond characteristics of high-strength steel with concrete
- c) The control of shear/flexural crack widths in the concrete under service loads
- d) Has not been necessary in design
- e) Other (specify): ___________________________________

RESPONSE:

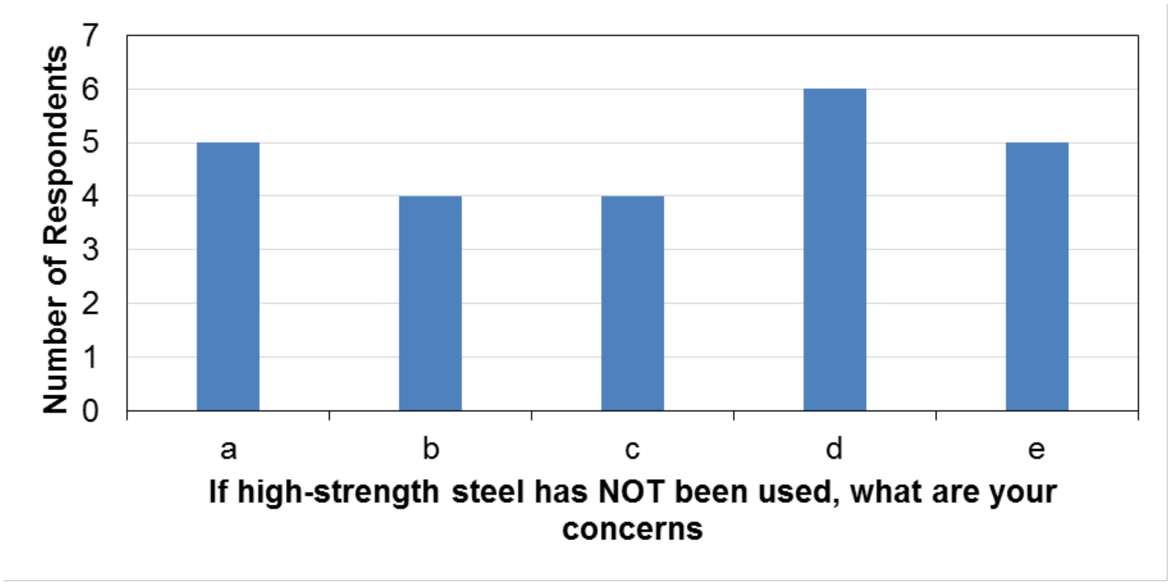

Comments:

Two respondents have the concerns of using high-strength steel on cost, two respondents do not use it due to the design specifications have not recommended high-strength steel in the design, and one respondent is due to unfamiliarity.

APPENDIX B CONE PENETRATION TEST (CPT) AND SEISMIC CONE PENETRATION TEST (SCPTS) RESULTS

This appendix presents the CPT and SCPT results used in this study.

Appendix B.1 SCPT-1

Operator: OGE TAJ
Sounding: P-1 2015
Cone Used: DDG1323

CPT Date/Time: 4/6/2015 9:19:10 AM
Location: OSU / P-1 2015 /Wave Lab Corvalis
Job Number: 15028 / OSU / P-1 2015 / Wave Lab Corvallis

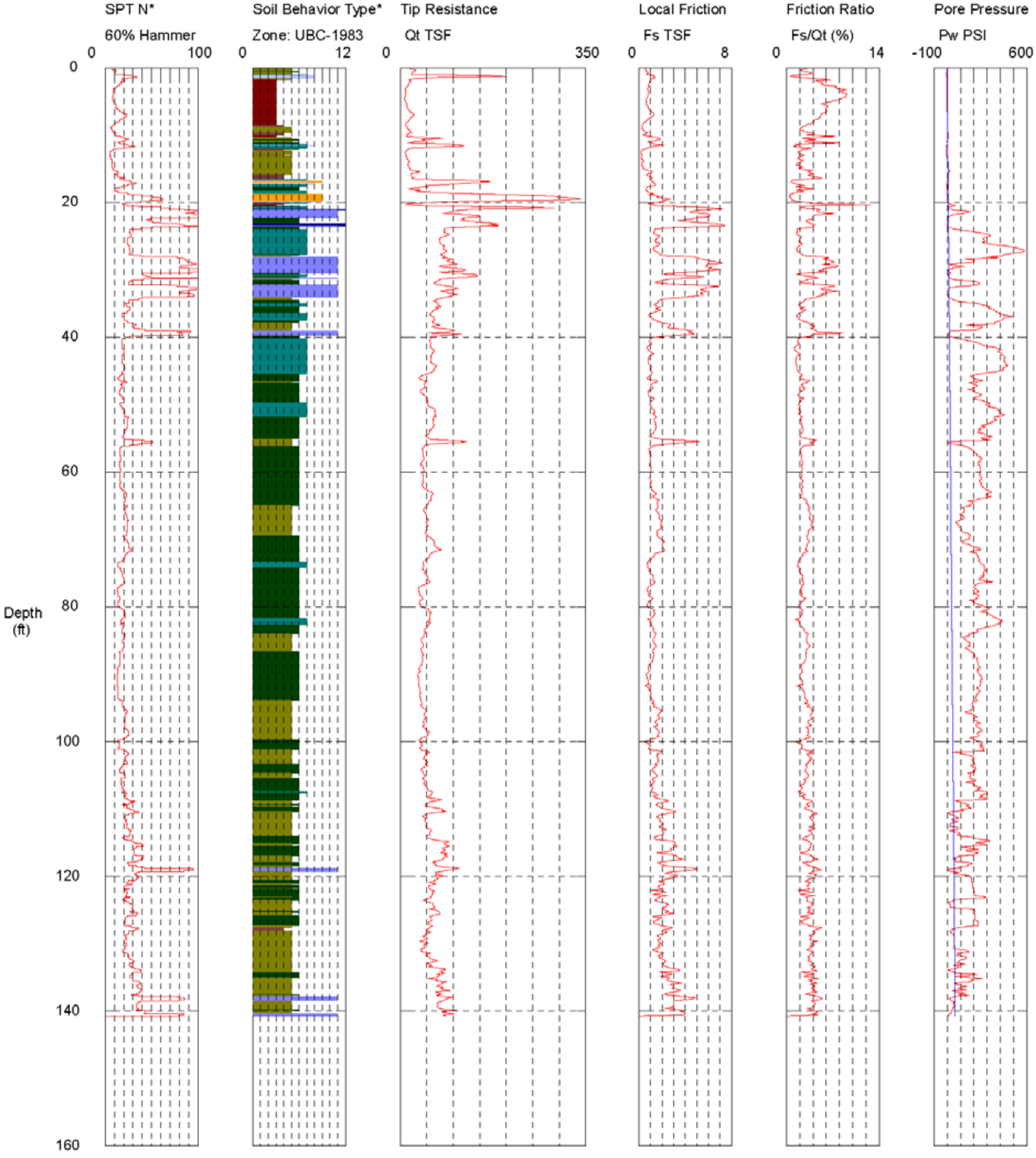

Maximum Depth = 140.75 feet

Depth Increment = 0.164 feet

■ 1 sensitive fine grained
■ 2 organic material
■ 3 clay
■ 4 silty clay to clay
■ 5 clayey silt to silty clay
■ 6 sandy silt to clayey silt
■ 7 silty sand to sandy silt
■ 8 sand to silty sand
■ 9 sand
■ 10 gravelly sand to sand
■ 11 very stiff fine grained (*)
■ 12 sand to clayey sand (*)

Soil behavior type and SPT based on data from UBC-1983

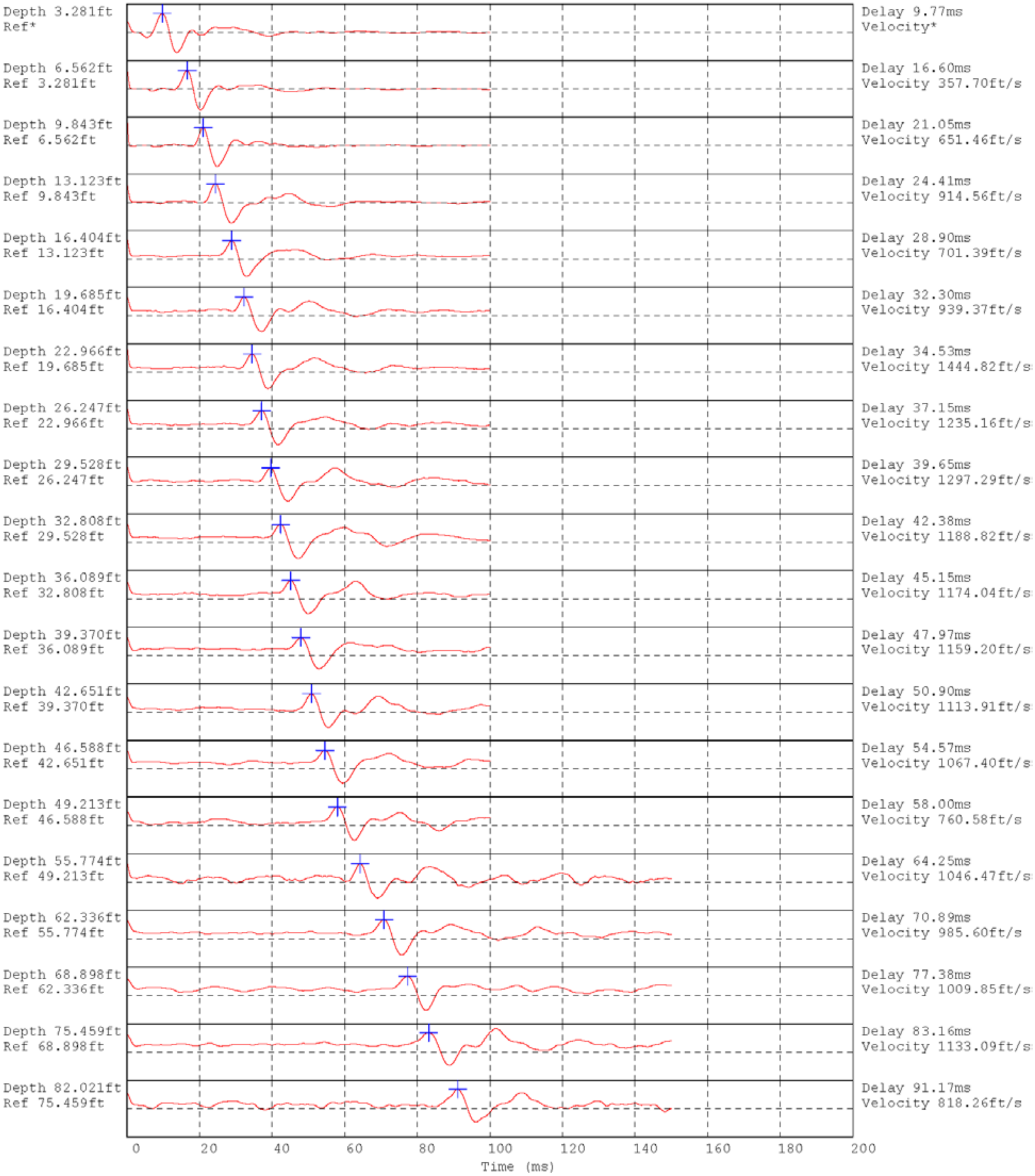

Hammer to Rod String Distance 1.3(m)
* = Not Determined

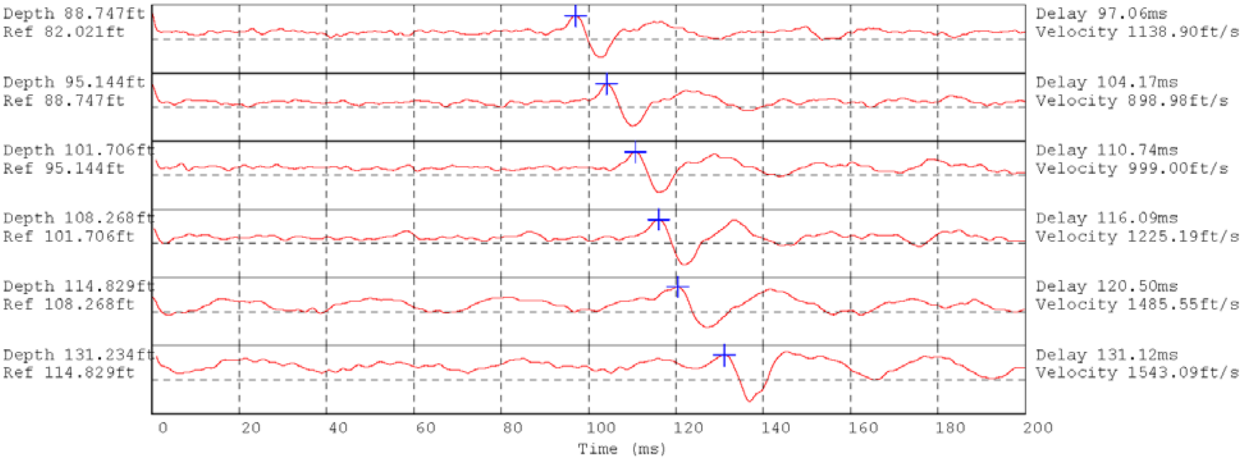

Hammer to Rod String Distance 1.3 (m)
* = Not Determined

Appendix B.2 SCPT-2

CUSTOMER: OSU / P-1 2016 / Wave Lab Corvallis
OPERATOR: OGE TAJ
CONE ID: DPG1211
LOCATION: OSU / P-1 2016 / Wave Lab Corvallis

JOB NUMBER: 16009 / OSU / P-1 2016 / Wave Lab Corvallis
HOLE NUMBER: P-1 2016
TEST DATE: 1/22/2016 10:05:14 AM

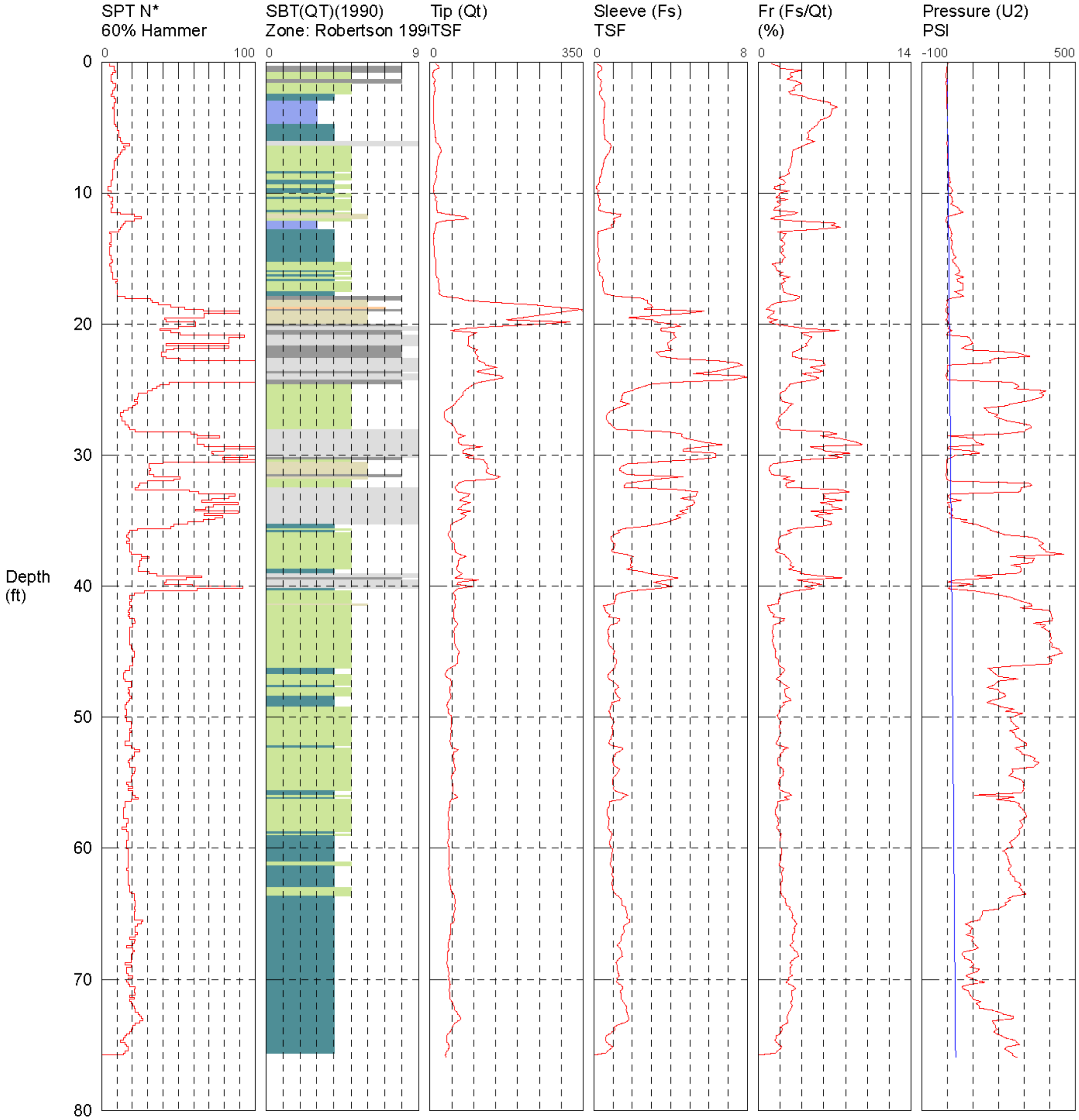

🟥 1 Sensitive, fine grained
🟥 2 Organic soils - peats
🟦 3 Clays - clay to silty clay
🟦 4 Silt mixtures - clayey silt to silty clay
🟩 5 Sand mixtures - silty sand to sandy silt
🟨 6 Sands - clean sand to silty sand
🟧 7 Gravelly sand to sand
⬛ 8 Very stiff sand to clayey sand **
⬜ 9 Very stiff, fine grained **

*SBT: Robertson 1990; **Overconsolidated or Cemented; *SBT/SPT CORRELATION: UBC-1983

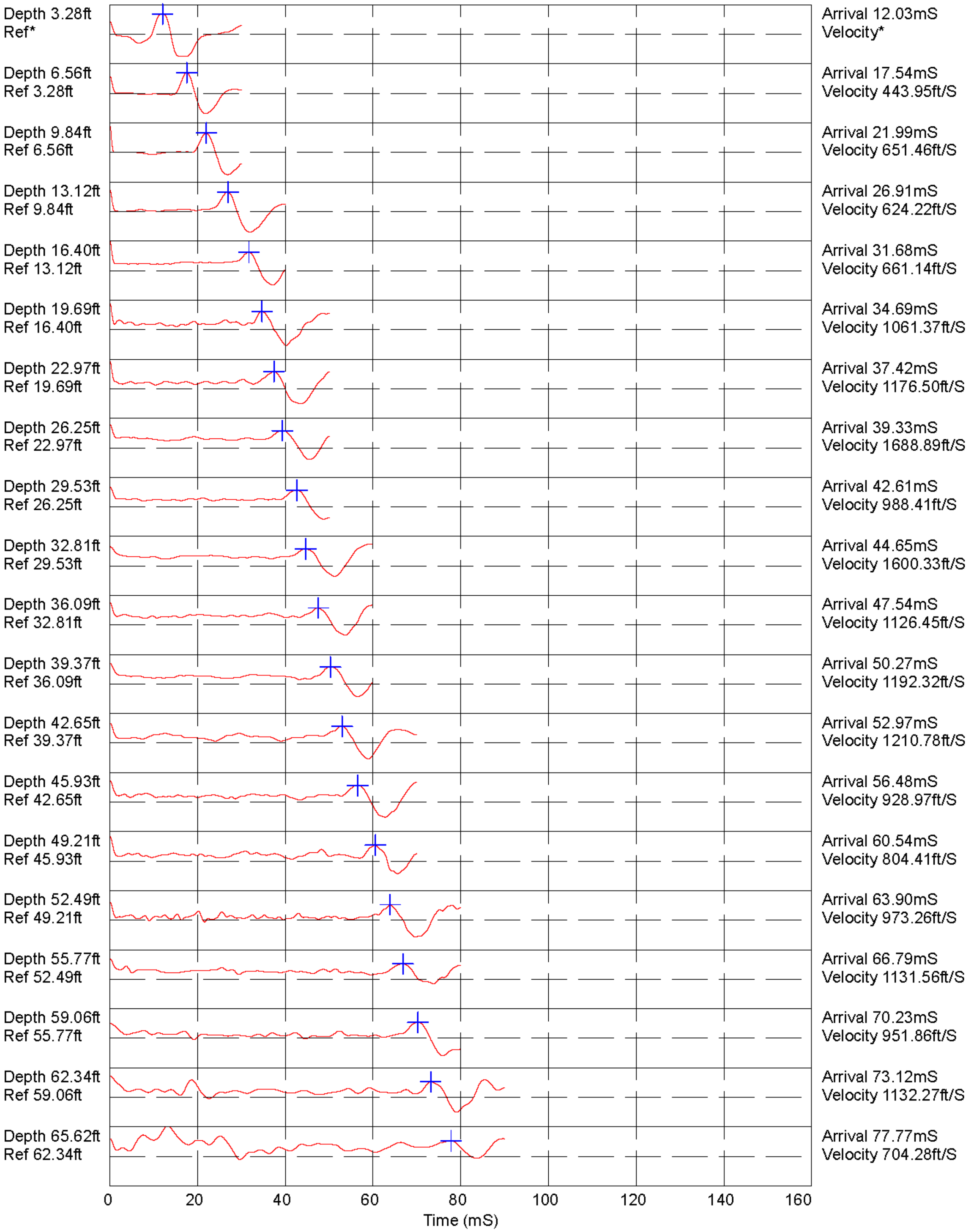
Depth 3.28ft
Ref*
Arrival 12.03mS
Velocity*
Depth 6.56ft
Ref 3.28ft
Arrival 17.54mS
Velocity 443.95ft/S
Depth 9.84ft
Ref 6.56ft
Arrival 21.99mS
Velocity 651.46ft/S
Depth 13.12ft
Ref 9.84ft
Arrival 26.91mS
Velocity 624.22ft/S
Depth 16.40ft
Ref 13.12ft
Arrival 31.68mS
Velocity 661.14ft/S
Depth 19.69ft
Ref 16.40ft
Arrival 34.69mS
Velocity 1061.37ft/S
Depth 22.97ft
Ref 19.69ft
Arrival 37.42mS
Velocity 1176.50ft/S
Depth 26.25ft
Ref 22.97ft
Arrival 39.33mS
Velocity 1688.89ft/S
Depth 29.53ft
Ref 26.25ft
Arrival 42.61mS
Velocity 988.41ft/S
Depth 32.81ft
Ref 29.53ft
Arrival 44.65mS
Velocity 1600.33ft/S
Depth 36.09ft
Ref 32.81ft
Arrival 47.54mS
Velocity 1126.45ft/S
Depth 39.37ft
Ref 36.09ft
Arrival 50.27mS
Velocity 1192.32ft/S
Depth 42.65ft
Ref 39.37ft
Arrival 52.97mS
Velocity 1210.78ft/S
Depth 45.93ft
Ref 42.65ft
Arrival 56.48mS
Velocity 928.97ft/S
Depth 49.21ft
Ref 45.93ft
Arrival 60.54mS
Velocity 804.41ft/S
Depth 52.49ft
Ref 49.21ft
Arrival 63.90mS
Velocity 973.26ft/S
Depth 55.77ft
Ref 52.49ft
Arrival 66.79mS
Velocity 1131.56ft/S
Depth 59.06ft
Ref 55.77ft
Arrival 70.23mS
Velocity 951.86ft/S
Depth 62.34ft
Ref 59.06ft
Arrival 73.12mS
Velocity 1132.27ft/S
Depth 65.62ft
Ref 62.34ft
Arrival 77.77mS
Velocity 704.28ft/S
0
20
40
60
80
100
120
140
160
Time (mS)

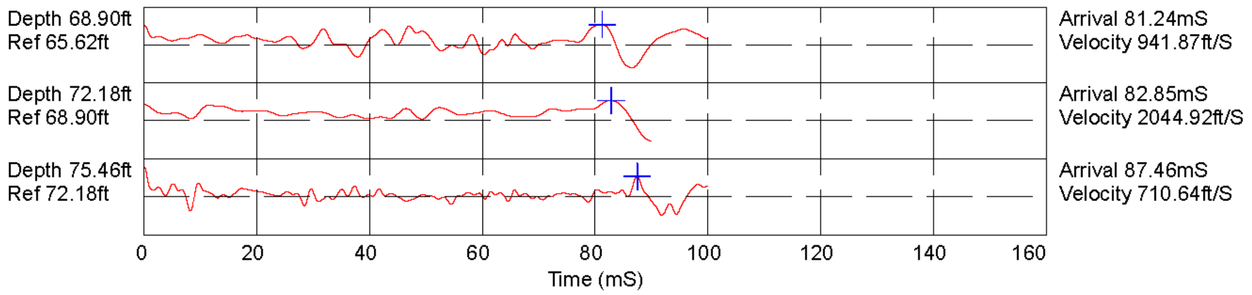

Hammer to Rod String Distance (ft): 4.27
* = Not Determined

JOB NUMBER: 16009 / OSU / P-1 2016 / Wave Lab Corvallis

Appendix B.3 SCPT-3

JOB NUMBER: 16009 / OSU / P-2 2016 / Wave Lab Corvallis
CUSTOMER: OSU / P-2 2016 / Wave Lab Corvallis
HOLE NUMBER: P-2 2016
OPERATOR: OGE TAJ
TEST DATE: 1/22/2016 12:16:21 PM
CONE ID: DPG1211
LOCATION: OSU / P-2 2016 / Wave Lab Corvallis

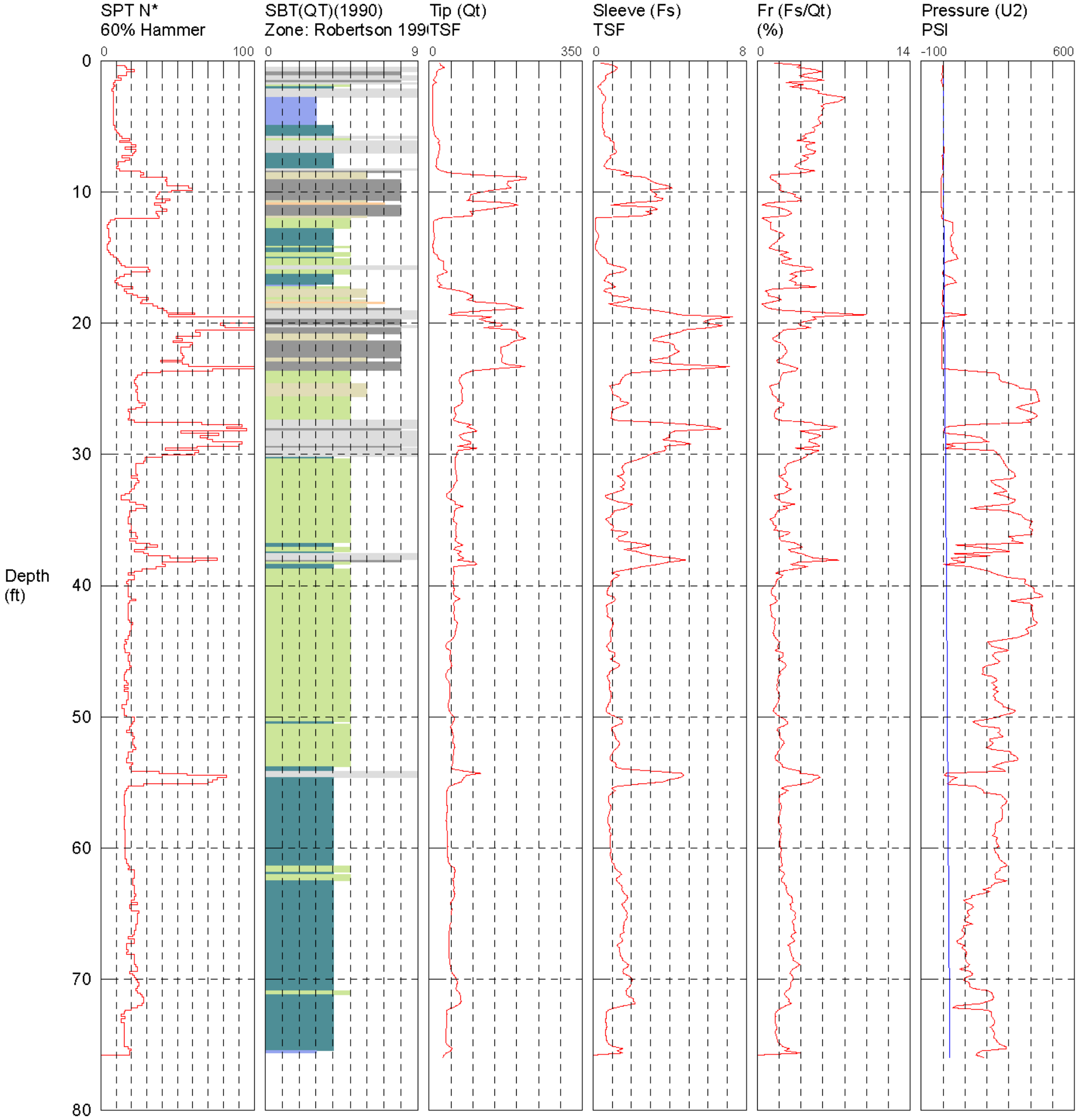

🟥 1 Sensitive, fine grained
🟥 2 Organic soils - peats
🟦 3 Clays - clay to silty clay
🟦 4 Silt mixtures - clayey silt to silty clay
🟩 5 Sand mixtures - silty sand to sandy silt
🟨 6 Sands - clean sand to silty sand
🟧 7 Gravelly sand to sand
⬛ 8 Very stiff sand to clayey sand **
⬜ 9 Very stiff, fine grained **

*SBT: Robertson 1990; **Overconsolidated or Cemented; *SBT/SPT CORRELATION: UBC-1983

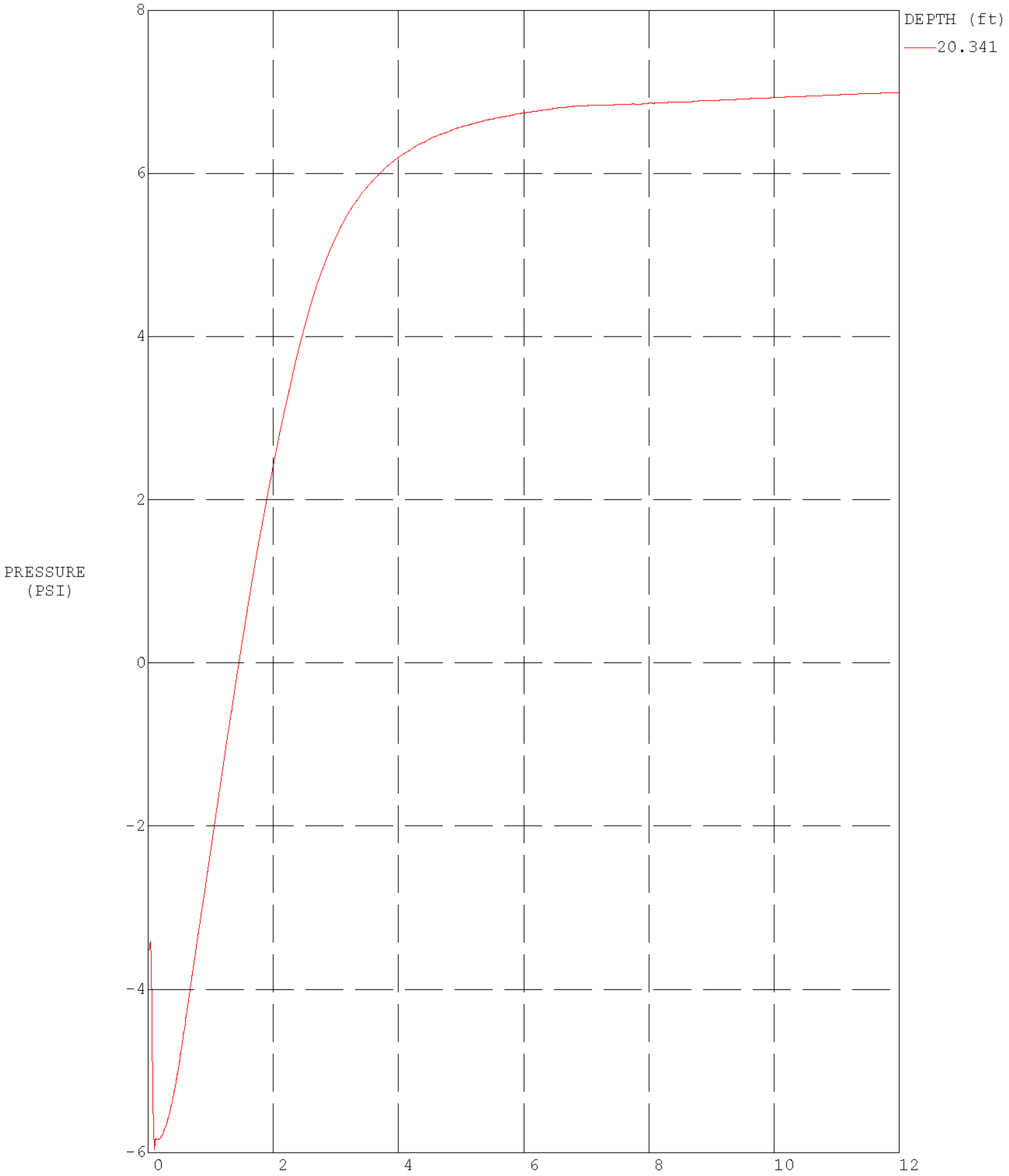

MAXIMUM PRESSURE = 6.992 (PSI)IME: (MINUTES)
HYDROSTATIC PRESSURE = 7.092 (PSI), WATER TABLE: 4.00 ft
JOB NUMBER: 16009 / OSU / P-2 2016 / Wave Lab Corvallis

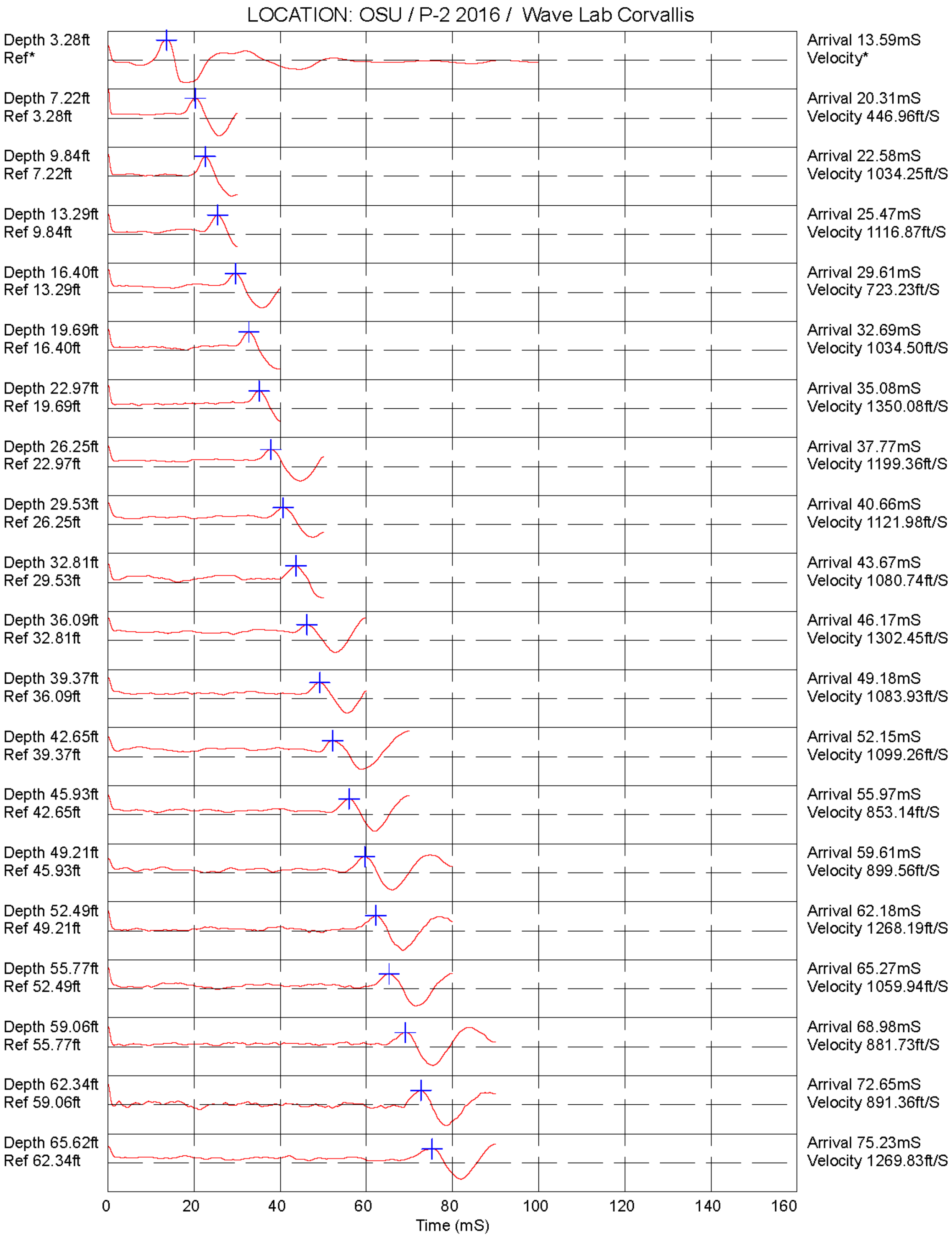
LOCATION: OSU / P-2 2016 / Wave Lab Corvallis
Depth 3.28ft
Ref*
Arrival 13.59mS
Velocity*
Depth 7.22ft
Ref 3.28ft
Arrival 20.31mS
Velocity 446.96ft/S
Depth 9.84ft
Ref 7.22ft
Arrival 22.58mS
Velocity 1034.25ft/S
Depth 13.29ft
Ref 9.84ft
Arrival 25.47mS
Velocity 1116.87ft/S
Depth 16.40ft
Ref 13.29ft
Arrival 29.61mS
Velocity 723.23ft/S
Depth 19.69ft
Ref 16.40ft
Arrival 32.69mS
Velocity 1034.50ft/S
Depth 22.97ft
Ref 19.69ft
Arrival 35.08mS
Velocity 1350.08ft/S
Depth 26.25ft
Ref 22.97ft
Arrival 37.77mS
Velocity 1199.36ft/S
Depth 29.53ft
Ref 26.25ft
Arrival 40.66mS
Velocity 1121.98ft/S
Depth 32.81ft
Ref 29.53ft
Arrival 43.67mS
Velocity 1080.74ft/S
Depth 36.09ft
Ref 32.81ft
Arrival 46.17mS
Velocity 1302.45ft/S
Depth 39.37ft
Ref 36.09ft
Arrival 49.18mS
Velocity 1083.93ft/S
Depth 42.65ft
Ref 39.37ft
Arrival 52.15mS
Velocity 1099.26ft/S
Depth 45.93ft
Ref 42.65ft
Arrival 55.97mS
Velocity 853.14ft/S
Depth 49.21ft
Ref 45.93ft
Arrival 59.61mS
Velocity 899.56ft/S
Depth 52.49ft
Ref 49.21ft
Arrival 62.18mS
Velocity 1268.19ft/S
Depth 55.77ft
Ref 52.49ft
Arrival 65.27mS
Velocity 1059.94ft/S
Depth 59.06ft
Ref 55.77ft
Arrival 68.98mS
Velocity 881.73ft/S
Depth 62.34ft
Ref 59.06ft
Arrival 72.65mS
Velocity 891.36ft/S
Depth 65.62ft
Ref 62.34ft
Arrival 75.23mS
Velocity 1269.83ft/S
0
20
40
60
80
100
120
140
160
Time (mS)

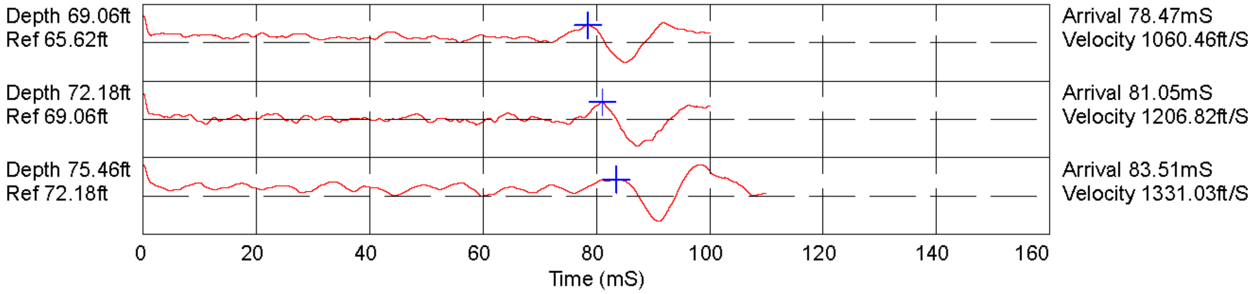

Hammer to Rod String Distance (ft): 4.27
* = Not Determined

Appendix B.4 CPT-4

Operator: OGE TAJ
Sounding: Uncased Center
Cone Used: DDG1323
GPS Data: NO GPS

CPT Date/Time: 6/15/2016 3:28:51 PM
Location: OSU / Uncased Center / Wave Lab Corvallis
Job Number: 16053 / OSU / Uncased Center / Wave Lab Corvallis

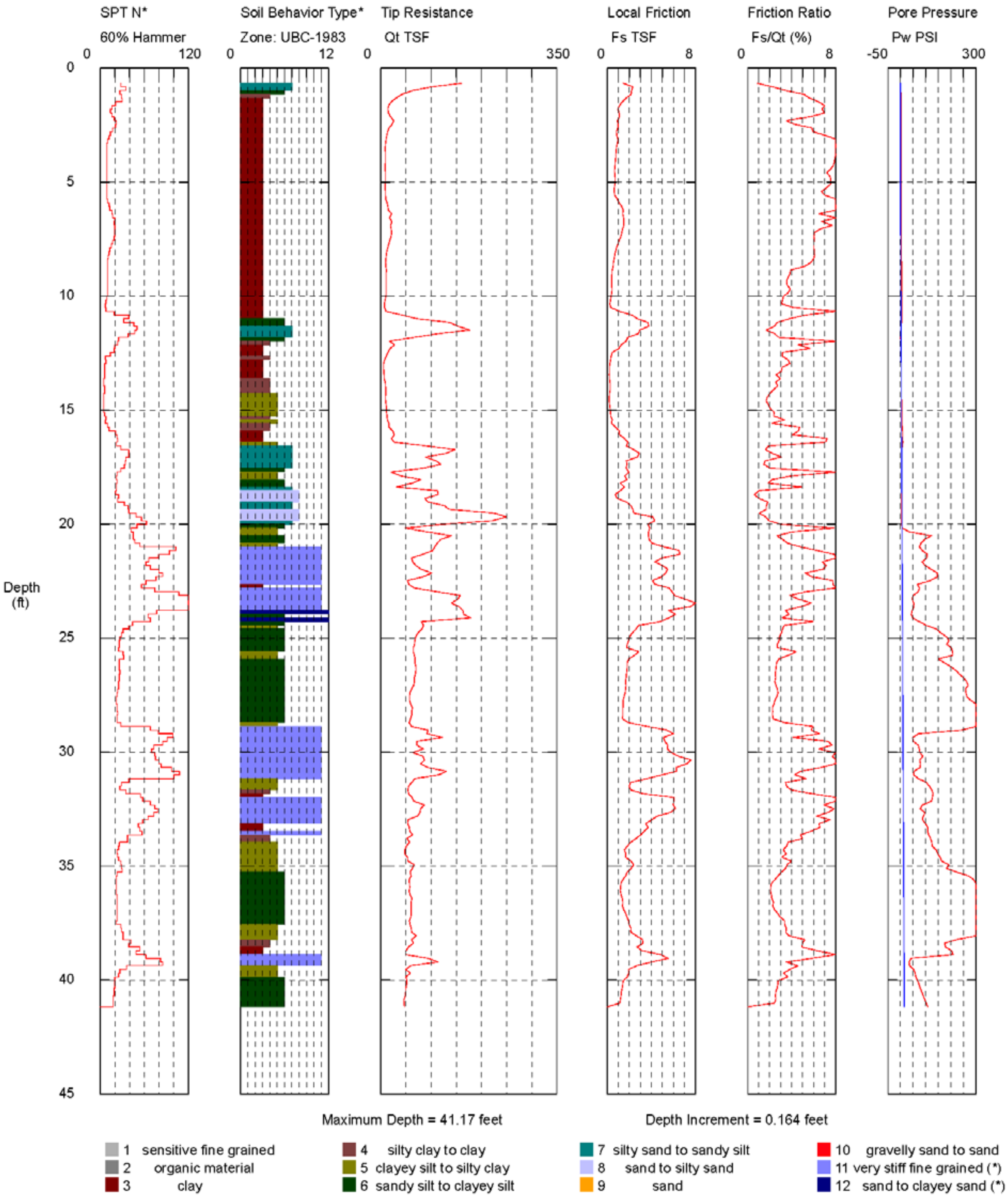

Appendix B.5 SCPT-5

Operator: OGE TAJ
Sounding: Cased Center
Cone Used: DDG1323
GPS Data: NO GPS

CPT Date/Time: 6/15/2016 1:12:11 PM
Location: OSU / Cased Center / Wave Lab Corvallis
Job Number: 16053 / OSU / Cased Center / Wave Lab Corvallis

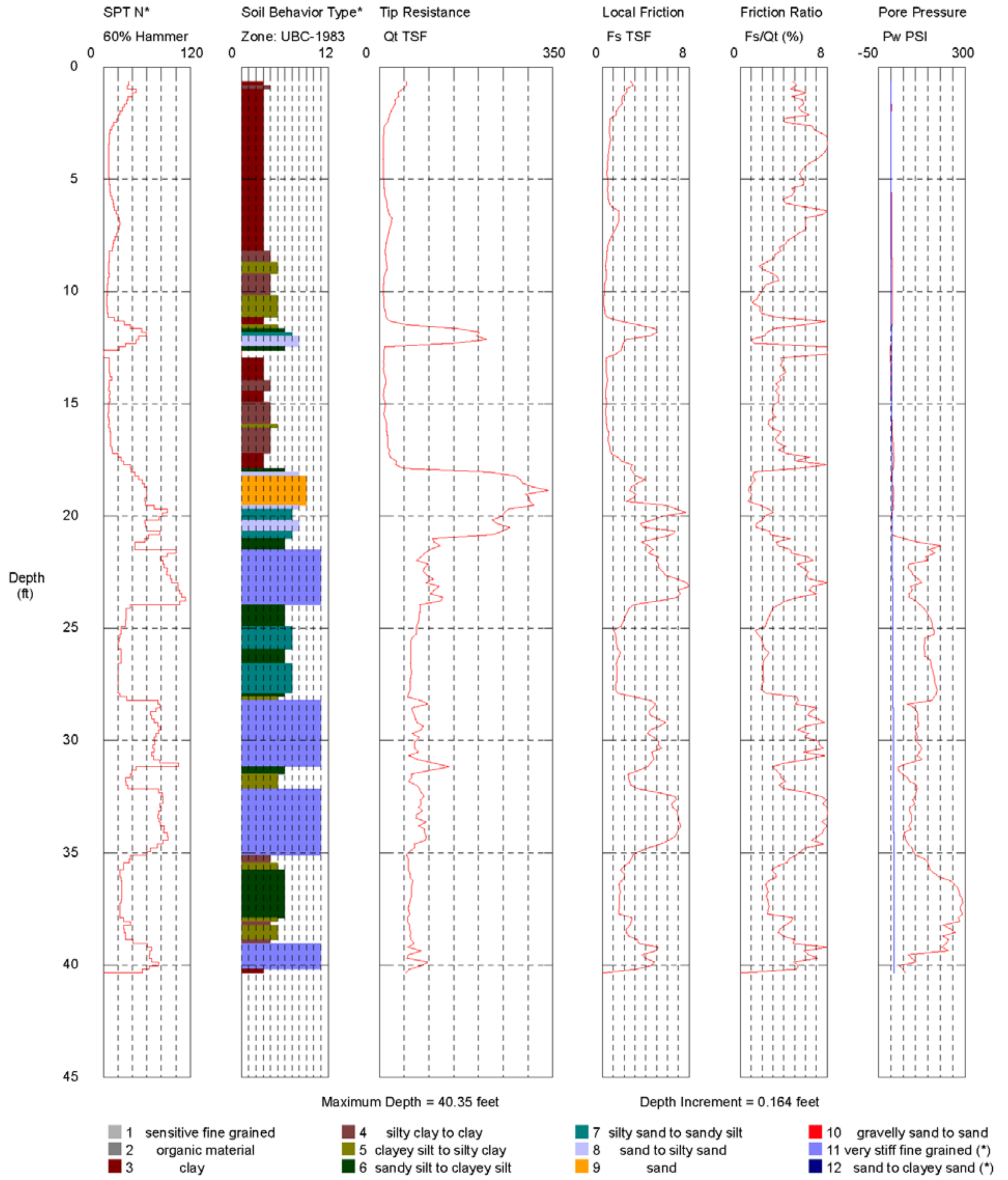

*Soil behavior type and SPT based on data from UBC-1983

Appendix B.6 SCPT-6

Operator: OGE TAJ
Sounding: Cased South
Cone Used: DDG1323
GPS Data: NO GPS

CPT Date/Time: 6/15/2016 2:24:35 PM
Location: OSU / Cased South / Wave Lab Corvallis
Job Number: 16053 / OSU / Cased South / Wave Lab Corvallis

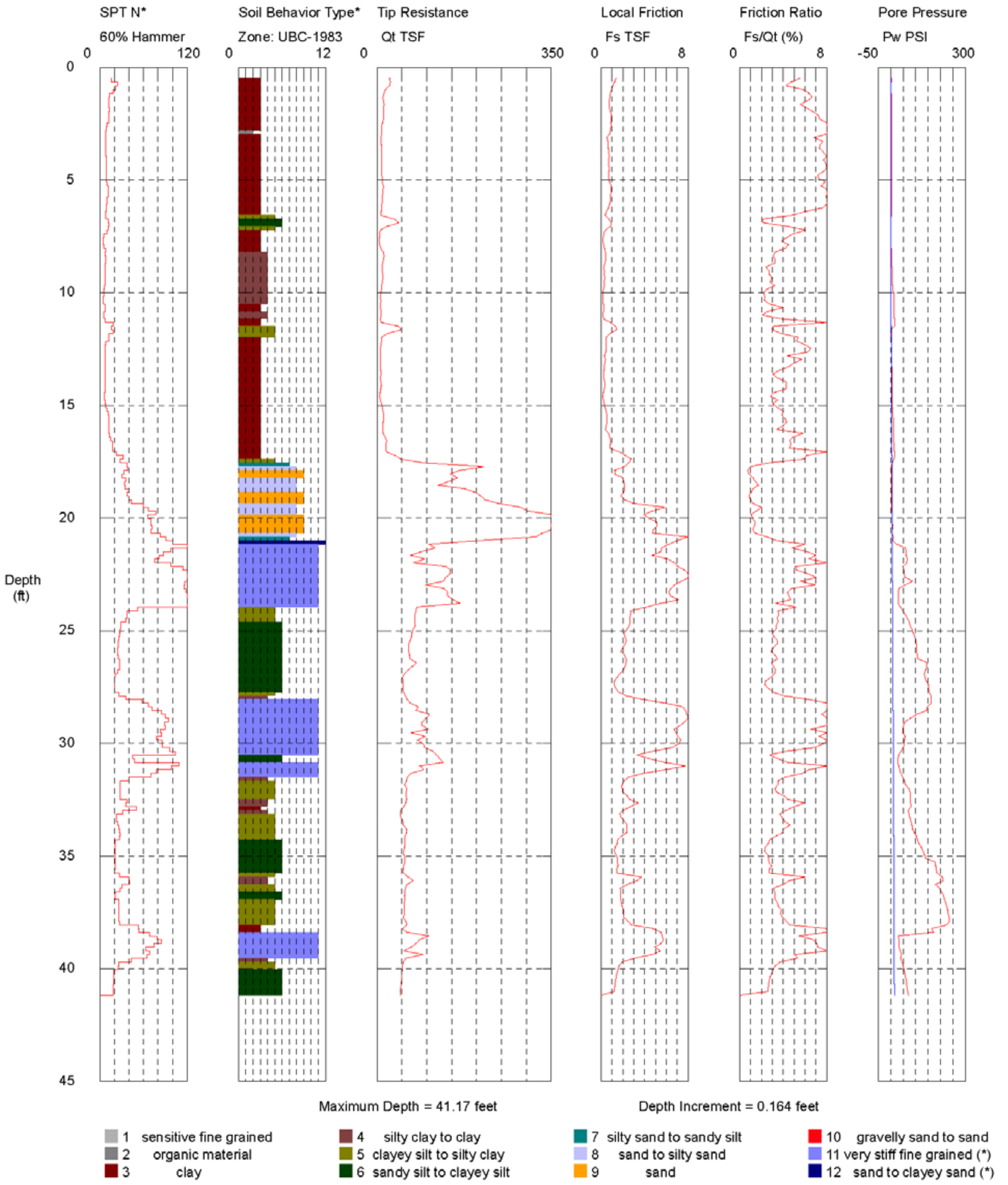

*Soil behavior type and SPT based on data from UBC-1983

Appendix B.7 SCPT-7

Operator: OGE TAJ
Sounding: Cased North
Cone Used: DDG1323
GPS Data: NO GPS

CPT Date/Time: 6/15/2016 11:55:28 AM
Location: OSU / Cased North / Wave Lab Corvallis
Job Number: 16053 / OSU / Cased North / Wave Lab Corvallis

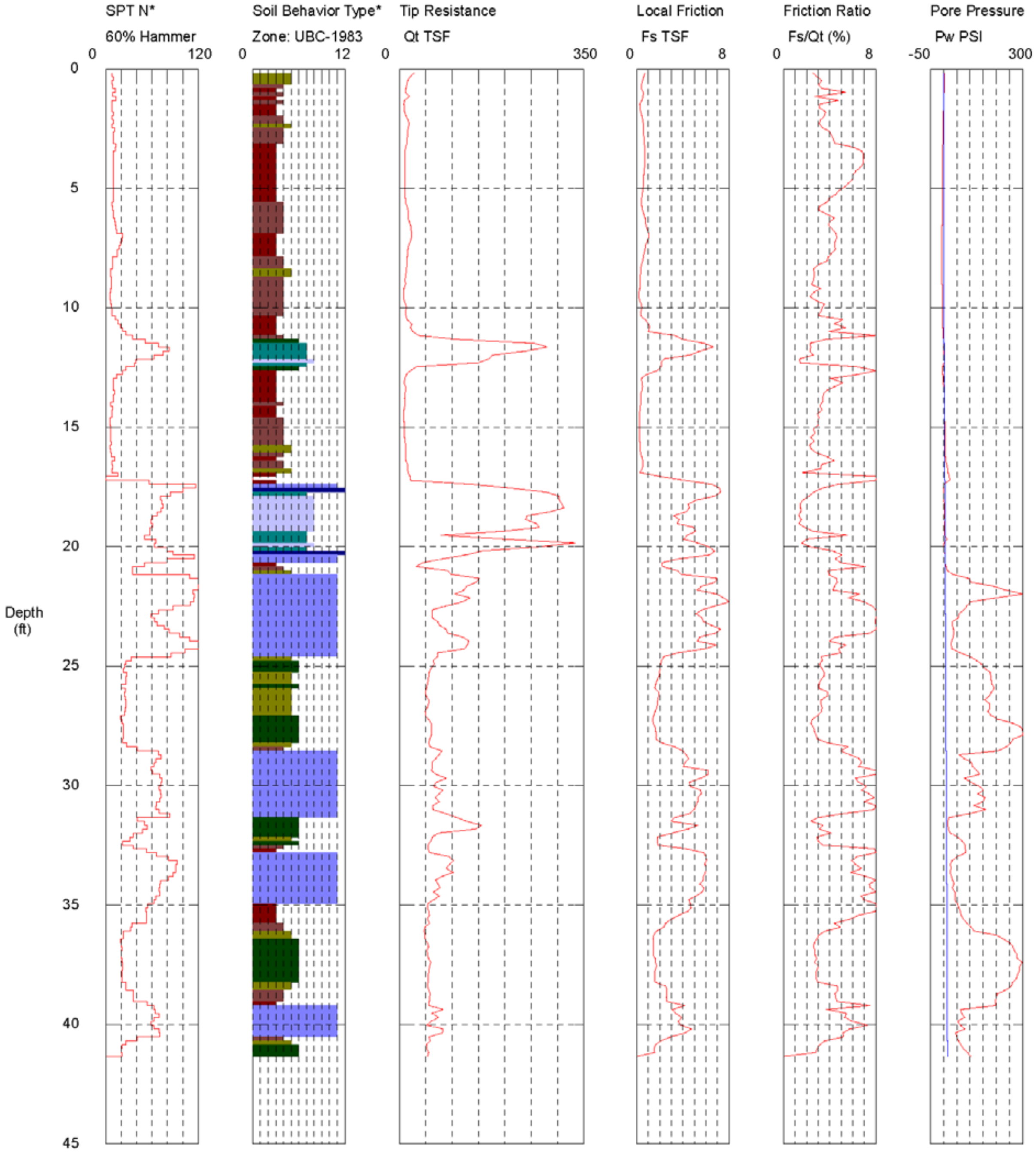

Maximum Depth = 41.34 feet

Depth Increment = 0.164 feet

■ 1 sensitive fine grained
■ 2 organic material
■ 3 clay
■ 4 silty clay to clay
■ 5 clayey silt to silty clay
■ 6 sandy silt to clayey silt
■ 7 silty sand to sandy silt
■ 8 sand to silty sand
■ 9 sand
■ 10 gravelly sand to sand
■ 11 very stiff fine grained (*)
■ 12 sand to clayey sand (*)

*Soil behavior type and SPT based on data from UBC-1983

Appendix B.8 1997 CPT-1

Operator: S.VAN/A.MES/W.Mc
Sounding: SND516
Cone Used: OSU

CPT Date/Time: 10-11-97 14:00
Location: P/1 OSU CORVALIS
Job Number: RESEARCH

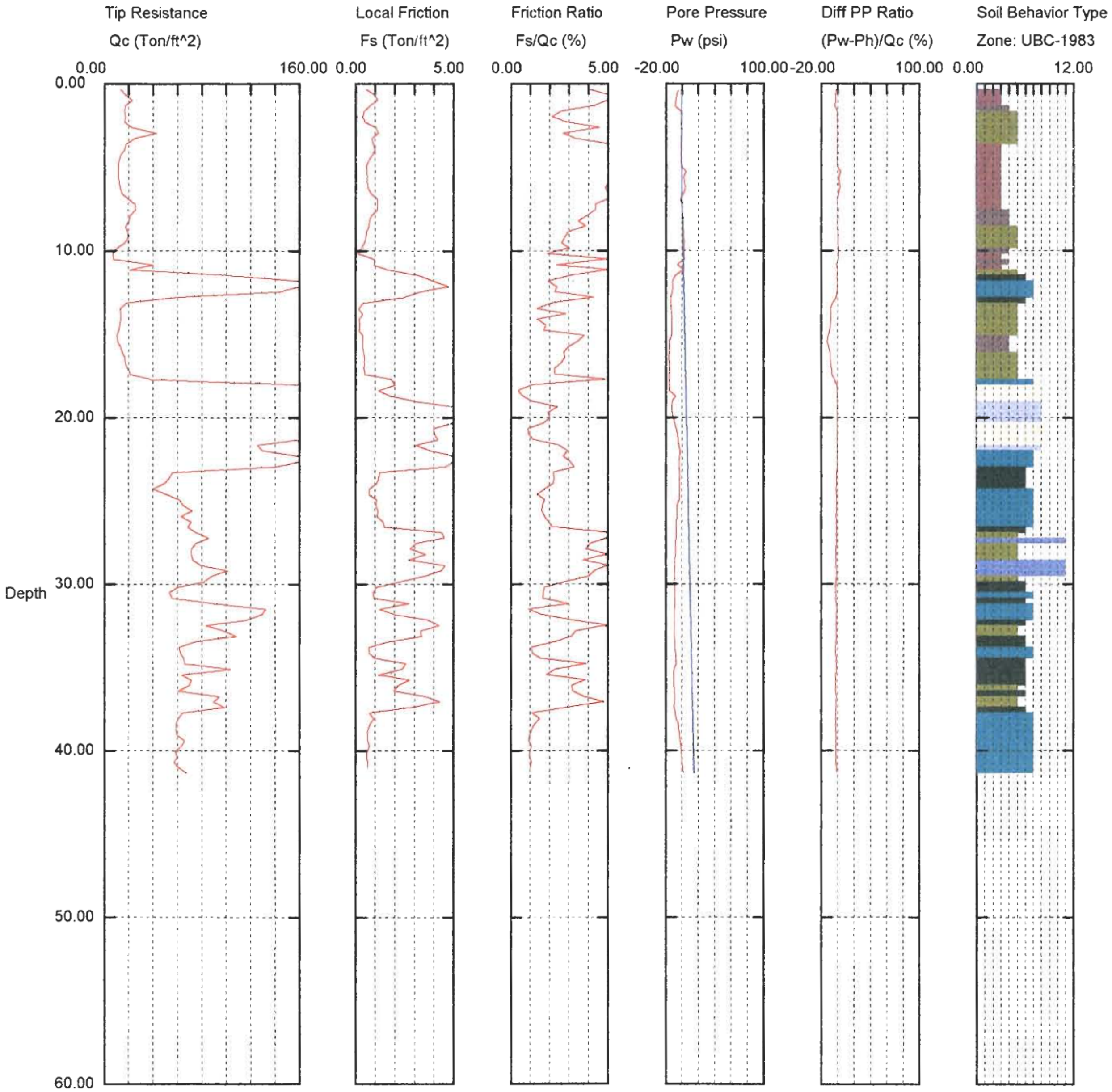

Maximum Depth = 41.34 feet

Depth Increment = 0.16 feet

1 sensitive fine grained
■ 2 organic material
■ 3 clay
■ 4 silty clay to clay
■ 5 clayey silt to silty clay
■ 6 sandy silt to clayey silt
■ 7 silty sand to sandy silt
■ 8 sand to silty sand
9 sand
10 gravelly sand to sand
■ 11 very stiff fine grained (*)
■ 12 sand to clayey sand (*)

APPENDIX C CROSSHOLE SONIC LOG (CSL) INTEGRITY TEST

This appendix presents the report of integrity testing of drilled foundation shafts using Crosshole Sonic Log (CSL) integrity test.

APPENDIX D THERMAL INTEGRITY PROFILING (TIP)

This appendix presents the report of integrity testing of drilled foundation shafts using Thermal Integrity Profiling (TIP) Thermal Wire method.